

ALMA MATER STUDIORUM  
UNIVERSITÀ DI BOLOGNA

Facoltà di Scienze Matematiche Fisiche e Naturali  
Dipartimento di Astronomia

DOTTORATO DI RICERCA IN ASTRONOMIA  
CICLO XXIII (2008-2010)

---

**EARLY-TYPE GALAXIES AS PROBES  
OF GALAXY FORMATION AND COSMOLOGY**

---

Tesi di Dottorato  
di  
**MICHELE ENNIO MARIA MORESCO**

COORDINATORE:  
Chiar.mo Prof. **Lauro MOSCARDINI**

RELATORE:  
Prof. **Andrea CIMATTI**

CORRELATORE:  
Dott. **Lucia POZZETTI**

Esame Finale Anno 2011

SCUOLA DI DOTTORATO IN SCIENZE MATEMATICHE, FISICHE E ASTRONOMICHE  
SETTORE SCIENTIFICO DISCIPLINARE: AREA 02 - SCIENZE FISICHE  
FIS/05 ASTRONOMIA E ASTROFISICA



*To my wife Caterina  
and my two daughters,  
Lucia and Agnese.*

*"What I like about experience is that it is such  
an honest thing. You may take any number  
of wrong turnings; but keep your eyes open  
and you will not be allowed to go very far  
before the warning signs appear. You may  
have deceived yourself, but experience  
is not trying to deceive you. The Universe  
rings true wherever you fairly test it."*

C. S. Lewis



# Contents

<b>List of figures</b>	<b>VII</b>
<b>List of tables</b>	<b>X</b>
<b>Preface and motivations</b>	<b>1</b>
<b>1 Cosmological background</b>	<b>7</b>
1.1 Brief History of the Universe . . . . .	7
1.2 Big Bang Theory basis . . . . .	9
1.2.1 Basic equations . . . . .	11
1.2.2 Redshift dependence . . . . .	12
1.2.3 Hubble parameter, distances and times . . . . .	14
1.3 Structure formation . . . . .	15
1.4 The dark Universe . . . . .	16
1.4.1 The discovery of dark energy . . . . .	17
1.4.2 Observational probes . . . . .	18
1.5 Cosmological parameters and $H(z)$ evaluation . . . . .	21
<b>2 A perspective on early-type galaxies</b>	<b>25</b>
2.1 Properties of ETGs . . . . .	26
2.1.1 Color-magnitude and color- $\sigma$ relation . . . . .	28
2.1.2 The fundamental plane . . . . .	31
2.1.3 The line-strength diagnostics . . . . .	31
2.2 Galaxy evolution . . . . .	32
2.3 Theories of formation of ETGs . . . . .	36
2.3.1 The downsizing scenario . . . . .	38
2.4 Conclusions on ETGs properties . . . . .	42

<b>3</b>	<b>Definition and characterization of ETGs samples</b>	<b>43</b>
3.1	Spectroscopic surveys . . . . .	43
3.1.1	Sloan Digital Sky Survey (ETGs at $0 < z < 0.5$ ) . . . . .	43
3.1.2	zCOSMOS (ETGs up to $z \sim 1$ ) . . . . .	45
3.2	Methods of analysis . . . . .	47
3.2.1	The stellar population synthesis models . . . . .	47
3.2.2	The SED-fitting technique . . . . .	48
3.2.3	The spectroscopic analysis . . . . .	49
3.3	Methods of selection . . . . .	51
3.3.1	Morphological criterion . . . . .	51
3.3.2	Photometric criterion . . . . .	53
3.3.3	Spectroscopic criterion . . . . .	54
3.4	The final ETGs samples . . . . .	56
3.5	SDSS and zCOSMOS Photometric data . . . . .	60
3.5.1	Zeropoint offsets and errors correction . . . . .	61
3.6	Estimate of physical and evolutionary parameters . . . . .	70
3.6.1	The stellar mass . . . . .	70
3.6.2	The star formation history . . . . .	72
3.6.3	The dust reddening . . . . .	74
3.6.4	The age . . . . .	76
3.6.5	Degenerations: the case of age-metallicity, but not only... .	77
3.7	ETGs sample in literature . . . . .	80
3.8	Conclusions about the selection of the ETGs samples . . . . .	83
<b>4</b>	<b>Early-type galaxies as evolutionary probes</b>	<b>85</b>
4.1	The data samples . . . . .	86
4.1.1	Color estimate . . . . .	86
4.1.2	Overdensity definition . . . . .	86
4.1.3	Mass estimate . . . . .	90
4.1.4	D4000 and $EW_0(H\delta)$ definitions . . . . .	91
4.2	The color analysis . . . . .	94
4.2.1	Color distribution of early-type galaxies . . . . .	94
4.2.2	Color-environment relation . . . . .	94
4.2.3	Color-mass relation . . . . .	96
4.3	The spectroscopic analysis . . . . .	99
4.4	Evidences of mass downsizing . . . . .	105
4.5	Conclusions about mass and environment dependence of ETGs . . . . .	108

<b>5</b>	<b>Early-type galaxies as cosmological probes</b>	<b>111</b>
5.1	The age-redshift relation . . . . .	113
5.1.1	Preliminary analysis . . . . .	114
5.2	The data sample . . . . .	118
5.2.1	Metallicity, mass and star formation history estimation . . . . .	118
5.3	Linking the 4000 Å break to the expansion history of the Universe: the D4000-redshift relation . . . . .	125
5.3.1	Calibration of the $D4000_n$ -age relation . . . . .	125
5.3.2	A linear model . . . . .	130
5.4	Deriving the $D4000_n$ -redshift relation . . . . .	132
5.5	Constraints on the cosmological parameters . . . . .	134
5.5.1	Statistical methods . . . . .	135
5.5.2	The Hubble constant . . . . .	136
5.5.3	The dark energy equation-of-state . . . . .	138
5.5.4	Study of the systematics . . . . .	138
5.6	Total systematic uncertainty and results . . . . .	145
5.7	Conclusions about constraining Universe expansion history with ETGs . . . . .	146
<b>6</b>	<b>Conclusions and future prospects</b>	<b>149</b>
6.1	Future prospects . . . . .	153
	<b>Bibliography</b>	<b>162</b>
	<b>Publications</b>	<b>163</b>



# List of Figures

1.1	Anisotropies of the CMB as seen by WMAP. . . . .	10
1.2	Evolution of radiation, matter, and dark energy densities with redshift. . . . .	13
1.3	Content of the Universe as seen by WMAP-5years data. . . . .	16
1.4	Contour plots of $(\Omega_M, \Omega_\Lambda)$ and $(\Omega_M, w)$ plane as found combining SNe, BAO and CMB. . . . .	22
1.5	$H(z)$ measurements. . . . .	23
2.1	Hubble tuning fork diagram. . . . .	26
2.2	Properties of galaxies as a function of the Hubble sequence. . . . .	27
2.3	Contributions to the total stellar mass and to the number of galaxies by early-type and late-type galaxies. . . . .	28
2.4	Color-magnitude relation and color-sigma relation for galaxies in the Coma cluster. . . . .	29
2.5	Average spectrum of 4 ETGs found at $1.6 \lesssim z \lesssim 1.9$ in the K20 survey. . . . .	34
2.6	Scenarios for ETGs formation. . . . .	40
3.1	SDSS galaxy map. . . . .	44
3.2	Theoretical spectra as a function of ages and metallicity. . . . .	49
3.3	Contamination between different morphological selection of ETGs. . . . .	52
3.4	Extended CWW templates used to evaluate photometric type of galaxies. . . . .	53
3.5	Redshift distributions of SDSS and zCOSMOS <i>ETGs</i> samples. . . . .	55
3.6	$K - 24\mu m$ color evaluated for various templates of galaxies as a function of redshift. . . . .	56
3.7	Example of outliers in the ETGs selection. . . . .	58
3.8	Example of early-type galaxies in the zCOSMOS “ <i>ETGs</i> ” sample. . . . .	59
3.9	SDSS filters transmission functions. . . . .	60

3.10	zCOSMOS filters transmission functions. . . . .	61
3.11	Distribution of $(m_{obs,i} - m_{ref,i} + \text{shift})$ for each zCOSMOS band using BC03 models. . . . .	64
3.12	Zeropoint shifts and resulting $(m_{obs,i} - m_{ref,i})$ for each filter of zCOSMOS survey using BC03 models. . . . .	65
3.13	Distribution of $(m_{obs,i} - m_{ref,i} + \text{shift})/\sigma(m_{obs,i})$ for each zCOSMOS band using BC03 models. . . . .	66
3.14	Distribution of $(m_{obs,i} - m_{ref,i} + \text{shift})$ for each SDSS+2mass band using BC03 models. . . . .	67
3.15	Zeropoint shifts applied and resulting $(m_{obs,i} - m_{ref,i})$ for each filter of SDSS+2MASS survey using BC03 models. . . . .	68
3.16	Distribution of $(m_{obs,i} - m_{ref,i} + \text{shift})/\sigma(m_{obs,i})$ for each SDSS+2MASS band using BC03 models. . . . .	69
3.17	Mass dependence of ETGs SED. . . . .	71
3.18	Mass distributions of SDSS and zCOSMOS <i>ETGs</i> samples with BC03 models. . . . .	72
3.19	Exponentially declining and delayed exponential SFHs. . . . .	73
3.20	SFH $\tau$ parameter distributions of SDSS and zCOSMOS <i>ETGs</i> samples. . . . .	74
3.21	$A_V$ distributions of SDSS and zCOSMOS <i>ETGs</i> samples. . . . .	75
3.22	Age distributions of SDSS and zCOSMOS <i>ETGs</i> samples. . . . .	77
3.23	Age-metallicity degeneracy in the SED-fitting. . . . .	78
3.24	Age- $\tau$ degeneracy in the SED-fitting. . . . .	79
3.25	Luminosity functions of early-type galaxies. . . . .	81
3.26	Galaxy stellar mass functions for early-type galaxies. . . . .	82
4.1	Distribution of $(U - V)_{rest}$ color and color-mass relation for the parent zCOSMOS bright 10k galaxies sample, <i>Red</i> galaxies, and <i>ETGs</i> . . . . .	87
4.2	Overdensity-redshift and mass-redshift distributions of the sample of <i>Red galaxies</i> and <i>ETGs</i> . . . . .	88
4.3	Stacked spectrum of zCOSMOS <i>ETGs</i> . . . . .	92
4.4	$(U - V)$ rest-frame color distribution for <i>Red galaxies</i> as a function of overdensity and mass. . . . .	93
4.5	Mean color of <i>Red galaxies</i> and <i>ETGs</i> as a function of environment in different mass bins. . . . .	95
4.6	Mean color of <i>Red galaxies</i> and <i>ETGs</i> as a function of mass in the four quartiles of environment. . . . .	97
4.7	Slopes of the color-mass relation evaluated in the four redshift bins and different environments. . . . .	98
4.8	$D4000_n$ evaluated for different mass bins in fixed environment quartiles and for different overdensity quartiles in fixed mass bins. . . . .	100

4.9	$EW_0(H\delta)$ evaluated for different mass bins in fixed environment quartiles and for different environment quartiles in fixed mass bins.	101
4.10	Stellar mass as a function of lookback time to formation and mass histograms of extreme tertiles for <i>ETGs</i> sample (CB07 models).	104
4.11	Stellar mass as a function of lookback time to formation and mass histograms of extreme tertiles for <i>ETGs</i> sample (M05 models).	105
4.12	Comparison between lookback time to formation evaluated with CB07 and BC03 models.	107
5.1	Theoretical age-redshift relations as a function of $H_0$ and $w$ .	114
5.2	Age-redshift relation for a sample of SDSS, zCOSMOS and GMSS ETGs.	115
5.3	Mean stacked spectrum of 10 of the oldest SDSS ETGs.	119
5.4	Distributions of the difference ( $Z_{Gallazzi} - Z_{VESPA}$ ).	120
5.5	Distribution of mass, metallicity and emission lines of SDSS ETGs	121
5.6	Distributions of $EW(H\alpha)$ and $EW([OII])$ emission lines of SDSS ETGs	123
5.7	$D4000_n$ -age relation for BC03 high resolution models.	126
5.8	$D4000_n$ -age relation for <i>Mastro</i> models.	127
5.9	Interpolation of the $\langle A \rangle - Z$ values obtained in different $D4000_n$ regimes and for different models.	129
5.10	$D4000_n$ -redshift relation for ETGs in different mass subsamples.	132
5.11	$D4000_n$ -redshift relation and $dz/dD4000_n$ relation for different theoretical models.	134
5.12	$\chi^2$ of the $H_0$ and of the $w$ evaluation for ETGs in different mass subsamples using BC03 models.	137
5.13	$\chi^2$ of the $H_0$ and of the $w$ evaluation for ETGs in different mass subsamples using <i>Mastro</i> models.	140
5.14	Study of the effect of metallicity and SFR cuts.	143
6.1	D4000-redshift relation obtained for a sample of ETGs in the range $0 \lesssim z \lesssim 1$ .	154



# List of Tables

1.1	Comparison of dark energy probes. . . . .	20
1.2	Cosmological parameters obtained for a $\Lambda$ CDM model using WMAP 7-years, BAO and $H_0$ data. . . . .	21
1.3	Results on cosmological parameters $\Omega_M$ , $\Omega_k$ and $w$ , including both statistical and systematic uncertainties. . . . .	22
2.1	Morphology- versus Color- versus Spectrum-Selected Samples. . . . .	26
3.1	Shift and error correction applied to zCOSMOS photometry. . . . .	63
3.2	Shift and error correction applied to SDSS photometry. . . . .	70
3.3	Median stellar mass for SDSS and zCOSMOS <i>ETGs</i> samples with different models. . . . .	71
3.4	Median $\tau$ value for SDSS and zCOSMOS <i>ETGs</i> samples with different models. . . . .	73
3.5	Median $A_V$ value for SDSS and zCOSMOS <i>ETGs</i> samples with different models. . . . .	75
3.6	Median age for SDSS and zCOSMOS <i>ETGs</i> samples with different models. . . . .	76
4.1	Definition of quartiles for the overdensities computed with the 5NN estimator. . . . .	89
4.2	Median overdensities and distances (in comoving Mpc/h) with their errors for the four environment quartiles averaged throughout the entire redshift range. . . . .	89
4.3	Slopes $S_\delta$ of the color-environment relation in different mass bins for <i>Red galaxies</i> and <i>ETGs</i> . . . . .	95
4.4	Slopes $S_M$ of the color-mass relation in different environment bins for <i>Red galaxies</i> and <i>ETGs</i> samples. . . . .	97

4.5	Slopes $S_M$ of the color-mass relation for <i>Red galaxies</i> in high and low environment and in given redshift bin. . . . .	98
4.6	Differences between $D4000$ for galaxies of high and low mass in a given environment and galaxies in high and low density environment quartiles at fixed mass, and their respective significances. . . . .	99
4.7	Differences (in Å) between $EW_0(H\delta)$ for galaxies of high and low mass in a given environment and galaxies in high and low environment quartiles at fixed mass, and the relative significances. . . . .	102
5.1	Median value of the stellar mass, of the metallicity $Z$ , and of the $H\alpha$ and $[OII]\lambda 3727$ equivalent widths of the SDSS ETGs in different mass subsamples. . . . .	123
5.2	slopes $\langle A \rangle$ of the $D4000_n$ -age relation for the BC03 and <i>Mastro</i> models. . . . .	128
5.3	Hubble constant and relative errors using BC03 models. . . . .	136
5.4	Dark energy equation-of-state parameter $w$ and relative errors using BC03 models. . . . .	138
5.5	Hubble constant and relative errors using <i>Mastro</i> models. . . . .	141
5.6	Dark energy equation-of-state parameter $w$ and relative errors using <i>Mastro</i> models. . . . .	141
5.7	Hubble constant and relative errors for $11 < \log(M/M_\odot) < 11.25$ sample selected for different metallicity and SFR cuts. . . . .	142
5.8	Dark energy equation-of-state $w$ and relative errors for $11 < \log(M/M_\odot) < 11.25$ sample selected for different metallicity and SFR cuts. . . . .	142
5.9	Summary of the sources of uncertainty and their impact on the cosmological parameters. . . . .	145

---

# Preface and motivations

The present time is a very special moment to study astrophysics and cosmology. In the last decades, many striking and phenomenal discoveries have been done, making giant leaps in understanding the formation and structure of our Universe. The studies of the cosmic microwave background (CMB), supernovae (SNe), baryonic acoustic oscillations (BAO), large-scale structures have provided observations fundamental to solve the puzzle of Universe evolutions, contributing to the formulation of the "*Big-Bang*" theory.

Despite the success of its first formulation in describing the Universe, the theory needs further studies, in order to include the results of more recent discoveries. In 1998 two independent teams studying distant Type Ia supernovae presented evidences that the expansion of the Universe is accelerating (Perlmutter et al., 1999; Riess et al., 1998), and many other independent probes confirmed their first results. This is nowadays one of the fundamental issue of modern cosmology: since Hubble, cosmologists had been trying to measure the slowing of expansion due to gravity, but the evidence of acceleration indicates that either gravity at some large scales can not be described by the standard General Relativity and/or that the Universe is filled with some sort of negative-pressure "dark energy" driving the accelerated expansion. Either way, this discovery requires new physics to be properly taken into account.

The second issue that highlights the lack of our knowledge of the Universe concerns the topic of galaxy evolution. In recent years many large galaxies-redshift surveys have been carried out, aimed to discover and study the nearby and far galaxies. 2dF Galaxy Redshift Survey (2dFGRS), DEEP2 Redshift Survey (DEEP2), VIMOS VLT Deep Survey (VVDS), zCOSMOS survey and especially the Sloan Digital Sky Survey (SDSS) are just some of the most important; many others are foreseen for the future, e.g. the SDSS-III. All these surveys were (or will be) able to give important insights in understanding the principal properties of galaxies, through the study of their structural parameters, types, environment and, most important, redshift.

Despite all these efforts, a key question is still unsolved: how galaxies did form. In fact, the precise process describing the formation of galaxies, the assembling of their mass, the evolution with cosmic time from the structure observed at high redshift to the well-known Hubble sequence identified in the local Universe, is still under debate. Moreover, the "nature vs nurture" scenario, that could be summarized by the question if the main driver of galaxy evolution is one of the structural parameter or the environment, has not been precisely understood yet.

All such exciting open questions makes the present time a very special moment to study astrophysics and cosmology, also because some tools to try to answer to

these questions are already on the ground.

This thesis is dedicated to the study of a particular type of galaxies that can help in looking for the answers.

In 1936 Hubble proposed to divide the galaxies on the base of their morphology, identifying three main groups: the elliptical galaxies (called also early-type galaxies), the spiral galaxies (called also late-type galaxies), and the irregular galaxies. From that time on, many analyses have been performed studying the properties of galaxies as a function of their types. It has been found that the color distribution exhibits a bimodality corresponding to a division between late-type (younger, star-forming, bluer) and early-type (older, passive, redder) galaxies.

Many recent works have given growing observational evidence that the most massive galaxies contain the oldest stellar populations up to redshifts of  $z \sim 1 - 2$  (Dunlop et al., 1996; Spinrad et al., 1997; Cowie et al., 1999; Cimatti et al., 2004; Heavens et al., 2004; Thomas et al., 2005; Cimatti et al., 2008; Thomas et al., 2010) and have less than 1% of their present stellar mass formed at  $z < 1$ .

Studying the mass function of early-type galaxies, it has been found that their massive end evolves very mildly (or not at all) from  $z \approx 0.7 - 0.8$  to  $z = 0$  (Fontana et al., 2004; Drory et al., 2005; Caputi et al., 2006; Cimatti et al., 2006; Pozzetti et al., 2010).

This population of massive, red, passive early-type galaxies (*ETGs*) consists of the oldest objects in the Universe at each redshift. Thus, as suggested by Jimenez & Loeb (2002), those galaxies can be considered as “*cosmic clocks*”, as they represent up to redshift  $z \approx 1$  a fairly homogenous population of galaxies able to trace the evolution of the Universe with cosmic time.

This property makes ETGs very important candidates to study the Universe both from the evolutionary and from the cosmological point of view.

The aim of this Thesis is to analyze the possibility of using ETGs to place evolutionary and cosmological constraints, by:

1. disentangling what is the main driver of ETGs evolution between mass and environment
2. developing a technique to constrain  $H(z)$  and the cosmological parameters (in particular the Hubble parameter  $H_0$  and the dark energy equation-of-state  $w$ ) studying the ETGs age-redshift relation

In the following, the two points are discussed with more details, describing the methods used and the topics developed.

1. **ETGs as evolutionary probes.** The goal of this work is to understand which is the main driver of galaxy evolution (Moresco et al., 2010a). The (U-V) rest-frame color distribution and some spectral features are studied as a function of mass and environment for two sample of early-type galaxies up to  $z = 1$ , extracted from the zCOSMOS spectroscopic survey. A first sample (“Red galaxies”) is defined applying only a photometric classification, while the second (“ETGs”) uses a newly defined criterion that combines morphological, photometric and spectroscopic properties to obtain a more reliable sample. The choice of using two different samples is due to the need of obtaining results both precise, exploiting the high statistics of the *Red galaxies* sample, and highly reliable, as guaranteed using the *ETGs* sample that has been built to be a safe reference sample of early-type galaxies. Both the distributions of the colors and the slopes of the color-mass and color-environment relations are studied, finding a strong dependence on mass and a minor dependence on environment. The spectral analysis performed on the *ETGs* sample is in good agreement with the photometric results: the D4000 and  $H\delta$  features are studied as a function of redshift for bins of different mass and overdensity, obtaining results that validate what found from the color analysis. Therefore, in the “nature vs nurture” scenario, this analysis supports that the main driver of galaxy evolution is the galaxy mass, the environment playing a subdominant role, even if non yet negligible. The lookback time of early-type galaxies is also analyzed, providing strong evidences supporting a downsizing scenario, for which massive galaxies with a stronger D4000 and an almost constant equivalent width of  $H\delta$  formed their mass at higher redshift than lower mass ones.
  
2. **ETGs as cosmological probes.** Following the approach suggested by Jimenez & Loeb (2002), a new methodology to determine the expansion history of the Universe is developed, analyzing the spectral properties of early type galaxies (Moresco et al., 2010b). In their preliminary work, Jimenez & Loeb (2002) show that the cosmic time as a function of redshift, and in particular its derivative  $dz/dt$ , depends critically on many cosmological parameters, such as  $\Omega_m$ ,  $\Omega_{DE}$ ,  $H_0$ ,  $w_{DE}$  and others. Thus, it can be used to constrain cosmological parameters. For this technique, it is fundamental to find a population of standard clocks able to trace the evolution of the relative age of the Universe, and they propose to use ETGs for the motivation previously discussed. However, the main weakness of this technique is that it suffers the fact that its primary parameter, the age, presents strong and well known degeneracies with other parameters (e.g. the metallicity, the star formation history, the dust content) that are evaluated simultaneously in the SED or spectral fitting. The possibility of setting cosmological constraints studying the age-redshift

relation is studied, discussing the relative problems, degeneracies and model dependencies that make hardly feasible this kind of analysis.

A new methodology, aiming to minimize the impact of systematics on the estimation of the relative ages of galaxies, which is the relevant quantity to determine  $H(z)$  using the cosmic chronometer method, is studied and developed. Analyzing different stellar population synthesis models, it is demonstrated that the 4000Å break (D4000) is a feature correlated almost linearly with age at fixed metallicity, depending only minorly on the synthetic stellar population models or on the star formation history (SFH) chosen. The analysis of a sample of ETGs extracted from the SDSS survey, in the redshift range  $0.15 < z < 0.3$ , shows that it is possible to use the differential D4000 evolution of the galaxies as a tracer for their differential age evolution, and thus to set constraints to cosmological parameters in an almost model-independent way.

From this analysis, a value of the Hubble constant is found which is not only fully compatible, but also with a comparable error budget with the latest results from Riess et al. (2009). Assuming  $w=\text{constant}$ , a value for the dark energy equation-of-state parameter in agreement with the value found from the WMAP 7-years analysis and with the one obtained from Amanullah et al. (2010) is found. Since the SDSS ETG sample only reaches  $z \approx 0.3$ , these results show the potential of the method.

This method seems promising also in view of the future massive spectroscopic surveys expected in the next decades from the ground (e.g. SDSS-III BOSS, BigBOSS) and from space (e.g. ESA Euclid, NASA WFIRST).

The future prospect of this work is to use this new technique to yield a determination of  $H(z)$  up to  $z \approx 1$ , selecting and analyzing samples of ETGs from different surveys (SDSS, zCOSMOS, K20, ...) to have the wider possible coverage in redshift. The strength of this method is to be completely independent on other probes (SNe, BAO, ...), so that the determination of  $H(z)$  is a fundamental step for a joint analysis which will help to obtain constraints on cosmological parameters to an even higher precision.

This Thesis is organized as follows.

- In Chapter 1 a short review of the fundamental elements of FRW cosmology will be provided, describing briefly the thermal history of the Universe, the *Big Bang Theory* paradigm and its fundamental equations. It will be discussed how *dark energy* has been discovered and what are the most important probes to study its properties, analyzing their strengths and weaknesses. At the end, the current results about cosmological parameters and the Hubble parameter  $H(z)$  will be shown.

- In Chapter 2 the basic observational evidences about early-type galaxies will be described, focusing the attention on the main characteristics that make them the ideal candidates to obtain both evolutionary and cosmological insights about the Universe. It will also be discussed how these properties evolve with redshift, and the possible theoretical scenarios that can synthesize the overall picture.
- In Chapter 3 it will be described how a reliable sample of early-type galaxies has been built, illustrating the surveys from which the galaxies have been extracted, the criteria used to select a sample of passive ETGs the less contaminated as possible from the presence of outliers and the method used to correctly set up their photometry. The properties obtained from the fit to their spectral energy distributions will also be analyzed, discussing the reliability of the retrieved parameters and their degenerations with other variables and/or their dependences on assumed models.
- In Chapter 4 the  $(U - V)$  restframe color distributions for two different samples of zCOSMOS ETGs will be analyzed, investigating the dependence of their shapes on mass and environment. In addition to colors, two spectroscopic line indices in galaxy spectra will be studied as a function of redshift in different mass and environment bins, the 4000 Å break (D4000) and the equivalent width of the  $H\delta$  Balmer line ( $EW_0(H\delta)$ ), which are proven to be good age indicators. Finally, evidences supporting a mass-downsizing scenario will be discussed, inspecting the lookback time of *ETGs* as a function of stellar mass.
- In Chapter 5 the possibility of setting cosmological constraints with the “*cosmic chronometers*” technique will be explored analyzing the age-redshift relation for a sample of ETGs in the range  $0 \lesssim z \lesssim 1$ . The ages will be estimated with a SED-fitting technique, and the feasibility of this approach will be discussed. To solve the various problems and degenerations, a new methodology will be introduced to determine the expansion history of the Universe analyzing the spectral properties of early-type galaxies (ETG), based on the study of the redshift dependence of the 4000 Å break. The method will be described, its robustness explored using theoretical synthetic stellar population models, and it will be applied using a SDSS sample of  $\sim 14\,000$  ETGs. The motivation to look for a new technique is to minimize the dependence of the “*cosmic chronometers*” method on systematic errors. In particular, as a test of the method, the Hubble constant and the value of the dark energy equation-of-state parameter (assuming  $w = \text{constant}$ ) will be estimated using SDSS data, obtaining results well in agreement with the latest WMAP analysis.



---

# Chapter 1

## Cosmological background

In this chapter, a brief review of the basic elements of FRW cosmology is provided, describing shortly the thermal history of the Universe, the *Big Bang Theory* paradigm and its fundamental equations. It is discussed how *dark energy* has been discovered, and also what are the most important probes to study its properties by analyzing their strengths and weaknesses. At last, the current results about cosmological parameters and the Hubble parameter  $H(z)$  are shown.

There are a lot of extensive and well-written reviews about dark energy and cosmology, both with a theoretical and an observational approach, and more detailed informations can be found in Carroll (2001); Peebles & Ratra (2003); Copeland et al. (2006); Frieman et al. (2008); Caldwell et al. (2009); Huterer (2010).

### 1.1 Brief History of the Universe

In the first stages of its life, giving the small dimension and the high temperatures, the Universe was filled with a huge amount of energy density. After the Big Bang, following its expansion, it started to freeze; at the same time, due to the gravitational attraction, the expansion slowed down. The expansion history of the Universe can be summarized following the cooling of the Universe. In the following are listed the various stages of the Universe, with the characteristic times and energy scales (following Mukhanov et al., 2005).

These are the main phases that describe the history of the Universe:

- $t \lesssim 10^{-43}$  sec ( $T \sim 10^{19}$  GeV). This is known as the **Planck epoch**. At this energy level, all the four fundamental forces may be unified in a single force. General Relativity can no longer be trusted due to quantum mechanics effects, and different theories are proposed to explain this early stage of the evolution of the Universe.

- $10^{-43} \lesssim t \lesssim 10^{-12}$  sec ( $T \sim 100$  TeV  $-10^{19}$  GeV). Below a temperature of  $10^{19}$  GeV, General Relativity can still be used, since the effect of quantum gravity should be negligible. With the cooling of the Universe, gravitation is the first force that is decoupled from the others. Below  $10^{16}$  GeV, also the electroweak force separates from the strong force. Many theories account for the presence of magnetic monopoles and cosmic strings during this epoch. The transition phase produced by the separation of electroweak and strong forces induces a period of exponential expansion of the Universe, known as **inflation**. The inflation has the effect of broadening the particle horizon, producing homogeneity and isotropy over larger scales; the total energy density reaches the critical value and the Universe is nearly flat. After inflation, two important events take place. First of all, the potential of the field responsible of the inflation decays into a hot relativistic plasma of particles: during this stage the first quarks, electrons and neutrinos are formed, but the dominant contribution is due to radiation. This phase is called **reheating**, and the Universe is now filled with a quark-gluon plasma. Subsequently, a small difference between the rates of production of matter and antimatter induces this balance to be broken, and a slight overproduction of protons respect to the antiprotons (1 over  $10^9$ ) leads to the **baryogenesis**. At this point the matter-antimatter annihilation takes place, leaving only matter and a very large number of photons.
- $10^{-6} \lesssim t \lesssim 1$  sec ( $T \sim 1 - 2$  MeV). With the expansion of the Universe, the quark-gluon plasma cools down, and at some points protons and neutrons are formed. The primordial neutrinos can now decouple from other particles and propagate freely (**neutrino decoupling**), producing the cosmic neutrino background. Due to the inefficiency of the interaction, the proton/neutron ratio is freezed at a value of  $\sim 6$ .
- $1 \lesssim t \lesssim 10$  sec ( $T \sim 0.5$  MeV). During this stage, when the temperature drops below the electron rest-mass, the lepton-antilepton annihilation takes place, and a small excess of electron over positrons survives ( $\sim 1$  over  $10^9$ ). The photons produced are in thermal equilibrium.
- $200 \lesssim t \lesssim 1200$  sec ( $T \sim 0.05$  MeV). At this temperature, nuclear reactions become efficient, and helium and other light elements are formed from free protons and neutrons (**primordial nucleosynthesis**). The nucleosynthesis continues until the temperature drops so much that the nuclear fusion is not allowed anymore. At this time, the predicted primordial abundance of helium is  $\sim 25\%$ , with the other fundamental contribution given by the hydrogen and only small traces of heavier elements.
- $t \sim 10^{11}$  sec ( $T \sim 1$  eV). This time and temperature marks the division

between the radiation-dominated epoch and the matter-dominated epoch: it is addressed as the **matter-radiation equality**.

- $t \sim 10^{12} - 10^{13}$  sec. **Recombination** takes place, with neutral hydrogen and helium beginning to form. At this point, the Universe become transparent to radiation, since all electrons are bound to the nuclei: this process is called **decoupling**. After decoupling, the photons can travel freely, and the cosmic microwave radiation (CMB) is formed. Therefore, the CMB gives us a picture of the Universe at this early stage, and of the small temperature anisotropies produced during the inflation.
- $t \sim 10^{16} - 10^{17}$  sec. The small anisotropies in the matter distribution that can be observed in the CMB act like seeds of structures. Following the gravitation, from these small seeds structures are formed. The relevant contribution of dark matter and dark energy in the process of structure formation is still an open issue.

## 1.2 Big Bang Theory basis

The standard cosmological model is built upon the hypothesis that space is homogeneous (i.e. having a constant density) and isotropic (i.e. being self-similar in every direction) at all times. These assumptions were firstly expressed by Einstein in its *Cosmological Principle*, which states that in the rest system of the matter there is no preferred point and no preferred direction. There are nowadays a lot of strong and independent observational evidences of the goodness of these assumptions: these are witnessed, for example, by the large-scale distribution of galaxies and the near-uniformity of the CMB temperature. Since COBE mission in 1994, it has been found that the spectrum of the cosmic background radiation is consistent with a black body at temperature  $2.726 \pm 0.010K$  over more than three decades in wavelength (Mather et al., 1994), showing anisotropies only of the order of  $\Delta T/T \approx 10^{-5}$ . Many other missions were devoted to the studies of these anisotropies, and of their impact in constraining cosmological parameters, e.g. WMAP (Jarosik et al., 2011; Komatsu et al., 2011), and the preliminary results of Planck satellite confirm the picture shown by COBE satellite with an extraordinary precision (see Fig. 1.1)

The condition of homogeneity means that at a given time the physical properties (e.g. particle number density, velocity, spacetime curvature) are the same everywhere. The condition of isotropy means that any physical quantity does not depend on the direction of an observer located in any spacetime point  $x$ .

These assumptions really simplify the structure of the metric tensor  $g_{\mu\nu}$ . Spherical symmetry around each space-time location is necessary, and no off-diagonal terms are left; homogeneity and isotropy leave essentially only two degrees of free-

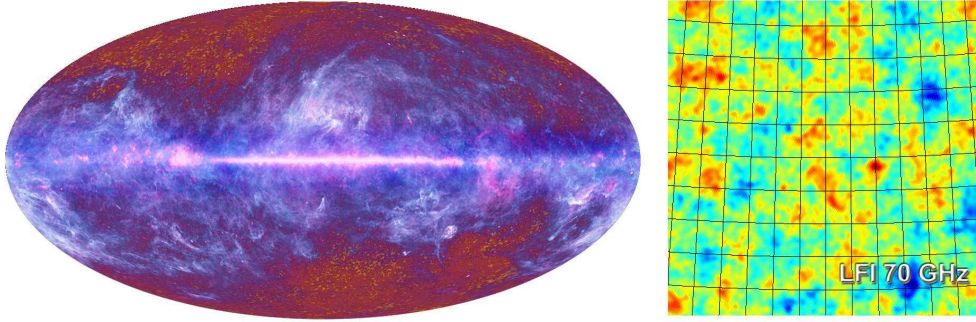


Figure 1.1: *Left panel: Planck first-year all-sky survey map. It is possible to see, below the Galactic emission in blue, the anisotropies of the CMB. Right panel: Map of the high-galactic-latitude sky at 70 GHz, detail from the Planck First Light Survey, showing a detail of the anisotropies of the CMB. Credit: ESA, LFI and HFI consortia.*

dom to the system. The first one is a global scale factor, fixing at each time the value of physical lengths; the second one is related to the spacetime curvature, as a homogeneous metric can be globally more or less curved. The line element of the *Friedmann-Robertson-Walker (FRW) metric* is therefore:

$$ds^2 = -dt^2 + a^2(t) \left[ \frac{dr^2}{1 - kr^2} + r^2(d\theta^2 + \sin^2 \theta d\varphi^2) \right] \quad (1.1)$$

where  $a(t)$  represents the cosmic-scale factor,  $R_{curv} = a(t)|k|^{-1/2}$  is the curvature-radius and the available values for the curvature signature  $k$  are  $k = 0, 1, -1$ ;  $r, \theta$  e  $\varphi$  are the usual spherical coordinates for radius, polar and azimuth angle, respectively. All the three models are without boundary: the positively curved model is finite and curves back on itself; the negatively curved and flat models are infinite in extent.

The coordinates  $(r, \theta, \varphi)$  are referred to as comoving coordinates, i.e. coordinates that are at rest with respect to the cosmological expansion: in other words a particle at rest in these coordinates remains at rest, with constant  $r, \theta$  and  $\varphi$ . Motion with respect to the comoving coordinates (or cosmic rest frame) is referred to as peculiar velocity. Physical separations between freely moving particles scale as  $a(t)$  (known as the *scale factor*), that means that the physical separation between two points is simply  $a(t)$  times the coordinate separation:

$$d(t) = a(t)R \quad (1.2)$$

Deriving the last expression w.r.t. time, it is possible to define the *Hubble parameter*:

$$H(t) = \frac{\dot{a}}{a} \quad (1.3)$$

where an overdot denotes a time derivative. The present value of the Hubble parameter is conventionally expressed as  $H_0 = 100 h \text{ km sec}^{-1} \text{ Mpc}^{-1}$ , where  $h$  is the dimensionless Hubble parameter. From this expression can be retrieved the well-known Hubble law  $v = Hd$  (Hubble, 1929).

As a consequence of Eq. 1.2, the wavelength of the propagating radiation is stretched by  $a(t)$  and this is the origin of the cosmological redshift. The redshift suffered by a propagating photon is:

$$\frac{\lambda_{obs}}{\lambda_{em}} = 1 + z = \frac{a(t_{obs})}{a(t_{em})} \quad (1.4)$$

Since, by convention,  $a = 1$  today, the relation between the expansion factor  $a(t)$  and the redshift  $z$  is  $a = (1 + z)^{-1}$ . Eq. 1.4 means that time intervals are related to redshift intervals by:

$$dt = -\frac{dz}{H(z)}(1 + z) \quad (1.5)$$

### 1.2.1 Basic equations

The evolution of the cosmic-scale factor is governed by the *first Friedmann equation*:

$$H^2 = \left(\frac{\dot{a}}{a}\right)^2 = \frac{8\pi G}{3}\rho - \frac{k}{a^2} + \frac{\Lambda}{3} \quad (1.6)$$

where  $\rho$  is the total energy density of the Universe (sum of matter, radiation, dark energy),  $p$  is the total pressure (sum of pressures of each component), and  $\Lambda$  is the cosmological constant; this latter term will be hereafter represented as vacuum energy (or also dark energy), with its pressure and density terms; the correspondence is:  $\Lambda = 8\pi G\rho_{vac} = -8\pi Gp_{vac}$ .

For each component, the conservation of energy is expressed by  $d(a^3\rho_i) = -p_ida^3$ , which can be rewritten as a function of the Hubble parameter as:

$$\dot{\rho}_i + 3H(\rho_i + p_i) = 0 \quad (1.7)$$

Deriving w.r.t. time the Eq. (1.6), and using Eq. (1.7), it is possible to derive the *second Friedmann equation*:

$$\frac{\ddot{a}}{a} = -\frac{4\pi G}{3}(\rho + 3p) + \frac{\Lambda}{3} \quad (1.8)$$

Combining the Eq. (1.6) and (1.8), it is possible to find:

$$\dot{H} = -4\pi G(\rho + p) \quad (1.9)$$

From this equation can be defined a *critical density*  $\rho_{crit}$  as the value that matches  $k = 0$  in the first Friedmann equation (i.e. a flat Euclidean Universe):

$$\rho_{crit} = \frac{3H^2}{8\pi G} = 8.10 \times 10^{-47} h^2 \text{ Gev}^4 \quad (1.10)$$

from which, for each component, can be defined the *density parameter* (adimensional):

$$\Omega_i \equiv \frac{\rho_i}{\rho_c} = \frac{8\pi G \rho_i}{3H^2} \quad (1.11)$$

Using the definition (1.10) and (1.11), the first Friedmann equation can be rewritten in the following way:

$$\Omega_0 - 1 = \frac{k}{a^2 H^2} \quad (1.12)$$

where  $\Omega_0 = \Omega_{M,0} + \Omega_{R,0} + \Omega_{vac,0}$  is the total energy density of the Universe. This equation gives a one to one correspondence between  $\Omega_0$  and the spatial curvature of the universe: positively curved corresponds to  $\Omega_0 > 1$ , negatively curved to  $\Omega_0 < 1$  and flat to  $\Omega_0 = 1$ . The curvature radius of the universe is related to the Hubble radius and  $\Omega_0$  by the relation:

$$R_{curv} = \frac{H^{-1}}{(\Omega_0 - 1)^{1/2}} \quad (1.13)$$

Finally, the *deceleration parameter* is defined as:

$$q = -\frac{\ddot{a}}{a} \left( \frac{\dot{a}}{a} \right)^{-2} = -\frac{\ddot{a}a}{\dot{a}^2} \quad (1.14)$$

### 1.2.2 Redshift dependence

In the case of a perfect fluid, the evolution of energy density is controlled by the ratio of the pressure to the energy density, the equation-of-state parameter,  $w_i \equiv p_i/\rho_i$ . For the general case, this ratio varies with time, and the evolution of the energy density for each component is given by:

$$\rho_i \propto \exp \left[ 3 \int_0^z [1 + w_i(z')] d\ln(1 + z') \right] \quad (1.15)$$

If  $w_i = \text{const}$ , Eq. 1.15 simply becomes:

$$\rho_i \propto (1 + z)^{3(1+w_i)} \quad (1.16)$$

It is therefore possible to find explicitly, from the equation-of-state, the redshift dependence of the density of each components:

- MATTER (non relativistic matter, dark matter and baryons)  $w_M = 0$ ,  $\rho_M \propto (1 + z)^3$ ;
- RADIATION (relativistic particles)  $w_R = 1/3$ ,  $\rho_R \propto (1 + z)^4$ ;
- VACUUM (or “dark-energy”)  $w_{vac} = -1$ ,  $\rho_{vac} \propto (1 + z)^0$ .

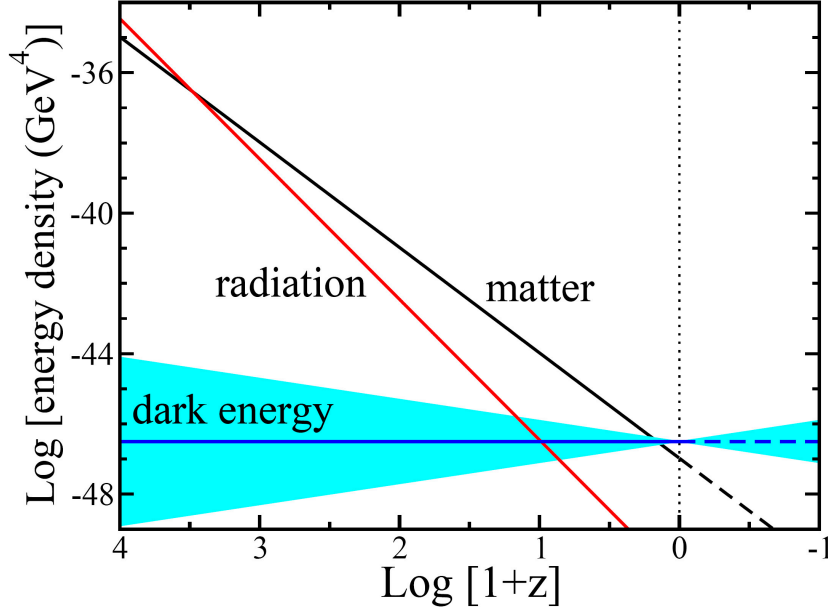


Figure 1.2: *Reproduced from (Frieman et al., 2008): evolution of radiation, matter, and dark energy densities with redshift. For dark energy, the band represents  $w = -1 \pm 0.2$ .*

These different redshift dependences express how the Universe experienced three completely different stages of evolution, during which there only a particular component was dominating: the first, right after the Big Bang, was radiation-dominated ( $z \gtrsim 3000$ ); the second one was matter-dominated ( $3000 \gtrsim z \gtrsim 0.5$ ); the last, and present, one is “dark-energy” dominated ( $z \lesssim 0.5$ ). Fig. 1.2 show the different evolutions of the energy densities as a function of redshift.

Using the second Friedmann equation (1.8) and the state equation for matter, radiation and vacuum, it is possible to express the deceleration parameter as a function of the energy densities:

$$q = \frac{1}{2} \sum_i \Omega_i(z)[1 + 3w_i(z)] \quad (1.17)$$

During the matter- and radiation-dominated era,  $\Omega_\Lambda$  was negligible with respect to matter and radiation, and therefore the gravity produces a  $q > 0$  and a slowing of the expansion. On the other side, given the form of Eq. 1.17, a component satisfying  $w < -1/3$  would produce a repulsion, causing an accelerated expansion.

### 1.2.3 Hubble parameter, distances and times

Considering the different redshift dependences of the components of the Universe, regarding the energy densities, it can be written:

$$\Omega_M = \Omega_{M,0} \frac{H_0^2}{H^2} (1+z)^3 \quad \Omega_R = \Omega_{R,0} \frac{H_0^2}{H^2} (1+z)^4 \quad \Omega_\Lambda = \Omega_{\Lambda,0} \frac{H_0^2}{H^2} \quad (1.18)$$

It is therefore possible to express the Hubble parameter as a function of the contributions of the different energy densities:

$$\begin{aligned} H^2 &= H_0^2 \left[ \Omega_{R,0} (1+z)^4 + \Omega_{M,0} (1+z)^3 + \Omega_{\Lambda,0} - \frac{k}{H_0^2} (1+z)^2 \right] \\ &= H_0^2 (\Omega_{R,0} (1+z)^4 + \Omega_{M,0} (1+z)^3 + (1 - \Omega_0) (1+z)^2 + \Omega_{\Lambda,0}) \end{aligned} \quad (1.19)$$

where Eq. (1.12) has been used to obtain the last expression.

The *luminosity distance* of an object of luminosity  $L$ , energy flux  $F$  at a redshift  $z$ , is defined to be  $d_L(z) \equiv \sqrt{\frac{L}{4\pi F}}$ , and, in a flat Universe:

$$d_L(z) = (1+z) \int_0^z \frac{dz'}{H(z')} = \int_{1/(1+z)}^1 \frac{da}{a^2 H(a)} \quad (1.20)$$

In the case of a constant  $w$ , it is possible to reformulate Eq. 1.20 expliciting the dependence on the energy density parameters:

$$d_L(z) = \frac{(1+z)}{H_0} \int_0^z \frac{dz'}{\sqrt{\Omega_{M,0}(1+z'^3) + (1 - \Omega_{M,0})(1+z'^{3(1+w)}) + \Omega_{R,0}(1+z'^4)}} \quad (1.21)$$

The luminosity distance can be also related to the distance modulus  $\mu$  through the relation:

$$\mu(z) = m - M = 5 \log_{10}(d_L/10\text{pc}) \quad (1.22)$$

where  $m$  is the apparent magnitude and  $M$  is the absolute magnitude of an object.

The *angular diameter distance* is defined to be the ratio between the diameter  $D$  of an object and the angle on the sky  $\delta\theta$ ,  $d_A = D/\delta\theta$ , so can be related with the luminosity distance:

$$d_A = \frac{d_L}{(1+z)^2} \quad (1.23)$$

From the equation  $H = \dot{a}/a$ , by expressing all in function of the time and integrating, it is possible to obtain an expression for the *age of the Universe* (using the Eq. (1.19)):

$$\begin{aligned} t(z) &= \int_z^{+\infty} \frac{dz'}{(1+z')H(z')} \\ &= \frac{1}{H_0} \int_z^{+\infty} \left[ \Omega_R (1+z')^2 + \Omega_M (1+z') + (1 - \Omega_0) + \frac{\Omega_\Lambda}{(1+z')^2} \right]^{-1/2} dz' \end{aligned} \quad (1.24)$$

### 1.3 Structure formation

Considering a “dark energy” term in the cosmological expansion history modifies the evolution from what it would have been in a purely matter dominated Universe; as a consequence, this influences the growth of large-scale structure, having an effect that can be compared to the one produced by the spatial curvature. The study of the evolution of structure is simplified by the fact that they can be treated within a linear theory, being the temperature anisotropies very small at recombination ( $\Delta T/T \approx 10^{-5}$ ). Within this approximation the evolution of the initial perturbation is driven by two competitive effects: on one side the initial overdensity regions tend to grow to the effect of gravity, on the other side the effect of expansion of the Universe is to tear particles apart one from the other.

The impact of the dark energy equation-of-state parameter  $w$  on the growth of structure is more subtle, as reported by Frieman et al. (2008): for larger  $w$  and fixed dark energy density  $\Omega_\Lambda$ , dark energy comes to dominate earlier, causing the growth of linear perturbations to end earlier; this means the growth factor since decoupling is smaller and that to achieve the same amplitude by today, the perturbation must begin with larger amplitude and is larger at all redshifts until today. The same is true for larger  $\Omega_\Lambda$  and fixed  $w$ . Finally, if dark energy is dynamical (not vacuum energy), then in principle it can be inhomogeneous, an effect ignored above. In practice, it is expected to be nearly uniform over scales smaller than the present Hubble radius, in sharp contrast to dark matter, which can clump on small scales.

Another key ingredient to understand the evolution of matter, and therefore the formation of structures, is unveiling the nature of *dark matter*, since, as shown in Fig. 1.3, it represents the dominant gravitational contribution ( $\sim 80\%$  versus  $\sim 20\%$  of the standard observable matter). Three different kind of dark matter can be postulated: a “hot dark matter” (HDM) composed by ultra-relativistic particles ( $v/c > 0.95$ ), a “warm dark matter” (WDM) composed by relativistic particles ( $0.1 < v/c < 0.95$ ), and a “cold dark matter” (CDM) composed by particle with non-relativistic speed ( $v/c < 0.1$ ).

These categories of dark matter, theoretically are equally valid and have all plausible candidates; however, in terms of structure formation, they differ substantially for their prediction. In particular, both WDM and HDM are characterized by temperatures and speeds too high to match many observed phenomena. Due to their properties, it is impossible to model them to explain the observed galactic rotational curves and velocity dispersions, since their particles move simply too fast to follow the galaxy distribution; moreover, at large scales, they can not account for the observed weak lensing properties for the same reasons.

The CDM has consequently become the most plausible candidate to explain structure formation in the Universe, becoming also a key ingredient in the es-

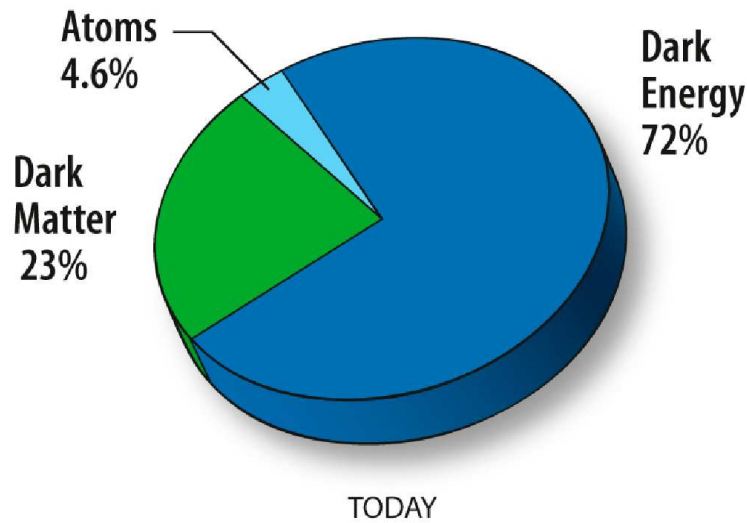


Figure 1.3: *Content of the Universe as unveiled by WMAP-5years data. Credit: NASA / WMAP Science Team.*

established  $\Lambda$ CDM model. This cosmological model has been built to explain both the past and present phases of the history of the Universe, e.g. accounting for the cosmic microwave background, the structure formation and the present day accelerated expansion. In order to do that, it includes the presence of a cosmological constant  $\Lambda$ , to explain the accelerated expansion of the Universe, and a form of cold dark matter to reproduce the observed effects in the large scale structures. The current WMAP measurements of the CMB (Komatsu et al., 2011), with other independent probes such as SNe (Amanullah et al., 2010) and BAO (Percival et al., 2010), strongly support this model.

## 1.4 The dark Universe

Modern observational cosmology has devoted, in the last decades, many efforts in studying the Universe and its contents, trying to unveil its composition with high precision. However, the picture that came out is still quite puzzling.

On one side, since 1930s it has been noted the existence of a form of matter that can be inferred from its gravitational effects, but that can not be detected by emitted or scattered electromagnetic radiation. The present extremely precise measurements provided by WMAP (Komatsu et al., 2011), in addition to a lot of complementary evidences, pointed out that ordinary matter accounts for only 4.6% of the energy density of the observable universe, while the 23% is made of

this undetectable form of matter, called *dark matter*.

Even more puzzling is that, with an analysis complementary to the measure of the total matter energy density  $\Omega_M \approx 0.3$ , WMAP has set with extreme accuracy also the value of the total energy density to be  $\Omega_0 \approx 1$ , pointing out the evidence of a flat Euclidean Universe. Since the contribution to the total energy density from radiation is known to be negligible at present times, this witness the presence of almost 70% of the energy of the Universe in an unknown form, that historically has been called *dark energy* (see Fig. 1.3).

In the following, it is reviewed how was historically firstly introduced the idea of *dark energy*, when was it firstly discovered and what are the main probes that can be used to constrain it.

### 1.4.1 The discovery of dark energy

The introduction of the concept of “dark energy” goes back to 1917 (Einstein, 1917). It was firstly proposed by Einstein as a modification of his equation in order to obtain a static and finite solution:

$$G_{\mu\nu} = 4\pi GT_{\mu\nu} + \Lambda g_{\mu\nu} \quad (1.25)$$

This cosmological constant  $\Lambda$  was a term acting as a repulsive gravity, able to balance the attractive gravity of matter and yield a solution compatible with a static Universe and the Mach’s principle.

However, many independent works demonstrated that Einstein’s solution was unstable to expansion or contraction; moreover in 1929 Hubble discovered the well-know “Hubble-law”, a linear relation between redshift and distance witnessing the expansion of the Universe (Hubble, 1929). In this way, the primary reason of the introduction of the theoretical extra factor of Eq. 1.25 was lost, and the concept of cosmological constant was more or less abandoned for the following years.

The ideas started to change in 1981, when Guth proposed his inflationary scenario (Guth, 1981), which predicted a spatially flat Universe and almost-scale-invariant density perturbations. By the same time, a variety of dynamical probes of the large-scale structure in the Universe started to indicate that the matter energy density is much lower than the value needed to make the Universe flat. When in 1992 the COBE satellite discovered that the total energy density of the Universe was nearly equal to the unity, the interest for a missing component, able to reproduce, combined with matter, the observed and predicted  $\Omega_0 = 1$  rose back to life.

Nevertheless, it was only in the late 1990s that observational evidences convinced definitely the cosmologists to take again in consideration the idea of a cosmological constant.

In 1998 two independent teams working on type Ia supernovae (Sne Ia), the Supernova Cosmology Project (Perlmutter et al., 1999) and the High-z SN Search

(Riess et al., 1998), found results in agreement indicating that more distant SNe are  $\sim 0.25$  mag dimmer than they would be expected in a matter-only, decelerating Universe. Those two measurements gave the first evidences that the expansion of the Universe is accelerating, implying the presence of a new component with strongly negative pressure. In term of equation-of-state, this means that this new component, the “dark energy”, should have  $w_{DE} < -1/3$  in order to produce an accelerated expansion, as expressed by Eq. 1.17.

### 1.4.2 Observational probes

Understanding and quantitatively constraining the nature of dark energy is a difficult task. The primary effect of dark energy is on the expansion rate of the Universe; in turn, this affects the redshift-distance relation and the growth of structure. This means that the most difficult issue is that there exist competitive effects: if we look at an object at redshift  $z$ , its properties may be affected and changed by their intrinsic evolution from that redshift to us and/or by the expansion that the Universe had undergone from then to now. If we are unable to disentangle this two aspects, we’ll never be able to say anything about the dark energy parameters. To solve this problem, it is therefore necessary to define and find some “*standard objects*”, whose properties are well-known and fixed independently on the redshift.

Almost all the probes of dark energy rely exactly on the measure of the fundamental physical properties of these standard objects, such as the intrinsic luminosity (*standard candles*), the size (*standard rulers*) or the age (*standard clocks*). In the following the most important probes of dark energy are briefly discussed, highlighting the strength and weakness of each one. In Tab. 1.1 the results are summarized following Frieman et al. (2008) (see Frieman et al., 2008, Sect. 7).

**Supernovae type Ia (SNe Ia).** A type Ia supernova represents the last stage of carbon-oxygen white dwarf accreting mass from a companion star; as it approaches the Chandrasekhar mass, it starts a thermonuclear explosion, and the peak luminosity is determined by the mass of  $^{56}\text{Ni}$  produced in the explosion. Therefore, SNe Ia are expected to have similar peak luminosities, and being as bright as a typical galaxy when they peak, they can be used as standard candles out to high redshifts. A more precise analysis shows that it is not completely true that they are “standard” candle, since they have a  $1\sigma$  spread of order 0.3 mag in peak B-band luminosity. However, it has been found that there exist an empirical correlation between SN Ia peak brightness and the rate at which the luminosity declines with time after peak (Phillips, 1993): this means that it is possible to correct with that correlation, obtaining excellent “standardizable” candles, with a dispersion of about 15% in peak brightness.

Knowing the peak brightness, and therefore the absolute magnitude  $M$  of a supernova, it is possible to constrain the cosmological parameters using Eq. 1.22. The major systematic concerns for supernova distance measurements are errors in correcting for host-galaxy extinction and uncertainty in the intrinsic colors of SNe Ia, luminosity evolution, and selection bias in the low-redshift sample.

**Baryon acoustic oscillations (BAO).** The acoustic oscillations of the coupled photon-baryon fluid in the early Universe are clearly imprinted in the angular power spectrum of the CMB temperature anisotropy. After decoupling, those oscillations leave an imprint also in the baryon distribution and, through gravitational interactions, in the dark matter distribution as well. Since the scale of these oscillations are set by the sound horizon at recombination, a measure of this scale (roughly  $100 h^{-1} \text{Mpc}$  comoving), as measured in the galaxy distribution, provides a standard ruler that enable inferring the angular diameter distance out to galaxies probed in a survey, and thus a robust way to measure the energy contents of the Universe. The main systematic uncertainties in the interpretation of BAO measurements are the effects of non-linear gravitational evolution, of scale-dependent differences between the clustering of galaxies and of dark matter (bias), and, for spectroscopic surveys, redshift distortions of the clustering, which can shift the BAO features.

**Weak gravitational lensing (WL).** The gravitational bending of light by structures in the Universe distorts or shears the images of distant galaxies. This distortion allows the distribution of dark matter and its evolution with time to be measured, thereby probing the influence of dark energy on the growth of structure. Systematic errors in weak lensing measurements arise from incorrect shear estimates, uncertainties in galaxy photometric redshift estimates, intrinsic correlations of galaxy shapes, and theoretical uncertainties in the mass power spectrum on small scales.

**Clusters of galaxies (CL).** Galaxy clusters are the largest virialized objects in the Universe. Therefore, not only they can be observed, but also their number density be predicted quite reliably, both analytically and from numerical simulations. Comparing these predictions to large-area cluster surveys that extend to high redshift can provide precise constraints on the cosmic expansion history. The primary systematic concerns are uncertainties in the mass-observable relation and in the selection function.

**Cosmic Microwave background (CMB).** Given the huge efforts involved in the last decades in the study of CMB, it indeed represents one of the most important tool to constrain the cosmological parameters. However the CMB probes

Method	Strengths	Weaknesses	Systematics
SN	purely geometric, mature	standard candle assumption	evolution, dust
BAO	largely geometric, low systematics	large samples required	bias, non-linearity
WL	growth+geometric, statistical power	CDM assumption	image quality, photo-z
CL	growth+geometric, X-ray+SZ+optical	CDM assumption	determining mass, selection function

Table 1.1: *Reproduced from (Frieman et al., 2008): Comparison of dark energy probes.*

a Universe in its earliest stage, in which dark energy contributed but a tiny part of the total energy density, as testified by Fig. 1.2. So it cannot be useful to constrain by itself dark energy parameters, even if its power in determining other cosmological parameters (such as the spatial curvature and matter density) results fundamental when used in combination with other probes.

## 1.5 Cosmological parameters and H(z) evaluation

The variety of probes that exists to constrain dark energy (and, generally speaking, cosmological) parameters have been discussed. As highlighted in Sect. 1.4.2, all of them have their strengths and weaknesses. However the real statistical power of this analysis depends exactly on having information from experiments probing completely different aspects. On the one side, having independent evidences for dark energy is important to strengthen the robustness of the analysis and cross-check the results. On the other side, even if each probe is only sensitive to a particular parameter, it is possible to take advantage of these difference by combining the analysis they provide.

The strength of combining data with different sensitivity to cosmological parameters is shown clearly by both Fig. 1.4 and Tab. 1.3 (taken from Amanullah et al. (2010)). In their work, they analyzed a sample of 557 SNe called Union2 compilation, obtained combining the Union compilation with the HST-light curves and spectra of six new high redshift SNe Ia, combining then their results with BAO analysis (Percival et al., 2010), the latest 7-years results of WMAP (Komatsu et al., 2011), and the latest estimate of  $H_0$  performed by Riess et al. (2009). As the figure shows, it is fundamental that the different techniques have completely different kind of degeneracies in the planes  $(\Omega_M, \Omega_\Lambda)$  and  $(\Omega_M, w)$ , so that the joint analysis reduces drastically the error on the estimate of the parameters. In Tab. 1.3 the different estimates of  $\Omega_M$ ,  $\Omega_k$  and  $w$  are reported as a function of the used probes.

In Tab. 1.2 are quoted as reference value the cosmological parameters obtained for a  $\Lambda$ CDM cosmology combining WMAP 7-years data, BAO informations and the estimate of  $H_0$ .

A fundamental step is, therefore, to increase the precision and the number of independent probes, in order to kill systematic errors and achieve the goal of precision cosmology. In this respect, an interesting and complementary approach

$H_0$	$70.4^{+1.3}_{-1.4}$ km/s/Mpc
$\Omega_M$	$0.272^{+0.016}_{-0.015}$
$\Omega_\Lambda$	$0.728^{+0.015}_{-0.016}$
$\Omega_b$	$0.0456 \pm 0.0016$
$z_{eq}$	$3232 \pm 87$
$z_{dec}$	$1088.2 \pm 1.1$
$z_{reion}$	$10.4 \pm 1.2$

Table 1.2: *Cosmological parameter obtained for a  $\Lambda$ CDM model using WMAP 7-years, BAO and  $H_0$  data.*

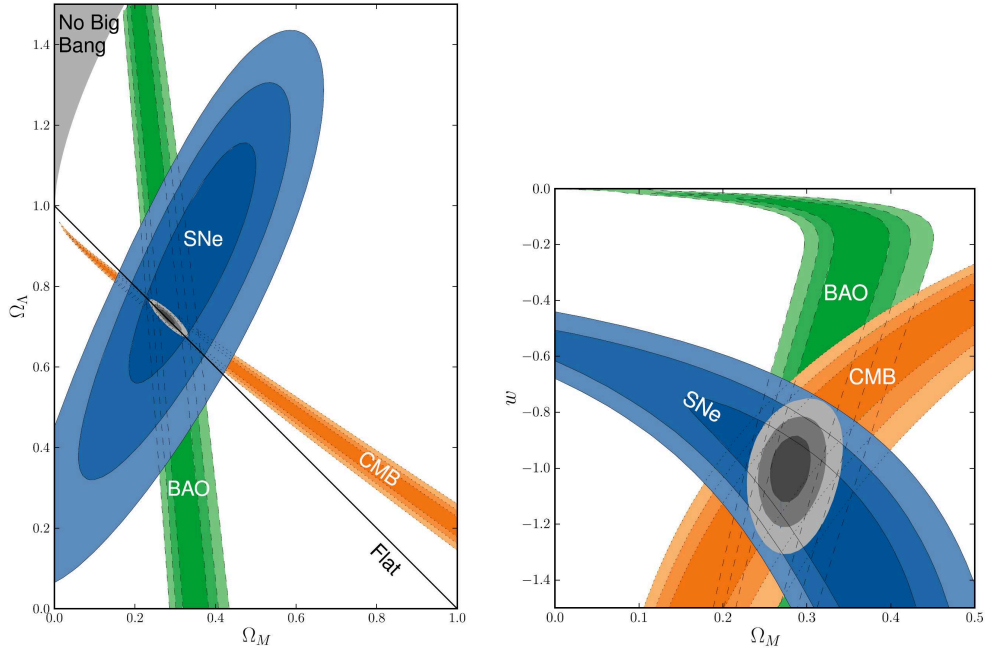


Figure 1.4: *Reproduced from Amanullah et al. (2010). Left panel: 68.3%, 95.4%, and 99.7% confidence regions in the  $(\Omega_M, \Omega_\Lambda)$  plane from SNe with systematic errors combined with the constraints from BAO and CMB (cosmological constant dark energy  $w = -1$  has been assumed). Right panel: 68.3%, 95.4%, and 99.7% confidence regions in the  $(\Omega_M, w)$  plane from SNe with systematic errors combined with the constraints from BAO and CMB (zero curvature and constant  $w$  have been assumed).*

Fit	$\Omega_M$	$\Omega_k$	$w$
SNe	$0.274^{+0.040}_{-0.037}$	0 (fixed)	-1 (fixed)
SNe+BAO+ $H_0$	$0.316^{+0.036}_{-0.035}$	0 (fixed)	$-1.154^{+0.131}_{-0.150}$
SNe+CMB	$0.269^{+0.023}_{-0.022}$	0 (fixed)	$-0.999^{+0.074}_{-0.079}$
SNe+BAO+CMB	$0.279^{+0.017}_{-0.016}$	0 (fixed)	$-0.997^{+0.077}_{-0.082}$
SNe+BAO+CMB	$0.281^{+0.018}_{-0.016}$	$-0.004^{+0.006}_{-0.007}$	-1 (fixed)
SNe+BAO+CMB	$0.281^{+0.018}_{-0.016}$	$-0.006^{+0.008}_{-0.007}$	$-1.035^{+0.093}_{-0.097}$

Table 1.3: *Reproduced from Amanullah et al. (2010). Results on cosmological parameters  $\Omega_M$ ,  $\Omega_k$  and  $w$ , including both statistical and systematic uncertainties.*

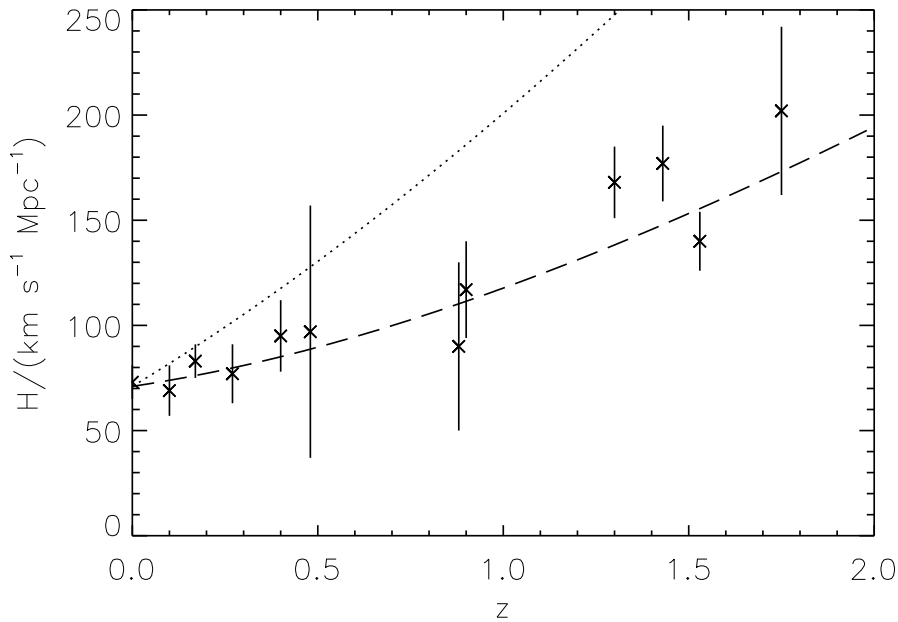


Figure 1.5: *Reproduced from Stern et al. (2010). The  $H(z)$  measurement from their sample of passively evolving galaxies. The dashed line is the  $\Lambda$ CDM model while the dotted line is an Einstein-de-Sitter model.*

to this problem has been proposed by Jimenez & Loeb (2002). In their work they propose to study the relative age evolution of the Universe as a function of redshift, since, as Eq. 1.5 shows, it would be a direct estimate of the Hubble parameter  $H(z)$ , and as a consequence of the cosmological parameters that regulate the evolution of the Universe. The strength of this method is that it avoids the common weakness of the other techniques, i.e. the reliance on integrated quantities to determine the expansion history. However, to fully exploit this approach, it is required to find a population of standard clocks able to trace the evolution of the relative age of the Universe. They proposed to use early-type galaxies (ETGs) as “*cosmic clocks*”, as they represent up to redshift  $z \approx 1$  a fairly homogenous population of galaxies sampling the oldest objects at each redshift. Recently, this approach has been applied to a sample of galaxies in a wide redshift range, obtaining at the present state the most accurate estimate of  $H(z)$  out to redshift  $z \approx 1$  (Stern et al. (2010), see Fig. 1.5).



---

# Chapter 2

## A perspective on early-type galaxies

Since Hubble's classification in 1936, galaxies have been divided between ellipticals, spirals and irregulars (see Fig. 2.1). Despite Hubble's classification was purely based on galaxies optical appearance, it has been found that morphology correlates with the characteristic properties of galaxies. Spirals and ellipticals differ in term of their stellar population content, with typical ellipticals being redder than the others, and showing purely stellar absorption-line spectra with no or very weak nebular emissions. As a consequence, it is possible to refer to early-type galaxies (ETGs) on the basis of a color (or spectroscopic properties) rather than morphological selection. Furthermore, the bulges of spirals of the earlier types show morphological as well as spectral similarities with ellipticals, and one often includes both ellipticals and bulges under the category of galactic spheroids. However this different selections do not fully overlap. For example, considering a study of ETGs from the Sloan Digital Sky Survey (SDSS) (Bernardi et al., 2006), it has been found that a sample selected using only a morphological, rather than a spectral or a color criterion, shows good correlation with the samples selected with the other criteria, but presents also some level of contamination, as reported by Tab. 2.1 (for more details, see Renzini, 2006).

In his pioneering work, Roberts (1963), reviewing the state of the art about the dependence of various parameter on the morphological type, indicated that the Hubble sequence corresponds also to an ordered succession in terms of present star formation rates and past star formation histories.

More recent studies, as reported in Renzini (2006), estimated that true ellipticals represent  $\sim 22\%$  of the total mass in stars in the local universe, a fraction amounting to  $\sim 75\%$  for spheroids (i.e., when including E0's and spiral bulges), whereas disks contribute only  $\sim 25\%$  and dwarfs an irrelevant fraction. Figure 2.3 (again taken from Renzini, 2006) shows the contributions to the total stellar mass by red and blue galaxies in the various mass bins, along with the contributions to

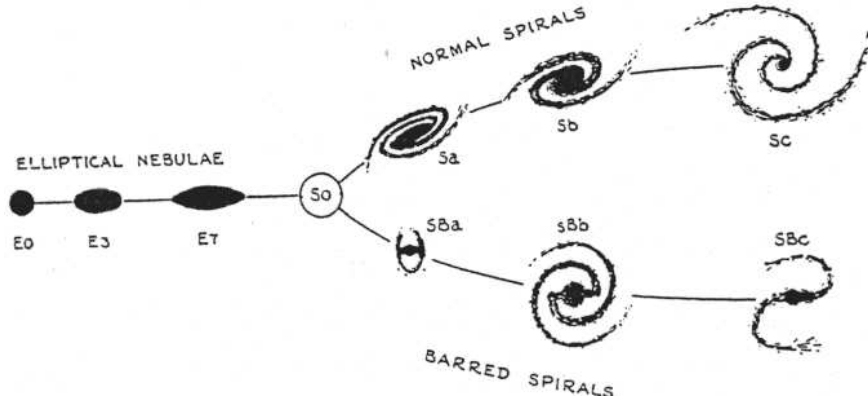


Figure 2.1: *Reproduced from Hubble (1936): Hubble's Tuning Fork diagram for classification of galaxies.*

the total number of galaxies, obtained from a sample based on SDSS data. It can be inferred that ETGs represent only 17% of the total number of galaxies in the sample, but contribute  $\sim 57\%$  of the total mass. Moreover,  $\gtrsim 80\%$  of the stellar mass in ETGs belongs to galaxies more massive than  $\sim 3 \times 10^{10} M_{\odot}$ .

In this chapter, the basic observational evidences about early-type galaxies are provided, focusing the attention on their main characteristics that make them the ideal candidates to obtain both evolutionary and cosmological insights about the Universe.

	MOR	COL	SPE
MOR	37151	70%	81%
COL	58%	44618	87%
SPE	55%	70%	55134

Table 2.1: *Reproduced from (Renzini, 2006): Morphology- versus Color- versus Spectrum-Selected Samples; the resulting numbers of galaxies fulfilling each criterion are given on the diagonal of the matrix.*

## 2.1 Properties of ETGs

Early-type galaxies are rather simple and homogeneous systems in terms of morphology, colors, stellar population content and scaling relations. These objects have been deeply studied in the last fifteen years, and various correlation have been found among their properties that could help to unveil their formation and evolution history. Here, only a brief review is given, summarizing their most im-

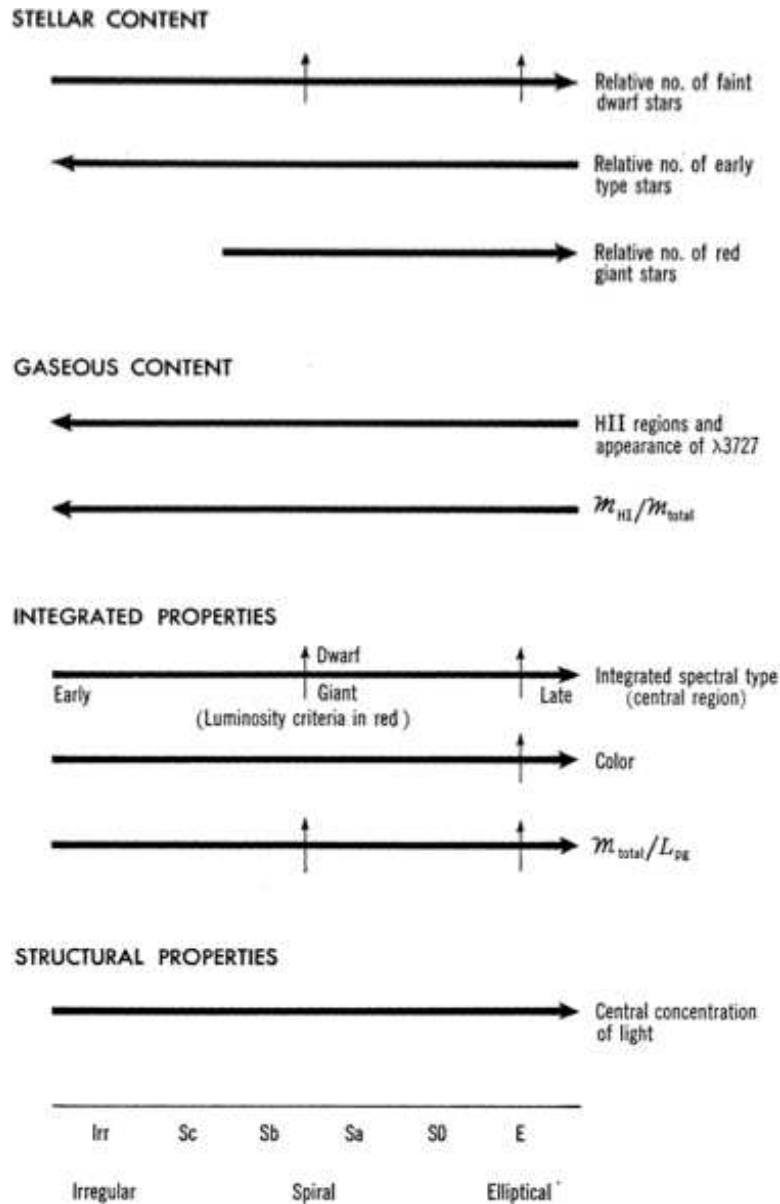


Figure 2.2: *Reproduced from Roberts (1963): the variation of characteristic properties of galaxies with morphological type. The horizontal arrow points in the direction of an increase in the parameter commonly used to describe the quantity indicated. When this parameter varies with the mass of the system, within a given morphological class, a vertical arrow indicates the sense of an increase with increasing mass. As the author underline, the absence of a vertical arrow do not imply necessarily the lack of a mass dependence: generally the data are insufficient to indicate a possible mass dependence.*

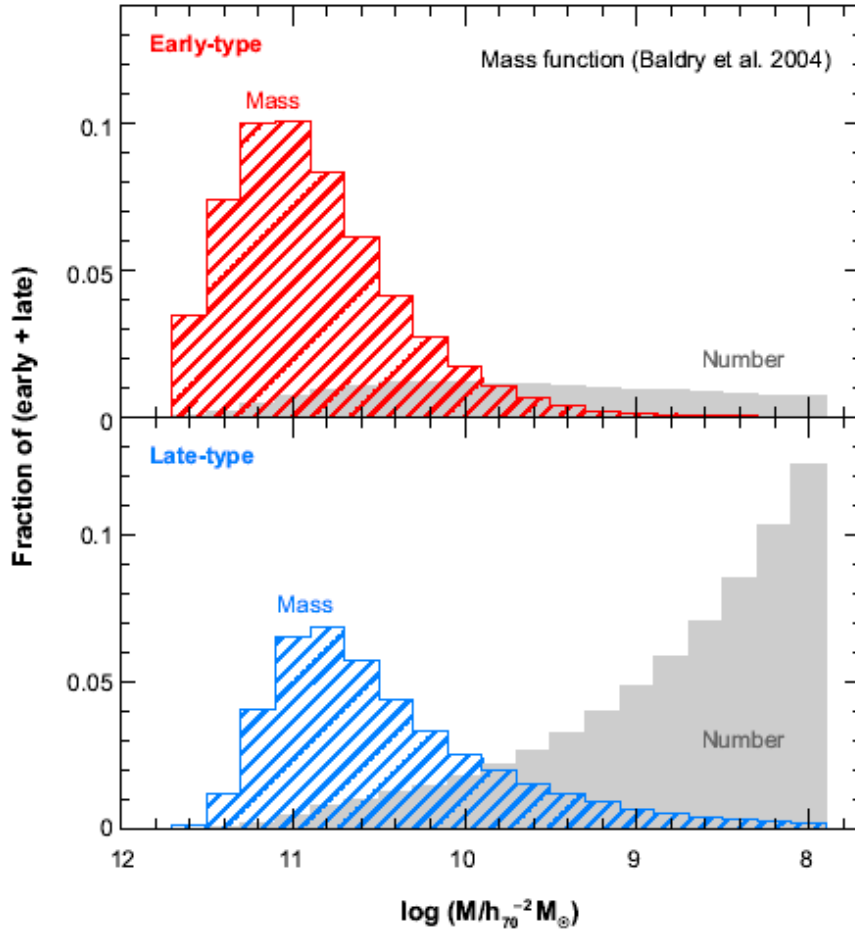


Figure 2.3: *Reproduced from Renzini (2006): the contributions to the total stellar mass and to the number of galaxies by early-type (red) and late-type (blue) galaxies in the various mass bins. The relative areas are proportional to the contributions of the early- and late-type galaxies to the total stellar mass and to the number of galaxies.*

portant relations and the constraints they set on galaxy evolution following the more comprehensive review by Renzini (2006).

### 2.1.1 Color-magnitude and color- $\sigma$ relation

The relation between color and magnitude (C-M) in ETGs was already found in early 1960s (Baum, 1959), and definitely established in late 1970s, with the work of Visvanathan & Sandage (1977) and Sandage & Visvanathan (1978a,b). In their analyses, they studied both E and S0 galaxies in Virgo cluster and in eight

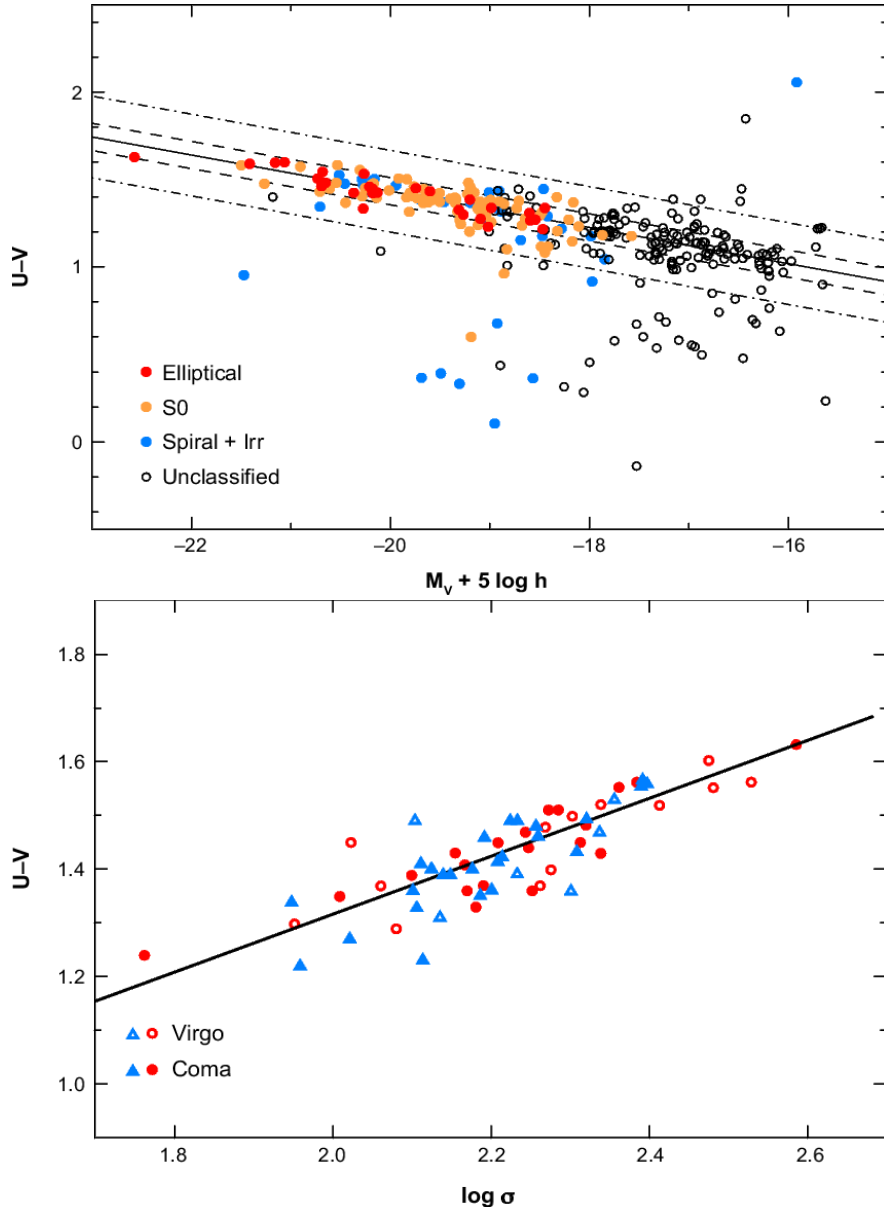


Figure 2.4: *Upper panel (reproduced from Bower et al., 1999): the  $(U - V)$  versus  $M_V$  color-magnitude relation for galaxies of the various morphological types that are spectroscopic members of the Coma cluster. Lower panel (reproduced from Bower et al., 1992): the relation between the  $(U - V)$  color and the central velocity dispersion ( $\sigma$ ) for early-type galaxies in the Virgo (open symbols) and Coma (filled symbols) clusters. Red circles represent ellipticals, blue triangles represent S0's.*

other groups, finding a similar C-M relation for all the galaxies, both in clusters and in the field. Given the equality of the color distribution, they argued that no significant episode of star formation as happened to those systems in the past  $\sim 1$  Gyrs, inferring also a uniformity of stellar content. Moreover they suggested that the universality of the relation can be used as a distance estimator. The upper panel of figure 2.4 shows the C-M plot for the Coma cluster galaxies as evaluated by Bower et al. (1999), demonstrating also how closely both S0's and ellipticals follow the same relation.

In their work Bower et al. (1992), analyzed the (U-V) color magnitude relation for early-type galaxies in Coma and Virgo clusters, and found really homogenous relations in both samples. They evaluated the intrinsic color scatter of ETGs about the mean C-M relation to be  $< 0.04$  mag, and used it to set constraints on the formation epoch of these systems. They used Bruzual & Charlot (1993) models to infer the implications of such a small scatter, transforming the color into age variation as follows:

$$\text{Scatter in (U - V) color} = \frac{\partial(U - V)}{\partial t} \times \text{scatter in time - formation epoch} \quad (2.1)$$

They parametrized the range of galaxy formation times as  $\beta(t_H - t_F)$ , where the parameter  $\beta$  quantifies the synchronization in the galaxy formation. In this way, they obtained that:

$$\text{Scatter in (U - V) color} = \frac{\partial(U - V)}{\partial t} \times \beta(t_H - t_F) \leq 0.04 \quad (2.2)$$

They evaluated that for a value  $\beta = 1$  (i.e. there is no coordination between the forming galaxies) the redshift of formation should be  $z_F \gtrsim 2.8$ , while for a more synchronous formation ( $\beta = 0.03$ ) the redshift of formation should be  $z_F \gtrsim 1.1$ . They therefore concluded that elliptical galaxies should have formed the bulk of their stars at  $z \gtrsim 2$ , providing the first clear evidence that ETGs must be old, passively evolving systems.

It has been shown that the tightness of the C-M (or color- $\sigma$ , where  $\sigma$  is the central stellar velocity dispersion of the galaxy) provides constraints about the age of the stellar populations of ETGs; at the same time, the slope of these relations can help in constraining the amount of merging occurred to those systems. In fact, if a merging without star formation is considered, it leaves the colors unchanged, but increases the luminosity and  $\sigma$ , reducing the slope and increasing the scatter; if it is considered a merging with star formation, this also produce a shift towards the blue of the colors, thus broadening and flattening the relations even more. By analyzing the slope of the C-M relation in rich clusters, Bower et al. (1998) concluded that the bulk of the stellar population must have formed before  $z = 1$ , but can not have formed in mass units much less than about half their present mass.

### 2.1.2 The fundamental plane

There exists an empirical law relating the three main parameters of elliptical galaxies, that are the effective radius  $R_e$ , the central velocity dispersion  $\sigma$ , and the effective surface brightness  $I_e$ . In the space  $(R_e, \sigma, I_e)$ , those galaxies are well represented from a plane, known as fundamental plane (FP), with  $R_e \propto \sigma^a I_e^b$  (Dressler et al., 1987; Djorgovski & Davis, 1987), where the exponents  $a$  and  $b$  depend on the specific band used for measuring the luminosity. The projection of the FP over the  $(\sigma, L = 2\pi R_e^2 I_e)$  coordinate plane generates the Faber-Jackson relation (Faber & Jackson, 1976), whereas a projection over the  $(R_e, I_e)$  plane generates the Kormendy relation (Kormendy, 1977).

The FP was firstly adopted as a distance estimator; however it is really important also to set constraints on the properties of the stellar content of galaxies, and on their formation. As argued by Renzini (2006), its existence implies that ellipticals (a) are virialised systems, (b) have self-similar (homologous) structures, or their structures (e.g., the shape of the mass distribution) vary in a systematic fashion along the plane, and (c) contain stellar populations which must fulfill tight age and metallicity constraints.

In their analysis, Renzini & Ciotti (1993) analyzed the small dispersion perpendicular to the FP of elliptical galaxies, concluding that this should imply a small age dispersion ( $\lesssim 15\%$ ) and high formation redshift, fully consistent with the Bower et al. (1992) argument based on the narrowness of the C-M and color- $\sigma$  relations.

### 2.1.3 The line-strength diagnostics

The optical spectra of ETGs have been demonstrated to be rich of informations, for the presence of numerous absorption lines that correlates with stellar ages, metallicity, and abundance ratios of those systems. Since the preliminary work of Burstein et al. (1984), it has been defined a complete set of twenty-one absorption features, known as *Lick-IDS system*, whose purpose was predicting index strengths in the integrated light of stellar populations of different ages and metallicities (Worthey et al., 1994).

The most used features have been the  $Mg_2$  (or  $Mgb$ ),  $\langle Fe \rangle$ , and the  $H\beta$  indices, measuring respectively the strength of  $MgH + MgI$  at  $\lambda \approx 5156 - 5197 \text{ \AA}$ , the average of two  $FeI$  lines at  $\lambda \approx 5248$  and  $5315 \text{ \AA}$ , and the strength of  $H\beta$  at  $\lambda = 4861 \text{ \AA}$ . Despite some doubts in the general interpretation of this approach, in particular due to the inadequacy of the theoretical models in describing data, it is now generally accepted that massive ellipticals are genuinely enriched in magnesium relative to iron.

Maraston et al. (2003) provided an empirical calibration for the synthetic Lick indices of Simple Stellar Population (SSP) models using a sample of Milky Way

globular clusters and several metal rich clusters belonging to the Galactic bulge; with their analysis, they shown that for the bulge globulars an alpha-enhancement  $[\alpha/Fe] = +0.3$ , in agreement with the available spectroscopic determinations, is needed to reproduce the indices at all metallicities.

In their work, Thomas et al. (2005) developed models of absorption-line indices accounting for variable abundance ratios, and used them to derive ages, total metallicities, and element ratios of 124 early-type galaxies in high- and low-density environments. They found that all three parameters (age, metallicity, and  $[\alpha/Fe]$  ratio) are correlated with velocity dispersion; moreover more massive galaxies ( $M \gtrsim 10^{11} M_{\odot}$ ) appear dominated by old stellar populations, while for less massive ones ( $\sim 10^{10} M_{\odot}$ ) there is evidence for the presence of intermediate-age stellar populations with low  $[\alpha/Fe]$  ratios. From their results, they concluded that most star formation activity in early-type galaxies is expected to have happened between redshifts  $\sim 3$  and 5 in high-density environments and between redshifts 1 and 2 in low-density environments, and that at least 50% of the total stellar mass density must have already formed at  $z \sim 1$ , in good agreement with observational estimates of the total stellar mass density as a function of redshift. These differential results as a function of the environment, however, are not confirmed in a subsequent analysis done by Thomas et al. (2011), finding nevertheless for these massive systems a high value of redshift of formation ( $z_F \sim 4$  for  $\log_{10}(M_{dyn}/M_{\odot}) \sim 12$ ).

## 2.2 Galaxy evolution

All the observational evidences highlighted in the previous section were firstly found, for historical reason, looking local or low-redshift galaxies. However, to disentangle in detail the evolution and formation history of galaxies, observation at higher redshifts, hence probing galaxies in a younger Universe, are necessary.

**The color-magnitude relation.** Considering the C-M relation, a lot of studies were made in trying to follow it up to  $z \sim 1$ . Following the approach of Bower et al. (1992), Ellis et al. (1997) studied the rest-frame UV optical photometry of a large sample of morphologically selected spheroidal galaxies in three  $z \sim 0.54$  clusters; they found a small scatter ( $< 0.1$  mag rms) for galaxies classified as E's and E/S0's, with no trend for the scatter to increase with decreasing luminosity. Therefore, they argued that most of the star formation in the elliptical galaxies in dense clusters was completed before  $z \simeq 3$ .

Stanford et al. (1998) extended these results to clusters up to  $z \approx 0.9$ , and shown that the slope and the intrinsic scatter of the C-M relation is nearly constant up to the probed redshift. From their results, they concluded that most early-type galaxies in rich clusters are old, formed the majority of their stars at high redshift in a well-synchronized fashion, and evolved quiescently thereafter.

The C-M relation has been followed also up to higher redshift: Blakeslee et al. (2003) investigated galaxies in a cluster at  $z = 1.24$ , finding for the early-type population a tight sequence in the CM diagram, with an intrinsic scatter of  $\sim 0.03$  mag. This corresponds in no evidence of evolution out to  $z \approx 1.2$ , with a mean age of  $\sim 3$  Gyr and no star formation activity up to  $z \gtrsim 1.5$ .

**The Fundamental Plane.** A lot of interest has been devoted also to the study of the redshift evolution of the FP, since its dependence on a variety of factors can help to set constraints on galaxy evolution. Renzini & Ciotti (1993) argued that, for passive evolution, the FP shifts by amounts that depend on a combination of IMF slope, formation redshift, and cosmological parameters. A systematic trend of the IMF slope with galaxy mass would cause the FP to rotate with increasing redshift, as it would do for a similar trend in galaxy age. An age dispersion ( $\Delta t$ ) would cause the scatter perpendicular to the FP to increase with redshift, as, for fixed  $\Delta t$ ,  $\Delta t/t$  increases for increasing redshift, i.e. decreasing galaxy age ( $t$ ).

Different independent works from middle 1990s up to the presents (van Dokkum & Franx, 1996; Kelson et al., 1997; van Dokkum et al., 1998; van Dokkum & Stanford, 2003; Wuyts et al., 2004; Holden et al., 2005) gave evidences that the FP actually shifts nearly parallel to itself by an amount that increases with redshift and is consistent with the passive evolution of stellar populations that formed at high redshifts.

**The luminosity and mass functions.** An important test of the high formation redshift of ETGs can be provided by the study of the luminosity function (LF) and mass function (MF) from the local Universe up to higher redshifts. If, for these galaxies, a passive evolution is confirmed, this should correspond to an increase in the luminosities as a function of redshift, depending on the redshift of formation and on the slope of the Initial Mass function (IMF).

de Propris et al. (1999) analyzed the evolution of the observed K-band LF in 38 clusters with  $0.1 < z < 1$ , and they results pointed out not only that the stellar populations of ETGs formed at high-redshift, but that the assembly of the galaxies themselves was largely complete by  $z \approx 1$  and that subsequent evolution down to the present epoch was primarily passive. Toft et al. (2004) extended this result by evaluating the K-band LF of a  $z = 1.237$  massive X-ray luminous cluster, concluding that the observed evolution is consistent with a scenario in which clusters are composed of a population of massive galaxies which formed at high redshift ( $z \gg 1$ ) and subsequently evolved passively, and a population of lower mass galaxies which are gradually accreted from the field, primarily at lower redshift ( $z < 1$ ).

Many studies have shown that there is a very weak evolution from  $z \approx 0.7 - 0.8$  to  $z \approx 0$  of the luminosity and stellar mass functions for luminous, massive

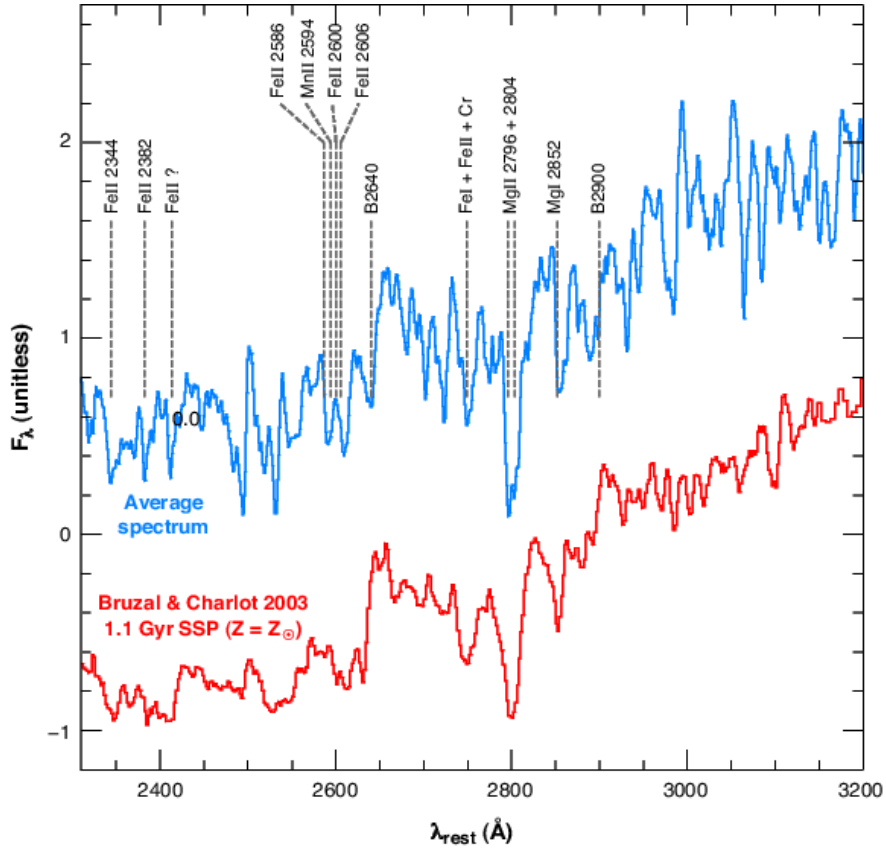


Figure 2.5: *Reproduced from Cimatti et al. (2004): a zoom on the average spectrum of the four ETGs found with K20 survey in the range  $1.6 \lesssim z \lesssim 1.9$  (blue) compared with the synthetic spectrum of a 1.1 Gyr old simple stellar population (SSP) with solar metallicity ( $Z = Z_{\odot}$ ) and Salpeter IMF (red).*

galaxies, but they evolve much faster for lower mass systems (Fontana et al., 2004; Bell et al., 2004; Drory et al., 2005; Yamada et al., 2005; Caputi et al., 2006; Bundy et al., 2006; Cimatti et al., 2006; Bundy et al., 2007; Pozzetti et al., 2007, 2010, and many others). If, on one side, the number density of luminous (massive) ETGs ( $M_B(z=0) < -20.5$  and  $M > 10^{11} M_{\odot}$ ) is nearly constant, at least up to  $z \approx 0.8$ , on the other side less luminous ETGs display a deficit which grows with redshift. Kaviraj et al. (2008), by inspecting the colors of a sample of ETGs at  $0.5 < z < 1$ , demonstrated that luminous ( $-23 < M_V < -20.5$ ) and less luminous galaxies formed respectively  $\approx 10 - 15\%$  and  $\approx 30 - 60\%$  of their mass since  $z \sim 1$ .

**High redshift ETGs.** The last piece of evidence was set by the impressive discovery of Glazebrook et al. (2004) and Cimatti et al. (2004), that found, re-

spectively, five passively evolving galaxies at  $1.57 \lesssim z \lesssim 1.85$ , and four other such objects at  $1.6 \lesssim z \lesssim 1.9$  (see Fig.2.5). All these galaxies were brighter than  $K = 20$  and quite massive ( $M \gtrsim 10^{11} M_{\odot}$ ). This suggests that they were (almost) fully assembled already at this early epoch, and having been passive since at least  $\sim 1.1$  Gyr had to form at redshift  $\gtrsim 2.7$  (see also McCarthy et al., 2004; Saracco et al., 2005; Daddi et al., 2005; Kriek et al., 2006).

In summary, the study of the stellar populations in ETGs belonging to distant clusters up to  $z \sim 1.3$  have unambiguously shown that these objects have evolved passively from at least  $z \sim 2 - 3$ . This came from the color, line strength, and luminosity evolution. Moreover, the brightest cluster members at  $z \sim 1 - 1.3$  and the characteristic luminosity of the LF appear to be brighter than their local counterpart by an amount that is fully consistent with pure passive evolution, indicating that these galaxies were already fully assembled at this high redshift.

## 2.3 Theories of formation of ETGs

Understanding the physical mechanisms behind galaxy evolution has been one of the most important tasks of astronomers. There are a lot of extensive and detailed works reviewing the models of ETGs formation (e.g. Baugh et al., 2006). In the following, the scheme used by Mo et al. (2010) has been followed.

The evidences found of complex dynamical structure of elliptical galaxies, testified by their internal velocity dispersion, suggest that their formation should include some violent process. A fundamental step in understanding this process has been the discovery that violent relaxation can produce elliptical systems with density profiles similar to those of elliptical galaxies. Historically, two has been the competing scenarios to explain galaxy evolution:

- the **Monolithic Collapse model** (e.g. Eggen et al., 1962; Larson, 1974; Arimoto & Yoshii, 1987; Bressan et al., 1994). In this scenario elliptical galaxies form on a short time scale through collapse and virialization. The star-formation is concentrated over a short time scale, and then the galaxy evolve passively to the present. Its main characteristic is that the stars form simultaneously with the assembly of the mass of the final galaxy; it is also referred as a “top-down” scenario.
- the **Hierarchical Merging model** (e.g. Blumenthal et al., 1984; White et al., 1978). For this model, elliptical galaxies result from the mutual disruption of pre-existing objects in a merging event. In this case, the formation of stars occurs independently and before the assembly of the final galaxy; it is also referred as a “bottom-down” scenario.

In the monolithic collapse scenario, elliptical galaxies have been formed from a single burst of star formation at high redshift, followed by passive evolution to the present. If the collapse responsible of the star formation activity is completely dissipationless (i.e. faster than the free-fall time scale), all the gas is turned into stars in the very first moments of the galaxy evolution. However, this would imply a redshift of formation for elliptical greater than  $\sim 20$ , that is quite incompatible with the more recent estimates for which only a small fraction of stars formed at  $z \gtrsim 6$ . Moreover another inconsistency is that in this scenario there is no way to produce a different evolution for stars and dark matter, that at the end should have a similar space distribution, which is again contradicted by observations. On the other hand, if dissipation is supposed to occur during the collapse, the gas evolution can be decoupled to the evolution of the stars. Despite some success in representing some observed properties of ellipticals (luminosity profiles, metallicity gradients, scaling relations) one of the major problem of this model is that it requires that the final assembly of the galaxy occurs almost simultaneously with the formation of stars; however both the study of the evolution total mass density

of ellipticals as a function of redshift, as well as the observation of their strong size evolution sharply contradicts this assumption.

In the hierarchical merging scenario, all the star formation is concentrated into disks, while ellipticals are formed through merger events. This assumptions seem plausible, since, at least in the local Universe, the amount of star formation outside galaxy disks, or irregulars, or starburst galaxies is really negligible, and since there are many observational evidences of merger. However the key point is if the observed merger rate can reproduce the abundance of elliptical galaxies as a function of their mass, age metallicity, and so on. Also in this case, the situation changes if dissipation or dissipationless merger are considered. In particular it has been suggested that massive ellipticals can be the remnants of a dissipationless merger event (also called “dry merging”) between elliptical progenitors, while less massive ones can be described by dissipational mergers (or “wet mergers”).

The problems with the merger models, given that mergers are effectively observed, is if real merger rates are compatible with the observed population of ellipticals and its properties. Since merger rate is a quantity rather complex to be measured with the needed precision, this issue has to be addressed theoretically. In order to do that, in addition to statistics modeling the accretion of dark matter halos and to convert gas into stars, some mechanisms of feedback is needed in order to trigger and/or stop star formation in these system. Since massive ellipticals are observed to have different properties with respect to less massive one (in particular they are systematically older), a process that prevent the formation of stars in these systems, other than supernova feedback, is needed, and active galactic nuclei (AGN) feedback has been proved to be a good candidate. With these prescriptions, many of the observed properties of ETGs can be reproduced and predicted within the hierarchical merging scenario. However some discrepancy between models and theory remains, and only observation can help in disentangling the history of evolution of these system; and it is plausible that processes invoked in the different scenarios has to be taken into account.

In particular, the determining properties to be checked in order to explain ETGs evolution are the star formation history, the assembly history and the progenitor properties, since these quantity are generally predicted systematically different in the two scenarios.

As argued in Sect. 1.3, the current CMB and LSS observations strongly support the  $\Lambda$ CDM model, that is based on a cosmological constant  $\Lambda$  and on the cold dark matter CDM in order to explain the observed cosmological expansion history of the Universe, from the CMB to the present accelerated expansion. Within this framework, it is predicted a structure formation “bottom-up”, for which first of all the small structures are formed, building gradually the bigger ones via merging processes. This model has been studied also numerically, testing its prediction with the development of large numerical simulations (for a discussion, see Springel et al., 2005).

The establishment of the  $\Lambda$ CDM model, together with the detailed and complementary observations supporting it (e.g. Percival et al., 2010; Amanullah et al., 2010; Komatsu et al., 2011), ruled out definitively the monolithic collapse model, since, on the contrary, it represents a “top-down” scenario.

### 2.3.1 The downsizing scenario

As underlined in the previous section, evidence has accumulated that the bulk of stars in spheroids are old, and most likely formed in major merging events. The analysis of the Millennium Simulation provided important insights for understanding the formation of elliptical galaxies within the concordance  $\Lambda$  cold dark matter (CDM) model; De Lucia et al. (2006), tuning the model to fit the joint luminosity/color/morphology distribution of low-redshift galaxies, confirmed that massive ellipticals should have higher metal abundances, older luminosity-weighted ages and shorter star formation time-scales, but lower assembly redshifts, than less massive systems. However the detailed process with which ETGs assemble their mass is still unclear.

On the one hand, dissipationless “dry merging” of ETGs has been suggested to build up the masses of massive ETGs (van Dokkum et al., 2005; Bell et al., 2006), reproducing results that are consistent with the high central densities of ellipticals, their old stellar populations, and the strong correlations of their properties; on the other hand, arguments based on the evolution of the shape of the stellar mass function (Bundy et al., 2006) and on the very small scale clustering ( $0.0 < r < 8 h^{-1}$  Mpc) of local SDSS ETGs at  $0.16 < z < 0.36$  (Masjedi et al., 2006) arise some problems in this scenario.

Cowie et al. (1996) (see also Gavazzi & Scodreggio, 1996), in order to solve all the open issues of the standard hierarchical scenario, introduced the possibility of a model for which the evolution of galaxies is triggered by galaxy mass, so that less massive systems have a more prolonged star formation with respect to more massive galaxies, these latter completing their star formation at higher redshifts. This model is known as **downsizing**, and a detailed review can be found in Cimatti (2007) and Cimatti (2009).

There are nowadays different observational evidences that support this scenario. Fontana et al. (2004), within the K20 survey, found that the typical  $M^*/L$  ratio of massive early-type galaxies is larger than that of less massive ones, suggesting that their stellar population formed at higher  $z$ . Thomas et al. (2005), and later Thomas et al. (2010), found that the star formation histories of ETGs at  $z \sim 0$  is strongly mass-dependent, with an evidence for more massive objects ( $\log_{10}(M_{dyn}/M_{\odot}) \sim 12$ ) to be have a much higher formation redshift ( $z_F \approx 3 - 5$ ) with respect to less massive galaxies ( $z_F \sim 1$  for  $\log_{10}(M_{dyn}/M_{\odot}) \sim 10.5$ ). Treu et al. (2005) analyzed the FP of galaxies in the range  $0.2 < z < 1.2$ , obtaining a strong evolution of the M/L ratio that depends significantly on the dynamical

mass of the galaxies. They argued that these trends are consistent with single-burst populations that formed at  $z_F > 2$  for high-mass spheroidals and  $z_F \sim 1.2$  for lower mass systems, being also the fraction of stellar mass formed at recent times strongly dependent on galactic mass, ranging from  $< 1\%$  for masses above  $10^{11.5} M_\odot$  to 20%-40% below  $10^{11} M_\odot$ . Several works found that there exist a differential and mass-dependent evolution of the stellar mass function, nearly constant from  $z \sim 0.7 - 0.8$  to  $z \sim 0$  for massive galaxies, but much faster for low-mass systems (Fontana et al., 2004; Drory et al., 2005; Caputi et al., 2006; Bundy et al., 2006; Cimatti et al., 2006). The specific star formation rate ( $SSFR = SFR/M$ ) has been found to be larger for lower mass galaxies in comparison to higher mass galaxies at all redshifts, with the SSFR for massive galaxies increasing by a factor of  $\approx 10$  at  $z > 2$  (Feulner et al., 2005; Juneau et al., 2005; Cimatti, 2007). Le Borgne et al. (2006) shown that there has been a significant decline in the abundance of massive galaxies with strong  $H\delta$  stellar absorption lines from  $z \sim 1.2$  to the present, with these “ $H\delta$ -strong” galaxies that have undergone a recent and rapid break in their star formation activity. Finally a lot of works documented the existence of old, massive, nearly passively evolving ETGs up to  $z \sim 2.5$  (Cimatti et al., 2004; McCarthy et al., 2004; Saracco et al., 2005; Daddi et al., 2005; Kriek et al., 2006).

On the basis of many recent observational evidences, it has been proposed that the downsizing scenario should apply not only to star formation (i.e. stars in more massive galaxies are older), but also to the stellar mass assembly, with more massive galaxies that have assembled before less massive ones. This is often referred as **mass-downsizing**. Although hierarchical models are able to successful reproduce the star formation downsizing, a coherent explication of the latter one within theoretical models still lacks.

A possible picture for the formation and evolution of massive ETGs is given by Cimatti (2009); in the following, is reported the basic scheme (see also Fig. 2.6):

1. A large fraction of massive star-forming galaxies selected in the optical/near-IR are gas-rich disk systems characterized by a “quiet” evolution with long-lived star formation (e.g.  $\approx 0.5 - 1$  Gyr) supported in some cases by “smooth accretion” of cold gas streams. These massive systems may later evolve into spheroids through disk instabilities and/or merging processes;
2. The submillimeter galaxy (SMG) phase corresponds to the cases of rapid, highly dissipative, gas-rich major mergers characterized by short-lived ( $\approx 0.1$  Gyr) starbursts. It is intriguing to notice that SMGs are the only star-forming systems at  $z > 2$  having the same small sizes and high (gas) mass surface density of ETGs at  $1 < z < 2$ . If the compact superdense ETGs at  $1 < z < 2$  are the descendants of SMGs, the duty cycle timescale of the SMG phase can be estimated as the ratio of the comoving number densi-

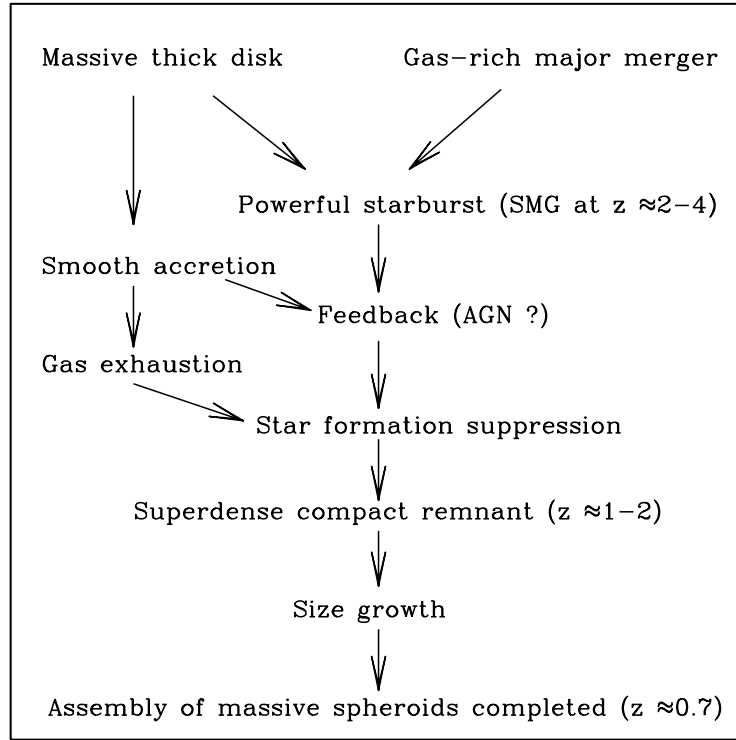


Figure 2.6: *Reproduced from Cimatti (2009): the variety of possible evolutionary paths for the formation of massive spheroidal galaxies.*

ties of the SMGs ( $\approx 10 - 5 Mpc^{-3}$ ) and ETGs ( $\approx 10 - 4 Mpc^{-3}$ ) and the amount of cosmic time available from  $z \approx 2.5$  to  $z \approx 1.5$  ( $\approx 1.5$  Gyr), i.e.  $\approx 0.15$  Gyr. This is broadly consistent with the e-folding timescale derived independently from the SED fitting and from the SMG molecular gas. AGN feedback would then be required to “quench” the star formation. This could also explain the origin of the relation between super-massive black hole and galaxy masses. Although the involved physical processes are different, this scenario is somehow reminiscent of the “old-fashioned” monolithic collapse;

3. the compact, superdense ETGs at  $1 < z < 2$  evolve by increasing gradually their sizes. A possible mechanism is major dissipationless (“dry”) merging. However, it is unclear how the “dry” merging scenario can be reconciled with the properties of the small-scale clustering of low- $z$  ETGs and with

the weak evolution of the high-mass end of their stellar mass function at  $0 < z < 0.7$ . Other processes which may increase the sizes at  $z < 1$  are the smooth envelope accretion and multiple frequent minor mergers;

4. the majority of most massive ETGs reaches the assembly completion around  $z \approx 0.7 - 0.8$ , while lower mass ETGs continue to assemble down to lower redshifts (downsizing).

## 2.4 Conclusions on ETGs properties

Summarizing the conclusions on ETGs that are strongly based on observational evidences, it is possible to say that:

- Elliptical galaxies represent a simple and homogeneous population in term of colors, morphology and stellar population content;
- spheroids (i.e., when including E0's and spiral bulges) represent  $\sim 75\%$  of the total mass in stars in the local universe, a fraction amounting to  $\sim 22\%$  when considering only true ellipticals;
- the C-M, color- $\sigma$  and FP relations for ETGs in clusters indicate that the bulk of stars in these galaxies formed at  $z \gtrsim 2 - 3$ ;
- the study of the luminosity and stellar mass functions, joint with the discovery of high-redshifts ETGs, suggests that not only the stellar populations of ETGs formed at high-redshift, but that the assembly of the galaxies themselves was largely complete by  $z \approx 0.7 - 0.8$ , at least for most massive ETGs;
- there are strong observational basis that support the mass-downsizing scenario, for which more massive galaxies have assembled before less massive ones;
- the weak evolution of the stellar mass function suggest that most massive ETGs suggests for these systems a nearly passive evolution in the last 7 billion years (i.e.  $\approx 50\%$  of the life of the Universe)
- this latter property makes ETGs among the oldest object of the Universe at each redshift.

All this properties make ETGs the ideal candidates to address several fundamental open questions of modern cosmology and astrophysics, such as the cosmic history of galaxy mass assembly, the evolution of large scale structure, the evolution of galaxy clusters, the link between supermassive black holes and host galaxies, the role of feedback in galaxy formation, the physical origin of the Hubble morphological classes, the constrain of cosmological parameters using them as “*cosmic chronometers*”.

---

# Chapter 3

## Definition and characterization of ETGs samples

In this chapter, it is described how a reliable sample of early-type galaxies have been built, illustrating the surveys from which galaxies have been extracted, the criteria used to select a sample of passive ETGs the less contaminated as possible from the presence of outliers and the method used to correctly set up their photometry. also the properties obtained from the fit to their spectral energy distributions are analyzed, discussing the reliability of the retrieved parameters and their degenerations with other quantities and/or their dependences on assumed models.

### 3.1 Spectroscopic surveys

In the framework of this analysis it is fundamental to obtain a sample with the widest possible redshift leverage, in order to follow the evolution of ETGs sampling a large range of lookback time (and hence age of the Universe).

Nowadays, there exist numerous massive spectroscopic surveys that have mapped the galaxies in the Universe, providing us their properties and, most important, redshifts both locally ( $z \sim 0$ ) up to  $z \sim 1.5$ ; this has been a fundamental step to build a 3D view of the Universe (e.g. see 3.1). In the following sections the two main spectroscopic surveys from which the sample of ETGs have been extracted are briefly described.

#### 3.1.1 Sloan Digital Sky Survey (ETGs at $0 < z < 0.5$ )

The Sloan Digital Sky Survey (SDSS) is one of the most ambitious and influential surveys in the history of astronomy. Over eight years of operations (SDSS-I, 2000-

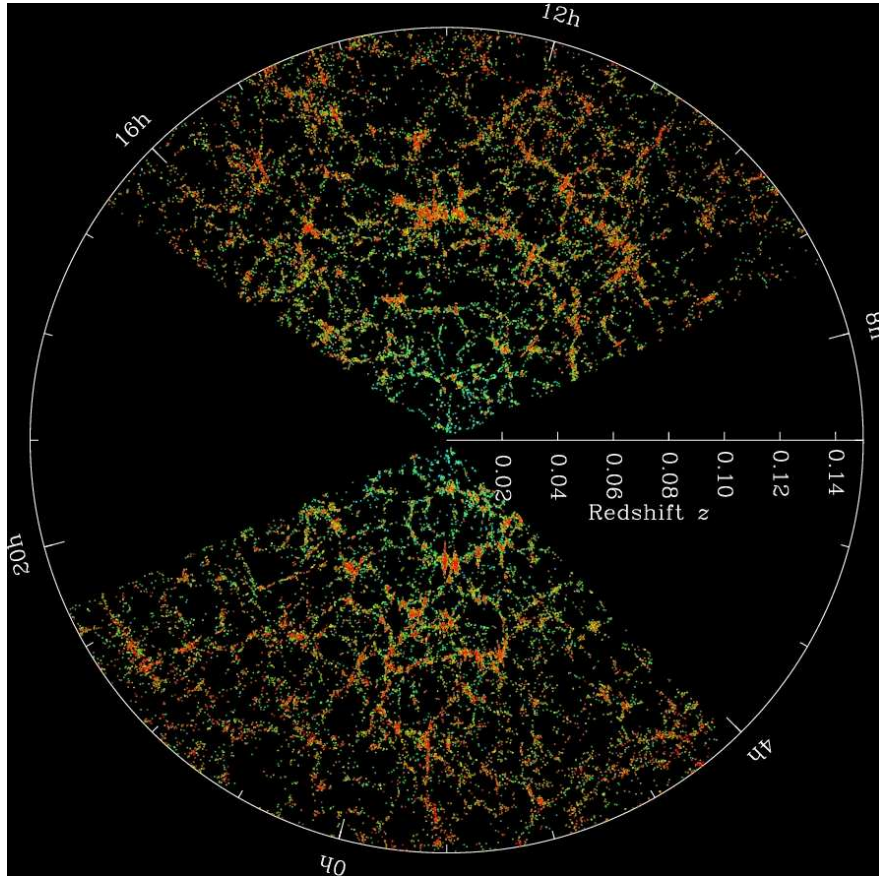


Figure 3.1: *Large scale structure in the northern equatorial slice of the SDSS main galaxy redshift sample. The slice is 2.5 degrees thick, and galaxies are color-coded by luminosity. Credit: M. Blanton and the Sloan Digital Sky Survey.*

2005; SDSS-II, 2005-2008), it obtained deep, multi-color images covering more than a quarter of the sky and created 3-dimensional maps containing more than 930,000 galaxies and more than 120,000 quasars.

The SDSS uses a dedicated wide-field 2.5 m telescope located at Apache Point Observatory near Sacramento Peak in Southern New Mexico. The telescope uses two instruments. The first is a wide-field imager with 24  $2048 \times 2048$  CCDs on the focal plane with  $0.396''$  pixels that covers the sky in drift-scan mode in five filters in the order riuzg. The imaging is done with the telescope tracking great circles at the sidereal rate; the effective exposure time per filter is 54.1 s, and  $18.75 \text{ deg}^2$  are imaged per hour in each of the five filters. The images are mostly taken under good seeing conditions (the median is about  $1.4''$  in r) on moonless photometric nights. The 95% completeness limits of the images are  $u, g, r, i, z = 22.0, 22.2,$

22.2, 21.3, 20.5, respectively, although these values depend as expected on seeing and sky brightness. The images are processed through a series of pipelines that determine an astrometric calibration and detect and measure the brightnesses, positions, and shapes of objects. The astrometry is good to 45 milliarcseconds (mas) rms per coordinate at the bright end. The photometry is calibrated to an AB system, and the zero points of the system are known to 1%-2%.

The photometric catalogs of detected objects are used to identify objects for spectroscopy with the second of the instruments on the telescope: a 640-fiber-fed pair of multiobject double spectrographs, giving coverage from 3800Å to 9200Å at a resolution of  $\Delta\lambda/\lambda \approx 2000$ . The objects chosen for spectroscopic follow-up are selected based on photometry corrected for Galactic extinction following Schlegel et al. (1998) and include a sample of galaxies complete to a petrosian magnitude limit of  $r = 17.77$ .

Spectra are extracted and calibrated in wavelength and flux. The typical S/N of a galaxy near the main sample flux limit is 10 per pixel. The broadband spectrophotometric calibration is accurate to 4% rms for point sources, and the wavelength calibration is good to 2 km s<sup>-1</sup>. The spectra are classified and redshifts determined using a pair of pipelines, which give consistent results 98% of the time; the discrepant objects tend to be of very low S/N, or very unusual objects, such as extreme broad absorption line quasars, superposed sources, and so on. The vast majority of the spectra of galaxies and quasars yield reliable redshifts; the failure rate is of order 1% for galaxies and slightly larger for quasars. Further details concerning the seventh data release (DR7) can be found at <http://www.sdss.org/dr7/> and in Abazajian et al. (2009).

### 3.1.2 zCOSMOS (ETGs up to $z \sim 1$ )

The Cosmic Evolution Survey (COSMOS; Scoville et al., 2007) is the largest contiguous HST survey ever undertaken ( $\approx 640$  orbits, Koekemoer et al., 2007), which has imaged a  $\sim 2$  deg<sup>2</sup> field using the Advanced Camera for Surveys (ACS) with single-orbit I-band exposures to a depth  $I_{AB} \simeq 28$  mag and 50% completeness at  $I_{AB} = 26.0$  mag for sources 0.5'' in diameter. COSMOS observations are implemented with an excellent coverage of the field with multiband photometry from the UV (with GALEX, Zamojski et al., 2007), optical (with Subaru and CFHT, Taniguchi et al., 2007; Capak et al., 2007), NIR (with CTIO, KPNO, and CFHT, Capak et al., 2007; McCracken et al., 2010), to MIR and FIR (with Spitzer, Sanders et al., 2007), in combination with a multi-wavelength dataset from radio (with VLA, Schinnerer et al., 2007), millimeter (with MAMBO, Bertoldi et al., 2007), to X-rays (with XMM and Chandra, Hasinger et al., 2007; Elvis et al., 2009).

The zCOSMOS project (Lilly et al., 2007) is a major redshift survey of galaxies in the COSMOS field using 600 hr of clear dark observing time on the VLT. It aims to map the COSMOS field with the Visible Multi-Object Spectrograph (VIMOS;

Le Fèvre et al., 2003). A medium resolution grism ( $R \approx 600$ ) was used with a slit width of 1 arcsec, to achieve a velocity accuracy of  $\sim 100\text{km/s}$  and enable redshifts to be measured with a high success rate using one hour integrations. The spectral ranges of the observations are typically  $5550 - 9650\text{\AA}$ . The survey consists of two parts. The first, zCOSMOS-bright, will ultimately consist of spectra of about 20,000 galaxies selected to have  $I_{AB} < 22.5$  across the full  $1.7\text{deg}^2$  of the COSMOS field. It was designed to yield a high and fairly uniform sampling rate across most of the field (about 70%), with a high success rate in measuring redshifts (approaching 100% at  $0.5 < z < 0.8$ ) and to have sufficient velocity accuracy to efficiently detect cosmic structures down to the scale of galaxy groups. The second part, zCOSMOS-deep, will consist of about 10,000 spectra of  $B_{AB} < 25.25$  galaxies, color-selected to have redshifts in the  $1.4 < z < 3.0$  redshift range and lying in the central  $1\text{deg}^2$  region of the COSMOS field. More detailed informations about zCOSMOS survey can be found in Lilly et al. (2007) and Lilly et al. (2009).

## 3.2 Methods of analysis

All the information that can be obtained about a galaxy comes from the light received from it; colors, morphology, physical dimension and all the other parameters are retrieved exactly from the analysis of its electromagnetic radiation. In the following are described the two main method of analysis used to recover information about galaxy properties, that are the analysis of the spectral energy distribution and of the spectrum.

### 3.2.1 The stellar population synthesis models

The topic of predicting theoretically the photometric and spectral evolution of a galaxy has been studied thoroughly in the past years; in particular it became fundamental, since it can provide the theoretical spectrum of a galaxy as a function of various structural parameter, that can be, thus, compared with the observed one in order to set constraints on galaxy properties. Such models, called also stellar population synthesis models, have been studied by different groups, assuming different prescriptions tuned on the most recent observation.

As discussed in details in Bruzual & Charlot (2003), the *isochrone technique* (Charlot et al., 1991; Bruzual & Charlot, 1993), at the basis of most of theoretical models, is built on the hypothesis that stellar populations with any star formation history can be expanded in series of instantaneous starbursts, conventionally named “simple stellar populations” (SSPs). The spectral energy distribution at time  $t$  of a stellar population characterized by a star formation rate  $\psi(t)$  and a metal-enrichment law  $\zeta(t)$  can be written as (e.g. Tinsley et al., 1980):

$$F_{\lambda}(t) = \int_0^t \psi(t-t') S_{\lambda}[t', \zeta(t-t')] dt' \quad (3.1)$$

where  $S_{\lambda}[t', \zeta(t-t')]$  is the power radiated per unit wavelength per unit initial mass by an SSP of age  $t'$  and metallicity  $\zeta(t-t')$ . The above expression assumes that the initial mass function (IMF) is independent of time. The function  $S_{\lambda}[t', \zeta(t-t')]$  is the sum of the spectra of stars defining the isochrone of an SSP of metallicity  $\zeta(t-t')$  at age  $t'$ . To compute  $S_{\lambda}[t', Z_i]$  at a given metallicity  $Z_i$  of the stellar evolutionary tracks, the isochrone at age  $t'$  is interpolated from the tracks in the HR diagram. In practice, each evolutionary stage defined in the tracks is interpolated separately. The different evolutionary stages along the isochrone are populated by stars of different initial masses in proportions given by the IMF weight  $\phi(m)$  (defined such that  $\phi(m)dm$  is the number of stars born with masses between  $m$  and  $m + dm$ ). To assign spectra to stars in the various evolutionary stages is then used a spectral library. The spectral energy distribution of the SSP is obtained by summing the spectra of individual stars along the isochrone.

The most used, and in particular in within this thesis project, are the one developed by (BC03; Bruzual & Charlot, 2003) and (Maraston, 2005, M05), recently updated with the new work of (*Mastro*; Maraston & Strömbäck, 2011). The main difference between the BC03 and M05/*Mastro* models is that BC03 models do not include a treatment of thermally pulsing asymptotic giant branch (TP-AGB) stars. Since this stellar phase is the dominant source of bolometric and NIR energy for a simple stellar population between 0.2 and 2 Gyrs, the main difference between these models are for relatively young population. A detailed study of all the ingredients with which are built the models is not the purpose of this thesis, and thorough discussions are developed in the original papers. For chronological reasons (the available codes at the time of the analysis), in Sect. 3.6 the discussed results are based on other different codes, such as CB07 (a version of BC03 updated with the treatment of TP-AGB stars, Charlot & Bruzual (2011)) and M09 (an intermediate new version of M05 models, Claudia Maraston private communication).

### 3.2.2 The SED-fitting technique

The Spectral Energy Distribution (SED) represents how the energy is spread as a function of the wavelength. Usually the electromagnetic spectrum of a galaxy is observed in a given broadband filter, that measures the power of electromagnetic radiation within a given range of wavelength; if a galaxies is observed with a set of different filters, the SED is made by combining all the data obtained with different filters.

The SED of a galaxies is rich of informations. Not only it basically contains the colors of the galaxy (the difference between the magnitude observed in two different filters represent the color of the galaxy between that bands), but it can also help us to identify what kind of galaxy it is and which are its properties. It has been found that the shape of a SED of an elliptical galaxies is completely different from the one of a starforming galaxies (that is dominated by bluer colors), and that the shape itself depends critically by a lot of structural parameters of the galaxy (mass, age, star formation history, and so on). In the left panel of Fig. 3.2 are shown the spectral evolutions of SSP with BC03 models as a function of their ages.

With the development of theoretical models able to analytically predict the SED of galaxies as a function of their fundamental parameters, it was possible to evaluate and study non-direct observables of galaxies by comparing the observed SED with the theoretical one. In order to extract informations about the galaxies, the code *HyperZmodel* has been used (see Pozzetti et al., 2007, for a description; in this paper the modified version is called *HyperZmass*), that is a modified version of the public photometric redshift code *HyperZ* (Bolzonella et al., 2000): like the public version, *HyperZmodel* uses the SED-fitting technique, computing the best

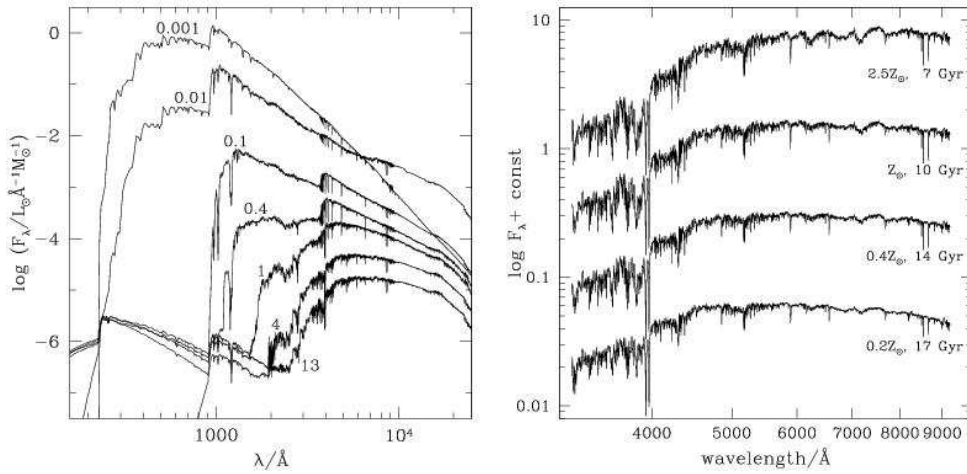


Figure 3.2: *Reproduced from Bruzual & Charlot (2003). Left panel: spectral evolution of BC03 SSP models as a function of their ages. Right panel: spectra of the standard SSP BC03 models at different ages for different metallicities.*

fit SED by minimizing the  $\chi^2$  between observed and model fluxes, defined as:

$$\chi^2(z) = \sum_{i=1}^{N_{filters}} \left[ \frac{F_{obs,i} - b \times F_{temp,i}(z)}{\sigma_i} \right]^2 \quad (3.2)$$

where  $F_{obs,i}$ ,  $F_{temp,i}$  and  $\sigma_i$  are, respectively, the observed and template fluxes and their uncertainty in the  $i$ -th filter and  $b$  is a normalization constant. The best-fit model is chosen among a library of models, built with different masses ( $M$ ), ages ( $t$ ), star formation histories (SFHs), metallicity ( $Z$ ) and dust reddening ( $A_V$ ); thus, given that the redshift of the galaxies is known, this procedure can give insights on all these parameters of a galaxy. This is one of the reason why it is so fundamental to study surveys in which the redshifts of the galaxies are known with the highest possible precision.

### 3.2.3 The spectroscopic analysis

Differently from the SED, the spectrum of a galaxy does not involve integrating the electromagnetic radiation in many given bands, but rather reports the entire radiation emitted by the galaxy within a given wavelength range. A spectrum is characterized by the signal-to-noise (S/N) ratio, which quantify the strength of the signal against the noise present in the data, and by the spectral resolution, defined as  $R = \lambda/\Delta\lambda$ , which quantifies the ability to resolve features in the spectrum.

Spectroscopy involves analyzing in detail the spectra of galaxy. Two kind of studies can be performed in order to retrieve information about the properties

of a galaxy from its spectrum. On the one hand, exactly as with the SED-fitting technique, the stellar population synthesis models provide theoretical spectra of galaxies as a function of their parameters, that can be compared with the observed spectra. The spectral fitting relies on the fact that the shape of the continuum of a spectra, the presence of features, the prominence of absorption or emission lines can constrain many structural properties of a galaxy. On the other hand, it has been demonstrated that also the single features of a galaxy spectrum correlate with some of their properties, such as age, metallicity,  $\alpha/Fe$  ratio, SFR: so a detailed combinate study of these feature can set constrain on those properties (e.g., see Worthey et al., 1994). The right panel of Fig. 3.2 shows, as an example, the spectra of SSP BC03 models for different ages as metallicity.

### 3.3 Methods of selection

As already underlined in Chapt. 2, selecting early-type galaxies is a difficult task. Despite their rather simple properties in term of photometry, morphology and spectroscopy, different criteria could and have been adopted to define samples of ETGs in literature. However, easily samples selected with different criteria do not fully overlap (see Tab. 2.1). In the following sections some criteria with which it is possible to define samples of ETGs are explored, in order to obtain a sample of ETGs the less contaminated by outliers.

#### 3.3.1 Morphological criterion

Historically, galaxies have been firstly characterized for their visual morphology; observed in the local Universe, they can be placed in a well-defined sequence, dividing between a peculiar elliptical or spiral shape. Since the beginning, the way to define the morphology of a galaxy has been refined, and many parameters quantifying it have been introduced.

Within the zCOSMOS collaboration, there exist two different estimate of galaxy morphology: the Zurich Estimator of Structural Types (ZEST; Scarlata et al., 2007) and a non-parametric estimate derived by zCOSMOS collaborators in Marseille (MRS; Cassata et al., 2007; Tasca et al., 2009).

On one hand, ZEST approach aims to quantitatively describe galaxy structure with a principal component analysis (PCA) using five parameters: asymmetry ( $A$ ), concentration ( $C$ ), Gini coefficient ( $G$ ), the second-order moment of the brightest 20% galaxy pixels ( $M20$ ), and the ellipticity of the light distribution ( $\epsilon$ ). PCA indicates that the first three PC variables account for more than 90% of the variance in the original data set, describing therefore almost completely the galaxy structure. The ZEST classification distinguish galaxies depending on the PC value into three types type (ZEST type=1 for early-type galaxies; =2 for disc galaxies; and =3 for irregular galaxies) and associates also a “bulgeness” parameter according to the median value of the distribution of Sérsic indices  $n$  of all galaxies brighter than  $I = 22.5$  (bulgeness = 0-3, from  $n > 2.5$  being bulge-dominated to  $n < 0.75$  being disc-dominated galaxies).

On the other hand, MRS classification separates galaxies on the basis of their position in the four-dimensional parameter space defined by the concentration, he asymmetry, the Gini coefficient, and axial ratio. The structural parameters are measured for all galaxies in the sample; then it is performed a visual classification on a randomly selected subsample of 500 galaxies, in order to have a reference catalog to study the dependence on the various parameters. For the galaxies not present in this subsample, is measured the distance in the parameter space to the 500 reference galaxies, and the 11 closest selected. To each galaxy is assigned to the most frequent visual class among these 11 nearest reference galaxies. At

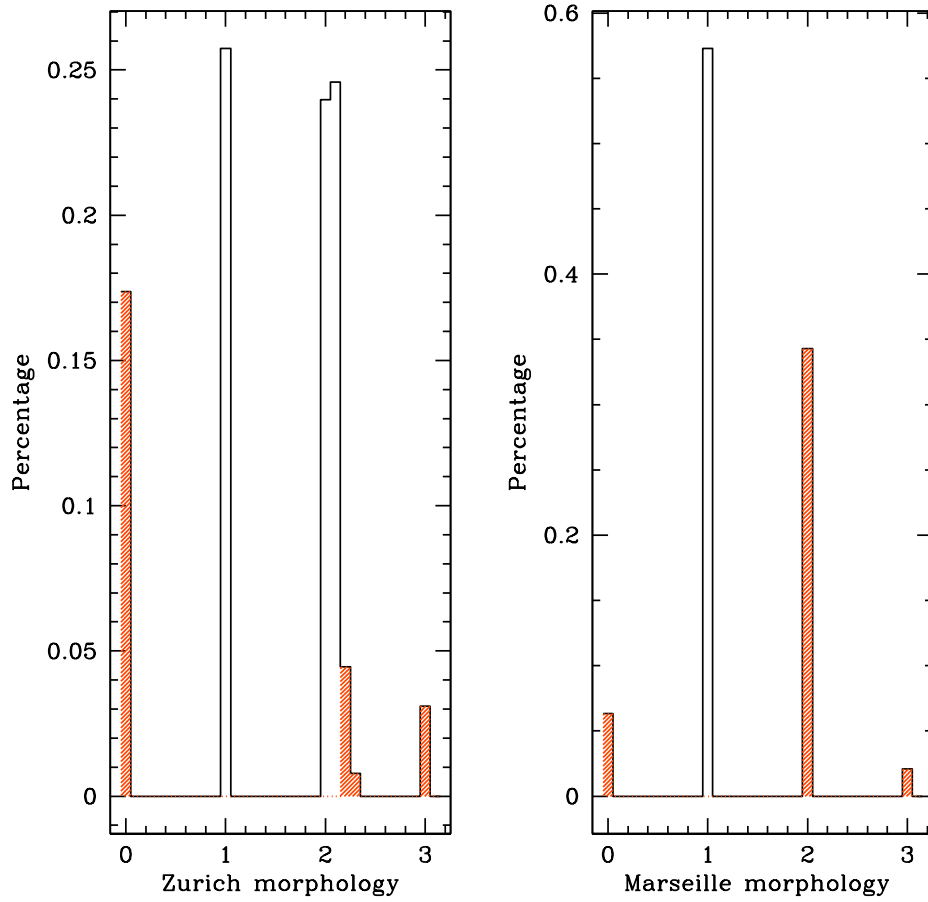


Figure 3.3: *Contamination between different morphological selection of ETGs. In the left plot is shown the histogram of the distribution in the MRS classification of galaxies selected to be elliptical in ZEST catalog. In the right plot is shown the histogram of the distribution in the ZEST classification of galaxies selected to be elliptical in MRS catalog. The red shaded area represents the galaxies misclassified by the two different methods.*

the end galaxies are divided into three morphological classes: spheroidals (MRS type=1), spirals (MRS type=2), and irregulars (MRS type=3).

However, no automatic (or even visual) classification is perfect, and a certain level of contamination remains for both ZEST and MRS methods: to demonstrate that, it was checked that selecting all zCOSMOS galaxies classified as elliptical from ZEST, the percentage classified as non-elliptical by MRS is 42.7%; on the

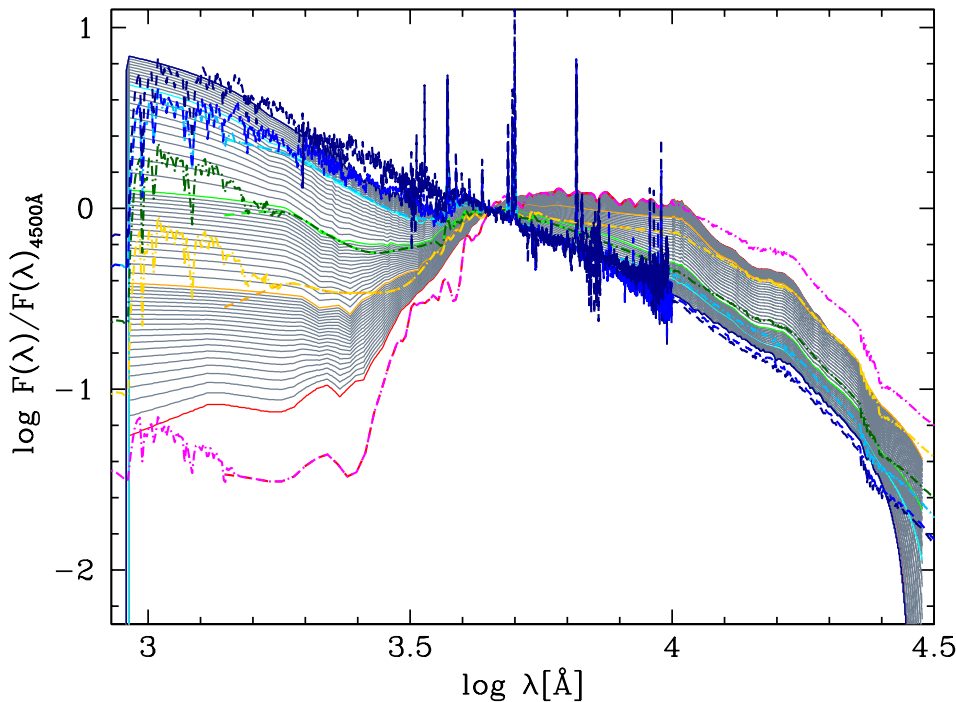


Figure 3.4: *The extended CWW templates used to evaluate the photometric type of galaxies. The dashed lines show the original CWW, with in red the Elliptical, in yellow the Sbc, in dark green the Scd, and in blue and dark blue the two starburst galaxies (the point-dashed lines represent where the curve is extended to higher and lower wavelengths); the grey curves are the extended CWW templates, with continuous red, orange, green, cyan, blue and dark blue representing the Elliptical, Sbc, Scd, Im and the two starburst galaxies. Courtesy of Micol Bolzonella.*

other way around, the percentage of galaxies classified as non-elliptical by ZEST in the elliptical sample of MRS is 25.7% (see Fig. 3.3).

Therefore, in order to be the less biased as possible by the presence of outliers, “*morphological ellipticals*” has been defined as those galaxies classified as elliptical by both methods.

### 3.3.2 Photometric criterion

It is well known that the color distribution of galaxies exhibits a bimodality that corresponds to a division between late-type (younger, star-forming, bluer) and early-type (older, passive, redder) galaxies; it is therefore possible, as explained before, to use colors instead of morphological types to classify and select galaxy populations (e.g., see Baldry et al., 2004).

However, it is straightforward that the spectral energy distribution (SED) of a galaxy, by definition, yields more informations than color. Therefore, to separate galaxies by types, Zucca et al. (2006) have developed a technique that use all the informations present in the SED: for each galaxy, the rest frame magnitudes were matched with the empirical set of (62) SEDs described in Ilbert et al. (2006). These SEDs were obtained by interpolating between the four local observed spectra of Coleman et al. (1980) (hereafter CWW), which include both M31 and M81 along with Sbc, Scd, and Im galaxy SEDs, and two starburst SEDs from Kinney et al. (1996). These templates were also linearly extrapolated to the ultraviolet ( $\lambda < 2000 \text{ \AA}$ ) and near-infrared wavelengths using the GISSEL synthetic models (Bruzual & Charlot, 2003). The match between observed and template SED is then performed by minimizing a  $\chi^2$  variable on these templates at the spectroscopic redshift of each galaxy. In Fig. 3.4 are reported the templates used to evaluate the *photometric types*: the dashed lines show the original CWW, with in red the Elliptical, in yellow the Sbc, in dark green the Scd, and in blue and dark blue the two starburst galaxies (the point-dashed lines represent where the curve is extended to higher and lower wavelengths); the grey curves are the extended CWW templates, with continuous red, orange, green, cyan, blue and dark blue representing the Elliptical, Sbc, Scd, Im and the two starburst galaxies. The colors are monotonically changing from redder to bluer with increasing photometric type.

A photometric type equal to one (1.1 up to 1.21) corresponds to a red E/Sa template, a photometric type equal to two (2.1 up to 2.16) correspond to an early spiral template, a photometric type equal to three (3.1 up to 3.11) corresponds to a late spiral template (PT = 3), and a photometric type equal to four (4.1 up to 4.14) corresponds to an irregular or a starburst template.

To select ETGs, “*photometric ellipticals*” have been defined as those galaxies with photometric type  $\leq 1.13$ .

### 3.3.3 Spectroscopic criterion

The works assessing that the Hubble sequence is ordered in terms of present Star Formation Rates (SFR) and past Star Formation Histories (SFH) go back to early 1960s (e.g., see Roberts, 1963). Since then, many studies has been performed in trying to quantify this dependence, and are well reviewed in Kennicutt (1998). As these authors summarize, when progressing along this sequence, are evident “*a broad rise in the blue continuum, a gradual change in the composite stellar absorption spectrum from K-giant dominated to A-star dominated, and a dramatic increase in the strengths of the nebular emission lines, especially H $\alpha$* ”.

The classical tracers studied to infer the SFR in galaxies are H $\alpha$  recombination line ( $\lambda_{rest} = 6583 \text{ \AA}$ ) and the forbidden-line doublet [OII] $\lambda$ 3727, since they can provide a probe sensitive to the young massive stellar population of the galaxy.

We refer to Kennicutt (1998) for the detailed insights about various recipes to convert those quantities to SFRs, with the relative calibrations.

Since, as underlined in Chapt. 2, ETGs are characterized to be passively evolving systems, the less star-forming objects have to be selected. Mignoli et al. (2009), in their analysis of a subsample of zCOSMOS catalog, found a clear bimodality in the distribution of equivalent width (EW) of [OII], and suggest that  $5 \text{ \AA}$  is a good choice of  $EW([OII])$  value to separate star-forming from passive galaxies, which are most commonly found below this value (see also Schiavon et al., 2006). However, given to the restframe wavelength range of zCOSMOS spectra, [OII] lines are visible only for redshift  $z \gtrsim 0.5$ ; on the contrary  $H\alpha$  line remains observable only for  $z \lesssim 0.5$ .

This problem does not occur for SDSS spectra, both for the wider wavelength range of the spectrograph and for the lower redshifts probed by the survey.

It has been decided to consider both these tracers to select ETGs, and to define as “*spectroscopic ellipticals*” those galaxies not presenting strong emission lines, with measured  $EW([OII]) < 5 \text{ \AA}$  and  $EW(H\alpha) < 5 \text{ \AA}$ .

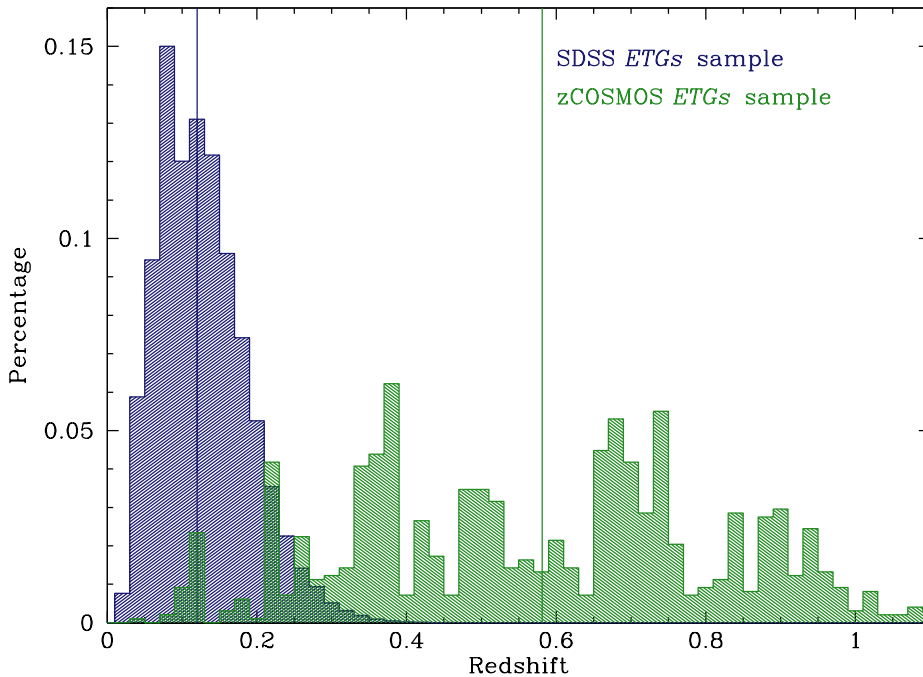


Figure 3.5: *Redshift distributions of SDSS (blue) and zCOSMOS (green) ETGs samples; the vertical lines show the median of the distributions.*

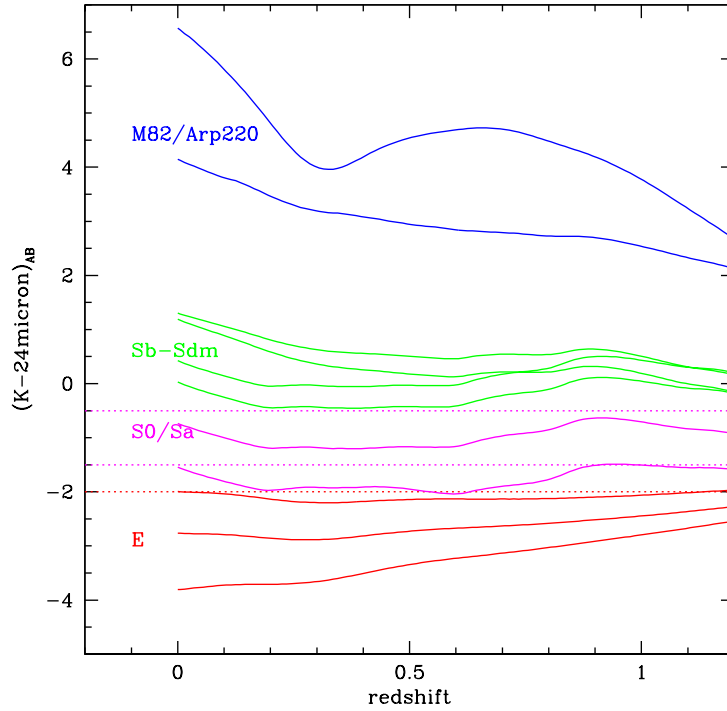


Figure 3.6:  $K-24\mu\text{m}$  color evaluated for various templates of galaxies as a function of redshift. Courtesy of Lucia Pozzetti.

### 3.4 The final ETGs samples

In order to obtain the more clean and robust sample of ETGs, it has been applied a really stringent selection, by combining all the previously discussed criteria of selection (where possible).

1. **SDSS ETGs sample.** For the SDSS survey, an ETG sample has been extracted from the SDSS Data Release 6 (SDSS-DR6) matching SDSS with 2MASS photometry (catalog provided by Jarle Brinchmann), and selected to have photometric type  $\leq 1.4$ ,  $EW([\text{OII}]) < 5 \text{ \AA}$ ,  $EW(\text{H}\alpha) < 5 \text{ \AA}$  and median  $S/N$  ratio per  $\text{\AA} > 3$ . In this sample are present in total 97,460 ETGs in the redshift range  $0.02 < z < 0.5$  (with a median redshift  $\langle z \rangle = 0.12$ , see Fig. 3.5).
2. **zCOSMOS “Red galaxies” and “ETGs” samples.** Concerning the zCOSMOS survey, two different selections have been applied. On one hand, giving the much lower statistics with respect to SDSS, at first a sample of ETGs

has been defined by only applying a photometric criterion, extracting from the zCOSMOS 10k bright catalog those galaxies having a photometric type  $\leq 1.13$ : hereafter this sample will be called zCOSMOS “*Red galaxy*” sample, and contains 2,093 galaxies.

On the other hand, to have a reference sample the less contaminated as possible from outliers, it has built also the zCOSMOS “*ETGs*” sample, rejecting from the *Red galaxies* the galaxies with:

- *significantly strong emission lines*, i.e., measured  $EW([OII]) > 5\text{\AA}$  ( $\sim 17\%$  of the *Red* sample) and  $EW(H\alpha) > 5\text{\AA}$  ( $\sim 14\%$  of the *Red* sample), to avoid selecting star-forming galaxies or galaxies that have experienced a recent episode of star formation. In this way, it is possible to be confident about the selection of a clearly defined sample of passive galaxies.
- *confirmed spiral morphology*, i.e. galaxies that both ZEST and MRS method classify as spiral ( $\sim 20\%$  of the *Red* sample). In this way, it is possible to be sure of a clear identification of the galaxy morphology.
- “*bluer*” *photometric types*, i.e. galaxies with photometric type  $\geq 1.05$  ( $\sim 31\%$  of the *Red* sample).
- *strong 24 $\mu$ m emission*, i.e., based on an observed color  $(K - 24\mu\text{m}) > -0.5$  ( $\sim 5\%$  of the *Red* sample).

The last cut, not discussed in the previous sections, is motivated to use also the information from MIPS 24 $\mu$ m filter: in this way it is possible both to isolate in a better way the early-type template, characterized by a low emission at 24 $\mu$ m (see Fig. 3.6), and to avoid the contamination of galaxies reddened by dust extinction.

Despite these really severe selection criteria, some contamination remained, and can only be avoided by a visual inspection of galaxies morphology. In Fig. 3.7 are shown some galaxies of the original zCOSMOS *ETGs* sample presenting clear spiral features, that have been removed afterwards. In Fig. 3.8 are shown, on the contrary, some typical true early-type galaxies of the final zCOSMOS *ETGs* sample.

The final zCOSMOS *ETGs* sample contains 981 galaxies in the redshift range  $0.05 < z < 1.2$  (with median redshift  $\langle z \rangle = 0.58$ , see Fig. 3.5).

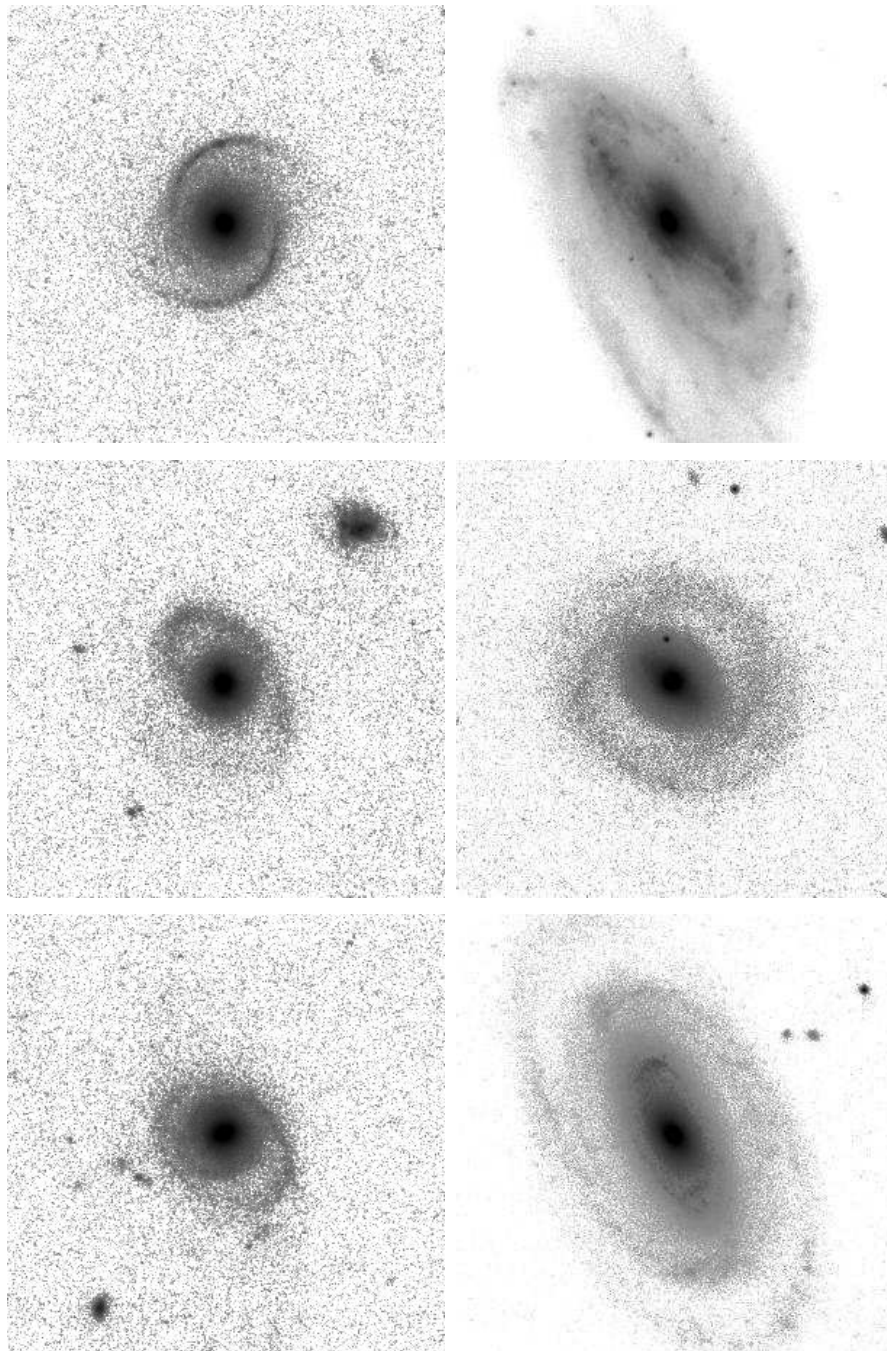


Figure 3.7: *Example of outliers in the ETGs selection: despite the restrictive criteria applied, some outliers with evident spiral features remain in the zCOSMOS ETGs sample, and have been removed after a visual inspection.*

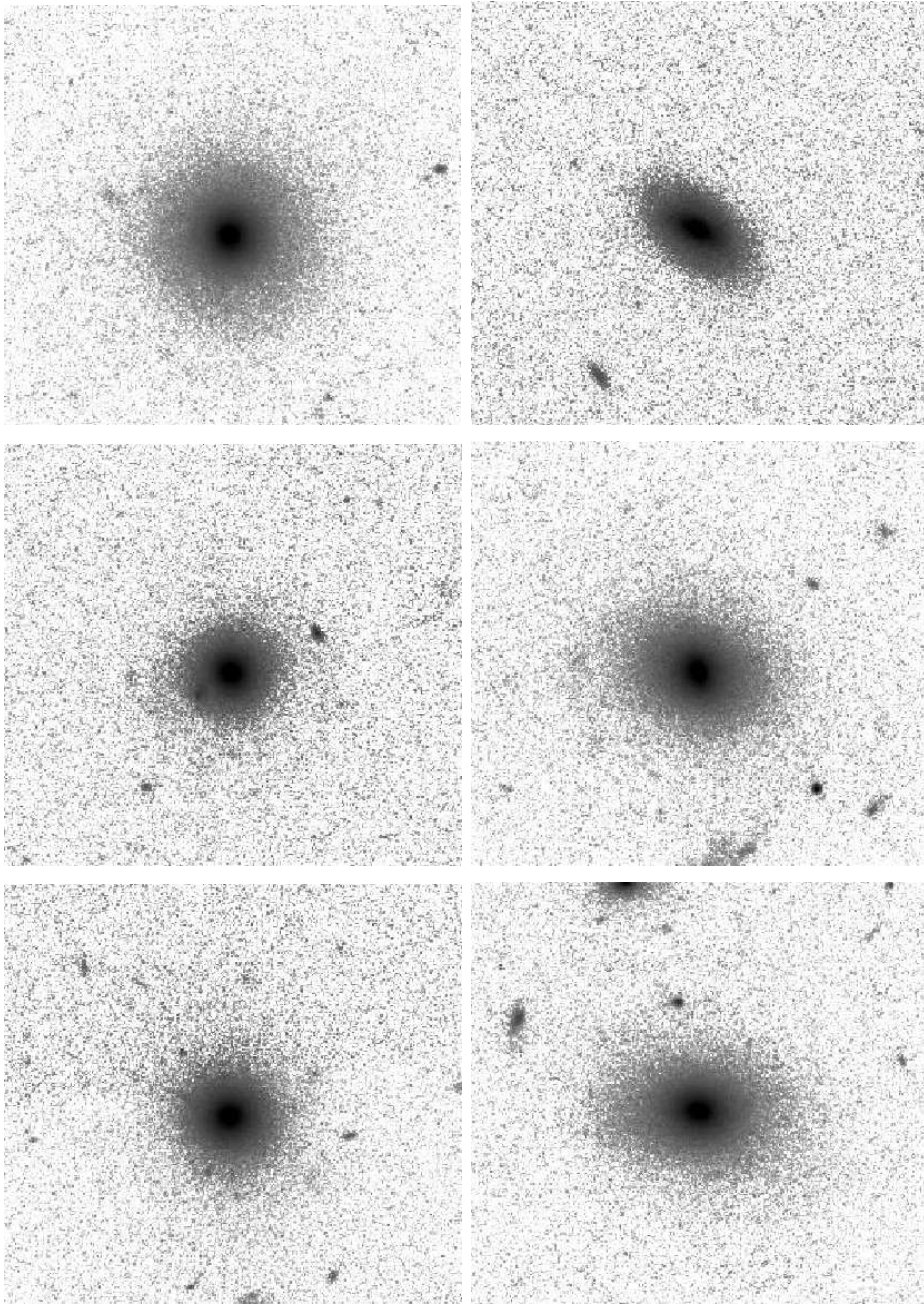


Figure 3.8: *Example of early-type galaxies in the zCOSMOS “ETGs” sample.*

### 3.5 SDSS and zCOSMOS Photometric data

The catalog of early-type galaxies used within this project is primarily extracted from the SDSS and zCOSMOS survey, since they can provide, covering both low and intermediate redshifts ( $0.05 \lesssim z \lesssim 1$ ), the most complete set of ETGs up to  $z \sim 1$ .

SDSS provides  $u$ ,  $g$ ,  $r$ ,  $i$ ,  $z$  photometry and spectra for almost 800 000 galaxies over  $\sim 7000$  square degrees. Galaxies have been extracted to have a Petrosian magnitude  $r < 17.77$ . The spectra are taken using 3-arcsec diameter fibres, positioned as close as possible to the centers of the target galaxies. The flux (and wavelength) calibrated spectra cover the range 3800-9200 Å, with a resolution of  $R \approx 1800$ .

To obtain a wider wavelength coverage for the photometry, a match between SDSS-DR6 galaxies and 2MASS survey (Skrutskie et al., 2006) (provided by Jarle Brinchmann, private communication) has been used, with which SDSS photometry has been extended with the J, H and K bands. The transmission functions of SDSS and 2MASS broadband filters are plotted in Fig. 3.9.

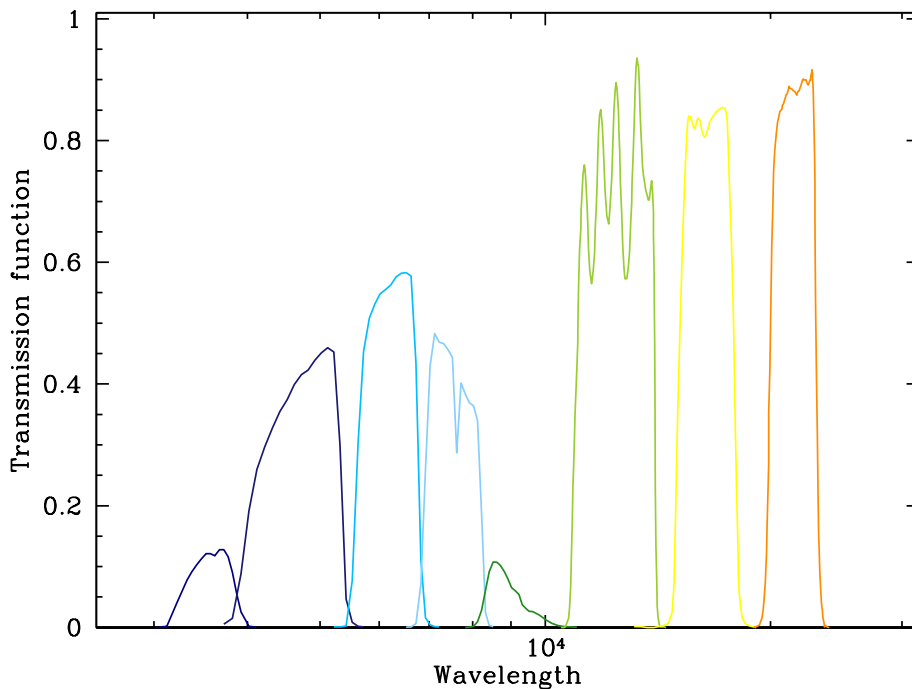


Figure 3.9: *Transmission functions of SDSS and 2MASS broadband filters.*

Considering the zCOSMOS survey, it has been used the *bright* part of zCOSMOS 10k catalog (the first publicly available), which consists of spectroscopy limited to objects in the magnitude range  $15.0 < I < 22.5$ . The spectral ranges of the observations are typically  $5550 - 9650 \text{ \AA}$ , with a resolution  $R \approx 600$ . Among the multi-band photometric data of the COSMOS field, the following observed magnitudes in 10 photometric bands have been used: CFHT  $u^*$  and  $K_s$ , Subaru  $B_J$ ,  $V_J$ ,  $g^+$ ,  $r^+$ ,  $i^+$ , and  $z^+$ , and Spitzer IRAC at  $3.6 \mu\text{m}$  and  $4.5 \mu\text{m}$ . The transmission functions of zCOSMOS broadband filters are plotted in Fig. 3.10; the photometric catalog is fully described in Capak et al. (2007).

All the magnitudes are quoted in the AB system.

### 3.5.1 Zeropoint offsets and errors correction

First of all the magnitudes were corrected for Galactic extinction using Schlegel maps (Schlegel et al., 1998).

Following the approach of Capak et al. (2007), the photometry has been optimized by applying zeropoint offsets to the observed magnitudes. This procedure consists in evaluating the difference between the observed magnitudes  $m_{obs,i}$  and reference

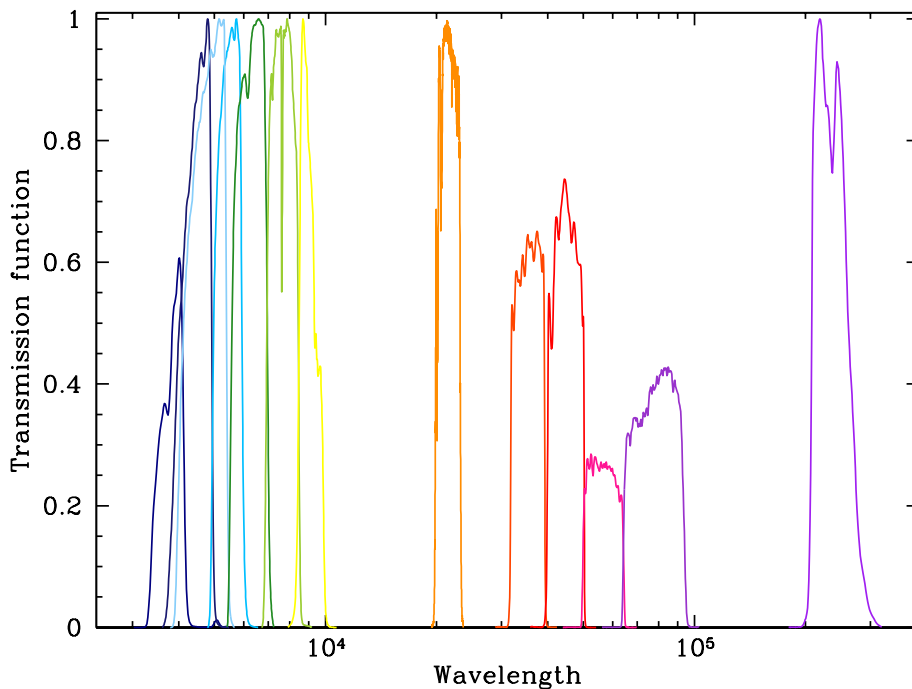


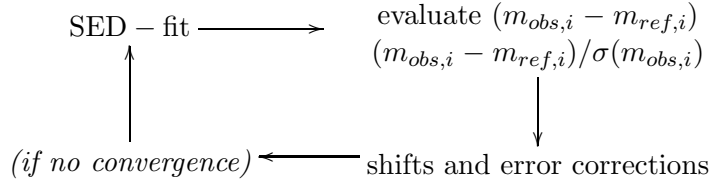
Figure 3.10: *Transmission functions of zCOSMOS broadband filters.*

magnitudes as obtained by theoretical models  $m_{ref,i}$ . In order to do that, three different library using BC03, CB07 and M05 models have been built for the zCOSMOS survey, each one with a grid of  $0 < A_V < 1$ ,  $Z = Z_\odot$ ,  $0.05 < \tau < 1$  (where  $\tau$  is the e-folding time of the SFH, assumed to be  $SFH \propto \tau^{-1}e^{-t/\tau}$ ). Afterwards, it has been evaluated the best-fit to the SED of the galaxies in the selected samples, as explained in Sect. 3.2.2; the value  $m_{ref,i}$  is then taken from the best-fit template. In this way it is possible to reduce differences between the observed and reference magnitudes by evaluating a zeropoint offset for each stellar population synthesis models, and the results are shown in Tab. 3.1. Figure 3.11 shows, for BC03 model, the distribution for each filter of the difference between observed and reference magnitudes after applying the shifts, i.e.  $(m_{obs,i} - m_{ref,i} + \text{shift})$ , quoting, for each filter, the shift applied, the median and the dispersion of the distribution. In Fig. 3.12 are shown the zeropoint offsets applied for each filter of the zCOSMOS photometry using BC03 model, and the resulting median  $(m_{obs,i} - m_{ref,i})$ ; this plot reveals how well this procedure behave in adjusting the photometric offsets.

For the SDSS survey the procedure applied is the same, but, since there were available the new M09 models, these models have been used instead of the M05 ones. In the case of SDSS, the shifts obtained with different models have been also averaged, obtaining a unique correction for the three models; the results are shown in Tab. 3.2. Figure 3.14 show, for BC03 models, the distribution for each filter of the difference between observed and reference magnitudes after applying the shifts, i.e.  $(m_{obs,i} - m_{ref,i} + \text{shift})$ , quoting, for each filter, the shift applied, the median and the dispersion of the distribution. In Fig. 3.15 are shown the zeropoint offsets applied for each filter of the zCOSMOS photometry using BC03 model, and the resulting median  $(m_{obs,i} - m_{ref,i})$ .

A procedure for correcting the errors of the photometry has also been taken into account, since it was known a problem, especially in the IRAC photometry, of underestimation of errors.

Statistically, the size of the errors  $\sigma(m_{obs,i})$  should be of the order of the dispersion of the distribution of  $(m_{obs,i} - m_{ref,i} + \text{shift})$ . The procedure applied was therefore to study the  $(m_{obs,i} - m_{ref,i} + \text{shift})/\sigma(m_{obs,i})$  distributions and to normalize them to a unit dispersion, by summing in quadrature the error corrections to  $\sigma(m_{obs,i})$ . The recursive procedure explained in the diagram below has been applied, for which firstly the data have been SED-fitted without shifts or error corrections, then the distributions of  $(m_{obs,i} - m_{ref,i})$  and of  $(m_{obs,i} - m_{ref,i})/\sigma(m_{obs,i})$  have been evaluated and finally the corresponding corrections have been obtained from these distributions, applied to the data that are, then, SED-fitted again, to look if second-order corrections were needed. This procedure stops when convergence is reached, i.e. the corrections are stable.



As expected, the bigger corrections are needed for IRAC photometry, while in the other bands they are much smaller. The discrepancy is so high in IRAC5.8 $\mu m$  and IRAC8 $\mu m$  because these bands were not used in the SED-fit.

In the case of SDSS, it has been applied an even simpler method to correct the errors, by multiplying the errors  $\sigma(m_{obs,i})$  with a parameter such that the resulting dispersion of the  $(m_{obs,i} - m_{ref,i})/\sigma(m_{obs,i})$  distribution is equal to one. The corrections to zCOSMOS photometry errors can be found in Tab. 3.1, while the corrections to SDSS photometry errors can be found in Tab. 3.2. In Figs. 3.13 and 3.16 can be found, for BC03 model and for each filter considered, the distributions of  $(m_{obs,i} - m_{ref,i} + \text{shift})/\sigma(m_{obs,i})$  after the error corrections, along with their medians and dispersions.

Filter	BC03 shift	CB07 shift	M05 shift	Error correction
u	-0.1870	-0.2162	-0.1739	0.025
B	0.2164	0.2070	0.2169	0.025
V	0.1240	0.1398	0.1124	0.025
g	-0.0145	-0.0183	-0.0228	0.025
r	0.0413	0.0840	0.0311	0.025
i	-0.0038	0.0758	0.0006	0.025
z	0.0680	0.1833	0.0564	0.025
K	0.0050	-0.0523	-0.0259	0.025
IRAC 3.6	-0.0647	-0.0998	-0.0153	0.075
IRAC 4.5	-0.0159	-0.0183	0.2647	0.1
IRAC 5.8	0.1213	0.0757	0.0000	0.1
IRAC 8	1.1358	1.0515	0.0000	0.1

Table 3.1: *Shift and error correction applied to zCOSMOS photometry.*

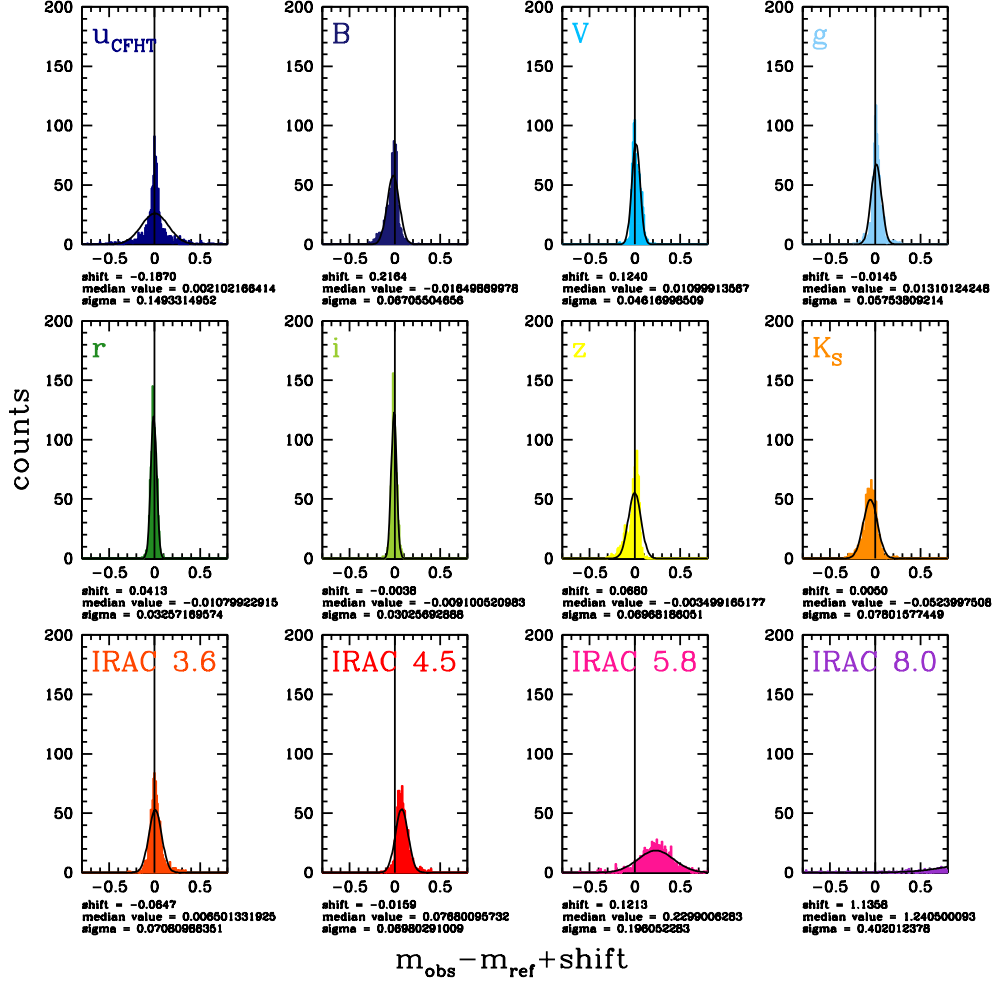


Figure 3.11: Distribution of  $(m_{\text{obs},i} - m_{\text{ref},i})$  for each zCOSMOS band after correcting with zeropoint shifts evaluated using BC03 models. For each band is also quoted the shift applied, along with the median and the dispersion of the distribution.

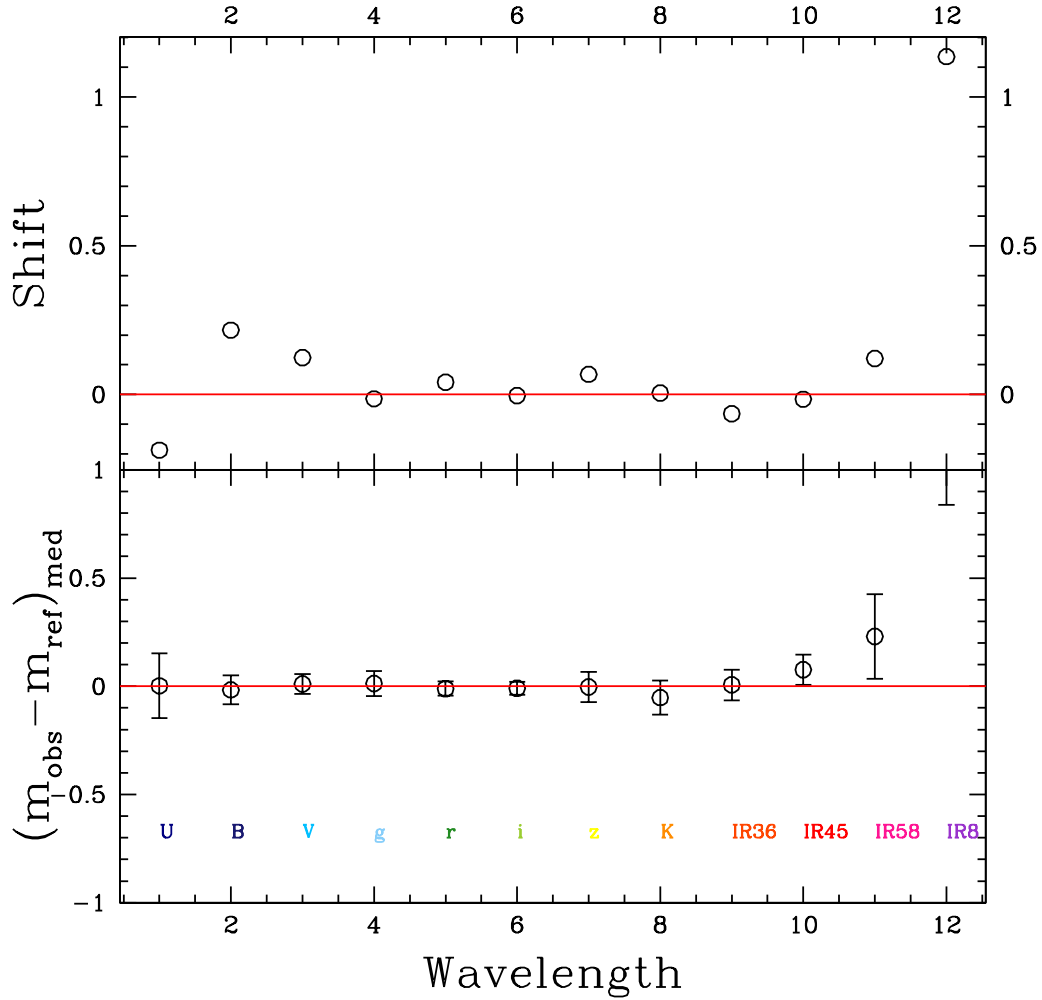


Figure 3.12: In the top panel: zeropoint shifts applied to the observed magnitudes in order to reproduce better the theoretical magnitudes, for each filter of zCOSMOS survey using BC03 models. In the bottom panel: resulting median of the difference  $(m_{obs,i} - m_{ref,i})$  for each filter.

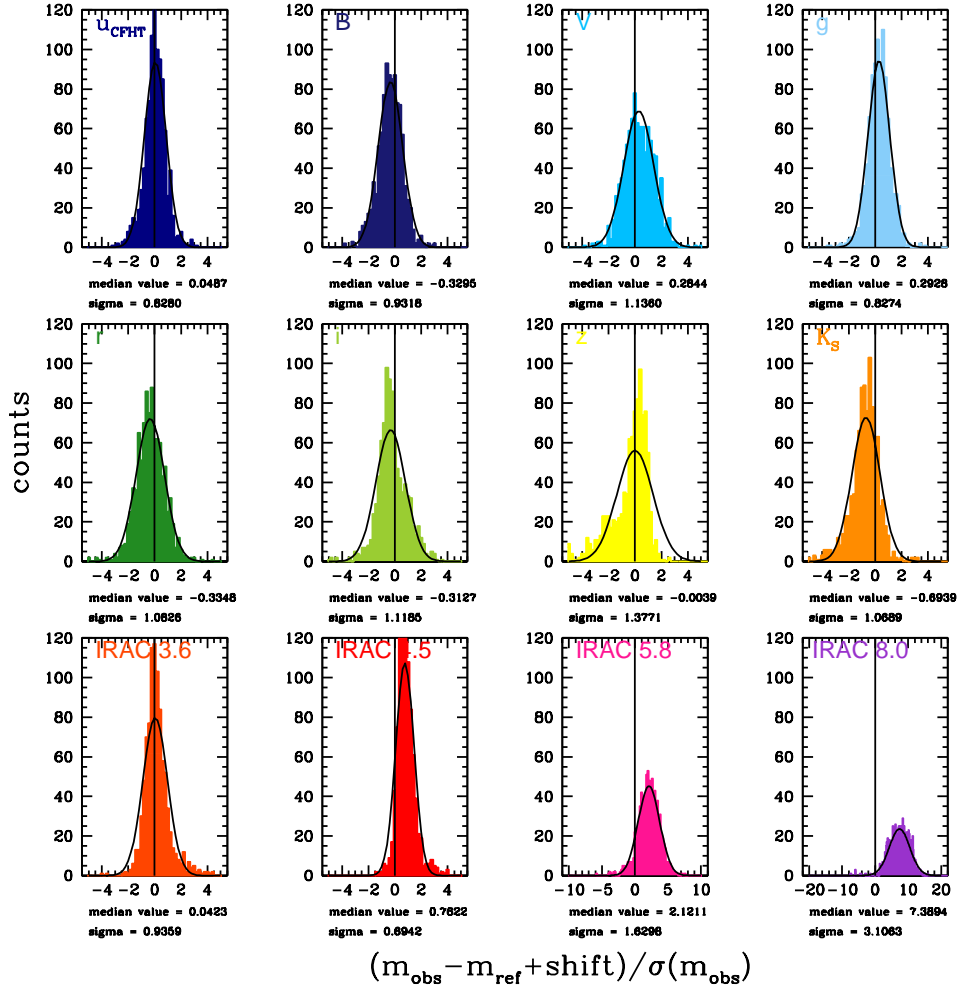


Figure 3.13: Distribution of  $(m_{\text{obs},i} - m_{\text{ref},i} + \text{shift}) / \sigma(m_{\text{obs},i})$  for each zCOSMOS band using BC03 models. For each band are also quoted the median and the dispersion of the distribution.

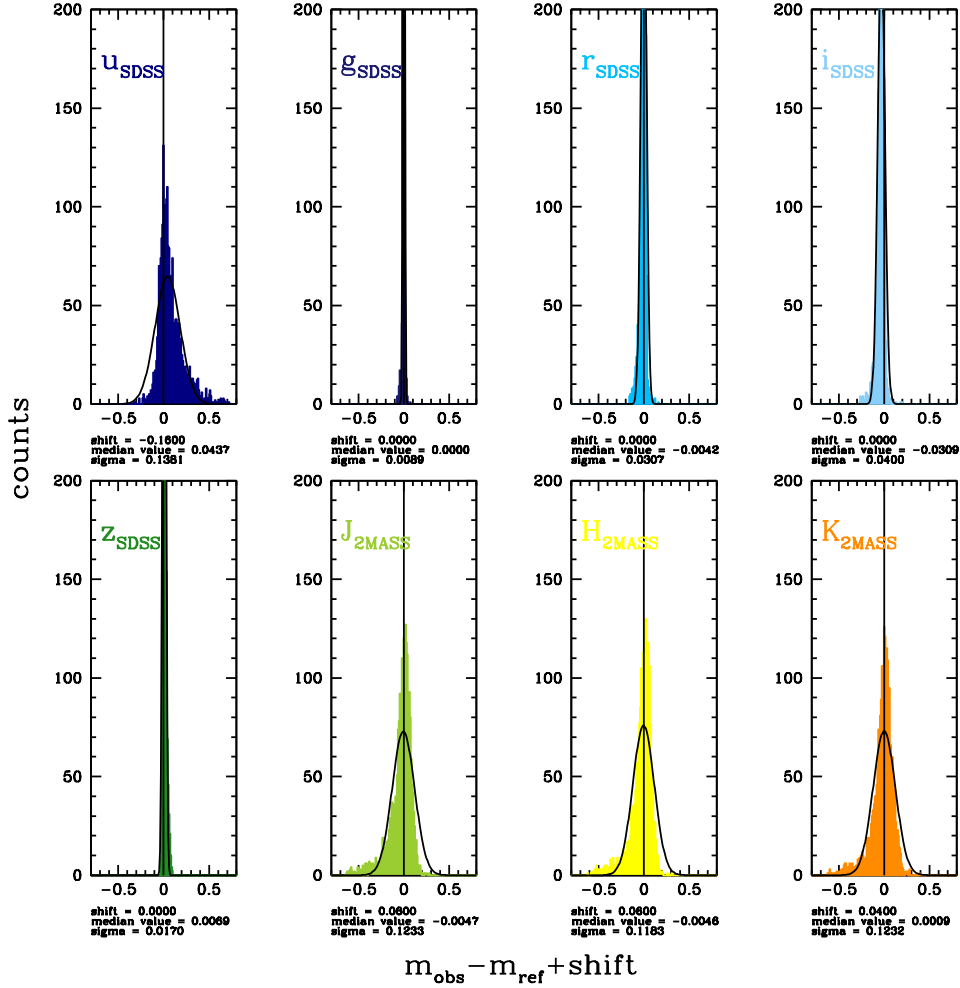


Figure 3.14: Distribution of  $(m_{obs,i} - m_{ref,i})$  for each SDSS+2MASS band after correcting with zeropoint shifts evaluated using BC03 models. For each band is also quoted the shift applied, along with the median and the dispersion of the distribution.

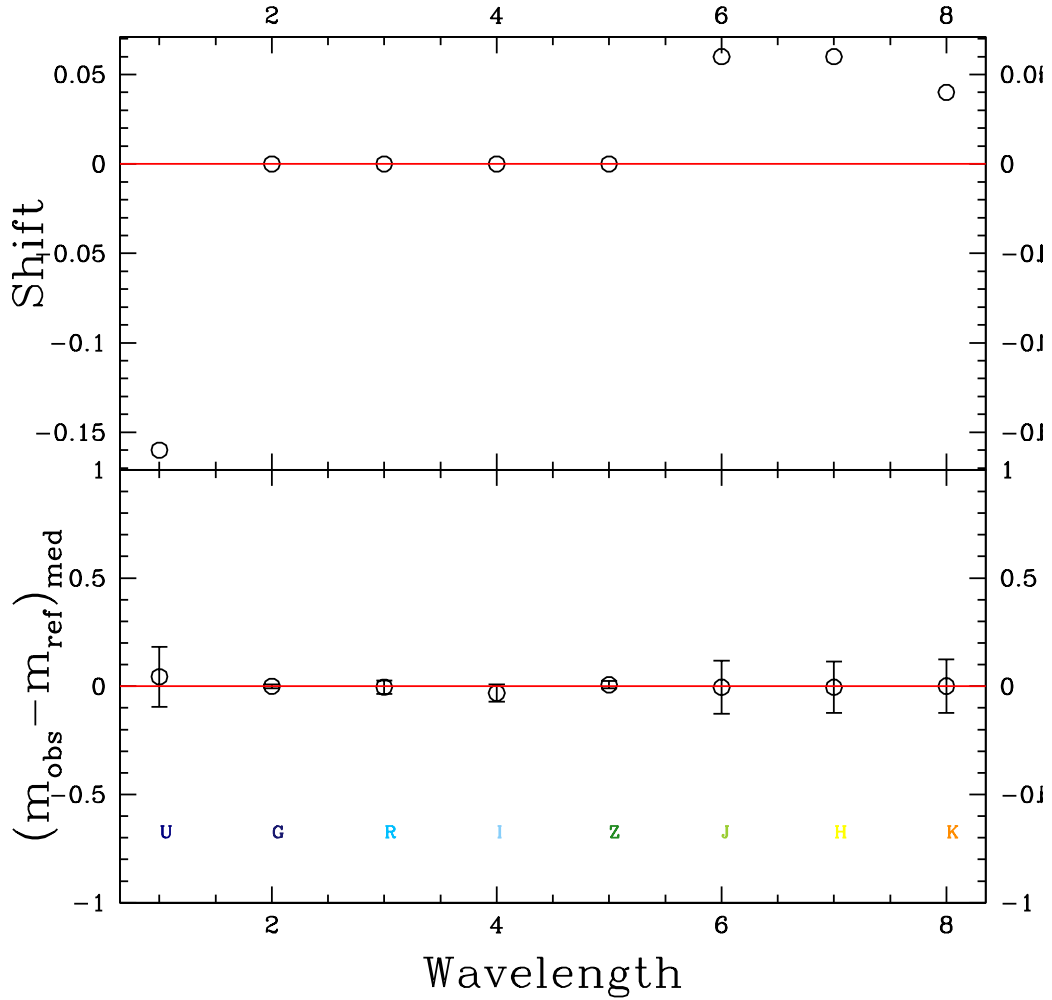


Figure 3.15: *In the top panel: zeropoint shifts applied to the observed magnitudes in order to reproduce better the theoretical magnitudes, for each filter of SDSS+2MASS survey using BC03 models. In the bottom panel: resulting median of the difference  $(m_{\text{obs},i} - m_{\text{ref},i})$  for each filter.*

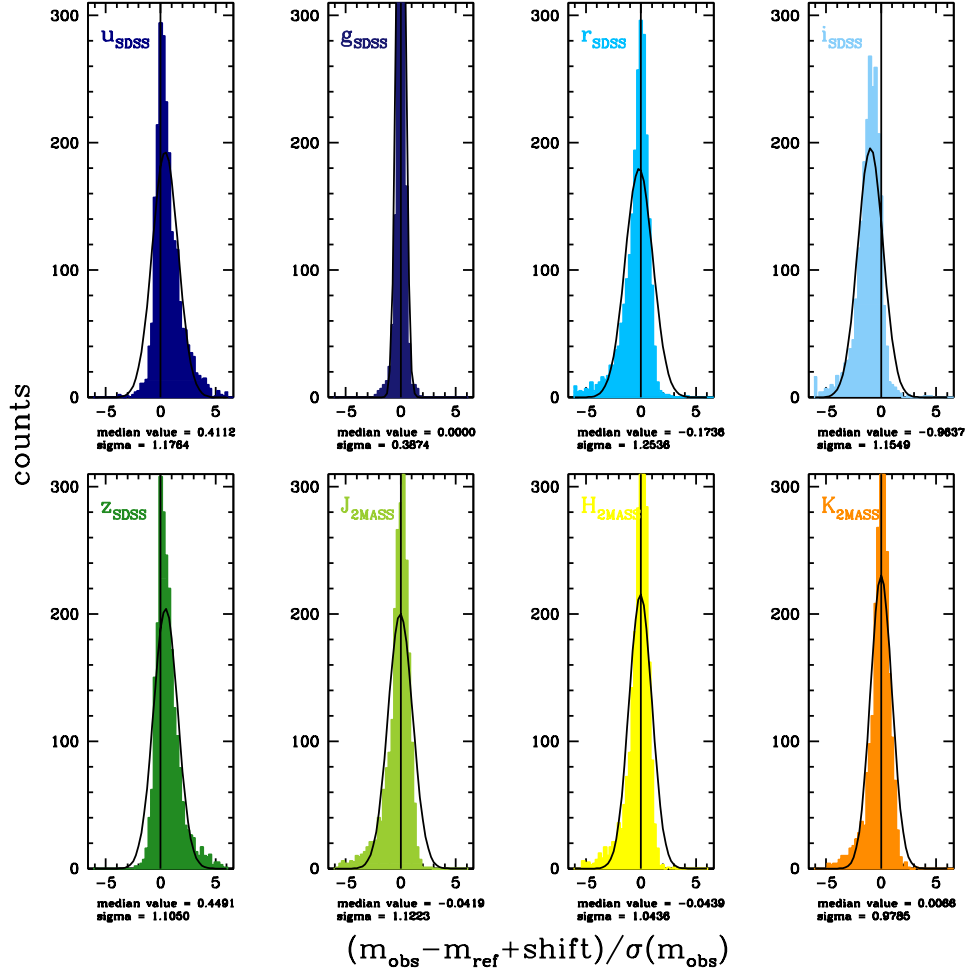


Figure 3.16: Distribution of  $(m_{\text{obs},i} - m_{\text{ref},i} + \text{shift}) / \sigma(m_{\text{obs},i})$  for each SDSS+2MASS band using BC03 models. For each band are also quoted the median and the dispersion of the distribution.

Filter	Shift	Error correction
u	-0.16	3.32
g	0	2.47
r	0	3.55
i	0	5.30
z	0	4.83
J	0.06	2.98
H	0.06	2.28
K	0.04	1.87

Table 3.2: *Shift and error correction applied to SDSS photometry.*

### 3.6 Estimate of physical and evolutionary parameters

In this section the results of the parameters estimate obtained with the fit to the broadband photometry of both SDSS and zCOSMOS *ETGs* samples are discussed, focusing in particular the attention to the problem of the degeneracies that arise in the SED-fitting technique.

As described in Sect. 3.2.2, the free parameters in the SED-fitting are the stellar mass ( $M$ ), the age ( $t$ ), the star formation histories (SFH), the dust reddening ( $A_V$ ), and the metallicity ( $Z$ ). I created a library of models with different values of these parameters, with delayed exponential SFHs ( $SFH(t) \propto \frac{t}{\tau^2} \exp(-t/\tau)$ ) with  $\tau \in [0.05 - 1]$  Gyrs, with age  $t \in [0, 20]$  Gyrs, dust reddening  $A_V \in [0, 1]$  and solar metallicity  $Z = Z_{\odot}$ . The metallicity has been fixed at a solar value for reasons that will be discussed in Sect. 3.6.5. The choice of the range of each of these values is motivated within each subsection.

#### 3.6.1 The stellar mass

Among all the galaxy parameter, the stellar mass is one of the best-constrained. Within the zCOSMOS collaboration, Bolzonella et al. (2010) found that the stellar mass is a rather stable parameter, and varying stellar population synthesis model, reddening law, SFH, and metallicity the typical dispersion is of the order of  $\approx 0.20$  dex. This is due to the fact that the SED of a galaxy is strongly dependent on this parameter. In Fig. 3.17, as an example, the SEDs of 28 galaxies randomly selected from the zCOSMOS *ETGs* sample in the range  $0.37 < z < 0.38$  are shown (the redshift range has been chosen narrow in order to avoid a strong redshift dependence): it is possible to see that the peak of the SED of a galaxy strongly correlates with its mass, independently on the other parameters that mainly regulate the shape of the SED.

In Fig. 3.18 the distribution of the stellar mass (in logarithmic units [ $\log_{10}(M/M_{\odot})$ ])

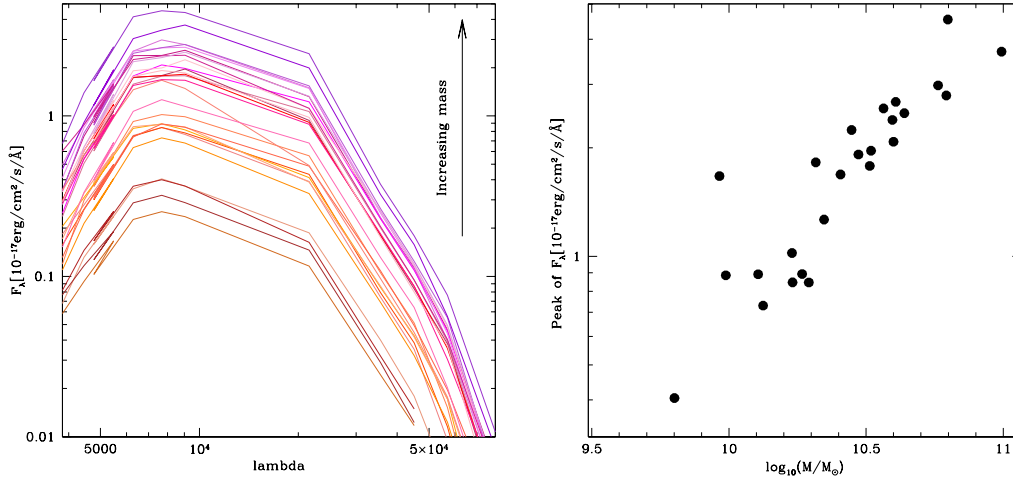


Figure 3.17: *Mass dependence of ETGs SED. In the left panel are plotted the SEDs of 28 ETGs at  $z = 0.37 - 0.38$  from the zCOSMOS ETGs sample, with mass increasing on average from the lowest one to the highest one. In the right panel is plotted the peak of the flux as a function of their mass for all those galaxies.*

Model	Mass zCOSMOS [ $\log_{10}(M/M_{\odot})$ ]	Mass SDSS [ $\log_{10}(M/M_{\odot})$ ]
CB07	$10.5 \pm 0.4$	
M05	$10.5 \pm 0.4$	
BC03	$10.6 \pm 0.4$	$10.8 \pm 0.4$
M09		$10.7 \pm 0.4$

Table 3.3: *Median stellar mass (in logarithmic units [ $\log_{10}(M/M_{\odot})$ ]) for SDSS and zCOSMOS ETGs samples with different models.*

for SDSS and zCOSMOS ETGs samples using BC03 models is shown; in Tab. 3.3 the median values (along with their dispersions<sup>1</sup>) obtained with different models are reported. From the figure, it can be observed that the ETGs samples really represent, independently on the survey, the most massive tail of the overall distribution of galaxy mass, with median mass always  $\gtrsim 10^{10.5} M_{\odot}$ . The difference in mass between the two surveys reflects a combination of two effects: on one side the difference in the selection of galaxies between the two surveys ( $r < 17.77$  for SDSS and  $I < 22.5$  for zCOSMOS), on the other side the different redshift ranges

<sup>1</sup>The dispersion on the median is evaluated as the "median absolute deviation" (MAD), defined as  $MAD = 1.482 * \text{median}(|x - \text{median}(x)|)$  (see Hoaglin et al., 1983)

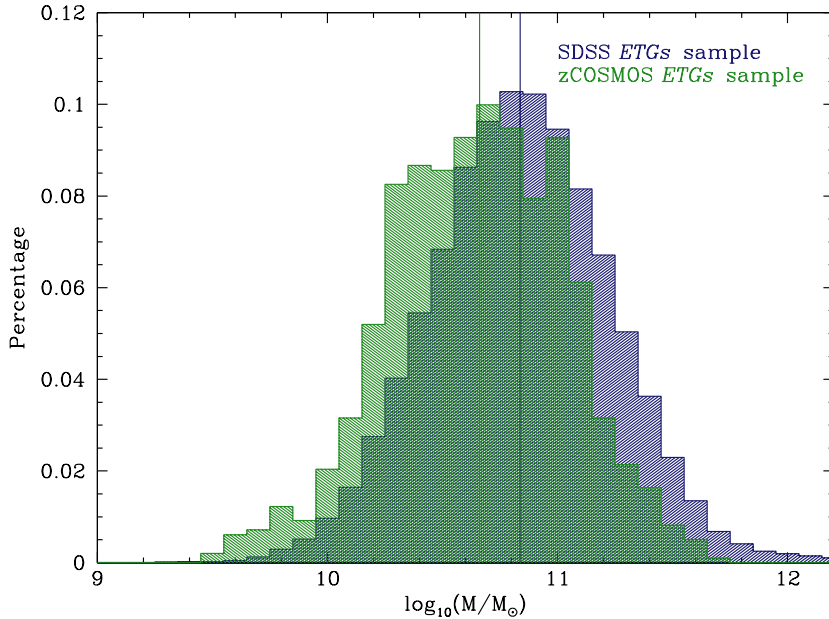


Figure 3.18: *Mass distributions (in logarithmic units [ $\log_{10}(M/M_{\odot})$ ]) of SDSS (blue) and zCOSMOS (green) ETGs samples obtained with BC03 models; the vertical lines show the median of the distributions.*

probed.

The table shows the dependence of the results on the stellar population synthesis model assumed. First of all it can be seen that the main difference is between BC03 models and the other two, that, as explained in Sect. 3.2.2, include both a treatment of TP-AGB stars. On the other side, as stressed before, the difference between the values obtained with different models do not exceed the value of  $\approx 0.2$  dex obtained also by Bolzonella et al. (2010).

### 3.6.2 The star formation history

There are different way to parametrize the SFH of a galaxy; the chosen delayed exponential SFH ( $SFH(t) \propto t/\tau^2 \exp(-t/\tau)$ ) is quite similar to the more common exponential declining SFH ( $SFH(t) \propto \tau^{-1} \exp(-t/\tau)$ ). It can be argued that both these two choices can not represent a generic SFH, since, by definition, these parametrizations tend to have the peak of star formation in the first stages of the life of a galaxy (see Fig. 3.19). Other models can be considered (a constant SFH, a reverse exponential SFH, a SFH with secondary bursts); however, giving that the sample to be analyzed is made of passive ETGs, for which, as shown in Chapt. 2, a passive evolution is inferred from  $z \sim 1$  to the present, these two models can

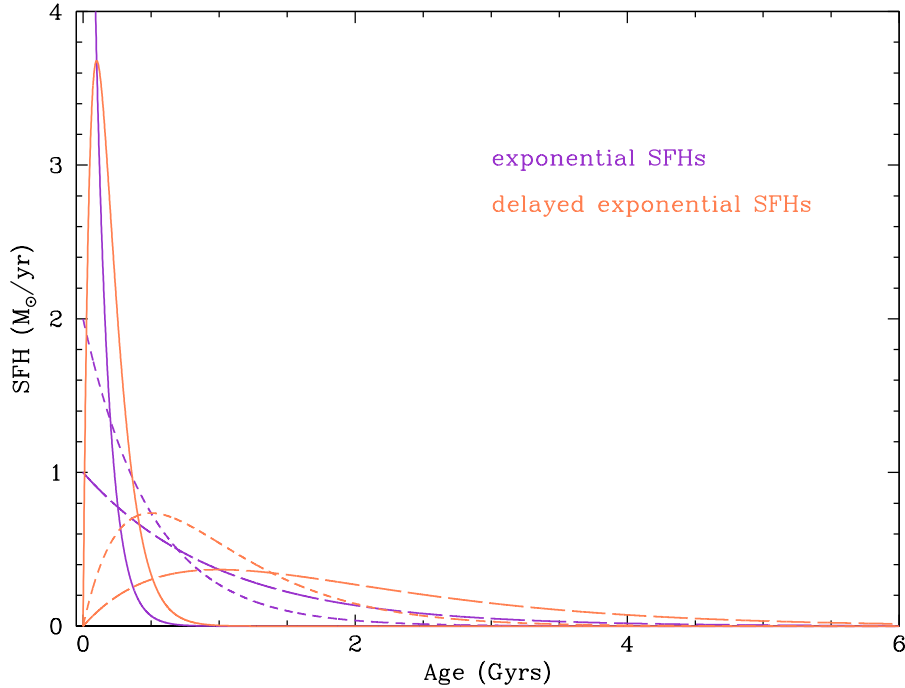


Figure 3.19: Plot of the exponentially declining (violet) and delayed exponential (orange) SFHs, for different values of  $\tau$ : continuous lines are created with  $\tau = 0.1$  Gyrs, dashed lines are created with  $\tau = 0.5$  Gyrs, and long-dashed lines are created with  $\tau = 1$  Gyrs,.

describe in a valid way the SFH of the *ETGs* samples.

The distributions of the  $\tau$  values for SDSS and zCOSMOS *ETGs* samples using BC03 models are shown in Fig. 3.20, while in Tab. 3.4 can be found the median  $\tau$  values (along with their dispersions). From Fig. 3.20 it is evident that the approximation of using a grid with low  $\tau$ s is good, with the bulk of *ETGs*

Model	$\tau$ zCOSMOS	$\tau$ SDSS
CB07	$0.2 \pm 0.2$	
M05	$0.2 \pm 0.2$	
BC03	$0.3 \pm 0.3$	$0.1 \pm 0.08$
M09		$0.2 \pm 0.2$

Table 3.4: Median  $\tau$  value for SDSS and zCOSMOS *ETGs* samples with different models.

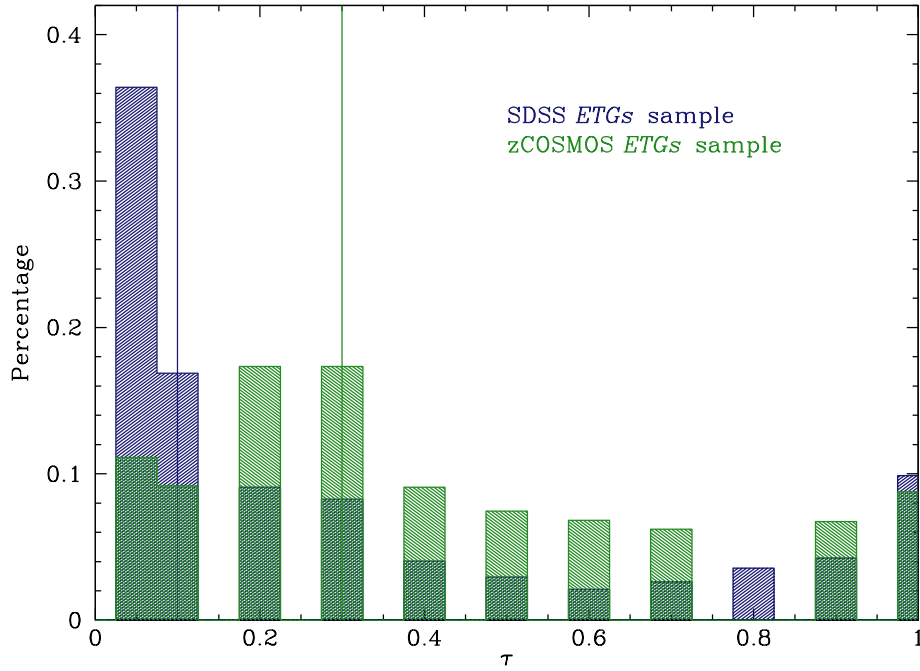


Figure 3.20: *SFH*  $\tau$  parameter distributions of SDSS (blue) and zCOSMOS (green) ETGs samples obtained with BC03 models; the vertical lines show the median of the distributions.

population at low  $\tau$  values and small tails. From the table it can be inferred that, independently on the model, these galaxies are compatible with a SFH peaked at younger ages and a passive evolution.

### 3.6.3 The dust reddening

Considering high-redshift galaxies, a fundamental parameter to be taken into account is the dust reddening, since it has been found that it can significantly change the colors of galaxies. There exist different possible reddening laws (Prevot et al., 1984; Bouchet et al., 1985; Fitzpatrick et al., 1986; Calzetti et al., 2000); if  $f_{obs}$  is the observed flux and  $f_{int}$  is the intrinsic flux, these two quantities can be related as follows:

$$f_{obs} = f_{int} 10^{0.4A_{\lambda}} \quad (3.3)$$

where the extinction at a wavelength  $\lambda$  is related to the color excess  $E(B - V)$  and to the reddening curve  $k(\lambda)$  by:

$$A_{\lambda} = k(\lambda)E(B - V) = \frac{k(\lambda)A_V}{R_V} \quad (3.4)$$

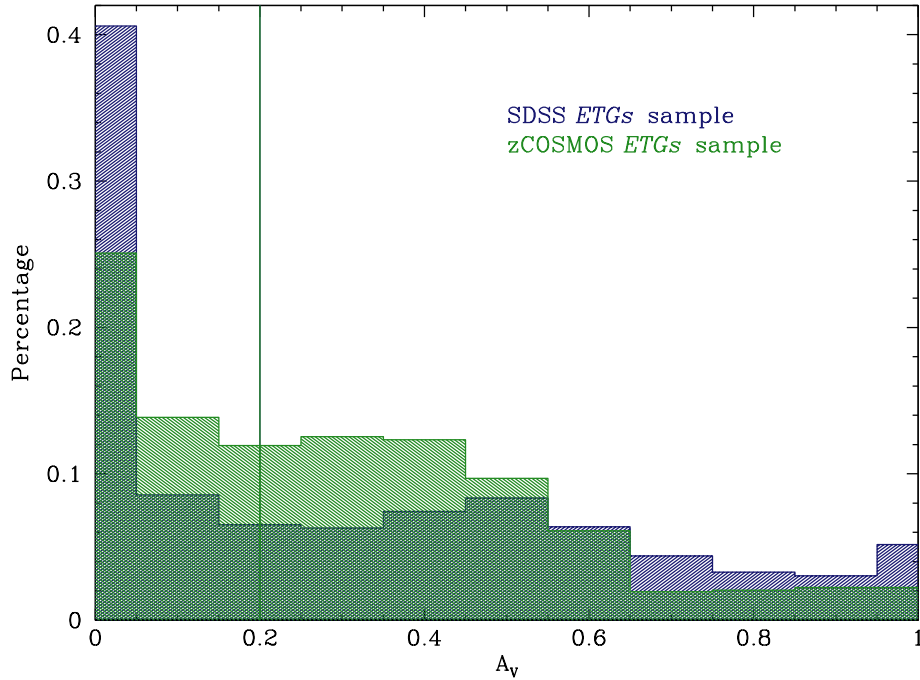


Figure 3.21:  $A_V$  distributions of SDSS (blue) and zCOSMOS (green) ETGs samples obtained with BC03 models; the vertical lines show the median of the distributions.

with  $R_V = 3.1$  (except for the Small Magellanic Cloud  $R_V = 2.72 \pm 0.21$  and for the Calzetti law  $R_V = 4.05 \pm 0.80$ ).

Here it has been studied the model with extinction from the Calzetti's law (Calzetti et al., 2000). A low contribution of extremely reddened objects is expected, since the selection method applied should reject (for the spectroscopic criterion) blue starforming objects that mimic red colors being extincted; therefore,

Model	$A_V$ zCOSMOS	$A_V$ SDSS
CB07	$0.1 \pm 0.2$	
M05	$0.3 \pm 0.2$	
BC03	$0.2 \pm 0.3$	$0.2 \pm 0.3$
M09		$0.2 \pm 0.2$

Table 3.5: Median  $A_V$  value for SDSS and zCOSMOS ETGs samples with different models.

even fixing a relatively wide range of  $A_V$ , the reddening extinction of *ETGs* samples should be relatively small. This conjecture is confirmed by the data analysis: both Fig. 3.21, that shows the distribution of  $A_V$  values for SDSS and zCOSMOS *ETGs* samples using BC03 models, and Tab. 3.5, quoting the median values and dispersions of  $A_V$  for different models, give strong evidences of the small amount of dust reddening present in both samples.

### 3.6.4 The age

The term “age” of a galaxy, evaluated with a SED-fitting approach, is used to indicate the mean luminosity-weighted age of its stellar population. This parameter has been proven to be the toughest to be constrained with SED-fitting.

This certainly depends on the fact that in this analysis this parameter is left it completely free, while many other works in literature assume, as a prior, that the ages of galaxies can not be higher than the age of the Universe at their redshift. However, aiming to understand the age evolution of ETGs as a function of redshift, fixing a prior on age could introduce a circularity in the procedure, for which the result of the analysis would have been exactly the prior assumed. This was indeed the case, since, in a test performed to explore this effect, using the prior all the galaxies having a best-fit with age greater than the age of the Universe have been assigned exactly the age of the Universe at that redshift.

On the other side, another important source of uncertainty are the degeneracies, that will be treated in detail in Sect. 3.6.5. Here are just plotted in Fig. 3.22 the histograms of the ages for SDSS and zCOSMOS *ETGs* samples using BC03 models, and in Tab. 3.6 the median age values and dispersions adopting for different models. The discrepancy between the ages evaluated with different models testify these problem. However, the fact that in average the SDSS ages are older than zCOSMOS ages is certainly also due to an evolution of the ages of ETGs with redshift.

Model	age zCOSMOS [Gyrs]	age SDSS [Gyrs]
CB07	$2.75 \pm 1.9$	
M05	$1.8 \pm 0.5$	
BC03	$2.25 \pm 1.3$	$3.75 \pm 2.9$
M09		$3.25 \pm 1.9$

Table 3.6: Median age for SDSS and zCOSMOS *ETGs* samples with different models.

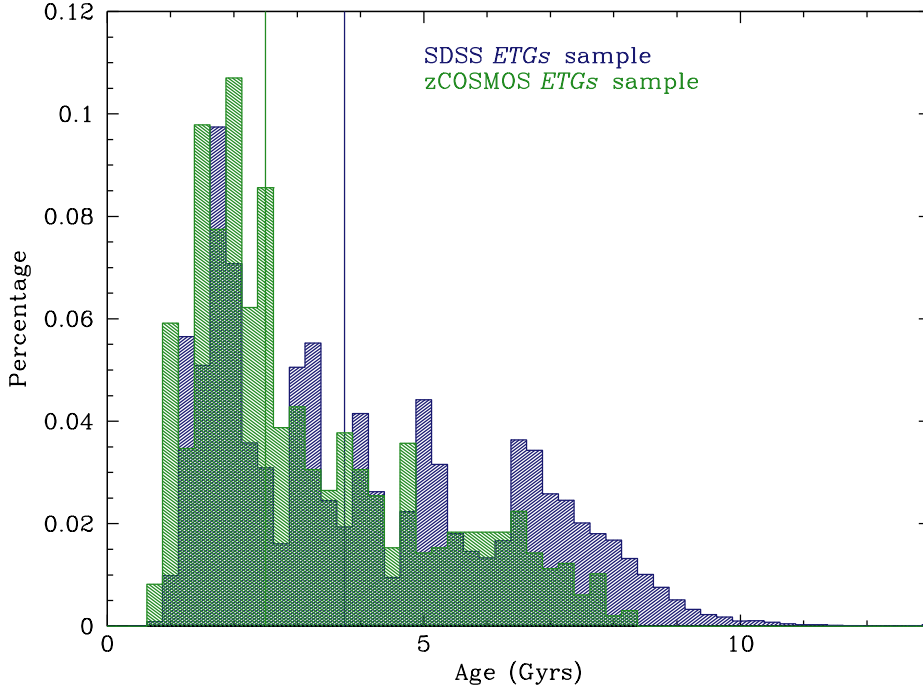


Figure 3.22: Age distributions of SDSS (blue) and zCOSMOS (green) ETGs samples obtained with BC03 models; the vertical lines show the median of the distributions.

### 3.6.5 Degenerations: the case of age-metallicity, but not only...

The most known problem when evaluating the age of a galaxy is the age-metallicity (e.g., see Worthey et al., 1994). In fact, it has been found that the colors (and also some spectroscopic features) of a galaxy with given age and metallicity can be mimicked from the ones of another galaxy with higher metallicity and lower age; the central point is that both age and metallicity are properties that tend to redden the spectrum of a galaxy, so they are hard to be disentangled. Moreover, a lot of other parameters can produce the same effect: it is easy to think how a combination of age and SFH could mix to produce basically the same SED.

To explore this issue, a test has been performed analyzing in detail the SED of a single galaxy of zCOSMOS ETGs sample, chosen to have a best-fit SED well reproducing the observed one ( $P(\chi^2) > 97\%$ ). In particular it was the galaxy with ID=817726 in zCOSMOS ETGs catalog, with a clear elliptical morphology at  $z = 0.8311$ . The best-fit to the SED of this object, letting the parameters free in the range  $t \in [0, 20]$  Gyrs,  $\tau \in [0.05 - 1]$  Gyrs,  $A_V \in [0, 1]$ , and  $Z = (0.08Z_\odot, 0.4Z_\odot, Z_\odot, 2.5Z_\odot)$ , gave:

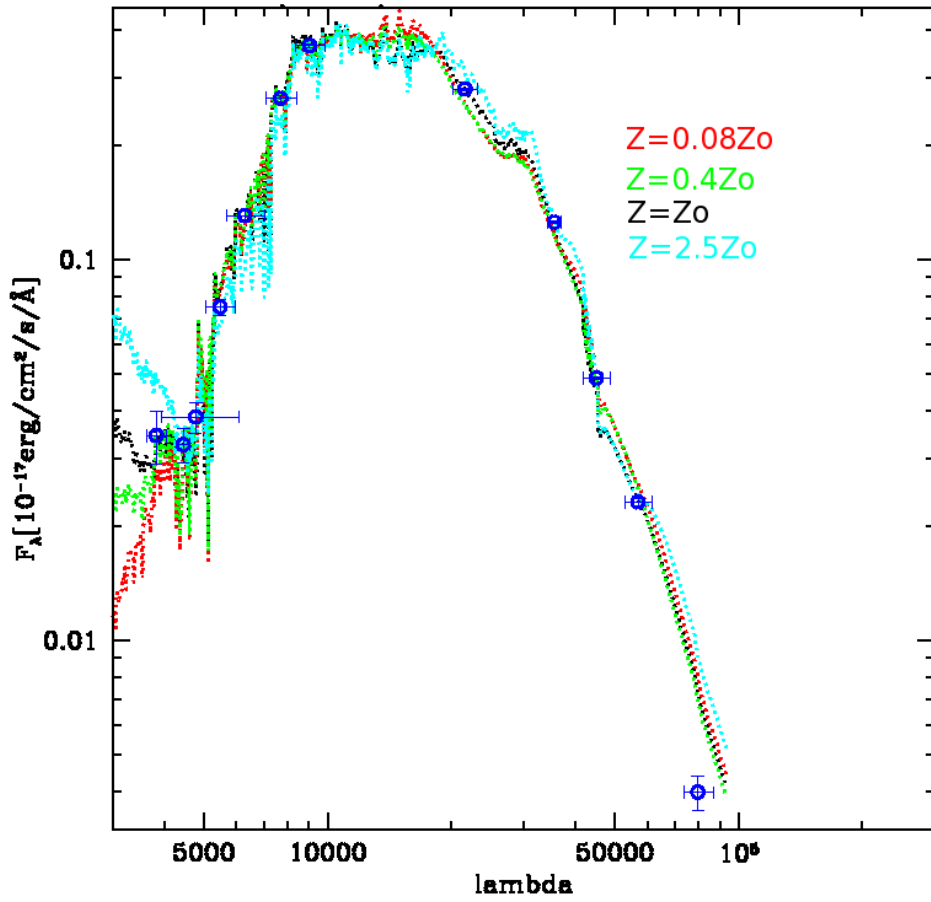


Figure 3.23: *Age-metallicity degeneracy in the SED-fitting of ID=817726 zCOSMOS early-type galaxy at  $z = 0.8311$ . In black it is shown the best-fit at  $Z = Z_{\odot}$ , in red the fit at  $Z = 0.008Z_{\odot}$ , in green the fit at  $Z = 0.4Z_{\odot}$ , and in cyan the fit at  $Z = 2.5Z_{\odot}$ .*

- age  $t=4.25$  Gyrs
- e-folding parameter  $\tau = 0.6$  Gyrs
- metallicity  $Z = Z_{\odot}$
- dust reddening  $A_V = 0.1$
- stellar mass  $\log_{10}(M/M_{\odot}) = 10.83$

However, the same fit performed fixing the age (near the best-fit value), and the  $\tau$  value ( $\tau = 0.6$  Gyrs), and varying the metallicity (respectively  $Z = 0.08Z_{\odot}, 0.4Z_{\odot}, Z_{\odot}, 2.5Z_{\odot}$ ) makes evident this degeneracy: the results are shown in Fig. 3.23. In blue are plotted the photometric points of the SED of the galaxy, while the dotted lines are the best-fit, red for  $Z = 0.08Z_{\odot}$ , green for  $Z = 0.4Z_{\odot}$ , black for  $Z = Z_{\odot}$ , and cyan for  $Z = 2.5Z_{\odot}$ . As it is possible to see, the resulting best-fit are almost identical, and the SEDs differ almost only in the UV part of the spectrum (the reduced  $\chi^2$  of the fit is not significantly different in 3 cases out of 4:  $\chi^2_{red} = 2.12$  for  $Z = 0.08Z_{\odot}$ ,

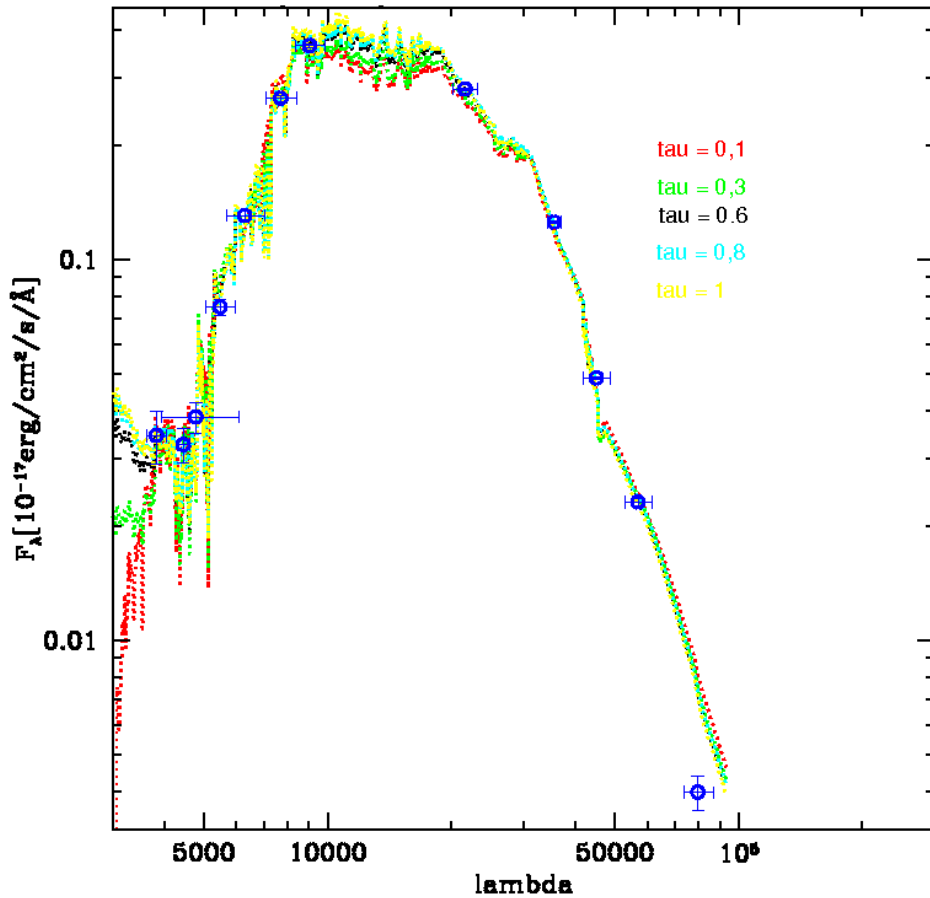


Figure 3.24: Age- $\tau$  degeneracy in the SED-fitting of ID=817726 *z*COSMOS early-type galaxy at  $z = 0.8311$ . In black it is shown the best-fit at  $\tau = 0.6$  Gyrs, in red the fit at  $\tau = 0.1$  Gyrs, in green the fit at  $\tau = 0.3$ , in cyan the fit at  $\tau = 0.8$  Gyrs, and in yellow the fit at  $\tau = 1$  Gyrs.

$\chi_{red}^2 = 1.28$  for  $Z = 0.4Z_{\odot}$ ,  $\chi_{red}^2 = 0.28$  Gyrs for  $Z = Z_{\odot}$ , and  $\chi_{red}^2 = 7.38$  Gyrs for  $Z = 2.5Z_{\odot}$ .

There are also problems related with the  $\tau$  parameter: Gavazzi et al. (2002) pointed out the danger of a degeneracy in the SED-fit between age and  $\tau$ . In this analysis a tight correlation between these parameters was also found, with galaxies fitted with a low  $\tau$  value having also systematically lower ages with respect to galaxies best-fitted with higher values of  $\tau$ . Figure 3.24 shows how strong is this degeneracy in the SED-fit: in this case, the metallicity ( $Z = Z_{\odot}$ ) and  $\tau$  have been fixed, while all the other parameters are let free. The black line represents the fit with  $\tau = 0.6$  Gyrs (and age  $t = 4.25$ ), the red line represents the fit with  $\tau = 0.1$  Gyrs (and age  $t = 1.14$  Gyrs), the green line represents the fit with  $\tau = 0.3$  Gyrs (and age  $t = 2.3$  Gyrs), the cyan line represents the fit with  $\tau = 0.8$  Gyrs (and age  $t = 5.5$  Gyrs), and the yellow line represents the fit with  $\tau = 1$  Gyrs (and age  $t = 7$  Gyrs), It is clearly evident the dependence of the best-fit age on the  $\tau$  value, and also in this case the best-fit SEDs are almost undistinguishable, with only differences in the UV part.

However, even if the age and  $\tau$  can be difficultly constrained in a precise way, as (Gavazzi et al., 2002) underline, the analysis can provide constraints on the age/ $\tau$  value; confirming their results, it has been found a value  $t/\tau > 5$  for every model considered, for both SDSS and zCOSMOS *ETGs* samples, supporting the hypothesis of passive evolution of these galaxies.

This twofold test prove the degeneracies present in the age obtained from the SED-fitting, and the consequent uncertainties in its evaluation.

### 3.7 ETGs sample in literature

Within the zCOSMOS collaboration, the *ETGs* sample has been used as a reference sample in two works, owing to the reliability of its selection.

Zucca et al. (2009) analyzed of the evolution of the Luminosity Function (LF) in the B band up to redshift  $z \sim 1$  for the zCOSMOS 10k sample, studying its dependence on galaxy types and environment. In this context, the *ETGs* sample defined in Sect. 3.4 (here called “bona-fide ETGs”) has been used as a reference sample of early-type galaxies, to cross-check the results obtained for samples selected with a pure photometric or spectroscopic criterion. Figure 3.25 shows the luminosity functions for different definitions of early-type galaxies: *bona-fide ETGs* in black, photometric ETGs in red, and morphological ETGs in green. The authors argued that photometric and *bona-fide ETGs* have similar shapes, but different normalizations. If the difference in normalization can be due to the different selection criteria adopted, the similarity of the shape implies the robustness of their results against a possible contamination of photometric ETGs by a fraction of “red” spirals. Pozzetti et al. (2010) investigated the total Galaxy Stellar Mass

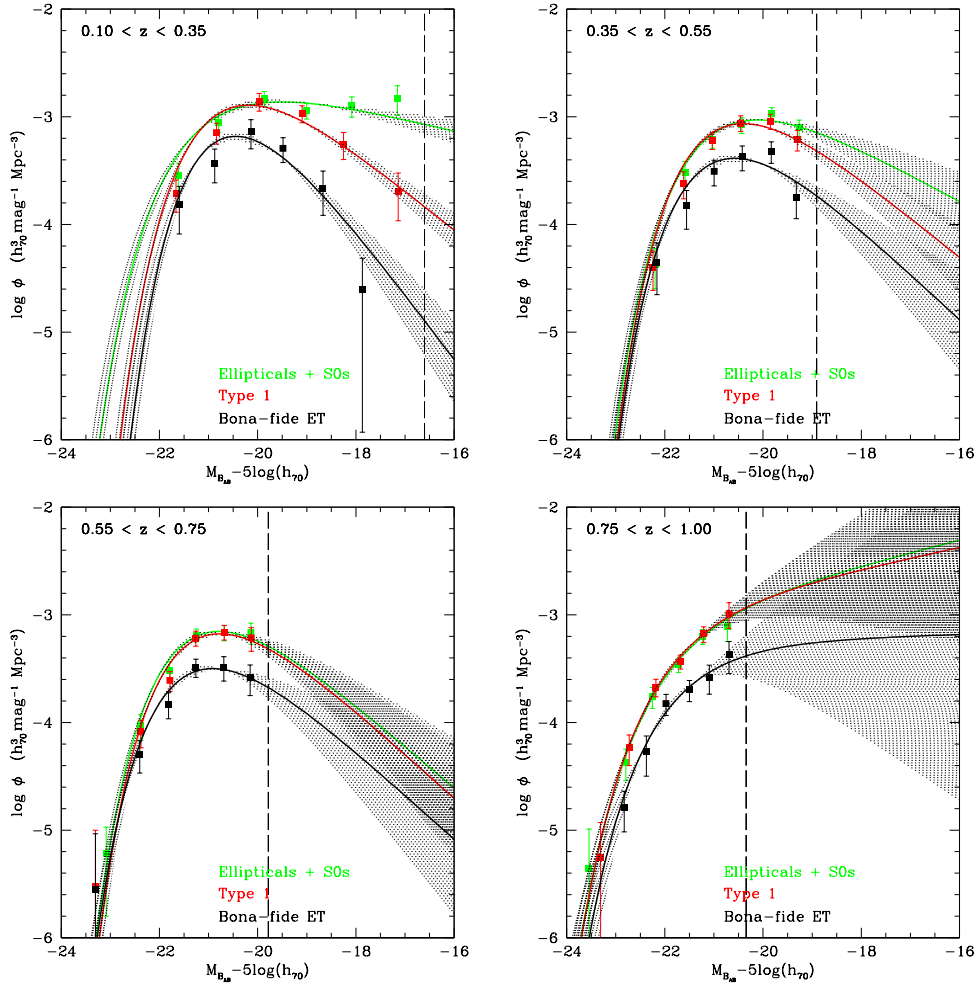


Figure 3.25: *Reproduced from Zucca et al. (2009): luminosity functions of early-type galaxies: bona-fide ET (black), photometric type 1 (red) and morphological early-type (in green) galaxies.*

Function (GSFM), separating the contributions of early- and late-type galaxies, and found a galaxy bimodality in the global GSMF, whose shape is more accurately represented by two Schechter functions, one linked to the early-type and the other to the late-type populations. Also in this case, the *ETGs* sample (also here called “bona-fide ETGs”) has been used to check that the results were not biased by the presence of outliers. Figure 3.26 show the GSMFs of ETGs as classified with a variety of criteria (red/passive/ellipticals/spheroids/absorption-line/*bona-fide*) at increasing redshift, and the authors use the similarity of the results between samples selected in different ways to strengthen their results.

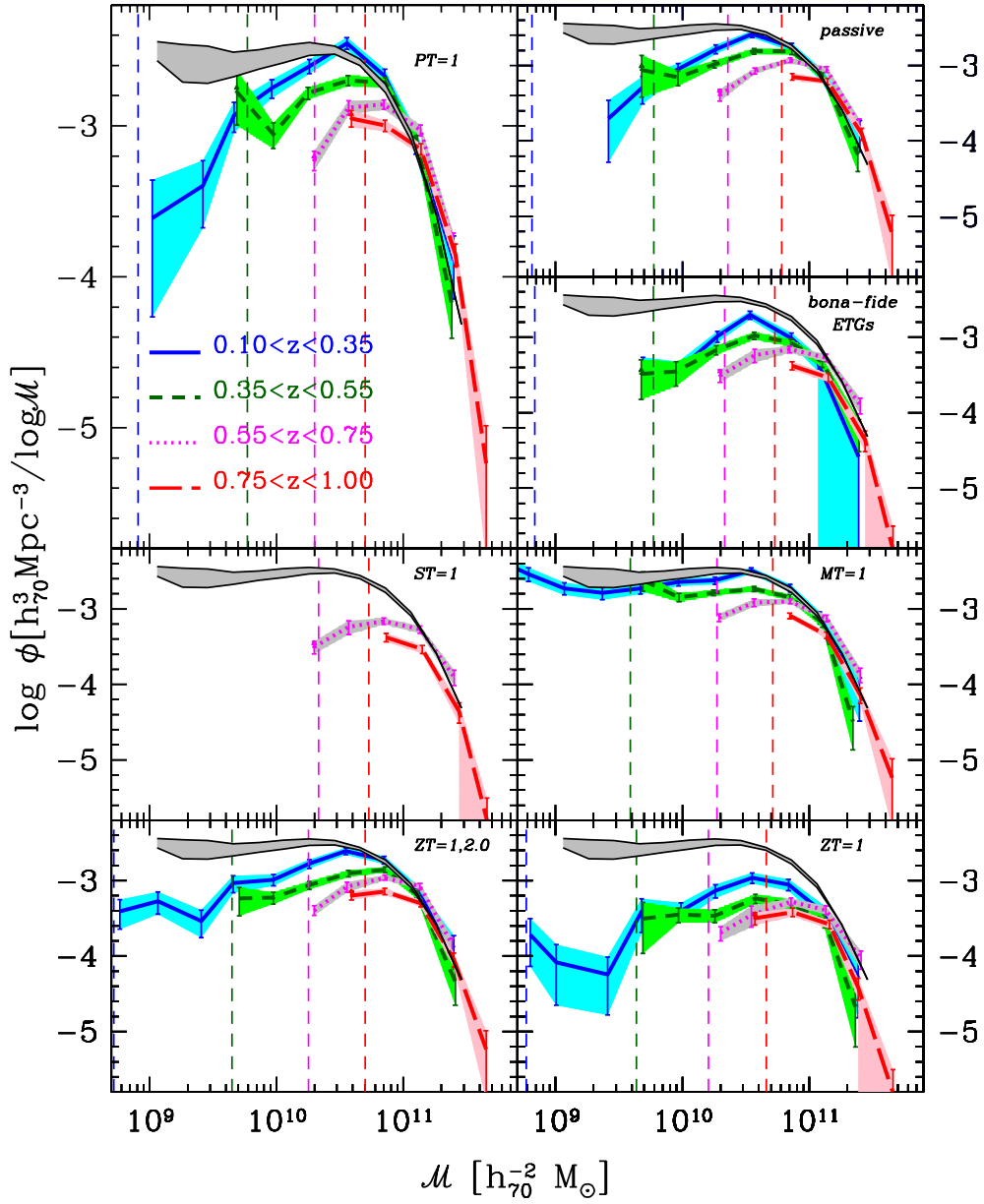


Figure 3.26: Reproduced from Pozzetti et al. (2010): GSMFs for ETGs using various classification schemes. Different lines and colours refer to different redshift ranges (see upper left panel). Grey hatched region, bounded by solid black lines, refer to local GSMF for ETGs derived from Baldry et al. (2008) and Baldry et al. (2006).

### 3.8 Conclusions about the selection of the ETGs samples

Two large spectroscopic survey have been examined, the SDSS and the zCOSMOS 10k bright spectroscopic sample, in order to select a sample of early-type galaxies covering the redshift range  $0 \lesssim z < \lesssim 1$ .

Using informations of both SED and spectrum of the galaxies (and, where available, morphology) three samples of ETGs have been extracted to be the less possible biased by the presence of starforming, blue outliers. Galaxies have been selected to have a photometric SED matching an early-type template (i.e. to be red), not to show prominent emission lines (i.e. passive), and, in the zCOSMOS sample, to have a confirmed and reliable classification in terms of morphology.

The photometry of all galaxies has been optimized applying zeropoint shifts and error corrections, by comparing the observed and the best-fit theoretical magnitude distributions.

The three final sample are:

- **SDSS ETGs sample.** Extracted from a matching between the SDSS-DR6 and the 2MASS survey, it has 8 photometric bands, the standard  $u$ ,  $g$ ,  $r$ ,  $i$ , and  $z$  from SDSS and the  $J$ ,  $H$ , and  $K$  bands from 2MASS. It has been selected in order to have photometric type  $\leq 1.4$ ,  $EW([OII]) < 5 \text{ \AA}$ ,  $EW(H\alpha) < 5 \text{ \AA}$  and median  $S/N$  ratio per  $\text{\AA} > 3$ . In this sample are present in total 97,460 ETGs in the redshift range  $0.02 < z < 0.5$  (with a median redshift  $\langle z \rangle = 0.12$ ). It is characterized by a median mass of  $\log(M/M_{\odot}) \sim 10.8$ , and SFHs with a median  $\tau \sim 0.1$ ;
- **zCOSMOS “Red galaxies” sample.** Extracted from the zCOSMOS 10k bright spectroscopic sample, it is provided of 10 photometric bands: CFHT  $u^*$  and  $K_s$ , Subaru  $B_J$ ,  $V_J$ ,  $g^+$ ,  $r^+$ ,  $i^+$ , and  $z^+$ , and Spitzer IRAC at  $3.6 \mu\text{m}$  and  $4.5 \mu\text{m}$ . It has been selected just with a wide photometric criterion (photometric type  $\leq 1.13$ ) in order to keep high the statistic. In this sample there are 2,093 ETGs, and it has been used to check the results of the more precisely selected *ETGs* sample, having almost double the statistic;
- **zCOSMOS “ETGs” sample.** This is a subsample of the *Red galaxies* zCOSMOS sample, so it has the same photometric coverage. It has been selected discarding from the previous sample all galaxies with: a) significantly strong emission lines (measured  $EW([OII]) > 5 \text{ \AA}$  and  $EW(H\alpha) > 5 \text{ \AA}$ ), b) confirmed spiral morphology (ZEST $\cap$ MRS classification as spiral), c) bluer colors (photometric type  $> 1.4$ ), and e) strong  $24\mu\text{m}$  emission ( $(K - 24\mu\text{m}) > -0.5$ ). This selections have been applied in order to have a more reliable,

even if less numerous, sample of old, red, and passive ETGs. This sample contains 981 galaxies in the redshift range  $0.05 < z < 1.2$  (with median redshift  $\langle z \rangle = 0.58$ ). It is characterized by a median mass of  $\log(M/M_\odot) \sim 10.5$ , and SFHs with a median  $\tau \sim 0.2$ .

---

# Chapter 4

## Early-type galaxies as evolutionary probes

In Chapt. 2 the status of the art about our understanding of galaxy evolution has been shown, focusing in particular the attention to early-type galaxies. Certainly deeper and more precise observation will help in deciphering this enigma. However, it is very likely that a simple answer do not exists, and that there are multiple parameters that tune this evolution. In this scenario, it is very important to understand what are the main ingredients, and what are the secondary ones.

In social sciences, one of the most important debate concerns the “nature vs nurture” dilemma, i.e. to understand the relative importance of the genetic inheritance (nature) and of the interaction with the environment (nurture) in determining the differences in the personal traits. Borrowing this picture from geneticists, astronomers are now facing the same question: are the observed difference between galaxies (in terms of their morphology, colors, star formation) primarily due to their internal properties (such as mass, luminosity, and so on) or instead depend on the environment in which they evolve?

In this chapter, this problem is addressed with an analysis of the  $(U - V)$  rest-frame color distributions for two different samples of zCOSMOS ETGs, investigating the dependence of the shape of their distribution on mass and environment. In addition to colors, two spectroscopic line indices in galaxy spectra are studied too, the 4000 Å break (D4000) and the equivalent width of the  $H\delta$  Balmer line ( $EW_0(H\delta)$ ), which have proven to be good age indicators (see Hamilton, 1985; Bruzual & Charlot, 1993; Kauffmann et al., 2003). The D4000 index is produced by the blending of a large number of spectral lines in a narrow wavelength region, which creates a break in the spectrum at this wavelength. The main contribution to the opacity of a star comes from ionized metals: in hot stars, the metals are multiply ionized and the opacity decreases, so the D4000 will be small for young

stellar populations and large for old, metal-rich galaxies. It is, therefore, an observable that is strongly dependent on the age and metallicity of a galaxy. On the other side, the  $EW_0(H\delta)$  correlates well with recent episodes of star formation. To verify the results from the analysis of colors, these spectral line strengths are analyzed as a function of redshift in different mass and environment bins.

Finally, evidences supporting a mass-downsizing scenario are discussed, inspecting the lookback time of *ETGs* as a function of stellar mass. Throughout this chapter, the following cosmological parameters will be adopted:  $H_0 = 70 \text{ km s}^{-1} \text{ Mpc}^{-1}$ ,  $\Omega_m = 0.25$ ,  $\Omega_\Lambda = 0.75$ .

The reference article for this analysis is Moresco et al. (2010a).

## 4.1 The data samples

To perform the analysis, the two samples of zCOSMOS early-type galaxies described in Sect. 3.3 has been used, the *Red galaxies* sample and the *ETGs* sample. The first sample, selected only with a photometric criterion, consists of 2,098 galaxies. The second one, based on a morphological/spectroscopic/photometric joint analysis, contains 981 galaxies. Two samples have been chosen because the first one allows to do a much precise analysis, having almost twice the statistics, while the second one provides a reliable reference sample of *ETGs*.

### 4.1.1 Color estimate

Absolute magnitudes and colors were evaluated using the “Algorithm for Luminosity Function” (ALF) software, following the method described in (Zucca et al., 2009); the  $(U - V)$  rest-frame color is analyzed (Buser’s filters, Buser, 1978). The upper panel of Fig. 4.1 shows the  $(U - V)_{rest}$  color for the parent zCOSMOS 10k galaxy sample (in black), as well for *Red galaxies* (in red) and *ETGs* samples (in green). It is evident a clear bimodality in the distribution and how both the adopted selections of early-type galaxies are well located in the red peak. Moreover it is important to stress that the *ETGs* sample, by definition, has a mean color that is even redder than the *Red galaxies* sample.

### 4.1.2 Overdensity definition

Determining an appropriate overdensity definition for the zCOSMOS 10k-bright sample is a difficult task. For zCOSMOS, Kovač et al. (2010) defined the density contrast to be  $\delta = (\rho - \bar{\rho})/\bar{\rho}$ , where  $\rho$  is a function of the position of the galaxy (RA, dec, and  $z$ ) and  $\bar{\rho}$  is the mean value measured at the same redshift. The density field of the COSMOS field was reconstructed for different choices of filters (a fixed comoving aperture or an adaptive aperture with a fixed number of neighbors), tracers (flux-limited or volume-limited subsamples), and weights (stellar

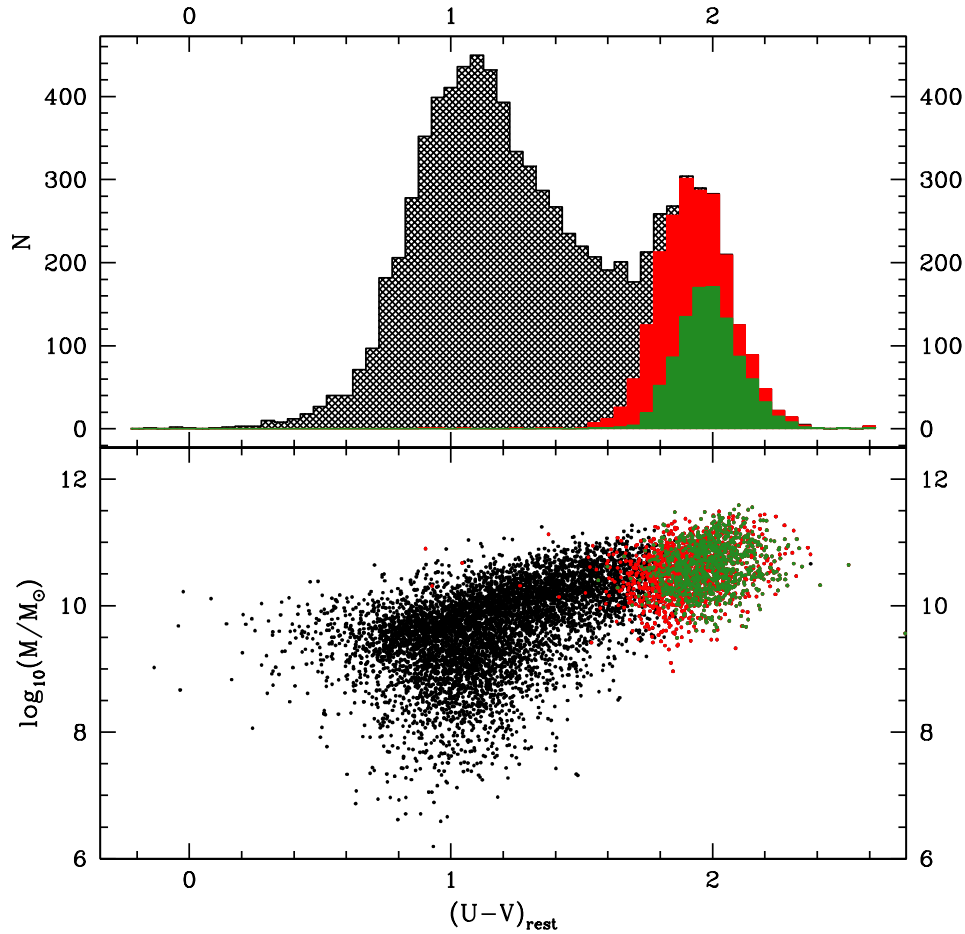


Figure 4.1: *Distribution of  $(U - V)_{rest}$  color (upper panel) and color-mass relation (lower panel) for the parent zCOSMOS bright 10k galaxies sample (in black), red galaxies (in red), and ETGs (in green).*

mass, luminosity, or no weight, i.e., considering only the number of galaxies); the reference article for a comprehensive explanation is Kovač et al. (2010). Following the approach of Bolzonella et al. (2010), the 5th nearest neighbor volume-limited (5NN) estimator of the density field has been used, because it has been shown that this represents a good compromise between the smallest accessible scales and the reliability of the overdensity values. It has been chosen a number-weighted estimator, and not a mass-weighted one, because in trying to distinguish a dependence on mass, introducing an estimator that itself depends on mass could bias the analysis. Good agreement between the results obtained with this estimator and a

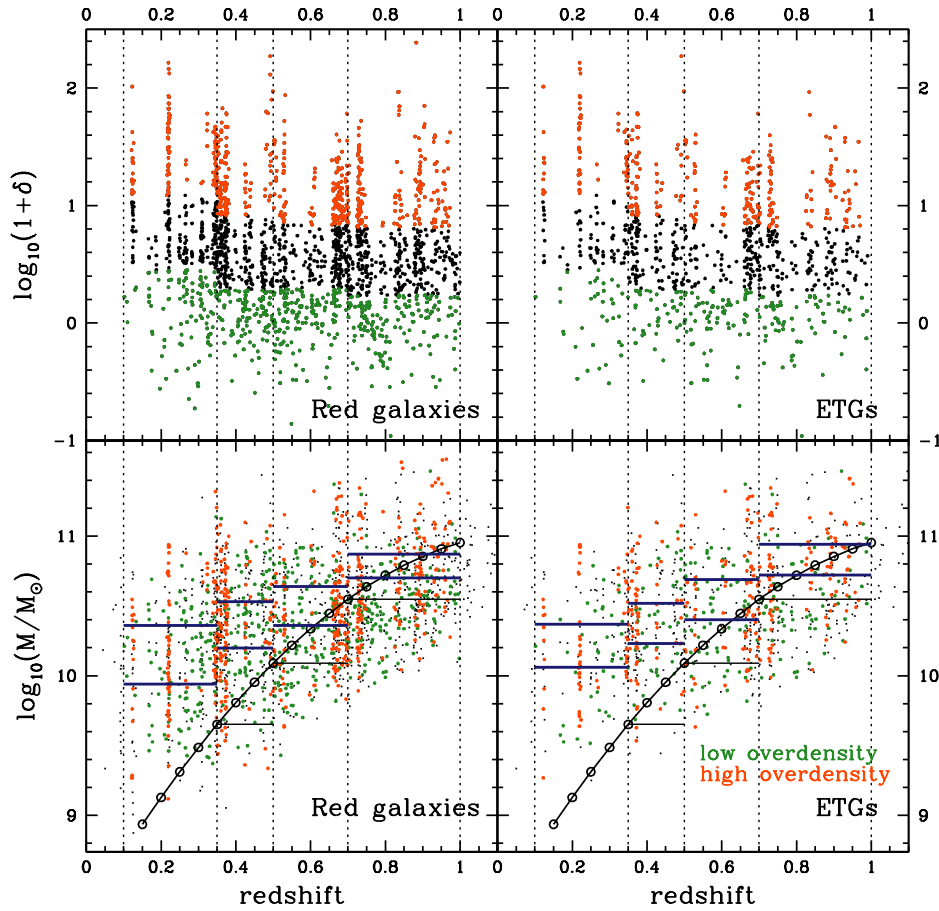


Figure 4.2: Overdensity-redshift (upper panels) and mass-redshift (lower panels) distributions of the sample of red galaxies (left columns) and ETGs (right columns). In the overdensity-redshift distribution, the galaxies residing in the lowest overdensity quartile are highlighted in green, and in red the ones in the highest. In the mass-redshift distributions, the black dotted vertical lines indicate the redshift division of the sample, the black horizontal lines indicate the lower mass limit adopted in each redshift bin, and the blue horizontal lines indicate the division into tertiles for each bin. The curve joining the open circles represents the mass completeness of the sample.

luminosity-weighted estimator has been found. Hence the results discussed in this chapter do not depend on the choice of the adopted estimator for the density field. In Table 4.1 are reported report the overdensity quartiles that were evaluated in

4 different redshift bins considering galaxies with  $\log_{10}(M/M_{\odot}) > 10.5$  (for a more detailed discussion, see Bolzonella et al., 2010). In the upper panels of Fig. 4.2, the overdensity-redshift relations for the *Red galaxies* and the *ETGs* samples are shown, highlighting in green the lowest and in red the highest overdensity quartile.

Table 4.2 provides information about the median overdensity measured in the four environment quartiles and the distance scale measured in the radius within the 5NN. The change in the median overdensity from one quartile to the next is by a factor of  $\sim 2$ .

Knobel et al. (2009) detected 102 groups with more than 5 observed members and 23 with more than 8 in the zCOSMOS 10k sample. Finoguenov et al. (2007) analyzed the XMM-COSMOS survey, finding an X-ray luminosity for extended sources between  $L_{0.1-2.4keV} = 3 \cdot 10^{42} \text{erg s}^{-1}$  and  $5 \cdot 10^{43} \text{erg s}^{-1}$ . Peng et al. (2010) made a detailed comparison between zCOSMOS and SDSS, evaluating the overdensities in the same way in the two surveys, and finding that SDSS spans a wider

$\Delta z$	1 <sup>st</sup> quartile	2 <sup>nd</sup> quartile
$0.1 < z < 0.35$	$x \leq 2.82$	$2.82 < x \leq 5.36$
$0.35 \leq z < 0.5$	$x \leq 1.94$	$1.94 < x \leq 3.57$
$0.5 \leq z < 0.7$	$x \leq 1.95$	$1.95 < x \leq 3.52$
$z \geq 0.7$	$x \leq 1.72$	$1.72 < x \leq 3.39$
$\Delta z$	3 <sup>rd</sup> quartile	4 <sup>th</sup> quartile
$0.1 < z < 0.35$	$5.36 < x \leq 12.21$	$x > 12.21$
$0.35 \leq z < 0.5$	$3.57 < x \leq 8.25$	$x > 8.25$
$0.5 \leq z < 0.7$	$3.52 < x \leq 6.84$	$x > 6.84$
$z \geq 0.7$	$3.39 < x \leq 6.49$	$x > 6.49$

Table 4.1: *Definition of quartiles for the overdensities computed with the 5NN estimator. The variable  $x$  represents the overdensity  $(1 + \delta)$ .*

quartile	median overdensity	median distance
1 <sup>st</sup>	$1.23 \pm 0.03$	$3.03 \pm 0.06$
2 <sup>nd</sup>	$2.81 \pm 0.04$	$1.83 \pm 0.03$
3 <sup>rd</sup>	$5.29 \pm 0.07$	$1.31 \pm 0.02$
4 <sup>th</sup>	$14.43 \pm 0.38$	$0.84 \pm 0.02$

Table 4.2: *Median overdensities and distances (in comoving Mpc/h) with their errors for the four environment quartiles averaged throughout the entire redshift range.*

range of overdensity, from  $\log_{10}(1 + \delta) = -1$  to almost 3, while the overall zCOSMOS range is  $-1 < \log_{10}(1 + \delta) < 2.3$ . For ETGs, as shown from Fig. 4.2, the range is a little smaller, with  $-0.5 < \log_{10}(1 + \delta) < 2$ .

Therefore, it should be underlined that the zCOSMOS survey does not contain any single rich cluster, e.g. comparable to the Coma cluster in the local Universe (the highest mass in the Knobel et al. (2009) sample is  $\approx 10^{14} M_{\odot}$ , while the mass of Coma cluster is  $\approx 10^{15} M_{\odot}$ ), but samples well the rich group environment (see also Iovino et al., 2010).

### 4.1.3 Mass estimate

The masses of *red* galaxies and *ETGs* were estimated by performing a best fit to the multicolor spectral energy distribution, using the observed magnitudes in 10 photometric bands from  $u^*$  to  $4.5\mu m$  (see Sect. 3.2.2). The assumptions about models and parameters in the SED-fitting are discussed in Sect. 3.6. The quoted values are obtained using CB07 stellar population synthesis models, decreasing SFHs with  $\tau < 1$  Gyr, solar metallicity, and  $0 < A_V < 1$  and free ages in the range  $t \in [0, 20]$  Gyrs.

The study of the color-mass diagram shows that both samples are well placed in the red sequence (see Fig. 4.1, lower panel). Considering the mass distribution, the *ETG* selection tends to include the more massive of the *Red galaxies* (see Fig. 4.1). This gives another proof that the more restrictive definition of *ETGs* has selected the more massive, passive, redder, and spheroidal galaxies of the zCOSMOS 10k-bright sample.

To search for any mass dependence of the color distribution, the sample has been divided into bins of stellar masses. The lower panel of Fig. 4.2 shows the different divisions adopted. Bolzonella et al. (2010) found that the mass function of ETGs does not vary significantly in the high and low-density environments probed by the zCOSMOS survey. Therefore, the first step taken was to simply divide the sample into equally populated mass tertiles over the entire redshift range for all the overdensity bins considered (each bin contains approximately 200 galaxies). The lowest tertile corresponds to the mass range  $\log_{10}(M/M_{\odot}) < 10.25$ , the intermediate tertile to  $10.25 < \log_{10}(M/M_{\odot}) < 10.6$ , and the upper tertile to  $\log_{10}(M/M_{\odot}) > 10.6$ . The choice of a division into mass tertiles instead of quartiles (as performed for the analysis of environment) is justified by the wish to keep the statistical accuracy high and the shot noise low.

**The redshift evolution and the  $V/V_{max}$  formalism.** Owing to the magnitude selection ( $I_{AB} < 22.5$ ), both samples are affected by mass incompleteness that increases with redshift (see lower panels of Fig. 4.2). This means that, at each redshift, it exists a minimum mass  $M_{min}(z)$  above which a sample can be considered complete, since all galaxies above that mass are potentially observable. The

limit of completeness of the sample has been evaluated following the procedure explained by Pozzetti et al. (2010), and is shown by the black curve in the lower panels of Fig. 4.2. This means that, giving a redshift interval  $[z_{min}, z_{max}]$ , galaxies should be considered over the completeness limit only for  $M > M_{min}(z_{max})$ .

To correct for the mass incompleteness effect, the classical non-parametric  $V/V_{max}$  formalism introduced by Schmidt (1968) (see also Avni & Bahcall, 1980) has been applied. Using this correction, galaxies can be considered over the completeness limit for  $M > M_{min}(z_{min})$ .

Both samples have been studied divided also into four redshift bins (identical to those adopted in the overdensity quartiles definition), evaluating the tertiles above the mass completeness limit in each redshift bin, as shown in the bottom part of Fig. 4.2. In this case, every bin contains approximately 40 galaxies. This procedure yielded a lower statistical accuracy, with the advantage of following in detail the redshift evolution.

#### 4.1.4 D4000 and $EW_0(H\delta)$ definitions

Combinations of spectroscopic line strengths measurable in galaxy spectra have been identified to be direct tracers of galaxy characteristic parameters, such as mass, age, and star-formation rate. In particular, the 4000 Å break (D4000) and the rest-frame equivalent width ( $EW_0$ ) of the  $H\delta$  Balmer line ( $\lambda_{rest} = 4100$  Å) are indicators of galaxy integrated or recent star formation, respectively. These same indicators were used in the zCOSMOS sample to study the activity of 24  $\mu m$  sources and their close neighbors (Caputi et al., 2009a,b) and to select post-starburst galaxies (Vergani et al., 2010).

To easily study the spectral properties of the zCOSMOS galaxies, a fully automatic spectral measurement code (PlateFit; Lamareille et al., 2006) has been used, which measures all the spectral features and equivalent widths of the prominent lines present in zCOSMOS spectra, given its spectral range. This code fits the stellar continuum and absorption lines making use of the STELIB library (Le Borgne et al., 2003) of stellar spectra and the GALAXEV Bruzual & Charlot (2003) stellar population synthesis models (see Lamareille et al., 2006, for further details). To investigate the influence of mass and environment on the spectral features, the values of D4000 and  $EW_0(H\delta)$  evaluated for single spectra have been averaged in bins of redshift, mass, and environment. Because of the wavelength coverage of the zCOSMOS spectra, the D4000 index is available only for  $0.45 \leq z \leq 1$ , which corresponds approximately to a time interval of 4 Gyrs. To follow the redshift evolution, This redshift range has been divided into four bins ( $0.45 \leq z < 0.6$ ,  $0.6 \leq z < 0.7$ ,  $0.7 \leq z < 0.8$ , and  $0.8 \leq z \leq 1$ ). Each redshift bin has been yet further divided using the four environment quartiles defined as before, to ensure a coherent analysis, and three equally populated mass tertiles, with the lowest one corresponding to  $\log_{10}(M/M_{\odot}) < 10.4$ , the intermediate to  $10.4 <$

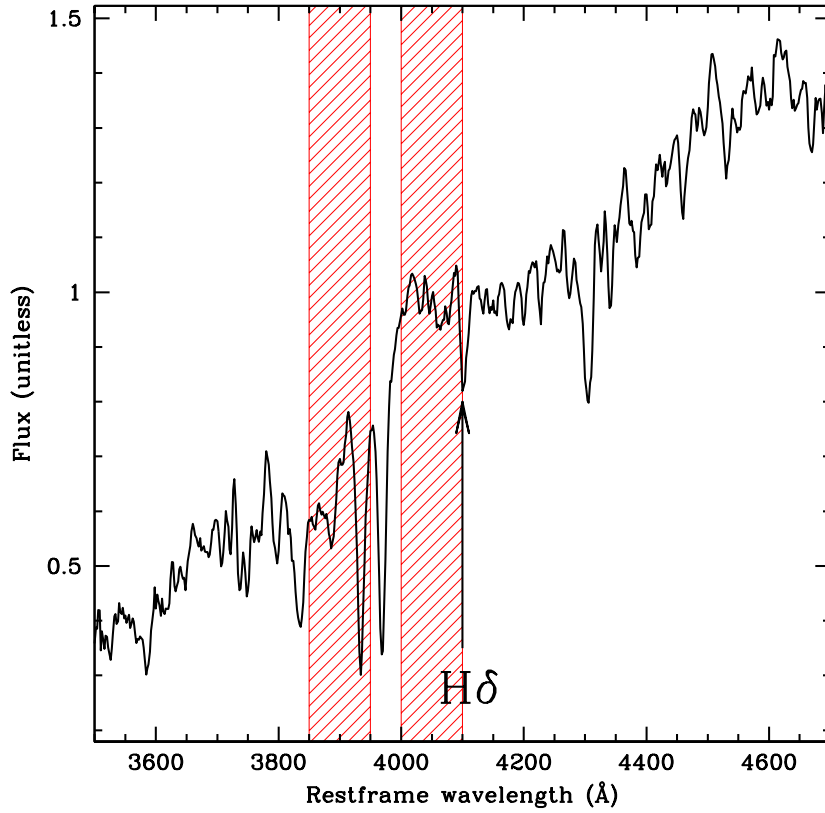


Figure 4.3: Stacked spectrum of the 607 ETGs in the range  $0.45 < z < 1$ . In red are plotted the regions of the red and blue continuum used in the computation of  $D4000$ .

$\log_{10}(M/M_{\odot}) < 10.7$ , and the highest one to  $\log_{10}(M/M_{\odot}) > 10.7$ . As a starting catalog, it has been used the *ETG* sample, because it is less contaminated by outliers. Figure 4.3 shows the average stacked spectrum of the 607 *ETGs* in the range  $0.45 < z < 1$ , the ranges of the blue and red bands used to evaluate  $D4000$  and  $H\delta$  indices. On average each bin contains 10 galaxies. The adopted definition of  $D4000$  is the one given by Balogh et al. (1999), where the average flux  $F_{\nu}$  in the red and blue wavelength bands are measured in the ranges  $4000 - 4100 \text{ \AA}$  and  $3850 - 3950 \text{ \AA}$  ( $D4000$  “narrow”):

$$D4000 = \frac{F_{red}}{F_{blue}} = \frac{(\lambda_2^{blue} - \lambda_1^{blue}) \int_{\lambda_1^{red}}^{\lambda_2^{red}} F_{\nu} d\lambda}{(\lambda_2^{red} - \lambda_1^{red}) \int_{\lambda_1^{blue}}^{\lambda_2^{blue}} F_{\nu} d\lambda}.$$

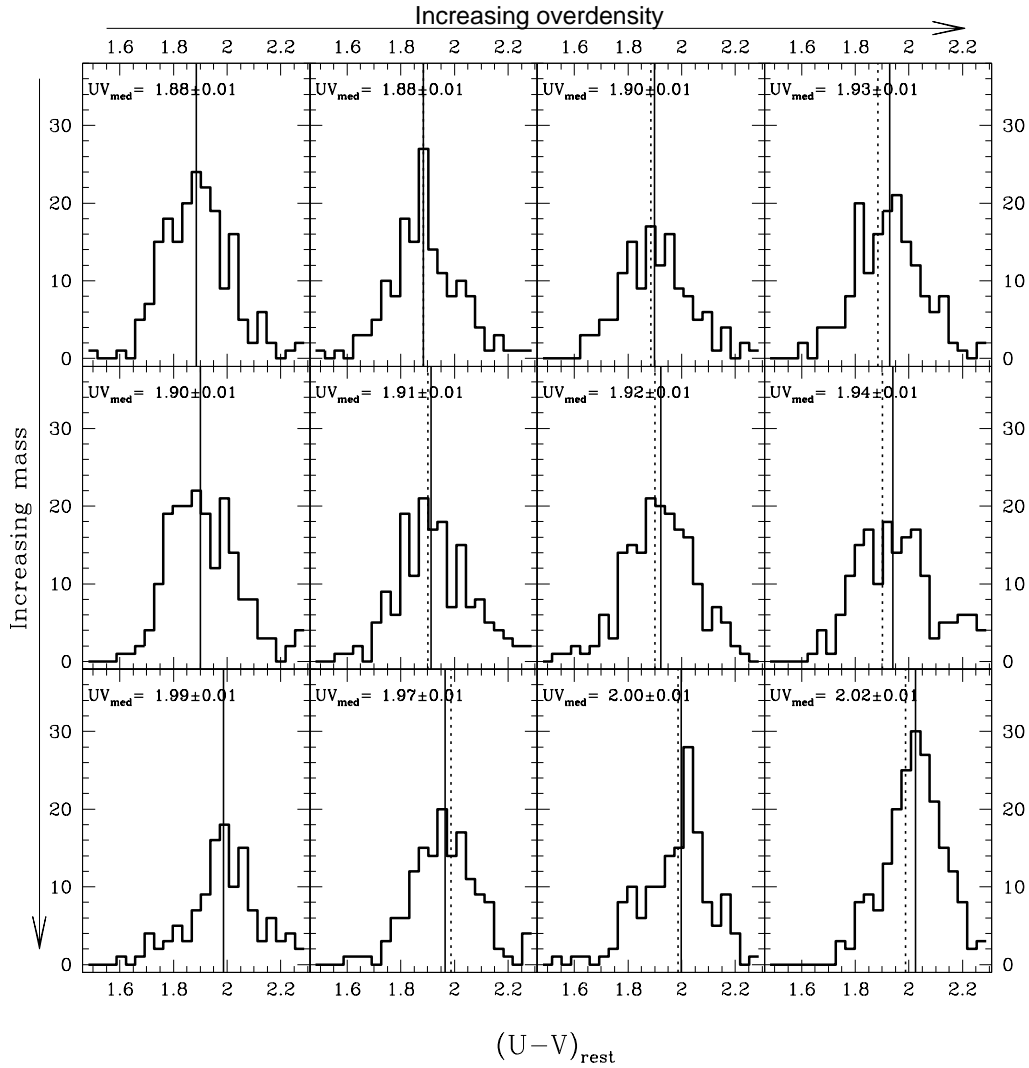


Figure 4.4:  $(U - V)_{\text{rest}}$  color distribution for Red galaxies as a function of increasing overdensities (horizontal panels) and increasing mass (vertical panels). The mass was divided into three ranges,  $\log_{10}(M/M_{\odot}) < 10.25$ ,  $10.25 \leq \log_{10}(M/M_{\odot}) < 10.6$ , and  $\log_{10}(M/M_{\odot}) \geq 10.6$  (panels from top to bottom), while the quartiles of environment are shown in Tab. 4.1 and 4.2 (panels from left to right). In each panel, the solid line represents the median of the distribution, while the dashed line is the median value corresponding to the color distribution in the same mass range but for the lowest environment, to make it easier to follow the environment dependence. In each panel, are also reported the value of the median  $(U - V)_{\text{rest}}$  with its error.

## 4.2 The color analysis

### 4.2.1 Color distribution of early-type galaxies

The  $(U - V)_{rest}$  color distributions for the total sample of *Red* galaxies are shown in Fig. 4.4. The color distributions and their medians have been evaluated in four quartiles of environment and three mass bins, as described in Sects. 4.1.2 and 4.1.3, and plotted in order of both increasing mass (from top to bottom) and increasing density environment (from left to right). In each panel, a dashed line indicate the median value corresponding to the color distribution in the same mass range but for the lowest density environment, in order to make it easier to follow the environment dependence. It is possible to see that, although the dispersion of the color distributions is almost the same in different mass and environment bins, there is evolution in the median color with mass for fixed environment, the medians shifting towards a redder color with increasing mass. On the other hand, focusing on environment, it is evident that this effect at fixed mass is not strong, there being only a small shift in the median value mostly for the highest density quartile. In the following sections, these dependences are explored quantitatively, studying also the effect of redshift evolution.

### 4.2.2 Color-environment relation

The mean color of *Red galaxies* and *ETGs* samples has been evaluated in the four quartiles of environment defined in Table 4.1; the results are plotted in Fig. 4.5 for the three mass bins. As explained in Sect. 4.1.3, a  $1/V_{max}$  correction has been applied to take into account the incompleteness in mass, evaluating the mean color by weighting each galaxy by its  $V/V_{max}$ ; therefore the values reported in Figs. 4.5 and 4.6 differ from to the values shown in Fig. 4.4. It is evident that within a fixed mass bin the dependence of the mean color on the overdensity parameter for both of the samples is really weak, showing on average an offset of  $\langle \Delta(U - V)_{rest} \rangle = 0.027 \pm 0.008$  mag redder in the highest density environments than in the lowest density environment for *Red galaxies* and  $\langle \Delta(U - V)_{rest} \rangle = 0.01 \pm 0.01$  mag for *ETGs*. Also the formal slopes  $S_\delta$  of this relation  $(U - V)_{rest} \propto S_\delta \cdot \log_{10}(1 + \delta)$  have been evaluated, within the overdensity range which spans the values  $0.1 \lesssim 1 + \delta \lesssim 200$ , and the results are shown in Table 4.3. All the slopes evaluated for the *red galaxy* sample are quite shallow, always being below a value of  $S_\delta \approx 0.04$ , with a hint of steepening with increasing mass. In the *ETG* sample, which is 50% smaller, the slopes are rather consistent with being flat.

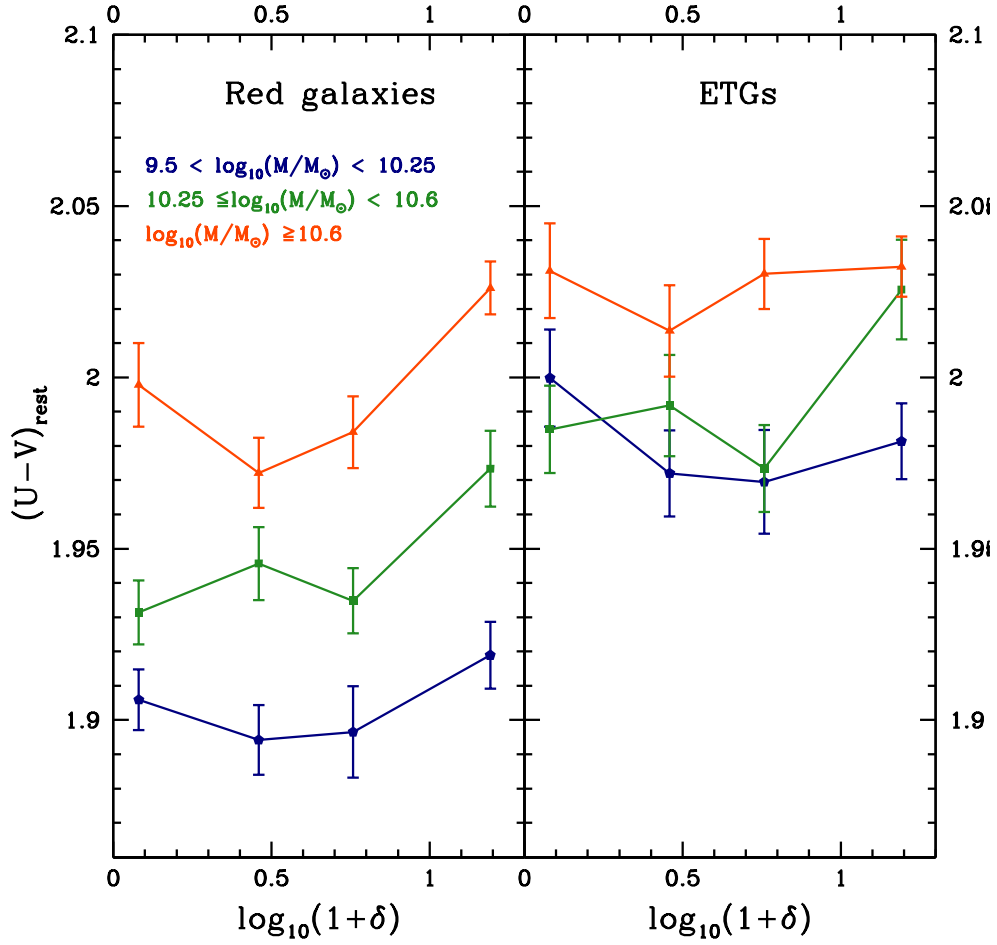


Figure 4.5: Mean color of Red galaxies and ETGs as a function of environment in different mass bins. In the x-axis, the quartile of overdensity are plotted, from the lowest (1) to the highest (4) value as shown in Table 4.1.

	Red galaxies	ETGs
low mass	$0.012 \pm 0.006$	$-0.011 \pm 0.008$
medium mass	$0.031 \pm 0.006$	$0.028 \pm 0.008$
high mass	$0.039 \pm 0.006$	$0.007 \pm 0.007$

Table 4.3: Slopes  $S_\delta$  of the color-environment relation  $(U-V)_{rest} \propto S_\delta \cdot \log_{10}(1+\delta)$  in different mass bins for Red galaxies and ETGs.

### 4.2.3 Color-mass relation

To study the color-mass relation of early-type galaxies, the mean of the color distribution as a function of mass has been computed in the four quartiles of environment. Figure 4.6 presents our results. From these plots, it is possible to see that for the sample of *Red galaxies* there is a mean reddening of  $\langle \Delta(U - V)_{rest} \rangle = 0.093 \pm 0.007$  mag between the lowest ( $9.5 < \log_{10}(M/M_{\odot}) < 10.25$ ) and highest masses ( $\log_{10}(M/M_{\odot}) > 10.6$ ), while for the *ETGs* the difference is smaller ( $\langle \Delta(U - V)_{rest} \rangle = 0.047 \pm 0.009$ ). Furthermore, in Fig. 4.6 the mean of the color distribution shown in black, evaluated for the whole sample, shows that the slopes of the relation are similar in different environments.

The slopes  $S_M$  of the relation  $(U - V)_{rest} \propto S_M \cdot \log_{10}(M/M_{\odot})$  found in the mass range of both samples, with mean values in the range  $10 < \log_{10}(M/M_{\odot}) < 10.8$ , are reported in Table 4.4. The values of the slopes confirm a rather strong dependence of the color on mass, presenting also a small steepening with increasing environment. The mean value of the slope is  $\langle S_M \rangle = 0.126 \pm 0.005$  for the *red galaxy* sample. The slopes found for the *ETG* sample are a little shallower ( $\langle S_M \rangle = 0.066 \pm 0.007$ ), mainly due to fact that the stricter color selection applied to obtain the *ETGs* sample reduces the range of variation in the  $(U - V)_{rest}$  color.

In the present study, no correction of the colors for redshift evolution has been taken into account. To verify that the results are not biased by this effect, *Red galaxies* have been studied, since they are the most numerous sample, dividing them into four redshift bins,  $0.1 < z < 0.35$ ,  $0.35 < z < 0.5$ ,  $0.5 < z < 0.7$ , and  $0.7 < z < 1$ ; in each bin are then evaluated equally populated tertiles of mass, and studied the slope of the resulting color-mass relation in the respective redshift bin. The result is shown in Fig. 4.7: the open squares represent the slope of the relation in each redshift range with its error, while the red shaded area represents the global slope found in the same environment when no division of the sample into redshift bins is applied. In seven out of eight bins, the slope is consistent, at  $1\sigma$  level, with the one evaluated over the entire range of redshift, showing only a hint of steepening in the last redshift bin (see also Table 4.5).

These results confirm those of Balogh et al. (2004) for the nearby Universe. They analyzed the SDSS-DR1 survey, finding a strong dependence of  $(u - r)_{rest}$  color on luminosity with a difference of  $\approx 0.25$  mag between the ranges  $-23 < M_r < -22$  and  $-19 < M_r < -18$ , with a corresponding slope  $\approx 0.15$ . Their dependence on environment is much smaller,  $\sim 0.03 - 0.06$  for a projected local density in the range  $0.1 - 10$ , which corresponds to a slope  $\sim 0.015 - 0.03$  that closely agrees with the results of this analysis. Cooper et al. (2010) analyzed the  $(U - B)_{rest}$  color searching for a dependence on environment for galaxies from the DEEP2 sample, in the mass range  $10.6 < \log_{10}(M/M_{\odot}) < 11.1$  and the redshift range  $0.75 < z < 0.95$ . They found that galaxies residing in high density environments have slightly redder colors than galaxies in low density environments;

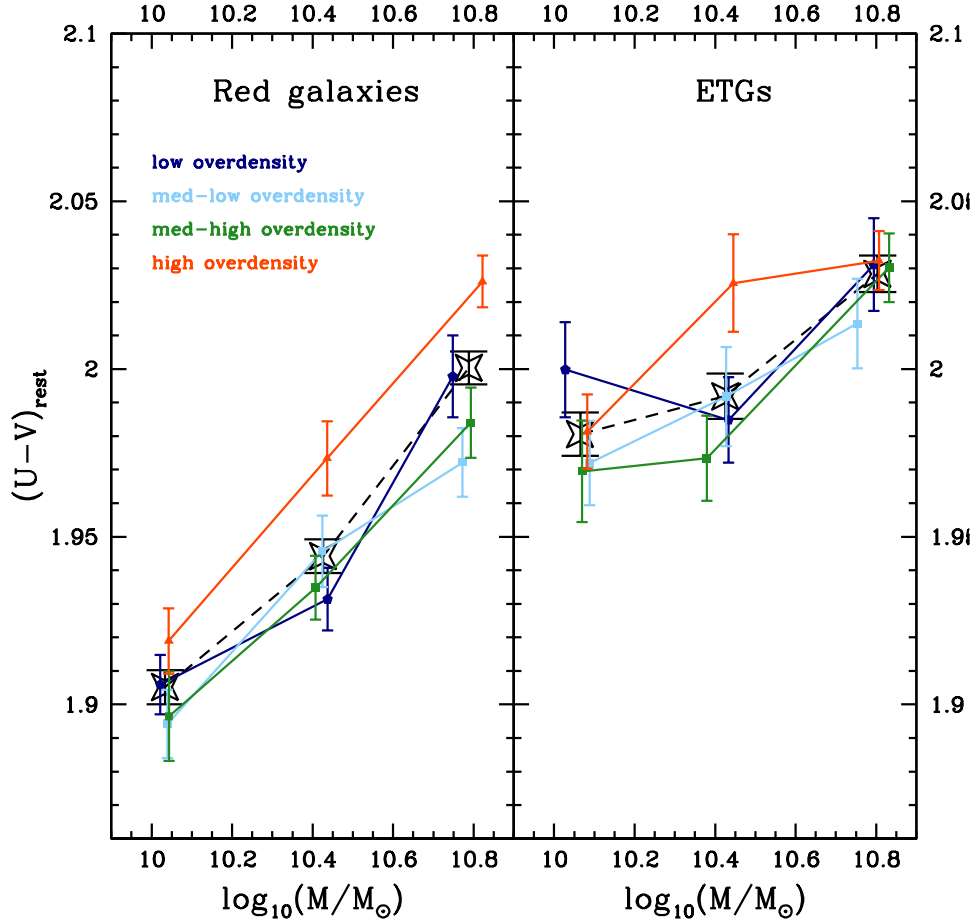


Figure 4.6: Mean color of Red galaxies and ETGs as a function of mass in the four quartiles of environment. Black stars connected with dashed lines show the mean colors for the entire Red galaxies and ETG sample, not divided into quartiles of environment.

	<i>Red galaxies</i>	<i>ETGs</i>
low env	$0.11 \pm 0.01$	$0.04 \pm 0.01$
med low env	$0.11 \pm 0.01$	$0.06 \pm 0.02$
med high env	$0.12 \pm 0.01$	$0.09 \pm 0.01$
high env	$0.14 \pm 0.01$	$0.07 \pm 0.01$
all env	$0.126 \pm 0.005$	$0.066 \pm 0.007$

Table 4.4: Slopes  $S_M$  of the color-mass relation  $(U - V)_{rest} \propto S_M \cdot \log_{10}(M/M_{\odot})$  in different environment bins for Red galaxies and ETGs samples.

however, here it is demonstrated that the dependence on the mass is much stronger.

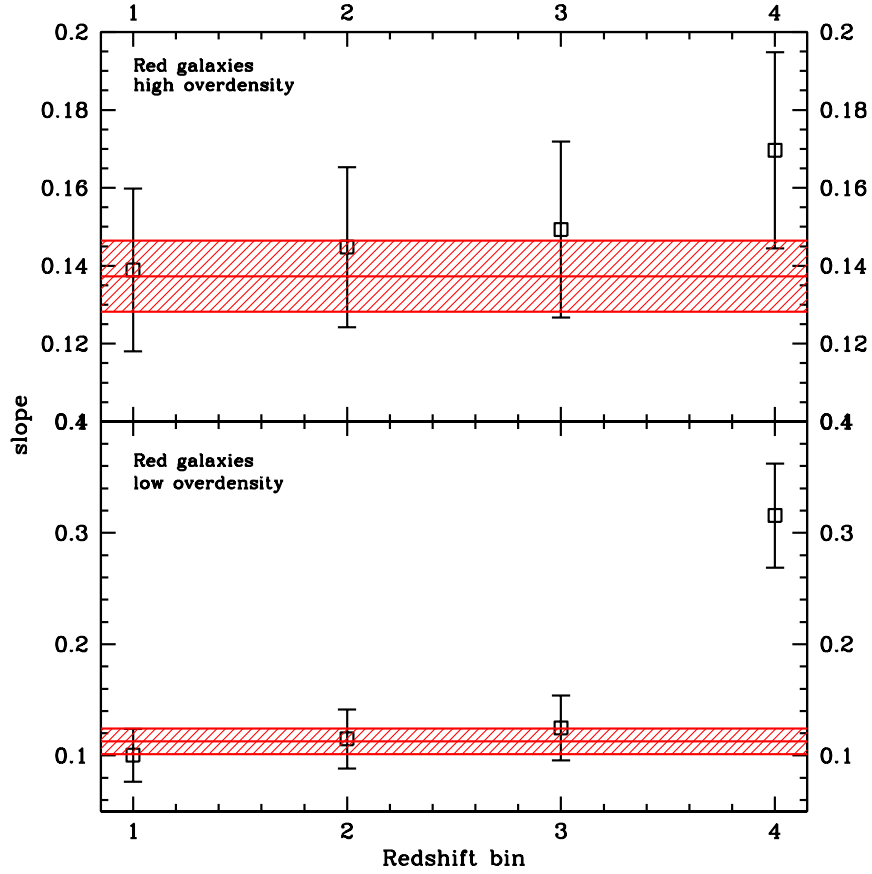


Figure 4.7: Slopes of the color-mass relation evaluated in the four redshift bins and different environments. The red lines represent the slope of the color-mass relation evaluated for the entire redshift sample in the corresponding overdensity bin.

	low env	high env
$z < 0.35$	$0.10 \pm 0.02$	$0.14 \pm 0.02$
$0.35 < z < 0.5$	$0.11 \pm 0.03$	$0.14 \pm 0.02$
$0.5 < z < 0.7$	$0.12 \pm 0.03$	$0.15 \pm 0.02$
$z > 0.7$	$0.32 \pm 0.05$	$0.17 \pm 0.03$

Table 4.5: Slopes  $S_M$  of the color-mass relation for Red galaxies in high and low environment and in given redshift bin.

### 4.3 The spectroscopic analysis

The  $D4000$  and the  $EW_0(H\delta)$  have been measured for the  $ETG$  samples by analyzing the mean of the values of the spectral measurements evaluated in each galaxy spectrum, and averaging in fixed redshift, mass, and environment bins, as explained in Sect. 4.1.4.

The results of the analysis of  $D4000$  as a function of redshift are shown in Fig. 4.8. In the upper panel, the environment quartiles are kept fixed and has been studied the dependence on mass, while in the second panel it has been studied instead the dependence on environment at fixed mass. In all the mass and overdensity bins, a redshift evolution in  $D4000$  has been detected, with the galaxies at low redshift always having a higher break value than at high redshift. This is a signature that higher redshift galaxy populations are statistically younger and/or have a higher metallicity. In searching for any mass dependence, massive galaxies have been found to exhibit a stronger  $D4000$  break in all environments. The effect of environment is smaller, showing a trend in which galaxies residing in high overdensity regions have, for all mass bins, a greater  $D4000$  value than galaxies in the lowest environment quartile. To study the influence of the mass and overdensity, the differences of  $D4000$  and  $EW_0(H\delta)$  have been evaluated between the extreme quartiles of mass and environment, along with their significance. The black points in the lower panels of each figure in Fig. 4.8 show the difference in  $D4000$  between high and low mass or environment regimes. To derive a mean value for each mass and environment regime, the differences found in each redshift bin have been averaged using their errors as weights; the red shaded area in Fig. 4.8 represents the mean difference integrated as a function of redshift. The significance has been defined to be the distance of this integrated difference of  $D4000$  between extreme quartiles of mass and environments in units of  $\sigma$ , where  $\sigma$  is the error in the integrated difference. Table 4.6 shows that the results are in agreement with those found in the color analysis: the dependence on mass is strong, with a mean

	low env	med-l env	med-h env	high env
$\langle \Delta D4000 \rangle_{mass}$	0.13	0.11	0.07	0.11
$\# \sigma$	3.8	3.5	2	3.7
	low mass	med mass	high mass	
$\langle \Delta D4000 \rangle_{env}$	0.06	0.04	0.05	
$\# \sigma$	1.8	1.5	1.5	

Table 4.6: Differences between  $D4000$  for galaxies of high and low mass in a given environment (upper table) and galaxies in high and low density environment quartiles at fixed mass (lower table), and their respective significances.

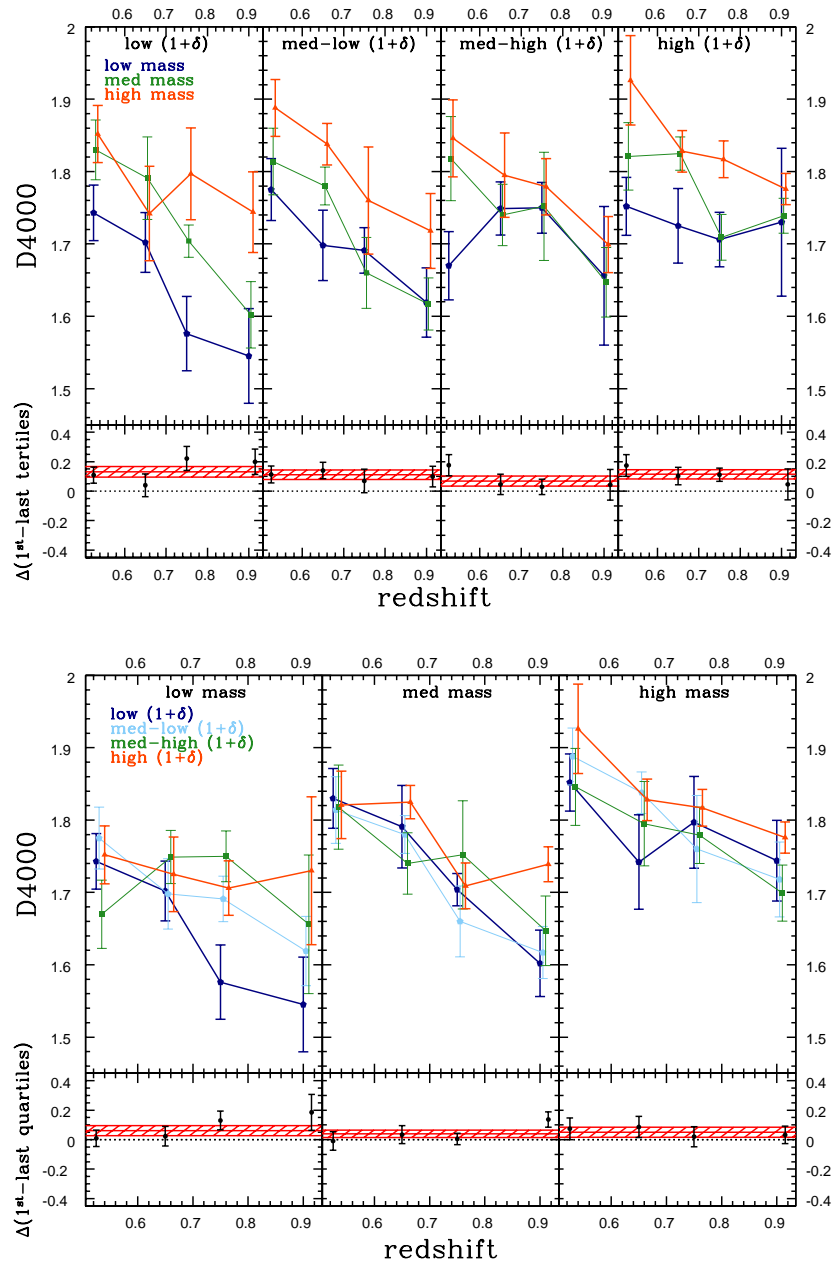


Figure 4.8:  $D_{4000}$  narrow evaluated for different mass bins in fixed environment quartiles (upper panels) and for different overdensity quartiles in fixed mass bins (lower panels). At the bottom of each panel, are also plotted the differences between  $D_{4000}$  in extreme mass/overdensity ranges, the red shaded area representing the weighted mean of these differences averaged over the redshift range (see Table 4.6).

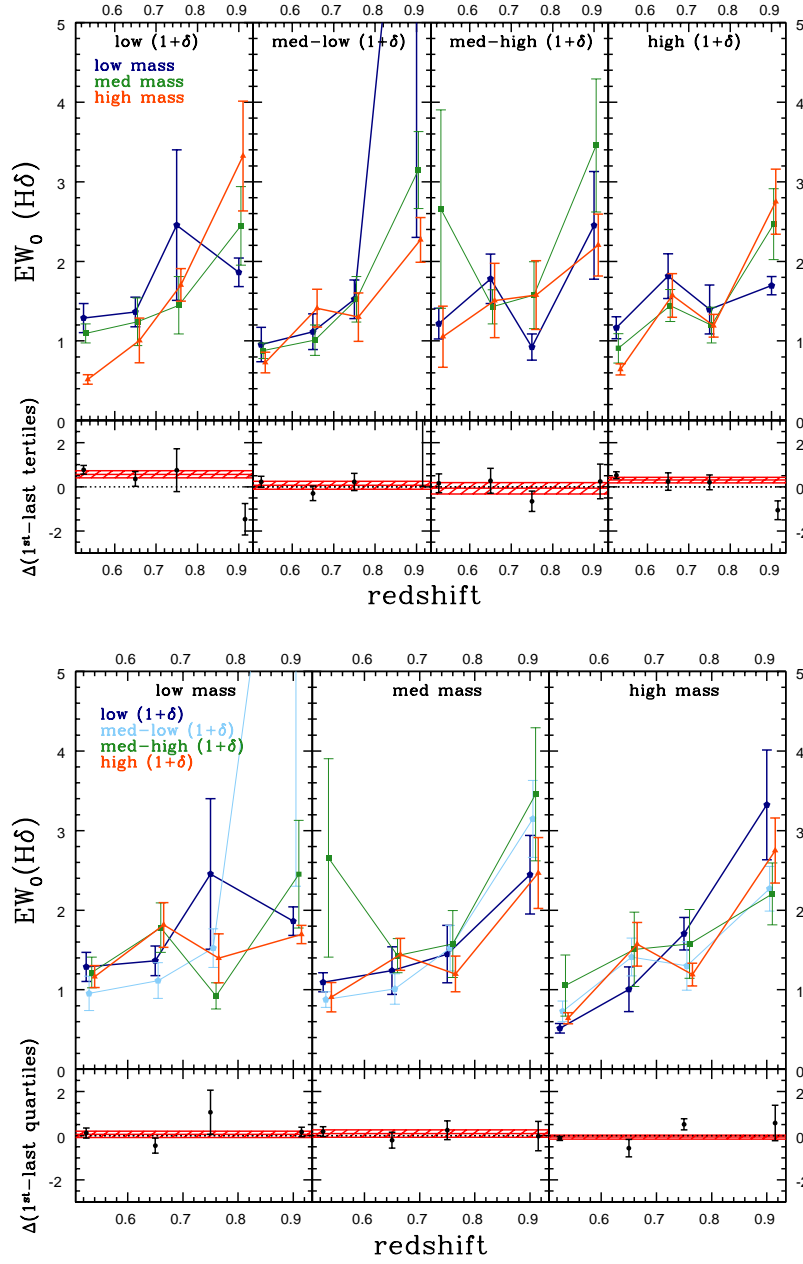


Figure 4.9:  $EW_0(H\delta)$  evaluated for different mass bins in fixed environment quartiles (upper panels) and for different environment quartiles in fixed mass bins (lower panels). At the bottom of each panel, are also plotted the differences between  $EW_0(H\delta)$  in extreme mass/overdensity ranges, the red shaded area being the weighted mean of these differences averaged over the redshift range (see Table 4.7).

$\langle \Delta D4000 \rangle = 0.11 \pm 0.02$  in a mass range  $10.2 \lesssim \log_{10}(M/M_{\odot}) \lesssim 10.8$  and a significance over  $3\sigma$  level (except for one overdensity bin), while the dependence on environment is weaker, with a mean  $\langle \Delta D4000 \rangle = 0.05 \pm 0.02$  and much lower significances.

The mass incompleteness is not a problem in the spectral analysis. Since it has been decided to divide the sample with a fixed mass cut as a function of redshift, the effect is a slight shift in the median value of mass at all redshifts in each mass bin, so that, for example, the median mass of low-mass galaxies change from  $\log_{10}(M/M_{\odot}) = 10.1$  to  $\log_{10}(M/M_{\odot}) = 10.25$  with increasing redshift. This shift in mass would have to be taken into account if one were trying to precisely establish the redshift evolution of D4000 at fixed mass. However, in this analysis the only interest is in identifying the main parameter relating mass to environment, so this shift should not affect our results. Moreover, even by correcting for it considering the relative lack of massive galaxies at low redshift and of less massive ones at high redshift, would at most increase the range of mass explored in the different redshift bins.

A similar consideration has to be made for the metallicity. As pointed out before, the D4000 index depends on both the age and metallicity of a galaxy. Over the mass range probed here, it is expected to find a metallicity range of  $-0.1 < \log_{10}(Z/Z_{\odot}) < 0.1$  (Gallazzi et al., 2006, assuming modest metallicity evolution to  $z \sim 0.5$ ); this corresponds to a variation in D4000 of approximately  $\pm 0.1$  for the models of Bruzual & Charlot (2003) at very old ages and  $\pm 0.06$  at ages of 5 Gyr, which is similar to the change detected. Hence, on the basis of these data, it is impossible to distinguish whether this change is due to a variation in either age or metallicity or both. Our sole interest here is not to differentiate the effect of mass from those of metallicity in producing the trends found, but to determine whether the difference in D4000 is, at each redshift, far more significant when I divide our sample into mass bins, or into environment bins. For the present

	low env	med-low env	med-high env	high env
$\langle \Delta H\delta \rangle_{mass}$	0.56	0.07	-0.06	0.31
$\# \sigma$	3.5	0.4	0.2	2.4
	low mass	med mass	high mass	
$\langle \Delta H\delta \rangle_{env}$	0.06	0.10	-0.06	
$\# \sigma$	0.4	0.6	0.8	

Table 4.7: Differences (in  $\text{\AA}$ ) between  $EW_0(H\delta)$  for galaxies of high and low mass in a given environment (upper table) and galaxies in high and low environment quartiles at fixed mass (lower table), and the relative significances.

analysis, our inability to differentiate between age and metallicity is therefore not a problem.

The results of the  $EW_0(H\delta)$  analysis are a bit noisier, as shown in Fig. 4.9 and Table 4.7. However, the trends found agree with the results of both the colors and D4000 analysis: the differences with mass ( $\langle\Delta EW(H\delta)\rangle = 0.28 \pm 0.08 \text{ \AA}$ ) have on average higher significance than the difference with environment ( $> 2\sigma$  in two bins over four), being these second ones not significant in every bin considered ( $\langle\Delta EW(H\delta)\rangle = 0.01 \pm 0.06 \text{ \AA}$ ).

In contrast to D4000,  $EW_0(H\delta)$  increases with redshift and decreases with increasing mass and environmental density. Moreover, very massive galaxies or galaxies residing in high density environments have an almost constant  $EW_0(H\delta)$  throughout the entire redshift range, of a value that indicates in these galaxies no recent episode of star formation has occurred within a timescale of  $\approx 5$  Gyrs.

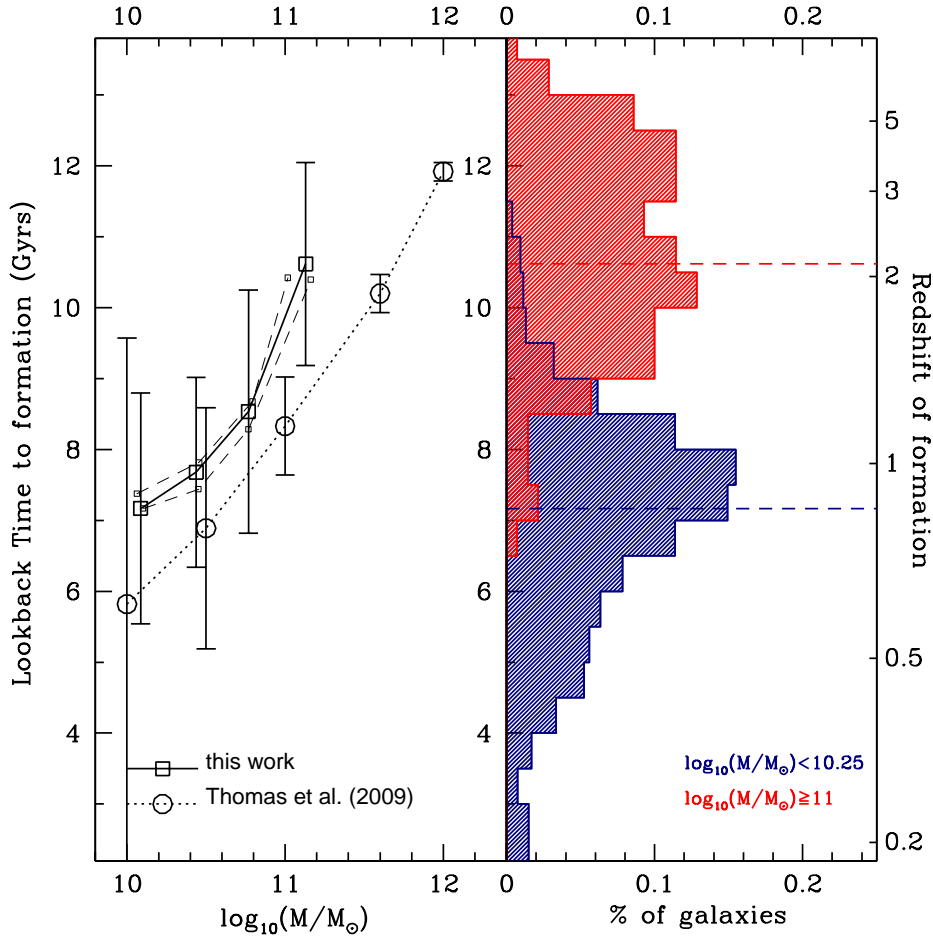


Figure 4.10: *Stellar mass as a function of lookback time to formation (left panel) and mass histograms of extreme tertiles for ETGs, evaluated with CB07 models. Squared symbols represent our data, where the errorbars plotted are the dispersions in the measurements. Circle points are data taken from the analysis of SDSS-DR4 by Thomas et al. (2010), showing the lookback time at which the 50% of the stellar mass has formed; the errorbars plotted are the differences between the lookback time of formation of 50% and of 80% of the stellar mass. The dashed lines represent the mass-lookback time relation computed in the extreme quartiles of overdensity. To compare data, here the following parameters have been adopted:  $\Omega_m = 0.24$ ,  $\Omega_\Lambda = 0.76$ , and  $H_0 = 73 \text{ km s}^{-1} \text{ Mpc}^{-1}$ .*

## 4.4 Evidences of mass downsizing

The analysis of ETGs shows clear indications of mass-downsizing, i.e. massive galaxies contain an older stellar population. The formation redshift of *ETGs* has been evaluated by performing a best fit to the SED of these galaxies using a library of models with exponentially decreasing star-formation histories, with  $\tau < 1$  Gyrs, and high age/ $\tau$  values have been found, compatible with passive galaxies. To check the robustness of the results, also different stellar population synthesis models have been considered, such as the BC03 models (Bruzual & Charlot, 2003) and the more recent ones M05 (Maraston, 2005) and CB07 (Charlot & Bruzual, 2011). In Fig. 4.10 is shown the lookback time to formation as a function of mass for *ETGs*, evaluated using CB07 models; both the histogram and the plot show that massive galaxies ( $\log_{10}(M/M_{\odot}) \sim 11$ ) formed their stars at  $z \sim 2$ , while less massive ones ( $\log_{10}(M/M_{\odot}) \sim 10.25$ ) at  $z \lesssim 1$ . The corresponding mean age difference between the extreme mass quartiles is  $\approx 3$  Gyrs, while the age difference between different

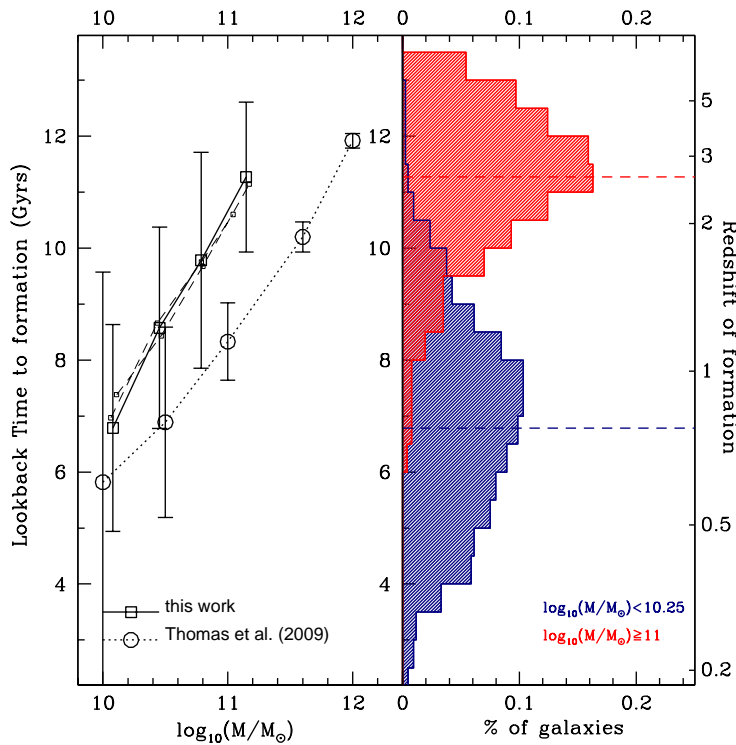


Figure 4.11: *Stellar mass as a function of lookback time to formation (left panel) and mass histograms of extreme tertiles for ETGs, evaluated with M05 models. The meaning of the symbols and the assumptions are the same as in Fig. 4.10.*

environments is insignificant ( $\lesssim 0.2$  Gyrs). In Fig. 4.10, also the relation between mass and lookback time for the two extreme overdensity quartiles (dashed lines) has been plotted, showing that galaxy formation age at fixed mass is not strongly dependent on environment.

The results from different models differ slightly, but the general picture is clear and any differences are within the  $1\sigma$  errors. In Fig. 4.11 it is possible to see the same plot shown in Fig. 4.10, but evaluated using M05 models; in Fig. 4.12 are shown, as a comparison, the differences between the relation obtained with CB07 and BC03 models.

This result agrees with Thomas et al. (2010), which was based on an analysis of SDSS-DR4 early-type galaxies. As in this analysis, they found that their scaling relations had no strong on environment, but provided support for a downsizing in formation age with mass. For a comparison, in Fig. 4.10 is overplotted their relation, where the points represent the lookback time at which the 50% of the stellar mass has formed and the errorbars are the differences between the lookback time of formation for 50% and 80% of the stellar mass. An interesting hint of downsizing can be inferred from the analysis of D4000 as a function of redshift. As can be seen in Fig. 4.8, more massive galaxies at each redshift have an higher D4000 value than to less massive galaxies. However, given the magnitude of the errors in D4000, and the inability to clearly distinguish the effect of metallicity on D4000, this can provide only a confirmation of the analysis performed on the ages of ETGs.

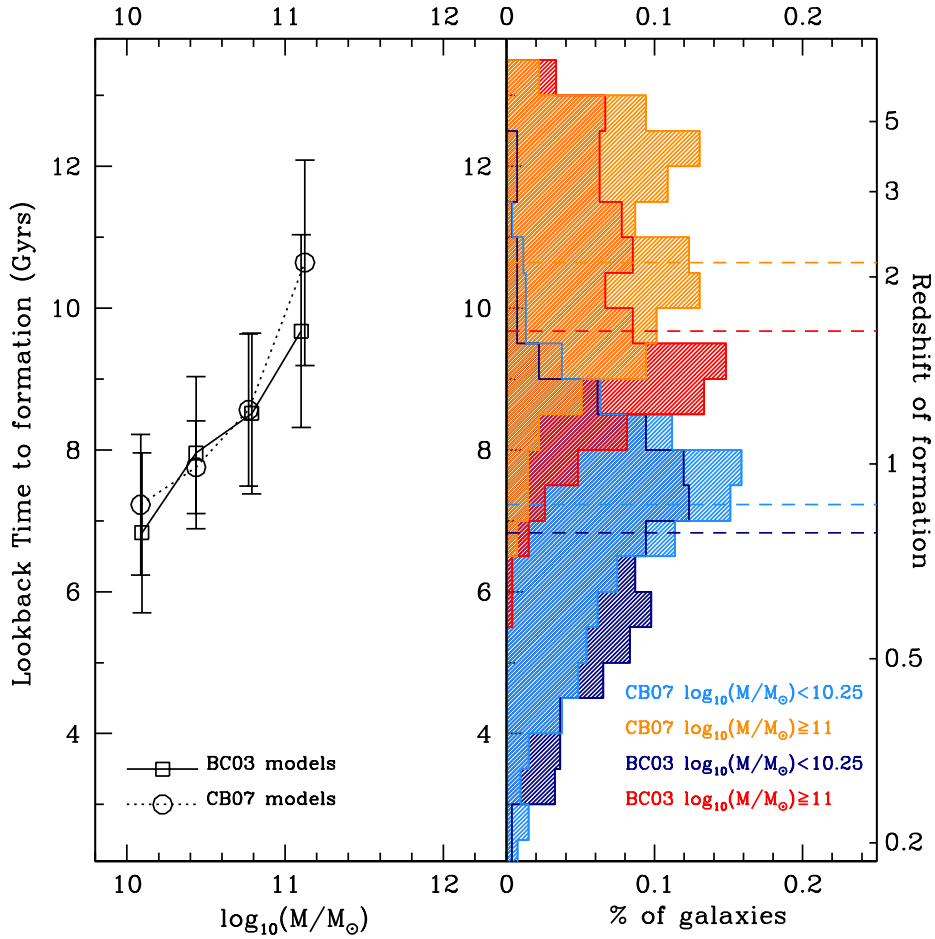


Figure 4.12: Comparison of the lookback time to formation-mass relations found with CB07 and BC03 models. In this plot, the following parameters have been adopted:  $\Omega_m = 0.24$ ,  $\Omega_\Lambda = 0.76$ , and  $H_0 = 73 \text{ km s}^{-1} \text{ Mpc}^{-1}$ .

## 4.5 Conclusions about mass and environment dependence of ETGs

The  $(U - V)$  colors and spectra of two subsamples of early-type galaxies have been studied, extracted from the zCOSMOS spectroscopic survey in the redshift range  $0.1 < z < 1$  as described in Sect. 3.3. Both color and spectral features (i.e., D4000 and  $EW_0(H\delta)$ ) have been analyzed to explore their dependence on mass and environment and provide some insights into the main drivers of galaxy evolution.

From the analysis of the  $(U - V)_{rest}$  color, it has been found:

- a dependence on mass ( $\langle \Delta(U - V)_{rest} \rangle = 0.093 \pm 0.007$  mag in the mass range  $10 < \log_{10}(M/M_\odot) < 10.8$ );
- a weaker dependence on the local density of the environment ( $\langle \Delta(U - V)_{rest} \rangle = 0.027 \pm 0.008$  mag in the overdensity range  $0.1 \lesssim \log_{10}(1 + \delta) \lesssim 1.2$ );

The mean slope of the color-mass relation is  $\langle S_M \rangle = 0.12 \pm 0.005$ , with a hint of steepening as a function of increasing environment. The color-environment relation is much flatter, with a slope that is always smaller than  $S_\delta \approx 0.04$ , confirming evidence that the dependence of galaxy properties on mass is much stronger than on environment. From the analysis of both samples, the results obtained are in complete agreement. The study of *ETG* sample, carefully selected to be less contaminated by outliers, enhances the reliability of the conclusions.

Many previous efforts have been made to differentiate between the effects of mass and environment in studying the colors of ETGs. The results found agree with Balogh et al. (2004), who found by analyzing the SDSS-DR1 survey, a strong dependence of ETG color on luminosity (measuring a difference of  $\approx 0.25$  mag between the ranges  $-23 < M_r < -22$  and  $-19 < M_r < -18$ , in the  $(u - r)_{rest}$  color) and a much smaller dependence on environment ( $\lesssim 0.1$  for a projected local density in the range  $0.1 - 10$ ). I effectively extend these results to  $z \sim 1$ . For the color-environment relation, Cooper et al. (2010) found a similar trend by analyzing galaxies observed by the DEEP2 survey in the mass range  $10.6 < \log_{10}(M/M_\odot) < 11.1$  and in the redshift range  $0.75 < z < 0.95$ . The results of this analysis agrees with their findings that at fixed mass the  $(U - B)_{rest}$  color in high density environments is slightly redder than in low density environments.

From the spectral analysis, it has been found:

- a dependence of spectroscopic index on mass ( $\langle \Delta D4000 \rangle = 0.11 \pm 0.02$  and  $\Delta EW_0(H\delta) = 0.28 \pm 0.08 \text{ \AA}$  in the mass range  $10.2 < \log_{10}(M/M_\odot) < 10.8$ ) when averaging over the entire redshift range;

- a weaker dependence on the local density of the environment ( $\langle \Delta D4000 \rangle = 0.05 \pm 0.02$  and an insignificant difference for  $EW_0(H\delta)$  in the environment range  $0.1 \lesssim \log_{10}(1+\delta) \lesssim 1.2$ ) when averaging over the entire redshift range.

Massive galaxies or galaxies residing in relatively high density environments have a stronger D4000 break and a small value of  $EW_0(H\delta)$  that is almost constant with redshift, implying that no significant episodes of star formation have occurred in these galaxies since  $z \sim 1$ , while for the low-mass galaxies the evolution remains ongoing at these redshifts. The different amplitude of the redshift evolution in colors and spectral features can be interpreted by comparison with stellar population synthesis models: old, red, passive galaxies (modeled with values of age/ $\tau$  ratio greater than 5) are not expected to have evolved much in color since  $z=1$ , while the evolution in D4000 is a bit clearer.

Combining the results of the color and spectral analysis, from this work can be concluded that the main driver of the the evolution of ETGs is mass, while environment plays a less important although non-negligible role. This result is also confirmed by the analysis of Cucciati et al. (2010); from their study of the  $(U - B)_{rest}$  color of the zCOSMOS bright sample, they suggest a scenario in which the color depends primarily on mass, but for a relatively low-mass regime ( $10.2 \lesssim \log_{10}(M/M_{\odot}) \lesssim 10.7$ ) the local environment modulates this dependence.

The analysis of ETGs also shows clear indications of mass-downsizing: from a SED-fitting analysis, it is possible to see that massive galaxies have older stellar populations, with an age difference of  $\approx 3$  Gyrs within a mass range  $10 < \log_{10}(M/M_{\odot}) < 10.8$ , using passive evolution models with high age/ $\tau$  values. The formation redshift of *ETGs* have been evaluated by performing a best fit to the SED of these galaxies using different stellar population synthesis models. The lookback times evaluated for ETGs provide additional support of a downsizing scenario; from Fig. 4.10 it is possible to see that massive galaxies ( $\log_{10}(M/M_{\odot}) \sim 11$ ) formed their stars at  $z \sim 2$ , while less massive ones ( $\log_{10}(M/M_{\odot}) \sim 10.25$ ) formed their stars at  $z \lesssim 1$ , almost independently of the models of stellar population synthesis considered. These results also agree with Thomas et al. (2010), which were based on an analysis of SDSS early-type galaxies.

Environment appears to have a far smaller influence than mass on galaxy properties studied. The age difference between different environments is insignificant ( $\lesssim 0.2$  Gyrs) and inconsistent with the difference of 2 Gyrs found by Thomas et al. (2005). Other studies found much smaller differences. For example, Bernardi et al. (2006) found differences in the  $Mg_2 - \sigma_V$  relation of galaxies in different environments implying that galaxies in dense environments are at most 1 Gyr older than galaxies in low density environments, Gallazzi et al. (2006) found that ETGs in dense environments are  $\sim 0.02$ -dex older than in the field, and later analysis by Thomas et al. (2007) and Thomas et al. (2010) of SDSS found no dependence of scaling relation on environmental density. Moreover, should be remembered that

the zCOSMOS survey samples a smaller range of overdensities than these previous studies, extending at most to rich groups but not clusters.

An interesting prospect of this work is the study of the evolution of the ages and spectral features of ETGs as a function of redshift, because that analysis would also help to place constraints on cosmological parameters, such as the Hubble constant  $H_0$  and the equation-of-state parameter of Dark Energy  $w$ .

---

# Chapter 5

## Early-type galaxies as cosmological probes

As argued in Chapt. 1, one of the crucial point to set precise constraints about  $H(z)$  and the various cosmological parameters is to analyze different probes, and to combine the results obtained with these techniques to minimize the errorbars. One fundamental step will be certainly to reduce the systematic errors of the “standard” approaches, i.e. Sne, BAO, and WL; and this is exactly the aim of some of the most important surveys planned in the future (e.g. BOSS and Euclid).

On the other hand, it will be crucial also the development of independent probes, that can provide cross-check of results obtained with the standard technique. As suggested by Jimenez & Loeb (2002), an interesting and complementary approach to this problem is the study of the change in the age of the Universe as a function of redshift. The strength of this method is that it avoids the common weakness of the other techniques, i.e. the reliance on integrated quantities to determine the expansion history. However, to fully exploit this approach, it is required to find a population of standard clocks able to trace the evolution of the relative age of the Universe.

Many recent works gave growing observational evidence that the most massive galaxies contain the oldest stellar populations up to redshifts of  $z \sim 1 - 2$  and have less than 1% of their present stellar mass formed at  $z < 1$  (Dunlop et al., 1996; Spinrad et al., 1997; Cowie et al., 1999; Heavens et al., 2004; Thomas et al., 2005; Cimatti et al., 2008; Thomas et al., 2010), and are extensively reviewed in Chapt. 2. This population of massive, red, passive early-type galaxies consists of the oldest objects in the Universe at each redshift. It is therefore possible, as introduced by Jimenez & Loeb (2002), to use ETGs as “*cosmic chronometers*”. The differential ages of these galaxies should thus be a good indicator for the rate of change of the age of the Universe as a function of redshift up to  $z \sim 2$ .

There are some works that try to constrain the cosmic expansion history using this approach (Ferreras et al., 2001; Jimenez et al., 2003; Krauss, 2003; Capozziello et al., 2004; Stern et al., 2010; Crawford et al., 2011). However, a problem of this technique is that it relies on the determination of a non-observable parameter using spectra and/or spectral energy distributions, i.e. the age of the stellar population, which presents strong and well known degeneracies with other parameters that are evaluated simultaneously, such as the metallicity, the star formation history, the dust content (see Sect. 3.6.5).

In this chapter, it is explored the possibility of setting cosmological constraints studying the “*cosmic chronometers*” approach, by analyzing the age-redshift relation for a sample of ETGs in the range  $0 \lesssim z \lesssim 1$ ; the ages are estimated with a SED-fitting technique, and the feasibility of this approach is discussed.

To solve the various problems and degenerations, a new methodology is introduced to determine the expansion history of the Universe analyzing the spectral properties of early-type galaxies (ETG), based on the study of the redshift dependence of the 4000 Å break. The method is described, its robustness explored using theoretical synthetic stellar population models, and it is applied using a SDSS sample of  $\sim 14\,000$  ETGs. The motivation to look for a new technique is to minimize the dependence of the “*cosmic chronometers*” method on systematic errors. In particular, as a test of the method, it is derived an estimate of the Hubble constant which is not only fully compatible with the value derived from the Hubble key project, but also with a comparable error budget. Moreover, a value for the dark energy equation-of-state parameter is obtained (assuming  $w = \text{constant}$ ) that is well in agreement with the latest WMAP analysis. Given the fact that the SDSS ETG sample only reaches  $z \sim 0.3$ , this result shows the potential of the method.

The reference article for this analysis is Moresco et al. (2010b).

## 5.1 The age-redshift relation

The basic idea of Jimenez & Loeb (2002) approach is that a measure of the Hubble parameter  $H(z) = -\frac{1}{1+z}dz/dt$  can place a direct constraint to the expansion history of the Universe, being straightforwardly linked to various cosmological parameters (see Eq. 1.19). Therefore a measure of the relative age evolution of the Universe as a function of redshift (i.e. the slope of the  $t(z)$  relation, Eq. 1.25) can help to set constrain to cosmological parameters in an independent way with respect to other analysis (SNe, BAO, ...). This relative change of age as a function of redshift can be reformulated expressing explicitly its dependence on the cosmological parameters (i.e.  $\Omega_\Lambda$ ,  $\Omega_m$ ,  $H_0$ ,  $w_0$ ,  $w_a$ ); in a flat Universe ( $\Omega_0 = 1$ ) with dominant contributions coming from dark energy and matter, it can be written:

$$\frac{dz}{dt} = -\frac{(1+z)^{5/2}}{H_0} \left\{ \Omega_m + \Omega_{DE} \exp \left[ 3 \int_0^z \frac{w(z')}{1+z'} dz' \right] \right\}^{1/2} \quad (5.1)$$

for  $w = w(z)$  and:

$$\frac{dz}{dt} = -\frac{(1+z)^{5/2}}{H_0} \left\{ \Omega_m + \Omega_{DE}(1+z)^{3w} \right\}^{1/2} \quad (5.2)$$

for  $w = \text{constant}$

In the same way, the age of the Universe at a given redshift depends critically on the cosmological parameters and (assuming with  $w=\text{const}$ ), it is possible to write:

$$t_U(z) = \frac{1}{H_0} \int_0^{\frac{1}{1+z}} y^{1/2} \left\{ \Omega_m + \Omega_{DE} \left[ y^{-3(w_0+w_a)} e^{3w_a(y-1)} \right] \right\}^{-1/2} dy + \text{constant} \quad (5.3)$$

where it has been used the standard parametrization  $w(z) = w_0 + \left(\frac{z}{1+z}\right)w_a$ . For a given galaxy that evolves passively from its formation to the present time, it can be written:

$$t_{gal}(z) = t_U(z) - t(z_{form}) \quad (5.4)$$

where  $z_{form}$  represents the redshift of formation of the galaxy. Fig. 5.1 shows how the theoretical relation expressed by Eq. 5.3 depends on the dark energy equation-of-state parameter  $w$  and on the Hubble constant  $H_0$ .

In order to apply this approach, Jimenez et al. (2003) suggested to consider a sample of early-type galaxies (that has been demonstrated to represent the oldest galaxy population at each redshift), and, among them, to select the oldest systems by considering the upper envelope of the age-redshift distribution. This upper envelope directly traces the age of the Universe, since these galaxies are

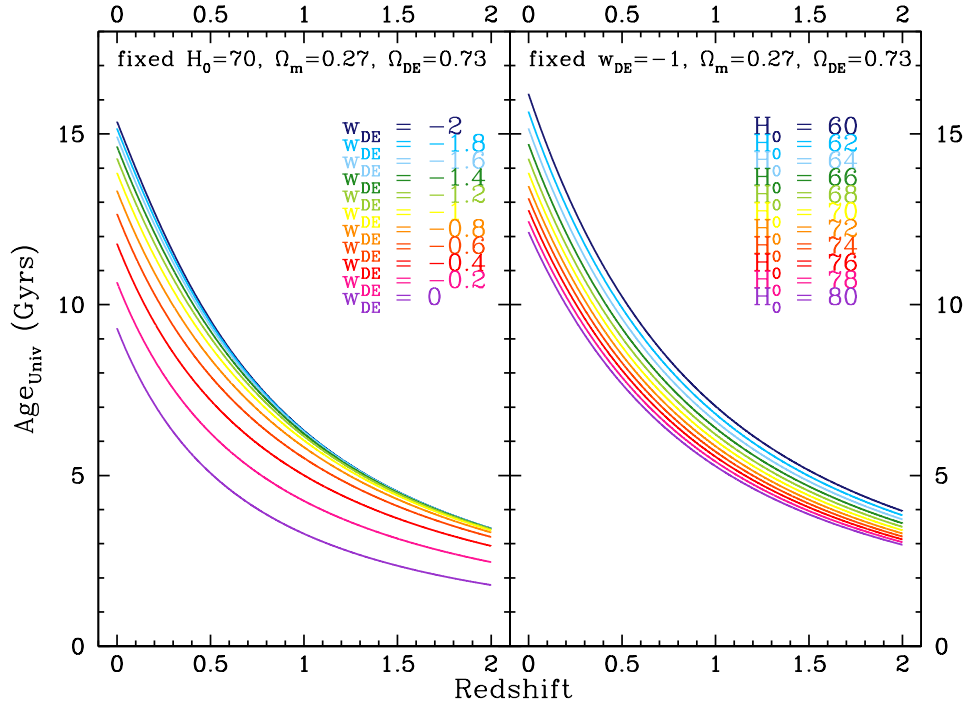


Figure 5.1: *Theoretical age-redshift relations as a function of  $w$  (left plot) and  $H_0$  (right plot).*

supposed to have undergone a passive evolution and to have an extremely uniform redshift of formation.

The main strengths of this approach is that the study of the slope of the age-redshift relation probes directly  $H(z)$ , thus setting constraints on the cosmological parameters, and that it is independent on the overall normalization, that it will be proved to be a fundamental point.

### 5.1.1 Preliminary analysis

Initially, to set constraints on the cosmological parameters the standard procedure explained in Jimenez et al. (2003) was followed. A sample of passive ETGs was selected following the criteria explained in Sect. 3.3, merging the 97,460 ETGs extracted from the SDSS-DR6 sample and the 981 *ETGs* from the zCOSMOS sample. In addition, to sample also the high- $z$  ETGs, also the 13 passive galaxies of the GMASS sample (Cimatti et al., 2008) have been included, covering the range  $1.3 < z < 2$ . The ages of these galaxies have been derived with the SED-fitting technique described in Sect. 3.2.2, considering different stellar population synthesis

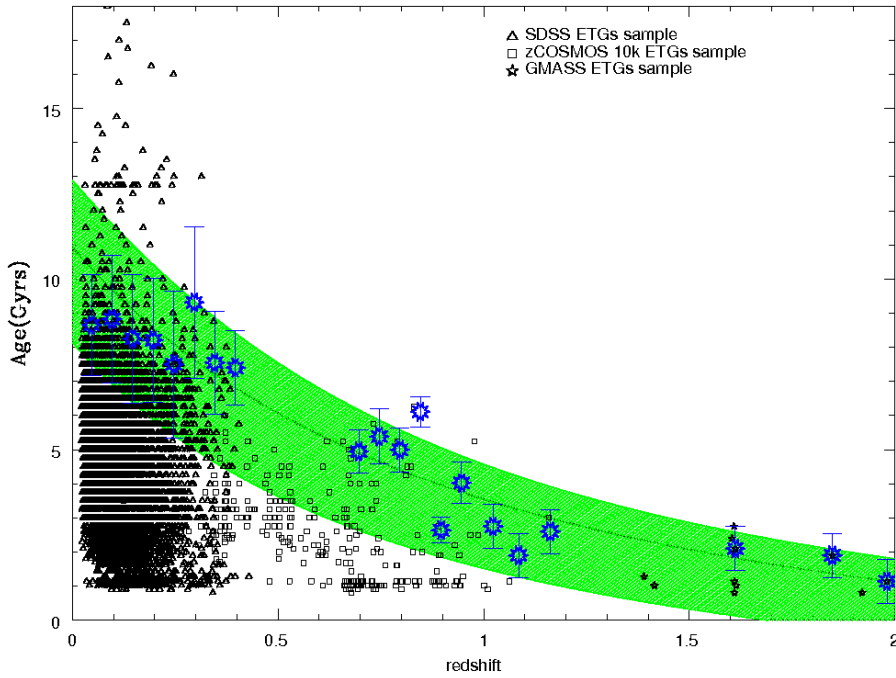


Figure 5.2: Age-redshift relation for a sample of SDSS, zCOSMOS and GMASS ETGs. The black points represent the estimated ages (open triangle for SDSS, open squares for zCOSMOS and open stars for GMASS); the blue points represent the upper envelope of the age-redshift relation, evaluated as the value below which the 95% of the ages lie in a given redshift bin; the green shaded area represent the 68% confidence level best-fit to the upper envelope, where it has been tried to constrain the dark energy equation-of-state parameter  $w$ . The area corresponds to the best-fit value  $w = 0.7^{+0.4}_{-0.6}$ .

models (BC03, CB07, M09), metallicities ( $Z/Z_{\odot} = 0.08, 0.4, 1, 2.5$ ), dust reddening ( $A_V \in [0, 1]$ ), SFHs (delayed exponential, with  $\tau \in [0.05 - 1]$  Gyrs). Figure 5.2 shows the results obtained with CB07 models and fixed solar metallicity. The black points represent the estimated ages (open triangle for SDSS, open squares for zCOSMOS and open stars for GMASS); the blue points represent the upper envelope of the age-redshift relation, evaluated as the value below which lies the 95% of the ages in a given redshift bin; the green shaded area represent the 68% confidence level best-fit to the upper envelope, where it has been tried to constrain the dark energy equation-of-state parameter  $w$ . The area corresponds to the best-fit value  $w = 0.7^{+0.4}_{-0.6}$ .

On the one hand, this approach seems promising, since it directly gives evi-

dences of the age-evolution of the Universe as a function of redshift, as suggests the evolution of the upper envelope of the distribution. On the other hand, many difficulties have been encountered in pursuing this direct approach:

- the dependence on assumed models is strong: changing between BC03, CB07, and M09, the shapes of the age- $z$  relations differ significantly, being steeper or flatter depending on which model has been considered (see also Sect. 3.6.4);
- the dependence on chosen SFHs is also a problem: as discussed in Sect. 3.6.5, a direct correlation between chosen  $\tau$  values and retrieved ages has been found, for which the choice of a particular range of  $\tau$  influences directly the range of ages estimated;
- the metallicity has to be taken into account: in Fig. 5.2 the metallicity has been fixed to the solar value, however it has been found that this assumption is not valid in the entire redshift range. Since the shape of the SED of a galaxy depends both on age and metallicity, this strong assumption has to be relaxed, allowing also different metallicity in the fit. However, as discussed in Sect. 3.6.5, there exists a severe degeneracy between age and metallicity that has been proven not to be breakable just analyzing the SEDs of galaxies;

All the issues described above affect directly the shape and the slope of the age- $z$  relation, and hence represent a problem for the cosmological parameters constrain.

In addition to “real” ETGs, also a study on a mock catalog has been performed: 100,000 galaxies have been generated with random SFHs ( $\tau \in [0.05 - 3]$  Gyrs), dust reddening ( $A_V \in [0, 1]$ ), ages ( $t \in [0, 20]$  Gyrs, but  $t(z) < T_U(z)$ ) and solar metallicity. The choice of this grid is due to the decision of creating a simulated catalog of ETGs. Apparent magnitudes have been assigned to the zCOSMOS bands following prescriptions to represent the same magnitude limits of zCOSMOS observations. This catalog has been, afterward, analyzed as a real catalog, selecting galaxies with photometric type  $< 1.4$  to reproduce the selection of the red and passive objects done for the *ETGs* sample. At the end, a SED-fitting analysis has been performed to this subsample of galaxies, using the same range of values adopted for the real zCOSMOS *ETGs* sample (see Sect. 3.6). Retrieved ages have been then compared with the “real”, theoretical ones. This test represents, from a certain point of view, a  $0^{th}$  order check, analyzing the precision of the age estimate between the same input and output models.

It has been found that the median difference ( $\text{age}_{\text{fit}} - \text{age}_{\text{mod}}$ ) is small for young galaxies ( $\sim 0$  for galaxies with age  $< 4$  Gyrs) but becomes significant (up to 1 Gyrs) for older galaxies, representing an offset of about  $\sim 10\%$ . Moreover, analyzing the scatter of the ( $\text{age}_{\text{fit}} - \text{age}_{\text{mod}}$ ) distribution, it has been found that is around 1 Gyrs for galaxies with  $5 \lesssim \text{age} \lesssim 10$ , but goes up to 3 Gyrs for galaxies with

$10 \lesssim \text{age} \lesssim 13$ . On average, even at fixed solar metallicity, the percentage error found in this  $0^{\text{th}}$  order analysis is of the order of 17%, that is significant especially because this result does not yet take into account also the uncertainties due to model and metallicity degeneracies.

This check demonstrates that, in addition to the open problems raised before, the intrinsic error in evaluating the age with SED-fitting is large.

In collaboration with Jacopo Chevallard (Jacopo Chevallard, master Thesis), it has also been explored in the zCOSMOS sample the possibility of a combined fit, merging to the photometric bands the informations available from the spectra. However this combined fit yields only to a reduction of the age dispersion of about 10%, this still not considering models and metallicity dependences.

Another common approach in the literature to constrain age and metallicity of a galaxy is the study of the various emission and absorption lines in the spectra, since their differential sensitivity to age and metallicity can help to break their degeneracy (e.g., see Gallazzi et al., 2005; Carson et al., 2010; Thomas et al., 2011). However, this approach requires both high-resolution spectra and high S/N ratios, both to identifying the spectral features and measure them precisely. This two requirements are not always available, and this is even more difficult for high- or intermediate redshift surveys; certainly zCOSMOS spectra do not allow such a study. However it is evident that the analysis of ages of galaxies obtained from the spectra can be much more precise than the one performed with the SED-fitting.

In collaboration with Raul Jimenez (University of Barcellona), it has been therefore developed a new methodology, that aims to use the “*cosmic chronometers*” approach but minimizing the model dependences and degeneracy. Following the idea of using information from galaxy spectra, it has been decided to analyze the possibility of using the D4000 as a proxy of galaxy age. The advantage of this spectral feature is that it does not require neither an extremely high S/N ratio nor resolution to be measured. In the following sections this new technique is describe, analyzed, and used to set constraints on the Hubble constant  $H_0$  and on the dark energy equation-of-state parameter  $w$ .

## 5.2 The data sample

This analysis has been carried out using the SDSS ETGs sample described in Sect. 3.3. The starting sample has been selected matching a photometric and a spectroscopic criterion (i.e. red galaxies without prominent emission lines), and consists of 97 460 galaxies. For each galaxy, the 4000 Å break has been taken from the MPA-JHU DR7 release of spectrum measurements (<http://www.mpa-garching.mpg.de/SDSS/DR7/>), which provides a complete emission line analysis for the SDSS Data Release 7 (DR7). The adopted D4000 definition is the one proposed by Balogh et al. (1999), that uses narrower bands in order to be less sensitive to reddening effects (3850-3950 Å and 4000-4100 Å); this index will be hereafter denoted as  $D4000_n$ :

$$D4000_n = \frac{F_{red}}{F_{blue}} = \frac{(\lambda_2^{blue} - \lambda_1^{blue}) \int_{\lambda_1^{red}}^{\lambda_2^{red}} F_\nu d\lambda}{(\lambda_2^{red} - \lambda_1^{red}) \int_{\lambda_1^{blue}}^{\lambda_2^{blue}} F_\nu d\lambda} \quad (5.5)$$

In Fig. 5.3 is plotted the average stacked spectrum of 10 random galaxies, selected to be in the highest tail of the  $D4000_n$  distribution ( $D4000_n > 2.1$ ) and for which the  $D4000_n$  has been measured with high accuracy ( $S/N \sim 70$ ). The dispersion of the  $D4000_n$  of the galaxies used for creating the stacked spectrum is  $< 0.01$ . In the figure are shown also the ranges used to evaluate the  $D4000_n$  and the mean fluxes in the corresponding regions.

As pointed out by Bernardi et al. (2006), the spectrophotometric calibration of the SDSS spectra is less reliable around 4000 Å, due to the throughput of the spectrometer. This means that the value of the  $D4000_n$  can be affected by this problem for galaxies in the lowest redshift range (Bernardi, private communication). In order to avoid this potential source of uncertainty, the final sample has been selected to have  $z > 0.15$ . Moreover, since the number of galaxies decreases very rapidly at  $z > 0.3$ , galaxies beyond  $z=0.3$  have been excluded. Thus, the final redshift range of the sample is  $0.15 < z < 0.3$ .

As explained in the forthcoming section, the metallicity estimate for these galaxies has been taken from the SDSS-DR4 analysis performed by Gallazzi et al. (2005). After the match between the sample described before and the galaxies for which the metallicity estimate is publicly available, the final sample consists of 13,987 galaxies, for each one having a wide photometry coverage (u to K), spectroscopic redshift, spectral index measures ( $D4000_n$ ,  $EW_0(H\alpha)$  and  $EW_0([OIII]\lambda3727)$ ), metallicity and mass estimates.

### 5.2.1 Metallicity, mass and star formation history estimation

To study the properties of this sample of ETGs, both photometric and spectroscopic informations have been taken into account. To retrieve information about

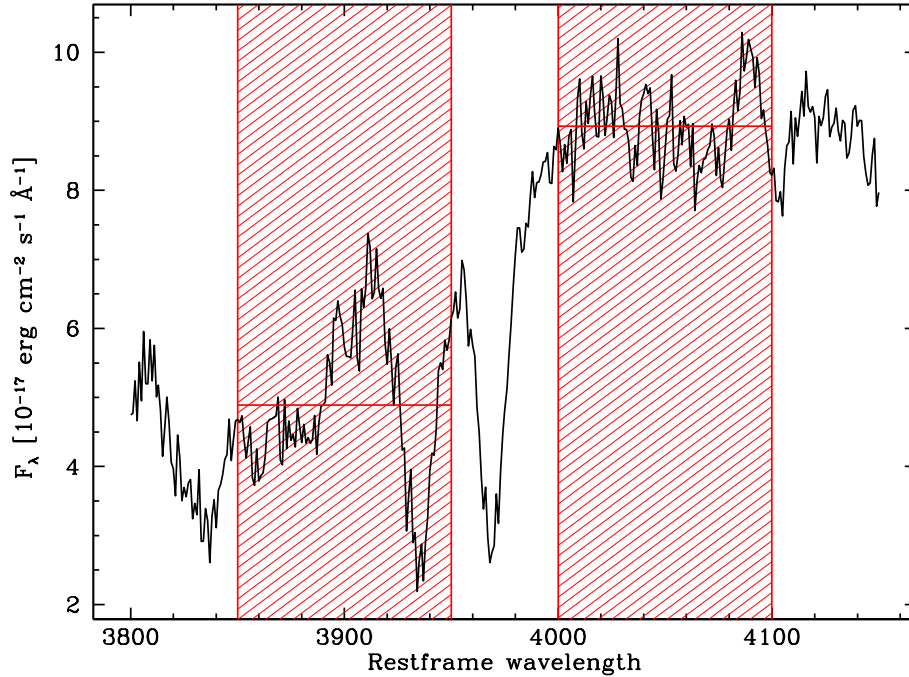


Figure 5.3: Mean stacked spectrum of 10 ETGs randomly selected from the extreme tail of the  $D4000_n$  distribution. The red shaded areas show the ranges used to evaluate the  $D4000_n$  and the red horizontal lines show the mean of the flux.

the metallicities of those galaxies, it has been used the analysis performed by Gallazzi et al. (2005), in which they derived stellar metallicities for a sample of SDSS-DR2, afterward extended to SDSS-DR4 ([www.mpa-garching.mpg.de/SDSS/DR4/Data/stellarmet.html](http://www.mpa-garching.mpg.de/SDSS/DR4/Data/stellarmet.html)). Their constraints are set by the simultaneous fit of five spectral absorption features ( $D4000$ ,  $H\beta$  and  $H\delta_a + H\gamma_a$  as age-sensitive indices and  $[Mg_2Fe]$  and  $[MgFe]'$  as metal-sensitive indices, all of which depend negligibly on the  $\alpha/Fe$  ratio), which are well reproduced by Charlot & Bruzual (2003, BC03) population synthesis models (for further details, see Gallazzi et al., 2005). To verify that the metallicity estimation is not biased by the choice of the particular star formation history done by Gallazzi et al. (2005), it has been decided to compare their estimates with the ones done with VESPA code (Tojeiro et al., 2007). The approach of VESPA is to recover robust star formation and metallicities histories using the full spectral range of a galaxy from synthetic models; in order to estimate those quantities, it allows for a completely free-form star formation, imposing no prior on it. This code has been applied to the entire SDSS-DR7, obtaining a catalog of stellar masses, detailed star formation and metallicity his-

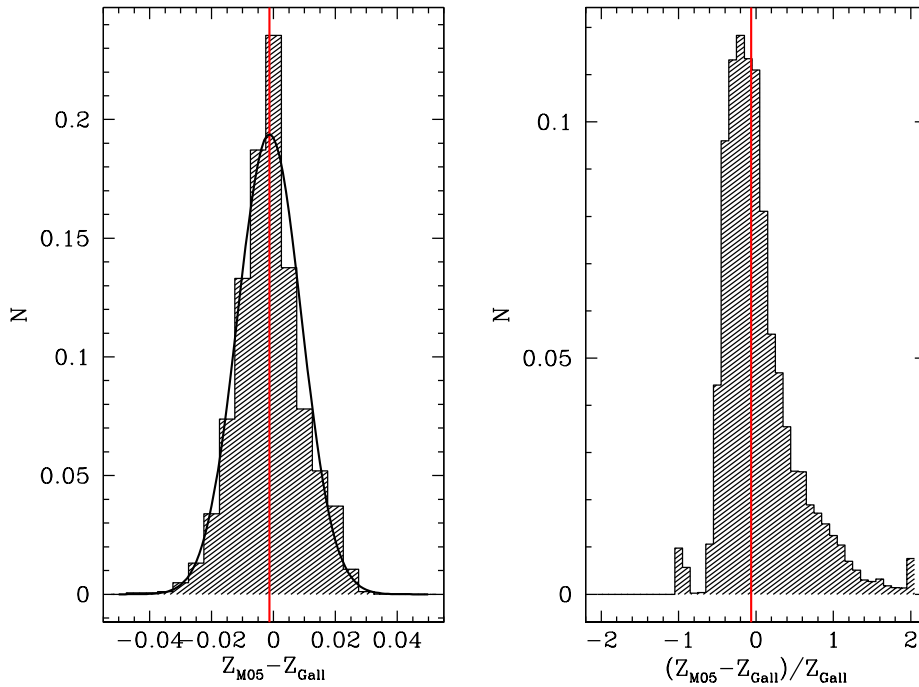


Figure 5.4: Distributions of the difference ( $Z_{Gallazzi} - Z_{VESPA}$ ) (left panel) and of the percentage difference  $(Z_{Gallazzi} - Z_{VESPA})/Z_{Gallazzi}$ .

tories (Tojeiro et al., 2009, , [www-wfau.roe.ac.uk/vespa/](http://www-wfau.roe.ac.uk/vespa/)).

Despite the completely different assumption on the star formation histories, the distribution of the difference ( $Z_{Gallazzi} - Z_{VESPA}$ ) is a gaussian with mean value -0.01 and dispersion 0.1; the distribution of the percentage difference  $(Z_{Gallazzi} - Z_{VESPA})/Z_{Gallazzi}$  has a mean value of 4.8%, with a 51.3% dispersion. So there exists no bias between the two metallicity evaluations, and this analysis ensures the reliability of Gallazzi et al. (2005) metallicity estimates (see Fig. 5.4).

The masses are estimated by performing a best-fit to the multicolor spectral energy distribution (SED), using the observed magnitudes in 8 photometric bands from  $u$  to  $K$ ; the fitting procedure is fully described in Sect. 3.2.2. Since, as underlined in Sect. 2.3.1, there are many recent works on early-type galaxies evolution that clearly shown the existence of a mass-downsizing effect, i.e. more massive galaxies have assembled their mass before less massive ones (see also Sect. 4.4), selecting a sample with a wide stellar mass range can bias the results, because its effect would be averaging between galaxies with different stellar populations.

In order to select the oldest population from the ETGs sample, the high-mass tail of the mass distribution has therefore been selected, considering  $\log(M/M_{\odot}) >$

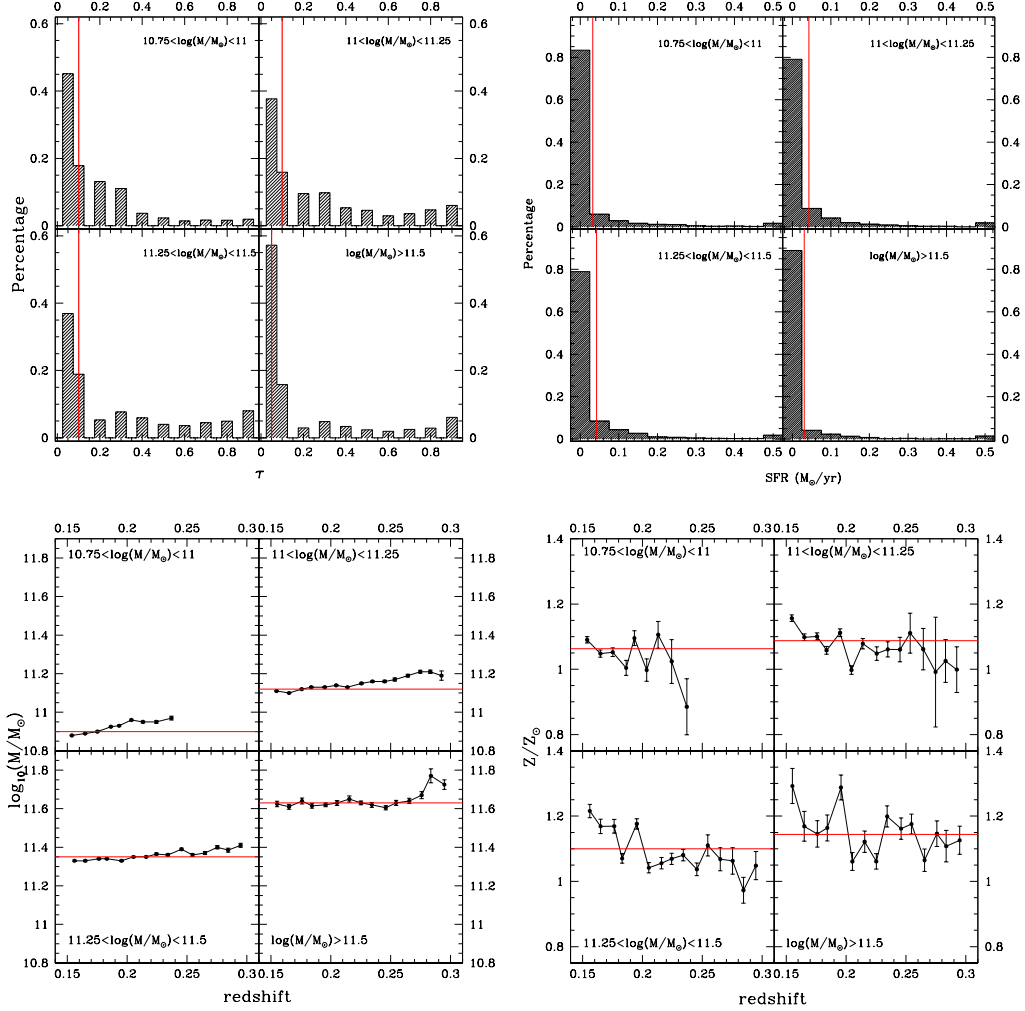


Figure 5.5: In the upper panels: distributions of  $\tau$  (left panel) and SFR values (right panel) in different mass subsamples. In the lower panels: mass-redshift relations (left panels) and metallicity-redshift relations (right panel), averaged in bin of redshift in different mass subsamples. The red lines represent the median of the distributions.

10.75. Moreover, to avoid possible bias from mass-downsizing effect, the sample has been splitted in narrow mass bins, to have a more homogenous sampling of redshift of formation and metallicity for these galaxies:  $10.75 < \log(M/M_\odot) < 11$ ,  $11 < \log(M/M_\odot) < 11.25$ ,  $11.25 < \log(M/M_\odot) < 11.5$ , and  $\log(M/M_\odot) > 11.5$ . The division of ETGs into four subsamples of the width of  $\Delta \log(M/M_\odot) = 0.25$  has been done to keep the statistical significance of the subsamples high enough, having for each subsample  $N_{gal} \gtrsim 3500$  (except for the highest mass bin, for which  $N_{gal} \sim 1500$ ); the adopted cut  $\log(M/M_\odot) > 10.75$  has been set in order both to select the most massive galaxies of the sample and to have four mass bins with a sufficient number of galaxies to perform a reasonable statistical analysis. The difference of the median mass along the redshift range has been checked to be 0.11 dex on average and the median metallicity to be constant in the considered range redshift within a 5% percent level, on average. The lower panels of Fig. 5.5 show the median values of the mass-redshift and metallicity-redshift relations for different mass subsample, with in red the median value of mass and metallicity averaged over the entire redshift range.

The  $\tau$  parameter of the SFH obtained from the best-fit to the SEDs of the galaxies shows a distribution characteristic of passive galaxies, with median values below 0.2 Gyrs for all the mass subsamples (see upper-left plot of Fig. 5.5). This result is in agreement with many ETGs analysis (Cimatti et al., 2008; Longhetti et al., 2009; Gobat et al., 2008), for which the majority of massive field early-type galaxies should have formed their stellar content around  $z \gtrsim 2$  over short (i.e.  $\tau < 0.1 - 0.3$  Gyrs) star formation time-scales. Also the distributions of the Star Formation Rate (SFR) obtained from the SED-fitting have been studied, finding a median SFR equal to zero  $M_\odot/\text{yr}$  for all the mass subsamples, with a scatter of 0.11, 0.17, 0.18, 0.2  $M_\odot/\text{yr}$ , respectively for the four mass subsamples. In the upper panels of Fig. 5.5 it is shown the  $\tau$  and SFR distributions for different mass-subsamples of SDSS ETGs; the red lines represent the medians of the distributions.

Since this approach depends strongly on the selection of a sample of galaxies passively evolving, also the emission lines distributions have been analyzed in details, because they can be linked with star formation or AGN activity. The median values of those distributions are  $EW_0(H\alpha) \lesssim 0.5 \text{ \AA}$  and  $EW_0([OII]\lambda 3727) \lesssim 1 \text{ \AA}$ , with tails up to 2  $\text{\AA}$  for the  $EW_0(H\alpha)$  and up to 4  $\text{\AA}$  for the  $EW_0([OII]\lambda 3727)$  (see Tab. 5.1). In Fig. 5.6 it is shown the  $EW_0(H\alpha)$  (left panel) and  $EW_0([OII]\lambda 3727)$  (right panel), each one for the four samples; the red lines represent the medians of the distributions. The median value of the specific star formation rate, obtained from the SED-fitting, for the galaxies with a significant detection of  $EW_0(H\alpha)$  is however null. Moreover, the  $D4000_n$  has been verified not to be significantly different between galaxies with  $EW_0(H\alpha) < 0$  and  $EW_0(H\alpha) > 0$ , finding respectively  $D4000_n = 1.948 \pm 0.002$  and  $D4000_n = 1.944 \pm 0.001$ .

Also the distribution of the eClass spectral parameter has been checked; this is a SDSS parameter quantifying the activity of a galaxy using a PCA analysis of

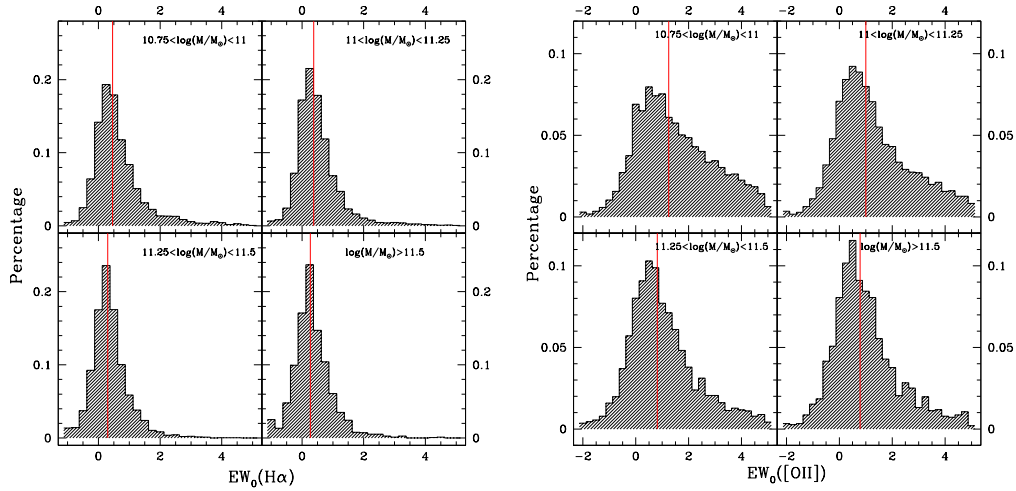


Figure 5.6: Distributions of the  $EW_0(H\alpha)$  (left panel) and  $EW_0([OII]\lambda 3727)$  (right panel). The red lines represent the median of the distributions.

mass range $\log(M/M_\odot)$	median mass $\log(M/M_\odot)$	median $Z/Z_\odot$ $Z/Z_\odot$	median $EW_0(H\alpha)$ [Å]	median $EW_0([OII])$ [Å]	# galaxies
10.75-11	$10.9 \pm 0.02$	$1.061 \pm 0.006$	$0.463 \pm 0.009$	$1.24 \pm 0.03$	3452
11-11.25	$11.12 \pm 0.03$	$1.088 \pm 0.004$	$0.376 \pm 0.007$	$1 \pm 0.02$	5429
11.25-11.5	$11.25 \pm 0.02$	$1.1 \pm 0.006$	$0.305 \pm 0.007$	$0.81 \pm 0.02$	3591
> 11.5	$11.63 \pm 0.04$	$1.144 \pm 0.009$	$0.27 \pm 0.01$	$0.78 \pm 0.03$	1515

Table 5.1: Median value of the mass (in logarithmic units), of the metallicity (in solar metallicity units), and of the  $H\alpha$  and  $[OII]\lambda 3727$  equivalent widths of the ETGs in different mass subsamples. Also the number of galaxies for each bin has been quoted.

the spectra of the galaxies, and it goes from -0.35 to 0.5 for early- to late-type galaxies. For each mass subsample, it shows a distribution always below -0.1, so this selection results even stricter than the one done from Bernardi et al. (2006), in which they chose ETGs with  $eClass < 0$ .

In Table 5.1 are reported the median values of mass, metallicity and equivalent widths of the emission lines for the different mass subsamples, with their errors; in the same table are reported also the number of galaxies in each bin.

Another possible systematic trend with redshift that could, in principle, bias this analysis is the effect of using, in SDSS, a fixed 3 arcsec fibre, which maps different physical sizes depending on the observed redshift. However Gallazzi et al. (2005) analyzed in details the effect of this aperture bias, finding no significant

difference in metallicity between high- and low-concentration galaxies (see their Sect. 3.2). The difference in D4000 between high- and low-concentration galaxies have been checked to be always  $< 2\%$ .

## 5.3 Linking the 4000 Å break to the expansion history of the Universe: the D4000-redshift relation

### 5.3.1 Calibration of the $D4000_n$ -age relation

In general the  $D4000_n$  is an index that is strongly sensitive to metallicity, star formation history and age of a stellar population. In order to break this degeneracy, it has been created a library of  $D4000_n$  as a function of age using stellar population synthesis models with different metallicity, star formation history (delayed exponential SFR with  $\tau = 0.05, 0.1, 0.2, 0.3$  Gyrs), and ages. In order to study the possible systematics due to the choice of a particular model, two different libraries have been created, one using Bruzual & Charlot (2003) stellar population synthesis models (hereafter BC03) and one using the new Maraston & Strömbäck (2011) stellar population synthesis models (hereafter *Mastro*), which are based on the MILES models (Sánchez-Blázquez et al., 2006). The metallicities studied with the two models are  $Z/Z_\odot = 0.4, 1, 2.5$  for BC03 and  $Z/Z_\odot = 0.5, 1, 2$  for *Mastro*. The resolution of the two models is similar, 3 Å across the wavelength range from 3200 Å to 9500 Å for BC03, and 2.3 Å across the wavelength range 3525 Å to 7500 Å for *Mastro*; moreover the resolution of both models is comparable to the resolution reachable with the SDSS spectrograph, which has  $R \sim 1800$  between 3900-9100 Å.

The choice of the grid of star formation histories and metallicities is motivated by the fact that the sample to be analyzed is composed of ETGs from the SDSS survey: a lower value in the range of metallicity would probe  $D4000_n$  values that are much lower than the average values found in this galaxy sample, and the SED-fitting analysis of the ETGs shows that the majority of the sample is best-fitted with SFHs with low values of  $\tau$ . Moreover, the choice of a passive sample strongly supports the decision of using these low  $\tau$  values.

The upper panels of Fig. 5.7 and 5.8 show the BC03 and *Mastro*  $D4000_n$ -age relations; the models with the higher metallicity ( $Z/Z_\odot = 2.5$  and  $Z/Z_\odot = 2$  respectively) are in red, the ones with  $Z/Z_\odot = 1$  in green, and the ones with the lower metallicity ( $Z/Z_\odot = 0.4$  and  $Z/Z_\odot = 0.5$  respectively) in blue. For each metallicity, the models are plotted with a continuous line for  $\tau = 0.05$  Gyrs, with a dotted line for  $\tau = 0.1$  Gyrs, with a dashed line for  $\tau = 0.2$  Gyrs and with a long-dashed line for  $\tau = 0.3$  Gyrs.

These relations have been studied in the  $D4000_n$  range spanned by the data, roughly  $1.8 \lesssim D4000_n \lesssim 2$ . For both the models considered, it has been found that the  $D4000_n - age$  relation presents, at each metallicity, two different slopes: one characteristic of the "low  $D4000_n$ " regime ( $1.8 < D4000_n < 1.95$  for BC03 and  $1.75 < D4000_n < 1.93$  for *Mastro*) and one characteristic of the "high  $D4000_n$ " regime ( $1.95 < D4000_n < 2.05$  for BC03 and  $1.93 < D4000_n < 2.05$  for *Mastro*). At the condition of studying the model separately in the two regimes, it is

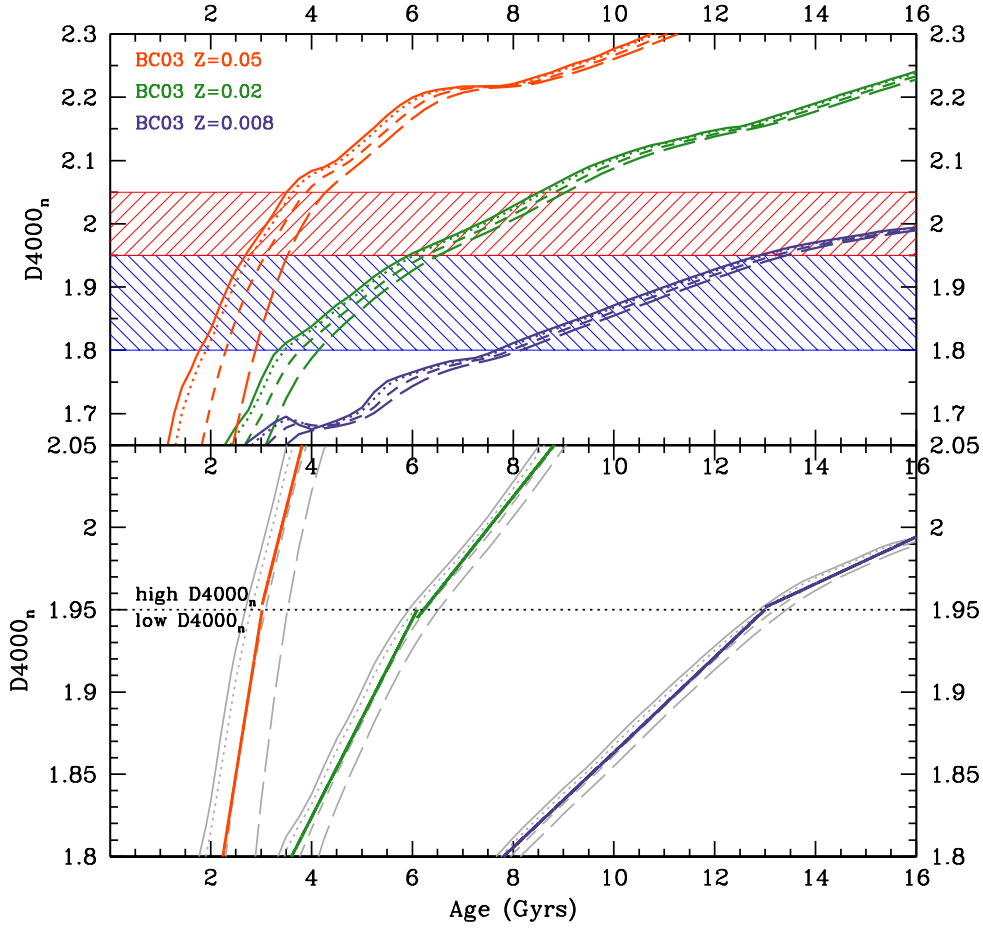


Figure 5.7:  $D4000_n$ -age relation for BC03 high resolution models. In the upper panels the colored lines represent models with different metallicities, with oversolar metallicity in red ( $Z/Z_\odot = 2.5$ ), solar in green, and undersolar in blue (respectively  $Z/Z_\odot = 0.4$ ). The blue and the red shaded area represent the ranges of  $D4000_n$  in the models (respectively the low  $D4000_n$  and the high  $D4000_n$  regime). The lower panel show a zoom of the interested area, where the models are shown in gray and the colored lines are the fit to the models. The dotted line shows where the change between the low  $D4000_n$  and the high  $D4000_n$  regime. It is possible to see the minor dependence of the slopes of the  $D4000_n$ -age relation on the SFH assumed both by visually comparing the average slopes (colored lined of the lower panels) and the slope of each single model (grey lines of the lower panels) and by looking the small errors associated to the mean values (see Table 5.2).

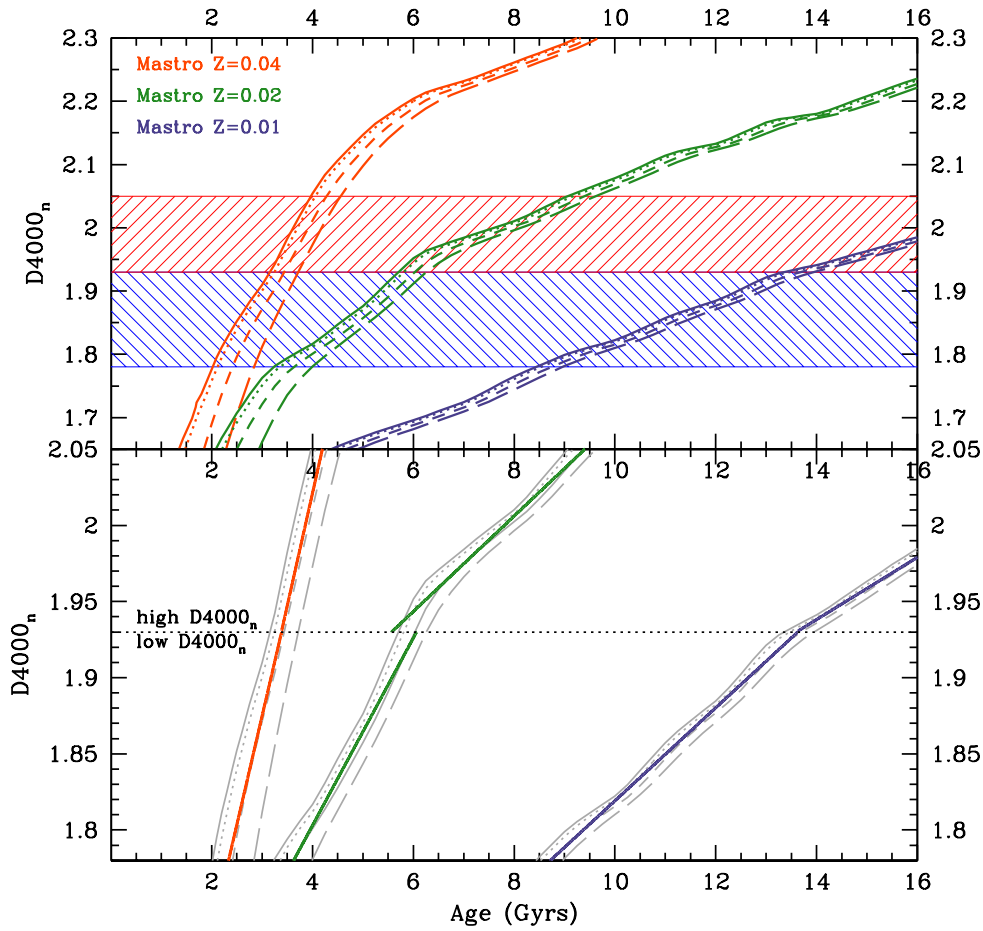


Figure 5.8:  $D4000_n$ -age relation for Mastro models (right panel). In the upper panels the colored lines represent models with different metallicities, with oversolar metallicity in red ( $Z/Z_{\odot} = 2$ ), solar in green, and undersolar in blue ( $Z/Z_{\odot} = 0.5$ ). For a discussion about the meaning of symbols and curves, see Fig. 5.7.

demonstrated that the linear approximation:

$$D4000_n(Z) = A(Z) \cdot age + B(Z) \quad (5.6)$$

is valid and accurate at fixed metallicity, having in the case of BC03 models correlation coefficients always  $> 0.996$  with a mean value of  $0.9987 \pm 0.0004$  for the "low  $D4000_n$ " regime and always  $> 0.994$  with a mean value of  $0.9976 \pm 0.0007$  for the "high  $D4000_n$ " regime; in the case of Mastro models the correlation coefficients are always  $> 0.997$  with a mean value of  $0.9984 \pm 0.0003$  for the "low  $D4000_n$ "

regime and always  $> 0.993$  with a mean value of  $0.9986 \pm 0.0005$  for the "high  $D4000_n$ " regime.

The only limitation of this approximation is that it requires a direct estimate of the metallicity of the sample. However, as it will be shown later, this method has been proven to be robust against the metallicity evaluation, since the analysis of subsample with a median metallicity completely different give results in full agreement. For each metallicity a mean slope  $\langle A \rangle$  has been defined averaging between the slopes with same metallicity and different SFHs. The mean values of the slopes are reported in Table 5.2. The use of an average slope instead of the single values is motivated by the fact that the dependence on the SFH is much less significant than the dependence on age and metallicity (see upper panels of 5.7 and 5.8), as testified by the small errors associated to the mean values (see Table 5.2). In the lower panels of Fig. 5.7 and 5.8 are plotted in gray the models, as explained before, while the colored lines represent the average linear fit to those models; the comparison between the colored and the grey lines shows visually the similarity between the average slopes and the slope of each single model. The dotted horizontal line represent the separation between the "low  $D4000_n$ " and the "high  $D4000_n$ " regime. From this figure are clearly evident the different slopes present in the two range of  $D4000_n$ , for each metallicity.

Since, as Eq. 5.6 shows, the slope  $A$  represents the conversion parameter between the  $D4000_n$  and the age of a galaxy, a fundamental step of this approach is to assign to correct  $A$  value to the metallicity evaluated in each sample. Therefore, the values reported in Tab. 5.2 with their errors have been interpolated with a quadratic function, obtaining a  $\langle A \rangle$ -metallicity relation; in this way it is possible to find the correct  $\langle A \rangle$  parameter considering the metallicities of each mass subsamples using this relation, and they are given in Tab. 5.1.

In this approach also the effect of averaging the slope  $A$  between different star formation histories has been taken into account, since the quadratic function has

		low $D4000_n$	high $D4000_n$
BC03	$\langle A \rangle (Z/Z_\odot = 0.4)$	$0.02893 \pm 0.00002$	$0.0159 \pm 0.0003$
BC03	$\langle A \rangle (Z/Z_\odot = 1)$	$0.0601 \pm 0.0006$	$0.0359 \pm 0.0005$
BC03	$\langle A \rangle (Z/Z_\odot = 2.5)$	$0.1926 \pm 0.0113$	$0.1223 \pm 0.0013$
<i>Mastro</i>	$\langle A \rangle (Z/Z_\odot = 0.5)$	$0.03136 \pm 0.0004$	$0.02427 \pm 0.00005$
<i>Mastro</i>	$\langle A \rangle (Z/Z_\odot = 1)$	$0.0582 \pm 0.002$	$0.0341 \pm 0.0005$
<i>Mastro</i>	$\langle A \rangle (Z/Z_\odot = 2)$	$0.135 \pm 0.0083$	$0.1257 \pm 0.004$

Table 5.2: Mean slopes  $\langle A \rangle$  of the  $D4000_n$ -age relation (see Eq. 5.6) for the BC03 and Mastro models with different metallicity and for the two  $D4000_n$  regimes.

been defined with a best fit to the  $\langle A \rangle$ -metallicity relation, where the errors in the parameter  $\langle A \rangle$  quantify exactly the difference of the slope between the different star formation histories considered. The size of the errors by themselves shows that the dependence of the slope on the star formation history is small. The percentage difference between models with different SFHs, averaged in the metallicity range spanned by the data, has been found to be 2.8% in the "low  $D4000_n$ " regime and 3.1% in the "high  $D4000_n$ " regime for BC03 models and 12.4% in the "low  $D4000_n$ " regime and 3.9% in the "high  $D4000_n$ " regime for *Mastro* models. The results are shown in Fig. 5.9. In the upper panels are shown the interpolation of the  $\langle A \rangle - Z$  values reported in Tab. 5.2 (black points), for BC03 (orange lines) and *Mastro* (green lines) models; the shaded area represent the 68% confidence level regions of the interpolation (considering the errors of

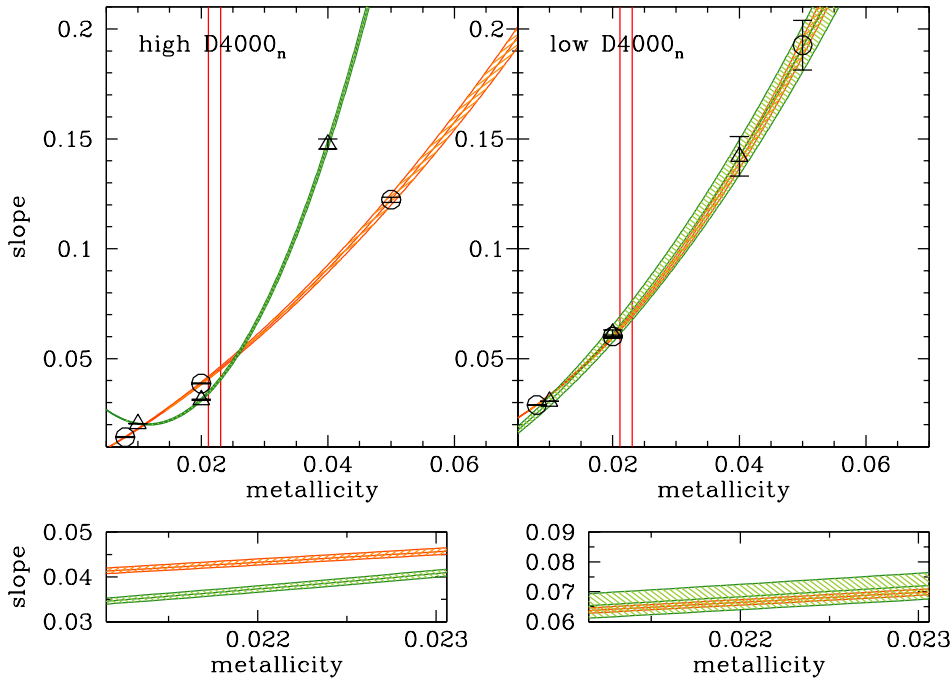


Figure 5.9: *Upper panels: Interpolation of the  $\langle A \rangle - Z$  values reported in Tab. 5.2. The orange lines represent the interpolation of BC03 data, and the green lines the interpolation of Mastro data, the shaded area showing the 68% confidence level regions (considering the errors of  $\langle A \rangle$  parameter quoted in Tab. 5.2); the area between the red lines represent the range of metallicity probed by the data. Lower panels: zoom of the above relations in the interested metallicity range, showing in detail the differences between the two models.*

$\langle A \rangle$  parameter quoted in Tab. 5.2). The area between the red lines represent the range of metallicity probed by the data. The lower panels show a zoom of the above relations in the interested metallicity range, showing in detail the differences between the two models.

It has been decided to take into account this difference in the analysis, adding these errors in the cosmological parameters evaluation.

This analysis has been carried out also with the new *Mastro* models to study the dependence of the cosmological parameters evaluation on a particular library of models. By comparing the plots from Fig. 5.7 and Fig. 5.8, it can be found that the  $D4000_n$ -age relations have a different normalization, the *Mastro* models yielding to younger ages, on average. However, even with different absolute  $D4000_n$  values, the study of the slope of the relations gives values in good agreement with the ones obtained from the BC03 models.

This results is of key importance in this approach. On one hand it is fundamental to remind that this analysis is based only on the *relative* change of  $D4000_n$ , and not on its *absolute* value. Thus, the variation in the normalization between the different models is irrelevant. On the other hand, the fact that the slope of the  $D4000_n$ -age relation remains almost unchanged passing from BC03 to *Mastro* models demonstrate the robustness of the method against the choice of different stellar population synthesis models. In Sect. 5.5.4 what is the effective consequence of this difference in the parameters estimation will be quantified.

### 5.3.2 A linear model

The cosmological expansion history is described by the Hubble parameter evolution:

$$H(z) = -\frac{1}{1+z} \frac{dz}{dt} \quad (5.7)$$

The analysis of the differential age evolution of ETGs, that trace the differential age evolution of the Universe, fully determine  $H(z)$ , and therefore the cosmological parameters.

As shown in section 5.3.1, there exists, in the range of  $D4000_n$  probed by the data and at fixed metallicity  $Z$ , a linear relation between the  $D4000_n$  and the age of a galaxy; therefore, using Eq. 5.6, Eq. 5.7 can be easily rewritten as a function of the differential evolution of the  $D4000_n$  with a proper conversion parameter, where this conversion parameter is given by the slope  $A$  of the  $D4000_n$ -age relation:

$$H(z) = -\frac{A}{1+z} \frac{dz}{dD4000_n} \quad (5.8)$$

This approach, provided that the galaxies are passive and evolved passively, is promising because:

- it relies on a direct observable of a galaxy, that can be easily measured from spectra;
- it depends only on the slope of the  $D4000_n$ -age relation, and not on its overall normalization;
- it depends only marginally on the SFH assumptions;
- it is not influenced by dust extinction (Hamilton, 1985; Balogh et al., 1999).

Equation 5.8 can be reformulated in order to make explicit the dependence on the various cosmological parameters in the following way:

$$D4000_n(z) = \frac{A}{H_0} \int_0^{\frac{1}{1+z}} y^{1/2} \left\{ \Omega_m + \Omega_{DE} \left[ y^{-3(w_0+w_a)} e^{3w_a(y-1)} \right] \right\}^{-1/2} dy + constant \quad (5.9)$$

where we have used the standard parametrization  $w(z) = w_0 + (\frac{z}{1+z})w_a$ .

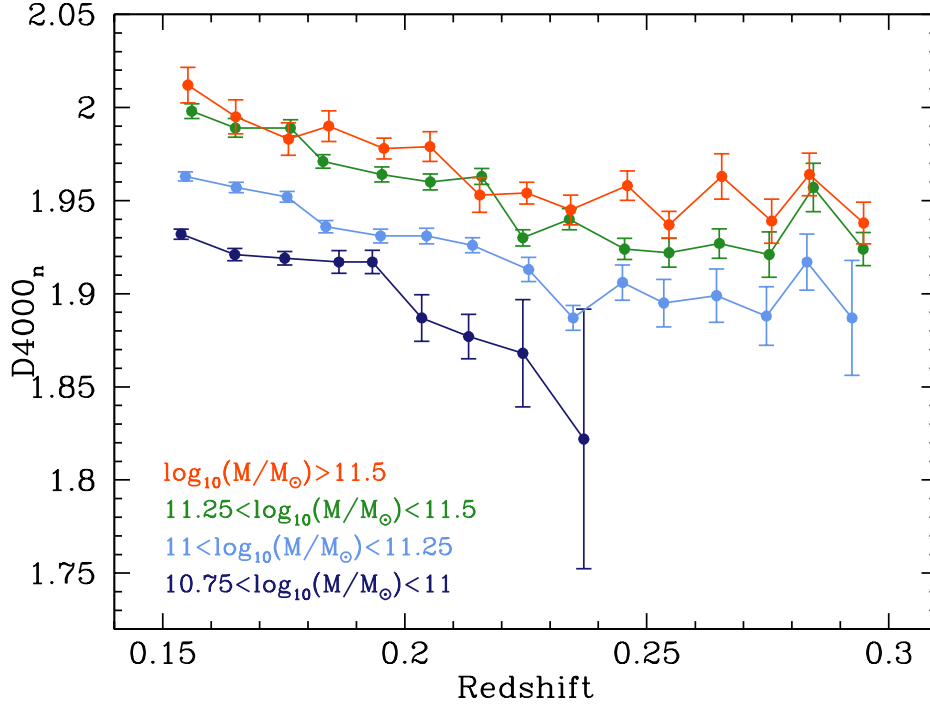


Figure 5.10:  $D4000_n$ -redshift relation for ETGs in different mass subsamples.

## 5.4 Deriving the $D4000_n$ -redshift relation

For each mass subsample, the median  $D4000_n$  has been evaluated in narrow redshift bins ( $\Delta z = 0.01$ ); the associated errors are standard errors on the median.<sup>2</sup>

The results are shown in Fig. 5.10. In the lower mass range, the analysis has been limited to  $z \lesssim 0.24$ , because, given the magnitude limit of the sample, above  $z \approx 0.24$  there are only  $N_{gal} = 9$ .

It is impressive that for each mass subsample we find a clear  $D4000_n$ - $z$  relation. Since it has been proven in Sect. 5.2.1 that the metallicity evolution with redshift is negligible within each mass subsample, this directly witnesses the differential age evolution of ETGs, making evident that galaxies at low redshift have always higher break with respect to galaxies at high redshift. Moreover Fig. 5.10 provide also good evidence of mass-downsizing, showing that more massive galaxies present, at each redshift, higher  $D4000_n$  breaks with respect to less massive ones, hence having higher ages, since the difference in metallicity is small.

Comparing the  $D4000_n$  values shown in Fig. 5.10 with theoretical values, can

<sup>2</sup>The error on the median are evaluated as the median absolute deviation/sqrt(N), where the "median absolute deviation" (MAD) is defined as  $MAD = 1.482 * median(|D4000_n - median(D4000_n)|)$ . (see Hoaglin et al., 1983)

be found that, with these metallicities, the relative age evolution of the ETGs is  $\approx 1.2$  Gyrs in the range  $0.15 < z < 0.3$ , fully compatible with the theoretical age evolution expected in a  $\Lambda$ CDM Universe within this redshift range.

The absolute ages of these ETGs go on average from  $\approx 5 - 6$  Gyrs in the lowest mass bin to  $\approx 6 - 7$  Gyrs in the highest mass bin, so it seems that there are some problems of normalization between the ages obtained from the  $D4000_n$  and the expected absolute ages, that are around  $\approx 8 - 10$  Gyrs for ETGs in this redshift range. However on the one hand, it is fundamental to remember again that this approach relies completely on the differential  $D4000_n$  evolution of ETGs, so in the cosmological parameters evaluation it is insensitive to the overall normalization. On the other hand, it is also important to stress that median values have been used, averaging between different galaxies ages; if only the upper envelope of the  $D4000_n$  distribution is considered, which represents the oldest population of ETGs, absolute ages of  $\approx 8$  Gyrs are again retrieved.

Another crucial point in favor of using this approach is that the use of this linear conversion from  $D4000_n$  to the age of a galaxy keeps, by definition, unchanged the slope of the redshift dependence, allowing a better estimate of cosmological parameters, especially with respect to indirect age evaluations (from SED or spectral fit) that, on the contrary, may affect the slope owing the various model dependencies and degenerations.

As stressed before, to apply this technique it is fundamental to obtain the correct  $A$  parameter, that is the conversion factor from the  $D4000_n$  to the age of a galaxy. Therefore, it is needed to associate the proper metallicity to each mass subsample. Since, as already underlined, the metallicity evolution with redshift has been verified to be negligible within each subsample, it have been studied the medians of the metallicity distribution, with their standard errors. As predicted by Gallazzi et al. (2006), all ETGs have slightly oversolar metallicity values, increasing as a function of mass.

The  $\langle A \rangle$ -metallicity relation defined in Sect. 5.3.1 has been used to find the proper  $\langle A \rangle$  parameter corresponding to the metallicity of each mass subsample, giving the median metallicity reported in Table 5.1. It has been decided to use the values corresponding to the "low  $D4000_n$ " regime for the lower mass bins ( $10.75 < \log(M/M_\odot) < 11$ ,  $11 < \log(M/M_\odot) < 11.25$ , and  $11.25 < \log(M/M_\odot) < 11.5$ ), and the values corresponding to the "high  $D4000_n$ " regime for the highest mass bin ( $\log(M/M_\odot) > 11.5$ ).

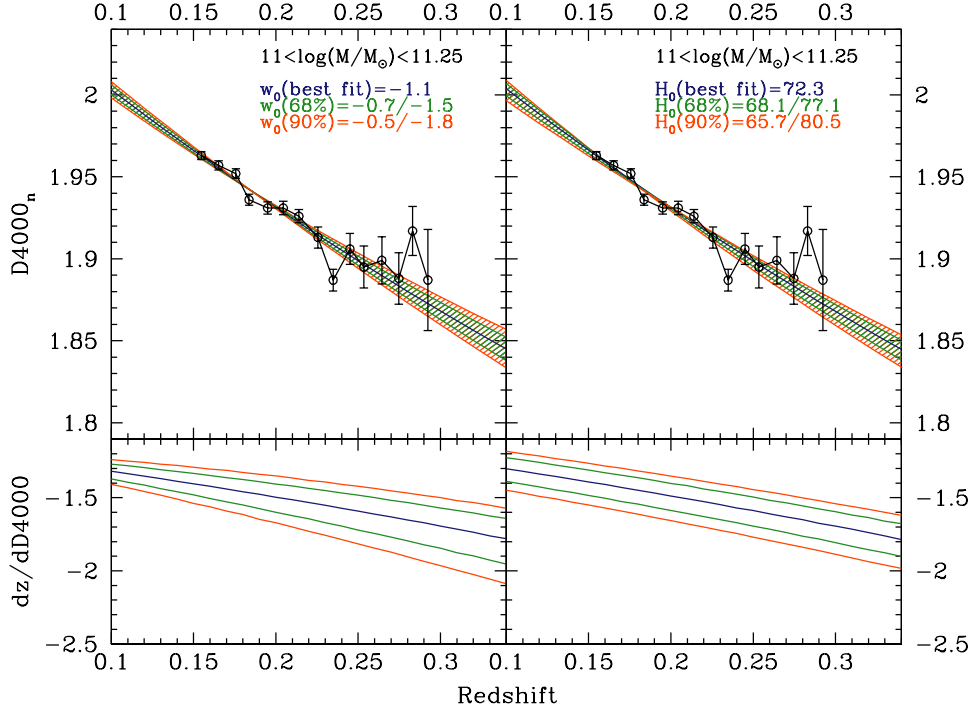


Figure 5.11:  $D4000_n$ -redshift relation (upper panels) and  $dz/dD4000_n$  relation (lower panels) for different theoretical models. In the upper panels the black points are the relation obtained for the  $11 < \log M/M_\odot < 11.25$  mass subsample. The blue lines represent the best-fit to the data, using  $\Omega_M = 0.27$ ,  $\Omega_{DE} = 0.73$ ,  $H_0 = 74.2$  in the left panels and  $\Omega_M = 0.27$  and  $\Omega_{DE} = 0.73$  in the right panels. The green and red lines show respectively the curves representing the 68% and 90% errors to the best-fit.

## 5.5 Constraints on the cosmological parameters

The  $D4000_n$ - $z$  relations, obtained from the selection of ETGs extracted from the SDSS-DR4, are then used to set constraints on the Hubble constant  $H_0$  and on the dark energy equation-of-state parameter  $w$ , assuming  $w = \text{constant}$  ( $w = w_0$ ,  $w_a = 0$ ).

The most recent evaluation of the Hubble parameter has been derived by Riess et al. (2009) by analyzing the magnitude-redshift relation of 240 low- $z$  Type Ia supernovae at  $z < 0.1$ . The absolute magnitudes of supernovae are calibrated using new observations from HST of 240 Cepheid variables in six local Type Ia supernovae host galaxies and the maser galaxy NGC 4258. This refurbished distance ladder based on extensive use of differential measurements allowed them to obtain

$H_0 = 74.2 \pm 3.6 \text{ km, s}^{-1} \text{ Mpc}^{-1}$ , including both statistical and systematic errors. This measurement has been proved to be extremely useful also for a new determination of the dark energy equation-of-state parameter obtained by the seven-year WMAP observation (Komatsu et al., 2011): by combining the WMAP data with the latest distance measurements from the Baryon Acoustic Oscillations (BAO) in the distribution of galaxies (Percival et al., 2010) and the Hubble constant ( $H_0$ ) measurement (Riess et al., 2009) it was possible to set the constraint  $w = -1.10 \pm 0.14$  (68% CL).

The most recent estimate of  $w$  comes from the analysis of a sample of 557 SNe called Union2 compilation, obtained combining the Union compilation with the HST-light curves and spectra of six new high redshift SNe Ia (Amanullah et al., 2010); their analysis gives results in full agreement with WMAP estimate, with a  $w = -0.997 \pm 0.08$  for a flat  $\Lambda$ CDM Universe and  $w = -1.038 \pm 0.09$  for a  $\Lambda$ CDM Universe with curvature, both assuming  $w = \text{constant}$ .

In the next sections it is shown the strength of this approach in determining both  $H_0$  and  $w$ , by analyzing individually the different mass subsample and then performing a joint analysis, unifying the constraints derived from the single measurements.

As an example, Figure 5.11 shows in black the  $D4000_n - z$  relation for the mass bin  $11 < \log M/M_\odot < 11.25$ . A best-fit to this relation has been performed, in order to obtain  $w$  (in the left plot) and  $H_0$  (in the right plot). The blue curves show the best-fits to the data; in green and red are also plotted the curves representing the 68% and 90% errors to the best-fits, respectively. In the upper-left panel, the best-fit model has been evaluated at fixed  $\Omega_M = 0.27$ ,  $\Omega_{DE} = 0.73$  (as obtained by WMAP 7-years analysis),  $H_0 = 74.2$  (as obtained by Riess et al. 2009), to set constraint on  $w = \text{constant}$ ; in the upper-right panel it has been set  $w = -1$ ,  $\Omega_M = 0.27$ ,  $\Omega_{DE} = 0.73$ , and searched for the best-fit  $H_0$  value. The size of the errors of the data makes clear the strength of the differential age approach to set constraints on the cosmological parameters. In the lower panels are shown the differential evolution of the  $D4000_n$ ,  $dz/dD4000_n$ , showing how much these relations are sensitive to the variation of  $H_0$  and  $w$ .

### 5.5.1 Statistical methods

The  $D4000_n - z$  relations shown in Fig. 5.10 have been fitted with the formula given in Eq. 5.8, using a standard  $\chi^2$  approach. The theoretical  $D4000_n(z)$  relation is a function of the  $A$  parameter and of various cosmological parameters ( $H_0$ ,  $\Omega_m$ ,  $\Omega_{DE}$ ,  $w$ ,  $w_a$ ). Therefore the  $\chi^2$  will be  $\chi^2(\alpha_1, \alpha_2, \dots, \alpha_N)$ , where  $\alpha_i$  are the free parameter of the fit. The associated likelihood is given by  $\mathcal{L}(\alpha_1, \alpha_2, \dots, \alpha_N) \propto e^{-(\chi^2(\alpha_1, \alpha_2, \dots, \alpha_N))/2}$ . Being interested only in the evaluation of one parameter, this likelihood have been marginalized over the parameters we are not interested, ob-

taining:

$$\mathcal{L}(\alpha_i) = \int e^{-\frac{\chi^2(\alpha_1, \alpha_2, \dots, \alpha_N)}{2}} d\alpha_1 \dots d\alpha_{i-1} d\alpha_{i+1} \dots d\alpha_N \quad (5.10)$$

In the following sections, the adopted priors and assumptions to estimate the Hubble constant  $H_0$  and the dark energy equation-of-state parameter  $w$  are explained and described.

### 5.5.2 The Hubble constant

To estimate  $H_0$ , the  $D4000_{n-z}$  relations given in Fig. 5.10 have been fitted with Eq. 5.8, fixing as a prior only a flat  $\Lambda$ CDM cosmology ( $\Omega_m + \Omega_{DE} = 1$ ,  $w = -1$  and  $w_a = 0$ ), letting  $\Omega_{DE}$  free to vary in the range provided by the latest WMAP 7-years analysis ( $0.7 < \Omega_{DE} < 0.76$ ) and the slope  $A$  free to vary within the values associated to the metallicity range found in the data within  $1\sigma$  error (see Table 5.1), considering also the spread due to the different SFHs considered (see the second point of Sect. 5.5.4).

As explained in Sect. 5.5.1, the best-fit has been evaluated with a standard  $\chi^2$  analysis, marginalizing the obtained likelihood over those parameters which have not to be constrained, that are  $\Omega_{DE}$  and  $A$ . At the end, four likelihoods of the Hubble constant for the mass bins have been created. The estimates obtained from the higher populated samples ( $11 < \log(M/M_\odot) < 11.25$  and  $11.25 < \log(M/M_\odot) < 11.5$ ) show a perfect agreement, with comparable errors; the analysis of the other two mass subsamples give slightly different results, but still within the  $1\sigma$  errors. However, it is also important to remember that the number of galaxies of these subsamples is quite lower with respect to the bin  $11 < \log(M/M_\odot) < 11.25$  (respectively 36% and 72% less), and therefore that the associated errors are larger (see Tab. 5.3).

Since those likelihoods are independent from each other, to reduce the statistical error and to obtain a better estimate on  $H_0$  they have been joined, obtaining  $H_0 = 72.6 \pm 2.9 \text{ km Mpc}^{-1}\text{s}^{-1}$ . In Fig. 5.12 are shown the  $\chi^2$  for each mass bin

Mass range [ $\log(M/M_\odot)$ ]	$H_0$ [ $\text{km Mpc}^{-1}\text{s}^{-1}$ ]	68% errors [ $\text{km Mpc}^{-1}\text{s}^{-1}$ ]	90% errors [ $\text{km Mpc}^{-1}\text{s}^{-1}$ ]	# galaxies
10.75 – 11	77.6	+16.6/–11	+31.2/–16.8	3452
11 – 11.25	72.2	+4.9/–4.2	+8.3/–6.7	5429
11.25 – 11.5	73.5	+4.7/–4.1	+8/–6.5	3591
> 11.5	66.9	+9.2/–6.9	+16.4/–10.8	1515
joint analysis	72.6	+3/–2.7	+5/–4.4	13987

Table 5.3: Hubble constant (in unit of  $\text{km Mpc}^{-1}\text{s}^{-1}$ ) and relative errors using BC03 models.

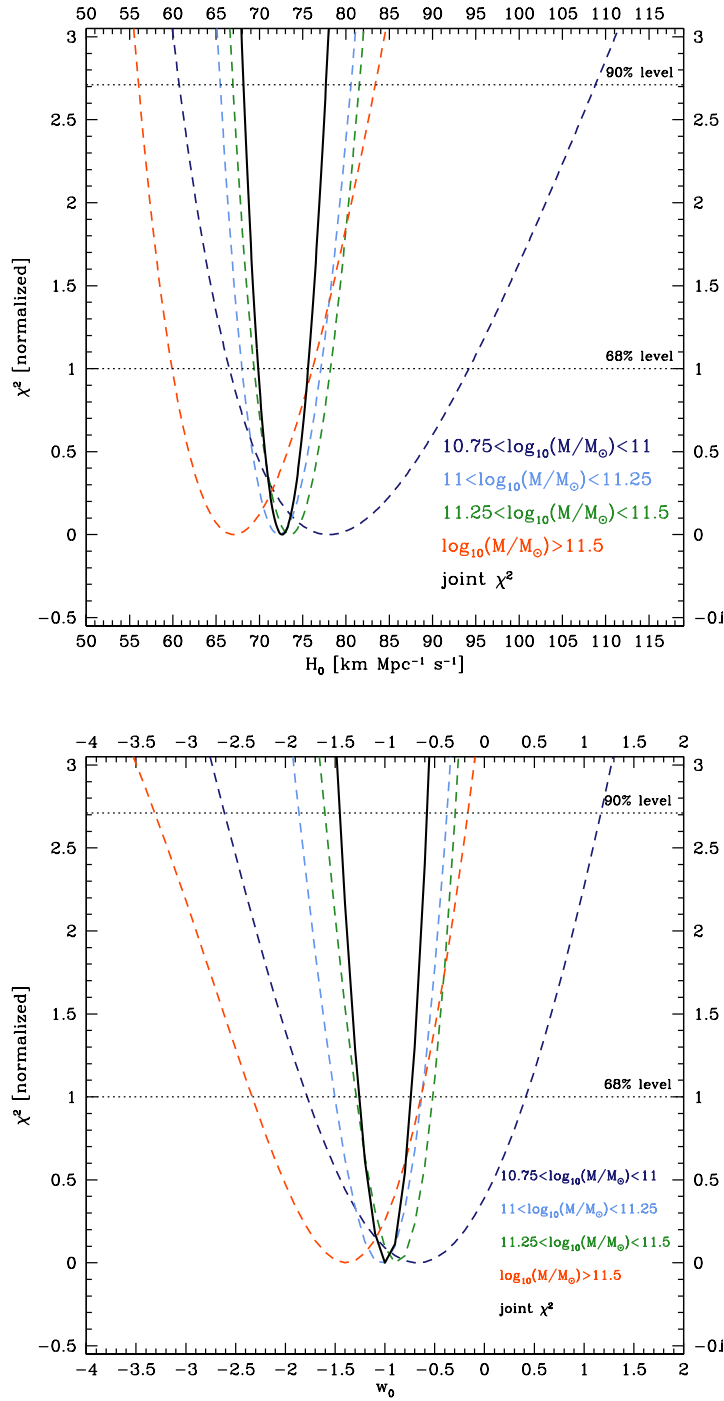


Figure 5.12:  $\chi^2$  of the  $H_0$  (left panel) and of the  $w$  (right panel) evaluation for ETGs in different mass subsamples using BC03 models.

and the joint  $\chi^2$ , and in Table 5.3 are reported the corresponding values of  $H_0$  and their errors.

### 5.5.3 The dark energy equation-of-state

To estimate the value of  $w$ , assuming  $w = \text{constant}$ , the  $D4000_{n-z}$  relations have been fitted using as priors the  $\Omega_{DE}$  value as found by the latest WMAP 7-years analysis considering a  $\Lambda$ CDM flat Universe (Larson et al. 2010,  $\Omega_m + \Omega_{DE} = 1$ ,  $w_a = 0$  and  $0.645 < \Omega_{DE} < 0.835$ ) and the estimate of  $H_0$  done by Riess et al. (2009) ( $70.6 \leq H_0 \leq 77.8$ ), the slope  $A$  free to vary within the values associated to the metallicity range found in the data within  $1\sigma$  error (see Table 5.1), considering also the spread due to the different SFHs considered (see the second point of Sect. 5.5.4).

The best-fit has been evaluated with a standard  $\chi^2$  analysis, marginalizing afterwards over  $H_0$ ,  $\Omega_{DE}$  and  $A$ . At the end, four likelihoods of  $w$  for the mass bins have been created. All the estimates obtained on  $w$  are in agreement within  $1\sigma$  error; only the value obtained in the highest mass bin shows a slight discrepancy, even if compatible with the other estimates within  $1\sigma$ . However, a similar discussion as the one introduced in the  $H_0$  estimate has to be done for this discrepancy, considering that it is the bin with the highest errors and the lowest galaxy number. As done in the  $H_0$  analysis, since those likelihood are independent one from the other a joint analysis has been performed by multiplying them, to reduce the statistical error. In Fig. 5.12 are shown the  $\chi^2$  for each mass bin and the joint  $\chi^2$ , and in Table 5.4 are reported the corresponding values of  $w$  and their errors. From the joint analysis we obtained  $w = -1 \pm 0.2$ .

Mass range [ $\log(M/M_\odot)$ ]	$w$	68% errors	90% errors	# galaxies
10.75 – 11	-0.7	+1.1/–1.0	+1.8/–1.9	3452
11 – 11.25	-1.0	+0.3/–0.5	+0.6/–0.8	5429
11.25 – 11.5	-0.9	+0.3/–0.3	+0.6/–0.7	3591
> 11.5	-1.4	+0.7/–0.9	+1.2/–1.9	1515
joint analysis	-1	+0.2/–0.2	+0.4/–0.4	13987

Table 5.4: *Dark energy equation-of-state parameter  $w$  and relative errors using BC03 models.*

### 5.5.4 Study of the systematics

For this new approach, the effect of different possible systematics from which the analysis may suffer have been studied. In particular, the most critical ones are the

dependence of the results on the estimate of the absolute age of a galaxy from the  $D4000_n$ , on the star formation histories considered, on the stellar population synthesis models assumed, on the metallicity evaluation and on the not perfect assumption of the passive evolution of the sample. In the following, all these sources of uncertainty are addressed separately:

- *Dependence on the absolute age evaluation.* Since this approach relies totally on the study of the differential age (or  $D4000_n$ ) evolution to constrain cosmological parameters, it is insensitive to a possible bias in the evaluation of the absolute age of a galaxy.

On the contrary, it is of key importance that the newly introduced technique do not smear in some way the slope of the age-redshift evolution, i.e. that the differential evolution is preserved unmodified. This approach, by definition, keeps the differential evolution unchanged, since a simple linear conversion between the  $D4000_n$  and the age of the galaxy has been used, justifying the robustness of this assumption in Sect. 5.3.1.

- *Dependence on the star formation histories considered.* In Sect. 5.3.1, the choice of using delayed exponentially declining star formation histories with low  $\tau$ 's has been justified by analyzing the SED-fit  $\tau$  distributions of the sample (see Fig. 5.5). However, indeed the study of models with different  $\tau$ 's introduces a spread in the conversion factor  $A$  between the  $D4000_n$  and the age of a galaxy, since the values found with the different SFHs at fixed metallicity have been averaged. The percentage spread in the slope, averaged in the metallicity range probed by the data, is 3.1% and 2.8% for BC03 models respectively in the "high  $D4000$ " regime and 13.4% in the "low  $D4000$ " regime), and 3.9% and 12.4% for *Mastro* models, and the effect is even smaller (almost negligible) in the estimated cosmological parameters. Even if this spread is small, we take in consideration this additional error in the analysis.
- *Dependence on the choice of the stellar population synthesis model.* In Sect. 5.3.1 the analysis of the slopes of the  $D4000_n$ -age relation has been performed both using BC03 and *Mastro* models. As pointed out before, these two models are completely different, being the *Mastro* models based on the latest MILES models and the BC03 models on the STELIB ones. In Tab. 5.2 are shown the values of the slopes in the two  $D4000_n$  regimes for the two models. To quantify the difference between these two models, the values of the slope  $\langle A \rangle$ -metallicity relation in Tab. 5.2 have been interpolated for both models with a quadratic function in the metallicity range probed by the

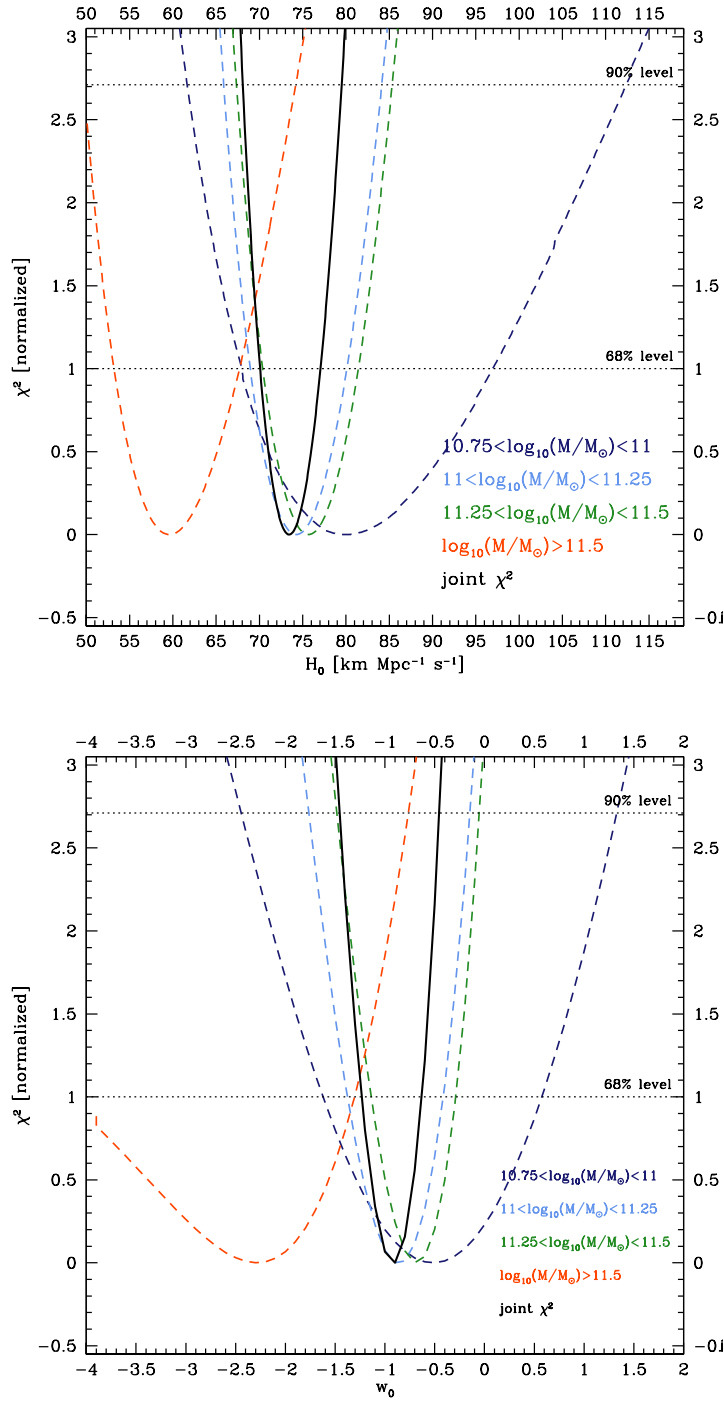


Figure 5.13:  $\chi^2$  of the  $H_0$  (left panel) and of the  $w$  (right panel) evaluation for ETGs in different mass subsamples using Mastro models.

Mass range [ $\log(M/M_\odot)$ ]	$H_0$ [ $\text{km Mpc}^{-1}\text{s}^{-1}$ ]	68% errors [ $\text{km Mpc}^{-1}\text{s}^{-1}$ ]	90% errors [ $\text{km Mpc}^{-1}\text{s}^{-1}$ ]	# galaxies
10.75 – 11	79.5	+17.4/–11.5	+32.8/–17.8	3452
11 – 11.25	74.1	+6/–5.1	+10/–8.2	5429
11.25 – 11.5	75.6	+5.8/–5.2	+9.7/–8.2	3591
> 11.5	59.4	+8.3/–6.1	+14.7/–9.3	1515
joint analysis	73.4	+3.6/–3.3	+6.1/–5.3	13987

Table 5.5: *Hubble constant (in unit of  $\text{km Mpc}^{-1}\text{s}^{-1}$ ) and relative errors using Mastro models.*

Mass range [ $\log(M/M_\odot)$ ]	$w$	68% errors	90% errors	# galaxies
10.75 – 11	-0.5	+1.0/–1.1	+1.8/–1.9	3452
11 – 11.25	-0.9	+0.4/–0.4	+0.7/–0.8	5429
11.25 – 11.5	-0.7	+0.4/–0.4	+0.6/–0.7	3591
> 11.5	-2.3	+0.9/–1.6	+1.5/–1.6	1515
joint analysis	-0.9	+0.2/–0.3	+0.4/–0.5	13987

Table 5.6: *Dark energy equation-of-state parameter  $w$  and relative errors using Mastro models.*

data, as reported in Fig. 5.9. The mean percentage difference between the slope obtained from the two models is 2.8% in the "low  $D4000$ " regime and 13.4% in the "high  $D4000$ " regime.

The effect of this percentage difference between the models has been evaluated by performing the same analysis described in Sect. 5.5.2 with *Mastro* models. The values of  $H_0$  and  $w$  obtained in the different mass bins are shown in Tab. 5.5 and Tab. 5.6, and the corresponding  $\chi^2$  are shown in Fig. 5.13. After marginalizing and doing the joint analysis combining the informations of all the mass bins, using *Mastro* models it has been found  $H_0 = 73.4 \pm 3.5 \text{ kmMpc}^{-1}\text{s}^{-1}$  and  $w = -0.9 \pm 0.3$ . Therefore no significant difference has been found between BC03 and *Mastro* models, obtaining values for both  $H_0$  and  $w$  compatible within the  $1\sigma$  errors.

- *Dependence on metallicity and on star formation.* An important test of this analysis is to verify the robustness of the results against the choice of the value of the metallicity, since it is the primary parameter to obtain the correct slope of the  $D4000_n$ -age relation. To check that the analysis is not biased in that sense, it has been studied the mass bin with the highest num-

Mass range [ $\log(M/M_\odot)$ ]	$H_0$ km Mpc $^{-1}$ s $^{-1}$	68% errors km Mpc $^{-1}$ s $^{-1}$	90% errors km Mpc $^{-1}$ s $^{-1}$	# galaxies
11 – 11.25	72.2	+4.9/-4.2	+8.3/-6.7	5429
"low Z"	71.7	+7.7/-6.1	+13.5/-9.6	2717
"high Z"	70.8	+5.3/-4.5	+9.1/-7.2	2712
$EW_0(H\alpha) < 0.5\text{\AA}$	70.4	+5.8/-4.8	+10/-7.7	3245

Table 5.7: Hubble constant (in unit of km Mpc $^{-1}$ s $^{-1}$ ) and relative errors for  $11 < \log(M/M_\odot) < 11.25$  sample, for the same mass bin sample divided below the median metallicity, above the median metallicity and selected with  $EW_0(H\alpha) < 0.5\text{\AA}$ , using BC03 models.

Mass range [ $\log(M/M_\odot)$ ]	$w$	68% errors	90% errors	# galaxies
11 – 11.25	-1	+0.3/-0.5	+0.6/-0.8	5429
"low Z"	-1.1	+0.5/-0.6	+0.9/-1.1	2717
"high Z"	-1.2	+0.4/-0.5	+0.7/-0.9	2712
$EW_0(H\alpha) < 0.5\text{\AA}$	-1.2	+0.4/-0.5	+0.7/-1	3245

Table 5.8: Dark energy equation-of-state  $w$  and relative errors for  $11 < \log(M/M_\odot) < 11.25$  sample, for the same mass bin sample divided below the median metallicity, above the median metallicity and selected with  $EW_0(H\alpha) < 0.5\text{\AA}$ , using BC03 models.

ber of galaxies ( $11 < \log(M/M_\odot) < 11.25$ ), dividing it into two subsample sampling different metallicity ranges; the sample has been divided below its median metallicity ("low metallicity" sample) and above its median metallicity ("high metallicity" sample), to keep the number size of the resulting subsamples similar. In this way, it has been created two subsample with significantly different values of metallicity ( $Z/Z_\odot = 0.92$  and  $Z/Z_\odot = 1.38$ , respectively).

In Fig. 5.14 (upper panel) it is shown the  $D4000_n$ -z relation of the parent sample (in black) and of the "low metallicity" and "high metallicity" subsamples (respectively in blue and red). The median metallicity of the two subsamples has been evaluated to obtain, for each one, the correct A parameter. The corresponding  $D4000_n$ -redshift relations result rather different between the "low metallicity" and the "high metallicity" sample; however, given the different metallicity and therefore conversion parameter A, the fit to  $H_0$  and  $w$  gives results in perfect agreement, as it is possible to see from the  $\chi^2$  in the lower panels of Fig. 5.14 and from the values reported in Table

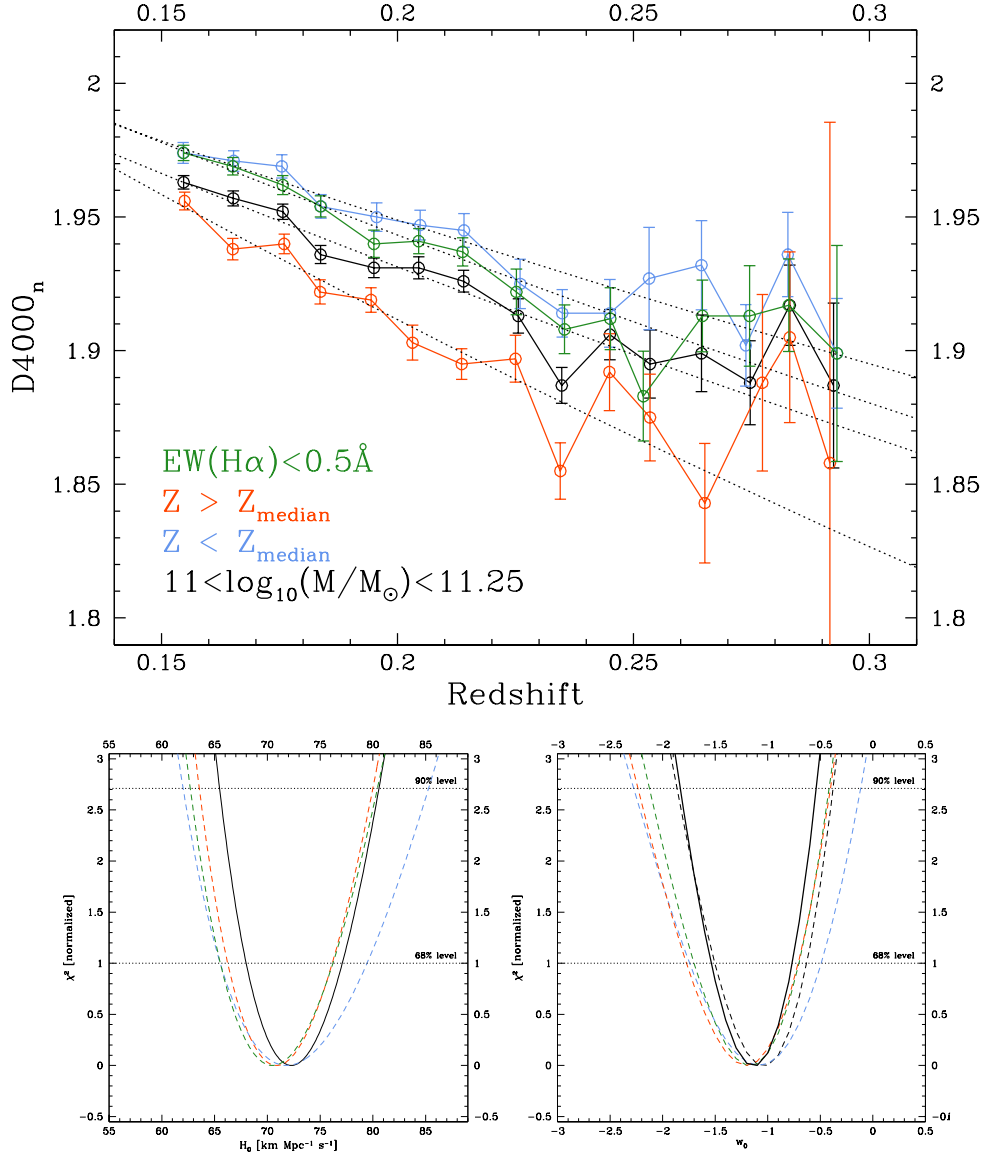


Figure 5.14: *Upper panel:  $D4000$ -redshift relation for ETGs with  $11 < \log(M/M_{\odot}) < 11.25$  (in black), for the same mass bin sample divided below the median metallicity (in blue) and above the median metallicity (in red), and for the same mass bin selected with  $EW_0(H\alpha) < 0.5 \text{ \AA}$  (in green). Lower panels: corresponding  $\chi^2$  for  $H_0$  and  $w$ .*

5.7 and Table 5.8.

Furthermore, from the analysis of the emission lines of the ETGs sample, it has been found that, in spite of the rather strict selection criterium applied, there still exist a tail in the  $EW_0(H\alpha)$  and  $EW_0([OIII]\lambda 3727)$ . On the one hand, as pointed out in Sect. 5.2.1, these are quite low levels of equivalent widths, and the distributions of the eClass parameter and the specific star formation rate obtained from the SED fitting for the galaxies with a significant detection are characteristic of a passive population. On the other hand, this may be an indication that the sample contains a certain number of galaxies with undergoing star formation or AGN activity. This approach relies strongly on the assumption that we are selecting a sample of passively evolving galaxies, that traces uniformly the age evolution of the Universe as a function of redshift. To test if there is a such kind of bias in the results, to the same mass subsample chosen before ( $11 < \log(M/M_\odot) < 11.25$ ) has been applied an even stricter selection, considering only those galaxies for which  $EW_0(H\alpha) < 0.5 \text{ \AA}$  (that is the median of the  $EW_0(H\alpha)$  distribution). The metallicity of this sample has been evaluated, and the analysis of the Hubble constant and dark energy equation-of-state parameter redone; and the results are shown in Fig. 5.14 (green lines), and Tab. 5.7 and Tab. 5.8. The value obtained from this analysis well agrees with the value obtained not cutting the sample in  $EW_0(H\alpha)$ . So, it can be concluded that the results are robust also against the presence of galaxies with small values of  $EW_0(H\alpha)$ .

Source of uncertainty uncertainty	Effect	Impact on $H_0$	Impact on $w$
Absolute age evaluation	possible underestimate of the absolute ages using $D4000_n$	none	none
SFHs assumption	spread in the conversion factor A	< 0.01%	< 0.1%
Stellar population synthesis model used	different $D4000_n$ -age relation within models	1.1%	10%
Metallicity estimate	if incorrect, may bias the A parameter	1.4%	15%
non-perfect approximation of passive evolution	possible bias in the $D4000_n$ -z evolution	2.5%	20%
<b>Total systematic error</b>		<b>3.1%</b>	<b>27%</b>

Table 5.9: Summary of the sources of uncertainty and their impact (in percentage) on the cosmological parameters.

## 5.6 Total systematic uncertainty and results

In Sect. 5.5.4 the impact of systematics on the estimate of both the Hubble parameter  $H_0$  and the dark energy equation-of-state parameter  $w$  (assuming  $w = \text{constant}$ ) is quantified. All these source of uncertainties, along with their effect, are summarized in Tab. 5.9; to evaluate the effect of systematics, most of the tests have been performed using the mass sample with the highest number of galaxies ( $11 < \log(M/M_\odot) < 11.25$ ). The total estimated effect has been evaluated by summing in quadrature the errors, and it is also reported in Tab. 5.9.

In conclusion:

- the estimated value for  $H_0$ , including both statistic and systematic errors, is  $H_0 = 72.6 \pm 2.9(stat) \pm 2.3(syst)$  km Mpc $^{-1}$ s $^{-1}$ ;
- the estimated value for  $w$ , including both statistic and systematic errors, is  $w = -1 \pm 0.2(stat) \pm 0.3(syst)$ .

## 5.7 Conclusions about constraining Universe expansion history with ETGs

The feasibility of a direct “cosmic chronometers” approach to constrain cosmological parameter has been studied, analyzing a sample of ETGs in the range  $0 < z < 2$  obtained matching the SDSS ETGs sample, the zCOSMOS “ETGs” sample described in Sect. ??sec:ETGs, and 13 high- $z$  ETGs from GMASS (Cimatti et al., 2008). Severe degenerations with SFHs and metallicity have been found to affect this kind of analysis. A mock catalog of 100,000 galaxies has been simulated in order to determine, with a  $0 - th$  order test, the errors associated with the age evaluation from SED-fitting. It has been found this error to be *at least* (averaging over the entire age range spanned from the simulation) of the order of 17%, estimated to be too large to reach the aim of constraining cosmological parameter (especially because this percentage error does not take into account also the metallicity degeneracy).

A new methodology to obtain the expansion rate of the Universe using the “cosmic chronometer” technique has been, therefore, developed, with the aim of minimizing the dependence on systematics. To this extent, the  $D4000_n$  feature at fixed metallicity has been found to correlate linearly with age, for the range of ages of interest. This feature has been studied using theoretical synthetic stellar population models and it has been shown that it is robust to choice of metallicity, star formation history, and different stellar population models. Within this linear approximation, the theoretical model  $D4000_n(z)$  as a function of the various cosmological parameters has been evaluated too.

A sample of ETGs has been obtained from the SDSS survey, using both photometric and spectroscopic informations to select the most passive and massive galaxies ( $\log(M/M_\odot) > 10.75$ ). The sample has been divided in small mass bins (0.25 dex), in order to avoid possible bias from mass downsizing and to have homogeneous redshift of formation and metallicity across the entire redshift range. The  $D4000_n - z$  relations show, in each subsample, a clear redshift evolution, with galaxies at low redshift having always a higher  $D4000_n$ , and hence higher ages. Moreover the four subsamples give an evident proof of mass-downsizing, since at each redshift galaxies with higher masses have always an higher  $D4000_n$  than galaxies at lower masses.

The Hubble constant  $H_0$  and the dark energy equation-of-state parameter  $w$  has been evaluated by fitting the  $D4000_n - z$  relations with the theoretical model defined before. From the joint analysis it has been found that  $H_0 = 72.6 \pm 2.9(stat) \pm 2.3(syst) \text{ km Mpc}^{-1} \text{ s}^{-1}$  and that  $w = -1 \pm 0.2(stat) \pm 0.3(syst)$ , assuming a constant  $w$ . The value obtained for  $w$  is in agreement with the value found from the WMAP 7-years analysis and with the one obtained from Amanullah et al. (2010); the value of  $H_0$  is within  $1\sigma$  error with the one obtained by Riess

et al. (2009), and a comparable level of precision is reached. Direct proof of the acceleration of the Universe has been provided, even if the sample only reaches up to  $z \sim 0.3$ .

The results have been demonstrated to be robust to the choice of galaxy mass, since the results in the single mass subsample are all within the  $1\sigma$  errors. Moreover, also the effect of the dependence of the results on different systematics (i.e. the estimate of the absolute age of a galaxy from the  $D4000_n$ , the star formation histories considered, the stellar population synthesis models assumed, the metallicity evaluation and the not perfect assumption of the passive evolution of the sample) has been studied. The dependence on the SFHs has been found to be small, and has been taken into account in the cosmological parameters evaluation. By studying the sample with different synthetic stellar populations models (BC03 and *Mastro*), in different metallicity regimes and for different selection of  $EW_0(H\alpha)$ , it has been shown that the analysis is also robust to the metallicity evaluation and to the non-perfect approximation of passive evolution of the sample, and that there is no significant difference when using different models for studying the  $D4000_n$ -age relation.



---

# Chapter 6

## Conclusions and future prospects

In Chapt. 2 growing observational evidences have been given supporting the fact that ETGs represent a simple and homogeneous population in terms of colors, morphology and stellar population contents; despite being less numerous than spiral and irregular galaxies, they sum up most of the mass of the Universe; analysis of their structural properties have highlighted that the bulk of the stars for these systems has formed at  $z \sim 2 - 3$ , and that the assembly of their mass was almost complete already at  $z \sim 0.7 - 0.8$ ; these galaxies, therefore are supposed to be evolved passively from that redshift to the present, representing at each redshift the oldest object of the Universe. These properties make ETGs really special candidates to probe the evolution of the Universe.

In this Thesis it has been presented a detailed study of the properties of early-type galaxies, aimed at a twofold goal: study which constraints can be set to disentangle which is the main driver of ETGs evolution between mass and environment, and develop a robust approach, using ETGs as “*cosmic chronometers*”, to measure the expansion history of the Universe minimizing the dependences on prior assumptions and the degeneracies.

In the following, are reviewed the main results of the work done in this Thesis:

1. **ETGs sample definition and characterization.** A sample of ETGs spanning a wide redshift range ( $0 \lesssim z \lesssim 1$ ) has been selected from SDSS and zCOSMOS survey, and its properties analyzed. The main steps developed have been:
  - development of a reliable selection criterion of ETGs, obtained from a exhaustive joint analysis of photometric, spectroscopic and morphologic properties, in order to reduce as much as possible the contamination by the presence of starforming, blue outliers;

- optimization of the photometry of the galaxy with the application of zeropoint shifts and error corrections, evaluated by comparing the observed and the best-fit theoretical magnitude distributions;
- definition of three ETGs sample. The SDSS ETGs sample has been extracted from a matching between the SDSS-DR6 and the 2MASS survey, and selected for its photometric and spectroscopic properties (97,460 ETGs in the redshift range  $0.02 < z < 0.5$ ); the zCOSMOS “*Red galaxies*” sample has been extracted from the zCOSMOS 10k bright spectroscopic sample, and selected just with a wide photometric criterion in order to keep high the statistic (2,093 galaxies); the zCOSMOS “*ETGs*” sample has been extracted from the *Red galaxies* zCOSMOS sample by discarding all galaxies with strong emission lines, confirmed spiral morphology, bluer colors, and strong  $24\mu\text{m}$  emission (981 galaxies in the redshift range  $0.05 < z < 1.2$ );
- evaluation of the physical parameters (mass, star formation history, dust reddening, age) of the selected ETGs, obtained with a SED-fitting technique using different stellar population synthesis models, and discussion of their robustness.

2. **Analysis of the dependence of ETGs properties on mass and environment.** The  $(U - V)$  restframe colors and spectra of two subsamples of early-type galaxies have been studied, extracted from the zCOSMOS spectroscopic survey in the redshift range  $0.1 < z < 1$ . Both color and spectral features (i.e., D4000 and  $EW_0(H\delta)$ ) have been analyzed to explore their dependence on mass and environment, and provide some insights into the main drivers of galaxy evolution.

From the performed analysis, the following results have been found:

- a dependence of the color on mass ( $\langle \Delta(U - V)_{rest} \rangle = 0.093 \pm 0.007$  mag in the mass range  $10 < \log_{10}(M/M_{\odot}) < 10.8$ ), with a mean slope of the color-mass relation  $\langle S_M \rangle = 0.12 \pm 0.005$ . A hint of steepening has been found as a function of increasing environment;
- a weaker dependence of the color on the local density of the environment ( $\langle \Delta(U - V)_{rest} \rangle = 0.027 \pm 0.008$  mag in the overdensity range  $0.1 \lesssim \log_{10}(1 + \delta) \lesssim 1.2$ ), with a slope always smaller than  $S_{\delta} \approx 0.04$ ;
- a dependence of spectroscopic index on mass ( $\langle \Delta D4000 \rangle = 0.11 \pm 0.02$  and  $\Delta EW_0(H\delta) = 0.28 \pm 0.08 \text{ \AA}$  in the mass range  $10.2 < \log_{10}(M/M_{\odot}) < 10.8$ ) when averaging over the entire redshift range;
- a weaker dependence on the local density of the environment ( $\langle \Delta D4000 \rangle = 0.05 \pm 0.02$  and an insignificant difference for  $EW_0(H\delta)$  in the environment range  $0.1 \lesssim \log_{10}(1 + \delta) \lesssim 1.2$ ) when averaging over the entire redshift range;

- a differential evolution has been found between more and less massive galaxies, with massive galaxies or galaxies residing in relatively high density environments having a stronger D4000 break and a small value of  $EW_0(H\delta)$  almost constant with redshift, implying that no significant episodes of star formation have occurred in these galaxies since  $z \sim 1$ , while low-mass galaxies having values of spectroscopic indices witnessing an ongoing evolution at these redshifts;
- strong evidences of mass-downsizing, obtained from the study of the lookback time to formation of ETGs (evaluated with SED-fitting) as a function of mass. Massive galaxies ( $\log_{10}(M/M_{\odot}) \sim 11$ ) have been found to form their stars at  $z \sim 2$ , while less massive ones ( $\log_{10}(M/M_{\odot}) \sim 10.25$ ) to form their stars at  $z \lesssim 1$ , almost independently on the models of stellar population synthesis considered;
- an age difference of  $\approx 3$  Gyrs within a mass range  $10 < \log_{10}(M/M_{\odot}) < 10.8$  (using passive evolution models with high age/ $\tau$  values), while an insignificant age difference between different environments (with the caveat of a small range of overdensities probed);

Combining the results of the color and spectral analysis, from this work can be concluded that the main driver of the the evolution of ETGs is mass, while environment plays a less important, although non-negligible, role.

3. **Development of an upgraded methodology to constrain the cosmic expansion history using ETGs as “cosmic chronometers”.** The standard “cosmic chronometers” approach has been studied by evaluating the age-redshift relation for a sample of ETGs in the range  $0 < z < 2$ . Many problem of degeneracy and model dependence have been found in evaluating the age with a SED-fitting technique, that make this direct approach unstable and unreliable.

A new methodology has, therefore, been developed, with the aim of minimizing the dependence on systematics. The main step undertaken have been:

- identification of a spectroscopic feature which correlates with the age of the galaxy, to be used as a proxy of age. The 4000 Å break has been selected, and found to correlate linearly with age at fixed metallicity, for the range of ages of interest; this feature has been selected also because is easily measurable also in spectra with intermediate S/N and resolution;
- study of the theoretical D4000-age relation using different synthetic stellar population models (BC03 and *Mastro*), that has been demonstrated to be robust to choice of metallicity, star formation history and different stellar population models;

- evaluation of the theoretical model  $D4000_n(z)$  as a function of the various cosmological parameters;
- selection of a sample of ETGs in the range  $0.15 < z < 0.3$  obtained from the SDSS, using both photometric and spectroscopic informations to select the most passive and massive galaxies ( $\log(M/M_\odot) > 10.75$ ). Their properties have been evaluated, obtaining stellar masses with a SED-fitting technique and metallicity from the spectroscopic analysis from Gallazzi et al. (2005), and the original sample has been divided into four mass subsamples, in order to avoid possible bias from mass downsizing and to have homogeneous redshift of formation and metallicity across the entire redshift range;
- inspection of the D4000-redshift relations obtained from the four mass subsamples, that gives clear evidences of both cosmological evolution of the Universe and mass-downsizing;
- evaluation of the Hubble constant from a joint analysis of the best-fit if the D4000-redshift relations of the four mass subsamples, obtaining  $H_0 = 72.6 \pm 2.9(stat) \pm 2.3(syst) \text{ km Mpc}^{-1}\text{s}^{-1}$
- evaluation of the dark energy equation-of-state parameter (assuming  $w = \text{constant}$ ) from a joint analysis of the best-fit if the D4000-redshift relations of the four mass subsamples, obtaining  $w = -1 \pm 0.2(stat) \pm 0.3(syst)$ ;
- detailed analysis of the possible systematic source of uncertainty of the approach, by studying the effect of the dependence of the results on different systematics, i.e. the estimate of the absolute age of a galaxy from the D4000, the star formation histories considered, the stellar population synthesis models assumed, the metallicity evaluation and the not perfect assumption of the passive evolution of the sample. All these systematic uncertainties have been taken into account in the systematic error associated to both evaluations.

This new method has been proven to be competitive with the “more standard” approaches (Sne studies, BAO, ...), obtaining results compatible with the most recent analysis of Riess et al. (2009) for  $H_0$  and Amanullah et al. (2010) for  $w$ , reaching also a comparable level of precision. Direct proofs of the acceleration of the Universe have been provided, even if the sample only reaches up to  $z \sim 0.3$ . These results, given in particular the narrow redshift leverage of the sample considered, show the potential of this approach.

## 6.1 Future prospects

The potential of the new introduced technique to constrain the expansion history of the Universe using the “*cosmic chronometers*” approach has been shown by evaluating the Hubble constant  $H_0$  and the dark energy equation-of-state parameter  $w$  with high accuracy even using only low-redshift ETGs, i.e. SDSS ETGs with  $0.15 < z < 0.3$ .

However, the full application of this approach would be in setting constraints to the Hubble parameter  $H(z)$  up to redshift  $z \sim 1$  with a better precision with respect to present measurements (see Sect. 1.5). On the one side, this task has become one of the golden goals of modern cosmology, since a measure of  $H(z)$  would provide a direct probe of the nature of dark energy and of its evolution, making possible to rule out a variety of cosmological models so far proposed and possibly to find a coherent model to explain Universe’s evolution. On the other side, this approach is an ideal candidate to probe  $H(z)$ , due to its strengths: i) studying the differential evolution of the Universe it probes *directly*  $H(z)$ , and not its integral (such as the luminosity distance used for supernovae); ii) it is independent on the overall normalization of the age- $z$  (or D4000- $z$ ) relation, since the constraints are set just by analyzing the derivative of the relations; iii) the study of the D4000- $z$  relations instead of the age- $z$  relation has been proven to be reliable, robust and with limited dependence on SFHs and model assumptions.

In Fig. 6.1 the D4000-redshift relation for a sample of ETGs in the range  $0 \lesssim z \lesssim 1$  is shown. The sample has been selected combining the SDSS ETGs sample described in the analysis of Chapt. 5, the zCOSMOS *ETGs* sample discussed in the spectroscopic analysis of Chapt. 4, a sample of red galaxies in 24 galaxy clusters in the redshift range  $0.17 < z < 0.92$  obtained by Stern and collaborators with the LRIS instrument on the Keck I telescope (Stern et al., 2010), and a sample of passive galaxies in a  $z > 1$  UDS VLT FORS2 study (provided by Henry Pearce and James Dunlop).

The possibility of obtaining a direct evaluation of  $H(z)$  will be studied analyzing the differential evolution of this relation, in combination with the study of similar relations obtained by spectroscopic indices known to correlate as well with age (such as  $H\beta$ ), and indeed Fig. 6.1 provides already a clear evidence of the redshift evolution of the Universe.

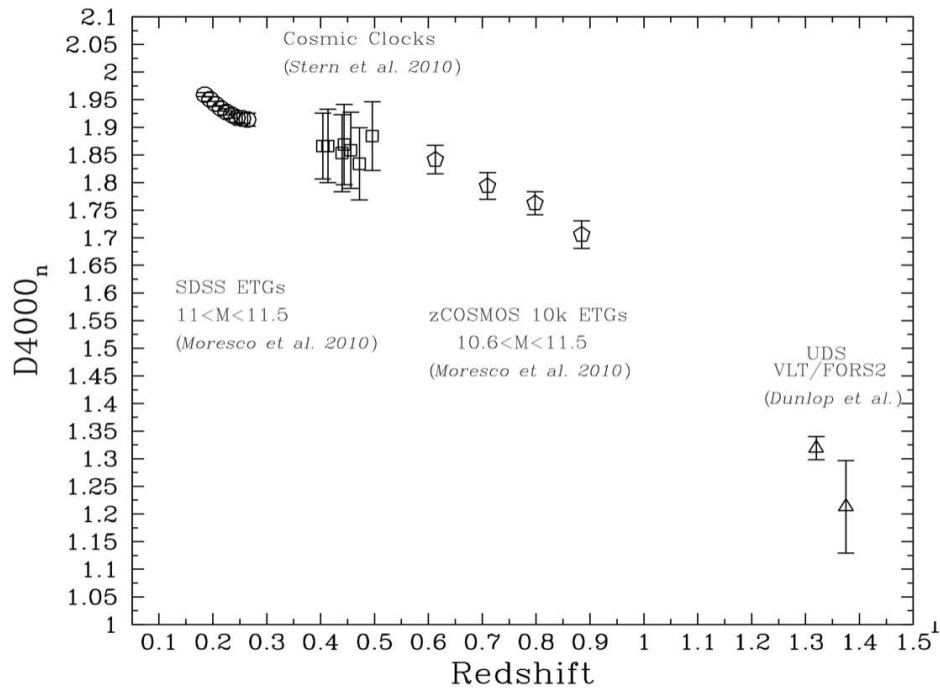


Figure 6.1:  $D_{4000}$ -redshift relation for a sample of ETGs obtained merging the SDSS ETGs sample, the zCOSMOS ETGs sample, a sample of red galaxies in 24 galaxy clusters in the redshift range  $0.17 < z < 0.92$  (Stern et al., 2010), and a sample of passive galaxies in a  $z > 1$  UDS VLT FORS2 study (provided by Henry Pearce and James Dunlop).

# Bibliography

- Abazajian K. N., Adelman-McCarthy J. K., Agüeros M. A., et al., 2009, *ApJS*, 182, 543
- Amanullah R., Lidman C., Rubin D., et al., 2010, *ApJ*, 716, 712
- Arimoto N., Yoshii Y., 1987, *A&A*, 173, 23
- Avni Y., Bahcall J. N., 1980, *ApJ*, 235, 694
- Baldry I. K., Glazebrook K., Brinkmann J., et al., 2004, *ApJ*, 600, 681
- Baldry I. K., Balogh M. L., Bower R. G., et al., 2006, *MNRAS*, 373, 469
- Baldry I. K., Glazebrook K., Driver S. P., 2008, *MNRAS*, 388, 945
- Balogh M. L., Morris S. L., Yee H. K. C., et al., 1999, *ApJ*, 527, 54
- Balogh M. L., Baldry I. K., Nichol R., et al., 2004, *ApJ*, 615, L101
- Baugh C. M., 2006, *RPPh*, 69, 3101
- Baum W. A., 1959, *PASP*, 71, 106
- Bell E. F., Wolf C., Meisenheimer K., et al., 2004, *ApJ*, 608, 752
- Bell E. F., Naab T., McIntosh D. H., et al., 2006, *ApJ*, 640, 241
- Bernardi M., Nichol R. C., Sheth R. K., et al., 2006, *AJ*, 131, 1288
- Bertoldi F., Carilli C., Aravena M., et al., 2007, *ApJS*, 172, 132
- Blakeslee J. P., Franx M., Postman M., et al., 2003, *ApJ*, 596, L143
- Blumenthal G. R., Faber S. M., Primack J. R., et al., 1984, *Natur*, 311, 517

- Bolzonella M., Miralles J.-M., Pelló R., 2000, *A&A*, 363, 476
- Bolzonella M., Kovač K., Pozzetti L., et al., 2010, *A&A*, 524, A76
- Bouchet P., Lequeux J., Maurice E., et al., 1985, *A&A*, 149, 330
- Bower R. G., Lucey J. R., Ellis R. S., 1992, *MNRAS*, 254, 601
- Bower R. G., Kodama T., Terlevich A., 1998, *MNRAS*, 299, 119
- Bower R. G., Terlevich A., Kodama T., et al., 1999, *ASPC*, 163, 211
- Bressan A., Chiosi C., Fagotto F., 1994, *ApJS*, 94, 63
- Bruzual A. G., 1983, *ApJ*, 273, 105
- Bruzual A. G., Charlot S., 1993, *ApJ*, 405, 538
- Bruzual G., Charlot S., 2003, *MNRAS*, 344, 1000
- Bundy K., Ellis R. S., Conselice C. J., et al., 2006, *ApJ*, 651, 120
- Bundy K., Treu T., Ellis R. S., 2007, *ApJ*, 665, L5
- Burstein D., Faber S. M., Gaskell C. M., et al., 1984, *ApJ*, 287, 586
- Buser R., 1978, *A&A*, 62, 411
- Caldwell R. R., Kamionkowski M., 2009, *ARNPS*, 59, 397
- Calzetti D., Armus L., Bohlin R. C., et al., 2000, *ApJ*, 533, 682
- Capak P., Aussel H., Ajiki M., et al., 2007, *ApJS*, 172, 99
- Capozziello S., Cardone V. F., Funaro M., et al., 2004, *PhRvD*, 70, 123501
- Caputi K. I., McLure R. J., Dunlop J. S., et al., 2006, *MNRAS*, 366, 609
- Caputi K. I., Kovač K., Bolzonella M., et al., 2009, *ApJ*, 691, 91
- Caputi K. I., Lilly S. J., Aussel H., et al., 2009, *ApJ*, 707, 1387
- Carroll S. M., 2001, *LRR*, 4, 1
- Carson D. P., Nichol R. C., 2010, *MNRAS*, 408, 213
- Cassata P., Guzzo L., Franceschini A., et al., 2007, *ApJS*, 172, 270
- Cassata P., Cimatti A., Kurk J., et al., 2008, *A&A*, 483, L39
- Charlot S., Bruzual A. G., 1991, *ApJ*, 367, 126

- Charlot S., Bruzual G., 2011, in preparation
- Cimatti A., Daddi E., Renzini A., et al., 2004, *Natur*, 430, 184
- Cimatti A., Daddi E., Renzini A., 2006, *A&A*, 453, L29
- Cimatti A., 2007, *IAUS*, 235, 350
- Cimatti A., Cassata P., Pozzetti L., et al., 2008, *A&A*, 482, 21
- Cimatti A., 2009, *AIPC*, 1111, 191
- Coleman G. D., Wu C.-C., Weedman D. W., 1980, *ApJS*, 43, 393
- Cooper M. C., Coil A. L., Gerke B. F., et al., 2010, *MNRAS*, 409, 337
- Copeland E. J., Sami M., Tsujikawa S., 2006, *IJMPD*, 15, 1753
- Cowie L. L., Songaila A., Hu E. M., et al., 1996, *AJ*, 112, 839
- Cowie L. L., Songaila A., Barger A. J., 1999, *AJ*, 118, 603
- Crawford S. M., Blyth S., Cress C., et al., 2011, *AAS*, 43, #214.06
- Cucciati O., Iovino A., Kovač K., et al., 2010, *A&A*, 524, A2
- Daddi E., Renzini A., Pirzkal N., et al., 2005, *ApJ*, 626, 680
- De Lucia G., Springel V., White S. D. M., et al., 2006, *MNRAS*, 366, 499
- de Propris R., Stanford S. A., Eisenhardt P. R., et al., 1999, *AJ*, 118, 719
- Dressler A., Lynden-Bell D., Burstein D., et al., 1987, *ApJ*, 313, 42
- Drory N., Salvato M., Gabasch A., et al., 2005, *ApJ*, 619, L131
- Djorgovski S., Davis M., 1987, *ApJ*, 313, 59
- Dunlop J., Peacock J., Spinrad H., et al., 1996, *Natur*, 381, 581
- Eggen O. J., Lynden-Bell D., Sandage A. R., 1962, *ApJ*, 136, 748
- Ellis R. S., Smail I., Dressler A., et al., 1997, *ApJ*, 483, 582
- Elvis M., Civano F., Vignali C., et al., 2009, *ApJS*, 184, 158
- Einstein A., 1917, *SPAW*, 142
- Faber S. M., Jackson R. E., 1976, *ApJ*, 204, 668
- Ferreras I., Melchiorri A., Silk J., 2001, *MNRAS*, 327, L47

- Feulner G., Gabasch A., Salvato M., et al., 2005, *ApJ*, 633, L9
- Finoguenov A., Guzzo L., Hasinger G., et al., 2007, *ApJS*, 172, 182
- Fitzpatrick E. L., 1986, *AJ*, 92, 1068
- Fontana A., Pozzetti L., Donnarumma I., et al., 2004, *A&A*, 424, 23
- Frieman J. A., Turner M. S., Huterer D., 2008, *ARA&A*, 46, 385
- Gallazzi A., Charlot S., Brinchmann J., et al., 2005, *MNRAS*, 362, 41
- Gallazzi A., Charlot S., Brinchmann J., et al., 2006, *MNRAS*, 370, 1106
- Gavazzi G., Scodreggio M., 1996, *A&A*, 312, L29
- Gavazzi G., Bonfanti C., Sanvito G., et al., 2002, *ApJ*, 576, 135
- Glazebrook K., Abraham R. G., McCarthy P. J., et al., 2004, *Natur*, 430, 181
- Gobat R., Rosati P., Strazzullo V., et al., 2008, *A&A*, 488, 853
- Guth A. H., 1981, *PhRvD*, 23, 347
- Hamilton D., 1985, *ApJ*, 297, 371
- Hasinger G., Cappelluti N., Brunner H., et al., 2007, *ApJS*, 172, 29
- Heavens A., Panter B., Jimenez R., et al., 2004, *Natur*, 428, 625
- Hoaglin D. C., Mosteller F., Tukey J. W., 1983, John Wiley & Sons, 404-414
- Mo H., van den Bosch F. C., White S., 2010, Cambridge University Press, 587-593
- Holden B. P., van der Wel A., Franx M., et al., 2005, *ApJ*, 620, L83
- Hubble E., 1929, *PNAS*, 15, 168
- Hubble E. P., 1936, Oxford University Press, 45
- Huterer D., 2010, arXiv, arXiv:1010.1162
- Ilbert O., Arnouts S., McCracken H. J., et al., 2006, *A&A*, 457, 841
- Iovino A., Cucciati O., Scodreggio M., et al., 2010, *A&A*, 509, A40
- Jarosik N., Bennett C. L., Dunkley J., et al., 2011, *ApJS*, 192, 14
- Jimenez R., Loeb A., 2002, *ApJ*, 573, 37
- Jimenez R., Verde L., Treu T., et al., 2003, *ApJ*, 593, 622

- Juneau S., Glazebrook K., Crampton D., et al., 2005, *ApJ*, 619, L135
- Kauffmann G., Heckman T. M., White S. D. M., et al., 2003, *MNRAS*, 341, 33
- Kaviraj S., Khochfar S., Schawinski K., et al., 2008, *MNRAS*, 388, 6
- Kelson D. D., van Dokkum P. G., Franx M., et al., 1997, *ApJ*, 478, L13
- Kennicutt R. C., Jr., 1998, *ARA&A*, 36, 189
- Kinney A. L., Calzetti D., Bohlin R. C., et al., 1996, *ApJ*, 467, 38
- Knobel C., Lilly S. J., Iovino A., et al., 2009, *ApJ*, 697, 1842
- Koekemoer A. M., Aussel H., Calzetti D., et al., 2007, *ApJS*, 172, 196
- Komatsu E., Smith K. M., Dunkley J., et al., 2011, *ApJS*, 192, 18
- Kormendy J., 1977, *ApJ*, 218, 333
- Kovač K., Lilly S. J., Cucciati O., et al., 2010, *ApJ*, 708, 505
- Krauss L. M., 2003, *ApJ*, 596, L1
- Kriek M., van Dokkum P. G., Franx M., et al., 2006, *ApJ*, 649, L71
- Lamareille F., Contini T., Le Borgne J.-F., et al., 2006, *A&A*, 448, 893
- Larson R. B., 1974, *MNRAS*, 166, 585
- Le Borgne J.-F., Bruzual G., Pelló R., et al., 2003, *A&A*, 402, 433
- Le Borgne D., Abraham R., Daniel K., et al., 2006, *ApJ*, 642, 48
- Le Fèvre O., Saisse M., Mancini D., et al., 2003, *SPIE*, 4841, 1670
- Lilly S. J., Le Fèvre O., Renzini A., et al., 2007, *ApJS*, 172, 70
- Lilly S. J., Le Brun V., Maier C., et al., 2009, *ApJS*, 184, 218
- Longhetti M., Saracco P., 2009, *MNRAS*, 394, 774
- Maraston C., Greggio L., Renzini A., et al., 2003, *A&A*, 400, 823
- Maraston C., 2005, *MNRAS*, 362, 799
- Maraston, C. & Strömbäck, G., 2011, *MNRAS* submitted
- Masjedi M., Hogg D. W., Cool R. J., et al., 2006, *ApJ*, 644, 54
- Mather J. C., Cheng E. S., Cottingham D. A., et al., 1994, *ApJ*, 420, 439

- McCarthy P. J., Le Borgne D., Crampton D., et al., 2004, *ApJ*, 614, L9
- McCracken H. J., Capak P., Salvato M., et al., 2010, *ApJ*, 708, 202
- Mignoli M., Zamorani G., Scodreggio M., et al., 2009, *A&A*, 493, 39
- Moresco M., Pozzetti L., Cimatti A., et al., 2010, *A&A*, 524, A67
- Moresco M., Jimenez R., Cimatti A., et al., 2010, *JCAP* accepted, arXiv:1010.0831
- Mukhanov V., 2005, Cambridge University Press, 72-74
- Peebles P. J., Ratra B., 2003, *RvMP*, 75, 559
- Peng Y.-j., Lilly S. J., Kovač K., et al., 2010, *ApJ*, 721, 193
- Percival W. J., Reid B. A., Eisenstein D. J., et al., 2010, *MNRAS*, 401, 2148
- Perlmutter S., Aldering G., Goldhaber G., et al., 1999, *ApJ*, 517, 565
- Phillips M. M., 1993, *ApJ*, 413, L105
- Pozzetti L., Bolzonella M., Lamareille F., et al., 2007, *A&A*, 474, 443
- Pozzetti L., Bolzonella M., Zucca E., et al., 2010, *A&A*, 523, A
- Prevot M. L., Lequeux J., Prevot L., et al., 1984, *A&A*, 132, 389
- Renzini A., Ciotti L., 1993, *ApJ*, 416, L49
- Renzini A., 2006, *ARA&A*, 44, 141
- Riess A. G., Filippenko A. V., Challis P., et al., 1998, *AJ*, 116, 1009
- Riess A. G., Macri L., Casertano S., et al., 2009, *ApJ*, 699, 539
- Roberts M. S., 1963, *ARA&A*, 1, 149
- Sánchez-Blázquez P., Peletier R. F., Jiménez-Vicente J., et al., 2006, *MNRAS*, 371, 703
- Sandage A., Visvanathan N., 1978, *ApJ*, 223, 707
- Sandage A., Visvanathan N., 1978, *ApJ*, 225, 742
- Sanders D. B., Salvato M., Aussel H., et al., 2007, *ApJS*, 172, 86
- Saracco P., Longhetti M., Severgnini P., et al., 2005, *MNRAS*, 357, L40
- Scarlata C., Carollo C. M., Lilly S., et al., 2007, *ApJS*, 172, 406

- Schiavon R. P., Faber S. M., Konidaris N., et al., 2006, *ApJ*, 651, L93
- Schinnerer E., Smolčić V., Carilli C. L., et al., 2007, *ApJS*, 172, 46
- Schlegel D. J., Finkbeiner D. P., Davis M., 1998, *ApJ*, 500, 525
- Schmidt M., 1968, *ApJ*, 151, 393
- Scoville N., Aussel H., Brusa M., et al., 2007, *ApJS*, 172, 1
- Skrutskie M. F., Cutri R. M., Stiening R., et al., 2006, *AJ*, 131, 1163
- Spinrad H., Dey A., Stern D., et al., 1997, *ApJ*, 484, 581
- Springel V., White S. D. M., Jenkins A., et al., 2005, *Natur*, 435, 629
- Stanford S. A., Eisenhardt P. R., Dickinson M., 1998, *ApJ*, 492, 461
- Stern D., Jimenez R., Verde L., et al., 2010, *ApJS*, 188, 280
- Stern D., Jimenez R., Verde L., et al., 2010, *JCAP*, 2, 8
- Taniguchi Y., Scoville N., Murayama T., et al., 2007, *ApJS*, 172, 9
- Tasca L. A. M., Kneib J.-P., Iovino A., et al., 2009, *A&A*, 503, 379
- Thomas D., Maraston C., Bender R., et al., 2005, *ApJ*, 621, 673
- Thomas D., Maraston C., Schawinski K., et al., 2007, *IAUS*, 241, 546
- Thomas D., Maraston C., Schawinski K., et al., 2010, *MNRAS*, 404, 1775
- Thomas D., Maraston C., Johansson J., 2011, *MNRAS*, 49
- Tinsley B. M., 1980, *FCPh*, 5, 287
- Toft S., Mainieri V., Rosati P., et al., 2004, *A&A*, 422, 29
- Tojeiro R., Heavens A. F., Jimenez R., et al., 2007, *MNRAS*, 381, 1252
- Tojeiro R., Wilkins S., Heavens A. F., et al., 2009, *ApJS*, 185, 1
- Toomre A., 1977, *egsp.conf*, 401
- Treu T., Ellis R. S., Liao T. X., et al., 2005, *ApJ*, 633, 174
- van Dokkum P. G., Franx M., 1996, *MNRAS*, 281, 985
- van Dokkum P. G., Franx M., Kelson D. D., et al., 1998, *ApJ*, 504, L17
- van Dokkum P. G., Stanford S. A., 2003, *ApJ*, 585, 78

- van Dokkum P. G., 2005, *AJ*, 130, 2647
- Vergani D., Zamorani G., Lilly S., et al., 2010, *A&A*, 509, A42
- Visvanathan N., Sandage A., 1977, *ApJ*, 216, 214
- Worthey G., Faber S. M., Gonzalez J. J., et al., 1994, *ApJS*, 94, 687
- White S. D. M., Rees M. J., 1978, *MNRAS*, 183, 341
- Wuyts S., van Dokkum P. G., Kelson D. D., et al., 2004, *ApJ*, 605, 677
- Yamada T., Kodama T., Akiyama M., et al., 2005, *ApJ*, 634, 861
- Zamojski M. A., Schiminovich D., Rich R. M., et al., 2007, *ApJS*, 172, 468
- Zucca E., Ilbert O., Bardelli S., et al., 2006, *A&A*, 455, 879
- Zucca E., Bardelli S., Bolzonella M., et al., 2009, *A&A*, 508, 1217

# Publications

## zCOSMOS 10k-bright spectroscopic sample. Exploring mass and environment dependence in early-type galaxies

Moresco, M.; Pozzetti, L.; Cimatti, A.; Zamorani, G.; Mignoli, M.; di Cesare, S.; Bolzonella, M.; Zucca, E.; Lilly, S.; Kovač, K.; Scodreggio, M.; Cassata, P.; Tasca, L.; Vergani, D.; Halliday, C.; Carollo, M.; Contini, T.; Kneib, J.-P.; Le Fèvre, O.; Mainieri, V.; Renzini, A.; Bardelli, S.; Bongiorno, A.; Caputi, K.; Coppa, G.; Cucciati, O.; de la Torre, S.; de Ravel, L.; Franzetti, P.; Garilli, B.; Iovino, A.; Kampczyk, P.; Knobel, C.; Lamareille, F.; Le Borgne, J.-F.; Le Brun, V.; Maier, C.; Pellò, R.; Peng, Y.; Perez Montero, E.; Ricciardelli, E.; Silverman, J. D.; Tanaka, M.; Tresse, L.; Abbas, U.; Bottini, D.; Cappi, A.; Guzzo, L.; Koekemoer, A. M.; Leauthaud, A.; Maccagni, D.; Marinoni, C.; McCracken, H. J.; Memeo, P.; Meneux, B.; Nair, P.; Oesch, P.; Porciani, C.; Scaramella, R.; Scarlata, C. and Scoville, N.

2010, A&A, 524, 67 (ArXiv:1009.3376)

### Abstract

*Aims.* We present the analysis of the U-V rest-frame color distribution and some spectral features as a function of mass and environment for a sample of early-type galaxies up to  $z = 1$  extracted from the zCOSMOS spectroscopic survey. This analysis is used to place constraints on the relative importance of these two properties in controlling galaxy evolution.

*Methods.* We used the zCOSMOS 10k-bright sample, limited to the AB magnitude range  $15 < I < 22.5$ , from which we extracted two different subsamples of early-type galaxies. The first sample ("red galaxies") was selected using a photometric classification (2098 galaxies), while in the second case ("ETGs") we combined morphological, photometric, and spectroscopic properties to obtain a more reliable sample of elliptical, red, passive, early-type galaxies (981 galaxies). The analysis is performed at fixed mass to search for any dependence of the color distribution on environment, and at fixed environment to search for any mass dependence.

*Results.* In agreement with the low redshift results of the SDSS, we find that the color distribution of red galaxies is not strongly dependent on environment for all mass bins, exhibiting only a weak trend such that galaxies in overdense regions ( $\log_{10}(1 + \delta) \sim 1.2$ ) are redder than galaxies in underdense regions ( $\log_{10}(1 + \delta) \sim 0.1$ ), with a difference of  $\langle \Delta(U - V)_{rest} \rangle = 0.027 \pm 0.008$  mag. On the other hand, the dependence on mass is far more significant, and we find that the average colors of massive galaxies ( $\log_{10}(M/M_{\odot}) \sim 10.8$ ) are redder by  $\langle \Delta(U - V)_{rest} \rangle = 0.093 \pm 0.007$  mag than low-mass galaxies ( $\log_{10}(M/M_{\odot}) \sim 10$ ) throughout the

entire redshift range. We study the color-mass  $(U - V)_{rest} \propto S_M \cdot \log_{10}(M/M_\odot)$  relation, finding a mean slope  $\langle S_M \rangle = 0.12 \pm 0.005$ , while the color-environment  $(U - V)_{rest} \propto S_\delta \cdot \log_{10}(1 + \delta)$  relation is flatter, with a slope always smaller than  $S_\delta \approx 0.04$ .

The spectral analysis that we perform on our *ETGs* sample is in good agreement with our photometric results: we study the 4000 Å break and the equivalent width of the  $H\delta$  Balmer line, finding for D4000 a dependence on mass ( $\langle \Delta D4000 \rangle = 0.11 \pm 0.02$  between  $\log_{10}(M/M_\odot) \sim 10.2$  and  $\log_{10}(M/M_\odot) \sim 10.8$ ), and a much weaker dependence on environment ( $\langle \Delta D4000 \rangle = 0.05 \pm 0.02$  between high and low environment quartiles). The same is true for the equivalent width of  $H\delta$ , for which we measure a difference of  $\Delta EW_0(H\delta) = 0.28 \pm 0.08 \text{ \AA}$  across the same mass range and no significant dependence on environment. By analyzing the lookback time of early-type galaxies, we support the possibility of a downsizing scenario, in which massive galaxies with a stronger D4000 and an almost constant equivalent width of  $H\delta$  formed their mass at higher redshift than lower mass ones. We also conclude that the main driver of galaxy evolution is the galaxy mass, the environment playing a subdominant role.

Based on data obtained with the European Southern Observatory Very Large Telescope, Paranal, Chile, program 175.A-0839.

## Constraining the expansion rate of the Universe using low-redshift ellipticals as cosmic chronometers

*Moresco, M. and Jimenez, R. and Cimatti, A. and Pozzetti, L.*

2010, JCAP accepted (ArXiv:1010.0831)

### *Abstract*

We present a new methodology to determine the expansion history of the Universe analyzing the spectral properties of early-type galaxies (ETG), based on the study of the redshift dependence of the 4000 Å break. In this paper we describe the method, explore its robustness using theoretical synthetic stellar population models, and apply it using a SDSS sample of  $\sim 14\,000$  ETGs. Our motivation to look for a new technique has been to minimize the dependence of the cosmic chronometer method on systematic errors. In particular, as a test of our method, we derive the value of the Hubble constant  $H_0 = 72.6 \pm 2.9(stat) \pm 2.3(syst)$  km, Mpc $^{-1}$ s $^{-1}$  (68% confidence), which is not only fully compatible with the value derived from the Hubble key project, but also with a comparable error budget. Using the SDSS, we also derive, assuming  $w = \text{constant}$ , a value for the dark energy equation of state parameter  $w = -1 \pm 0.2(stat) \pm 0.3(syst)$ . Given the fact that the SDSS ETG sample only reaches  $z \sim 0.3$ , this result shows the potential of the method. In future papers we will present results using the high-redshift universe, to yield a determination of  $H(z)$  up to  $z \sim 1$ .

**The zCOSMOS survey:  
the role of the environment in the evolution of the  
luminosity function of different galaxy types**

*Zucca, E.; Bardelli, S.; Bolzonella, M.; Zamorani, G.; Ilbert, O.; Pozzetti, L.; Mignoli, M.; Kovač, K.; Lilly, S.; Tresse, L.; Tasca, L.; Cassata, P.; Halliday, C.; Vergani, D.; Caputi, K.; Carollo, C. M.; Contini, T.; Kneib, J.-P.; Le Fèvre, O.; Mainieri, V.; Renzini, A.; Scodreggio, M.; Bongiorno, A.; Coppa, G.; Cucchiati, O.; de La Torre, S.; de Ravel, L.; Franzetti, P.; Garilli, B.; Iovino, A.; Kampczyk, P.; Knobel, C.; Lamareille, F.; Le Borgne, J.-F.; Le Brun, V.; Maier, C.; Pellò, R.; Peng, Y.; Perez-Montero, E.; Ricciardelli, E.; Silverman, J. D.; Tanaka, M.; Abbas, U.; Bottini, D.; Cappi, A.; Cimatti, A.; Guzzo, L.; Koekemoer, A. M.; Leauthaud, A.; Maccagni, D.; Marinoni, C.; McCracken, H. J.; Memeo, P.; Meneux, B.; Moresco, M.; Oesch, P.; Porciani, C.; Scaramella, R.; Arnouts, S.; Aussel, H.; Capak, P.; Kartaltepe, J.; Salvato, M.; Sanders, D.; Scoville, N.; Taniguchi, Y. and Thompson, D.*

2009, A&A, 508, 1217 (ArXiv:0909.4674)

*Abstract*

*Aims.* An unbiased and detailed characterization of the galaxy luminosity function (LF) is a basic requirement in many astrophysical issues: it is of particular interest in assessing the role of the environment in the evolution of the LF of different galaxy types.

*Methods.* We studied the evolution in the B band LF to redshift  $z \sim 1$  in the zCOSMOS 10k sample, for which both accurate galaxy classifications (spectrophotometric and morphological) and a detailed description of the local density field are available.

*Results.* The global B band LF exhibits a brightening of 0.7 mag in  $M^*$  from  $z \sim 0.2$  to  $z \sim 0.9$ . At low redshifts ( $z < 0.35$ ), spectrophotometric late types dominate at faint magnitudes ( $M_{B-AB} > -20$ ), while the bright end is populated mainly by spectrophotometric early types. At higher redshift, spectrophotometric late-type galaxies evolve significantly and, at redshift  $z \sim 1$ , the contribution from the various types to the bright end of the LF is comparable. The evolution for spectrophotometric early-type galaxies is in both luminosity and normalization:  $M^*$  brightens by 0.6 mag but  $\phi^*$  decreases by a factor 1.7 between the first and the last redshift bin. A similar behaviour is exhibited by spectrophotometric late-type galaxies, but with an opposite trend for the normalization: a brightening of 0.5 mag is present in  $M^*$ , while  $\phi^*$  increases by a factor 1.8. Studying the role of the environment, we find that the global LF of galaxies in overdense regions

has always a brighter  $M^*$  and a flatter slope. In low density environments, the main contribution to the LF is from blue galaxies, while for high density environments there is an important contribution from red galaxies to the bright end. The differences between the global LF in the two environments are not due to only a difference in the relative numbers of red and blue galaxies, but also to their relative luminosity distributions: the value of  $M^*$  for both types in underdense regions is always fainter than in overdense environments. These results indicate that galaxies of the same type in different environments have different properties. We also detect a differential evolution in blue galaxies in different environments: the evolution in their LF is similar in underdense and overdense regions between  $z \sim 0.25$  and  $z \sim 0.55$ , and is mainly in luminosity. In contrast, between  $z \sim 0.55$  and  $z \sim 0.85$  there is little luminosity evolution but there is significant evolution in  $\phi^*$ , that is, however, different between the two environments: in overdense regions  $\phi^*$  increases by a factor 1.6, while in underdense regions this increase reaches a factor 2.8. Analyzing the blue galaxy population in more detail, we find that this evolution is driven mainly by the bluest types. *Conclusions.* The “specular” evolution of late- and early-type galaxies is consistent with a scenario where a part of blue galaxies is transformed in red galaxies with increasing cosmic time, without significant changes in the fraction of intermediate-type galaxies. The bulk of this transformation in overdense regions probably happened before  $z \sim 1$ , while it is still ongoing at lower redshifts in underdense environments.

Based on data obtained with the European Southern Observatory Very Large Telescope, Paranal, Chile, program 175.A-0839.

**zCOSMOS - 10k-bright spectroscopic sample.  
The bimodality in the galaxy stellar mass function:  
exploring its evolution with redshift**

*Pozzetti, L.; Bolzonella, M.; Zucca, E.; Zamorani, G.; Lilly, S.; Renzini, A.; Moresco, M.; Mignoli, M.; Cassata, P.; Tasca, L.; Lamareille, F.; Maier, C.; Meneux, B.; Halliday, C.; Oesch, P.; Vergani, D.; Caputi, K.; Kovač, K.; Cimatti, A.; Cucciati, O.; Iovino, A.; Peng, Y.; Carollo, M.; Contini, T.; Kneib, J.-P.; Le Fèvre, O.; Mainieri, V.; Scodreggio, M.; Bardelli, S.; Bongiorno, A.; Coppa, G.; de la Torre, S.; de Ravel, L.; Franzetti, P.; Garilli, B.; Kampanczyk, P.; Knobel, C.; Le Borgne, J.-F.; Le Brun, V.; Pellò, R.; Perez Montero, E.; Ricciardelli, E.; Silverman, J. D.; Tanaka, M.; Tresse, L.; Abbas, U.; Bottini, D.; Cappi, A.; Guzzo, L.; Koekemoer, A. M.; Leauthaud, A.; Maccagni, D.; Marinoni, C.; McCracken, H. J.; Memeo, P.; Porciani, C.; Scaramella, R.; Scarlata, C. and Scoville, N.*

2010, A&A, 523, 13 (ArXiv:0907.5416)

*Abstract*

We present the galaxy stellar mass function (GSMF) to redshift  $z \approx 1$ , based on the analysis of about 8500 galaxies with  $I_j < 22.5$  (AB mag) over  $1.4 \text{ deg}^2$ , which are part of the zCOSMOS-bright 10k spectroscopic sample. We investigate the total GSMF, as well as the contributions of early- and late-type galaxies (ETGs and LTGs, respectively), defined by different criteria (broad-band spectral energy distribution, morphology, spectral properties, or star formation activities). We unveil a galaxy bimodality in the global GSMF, whose shape is more accurately represented by 2 Schechter functions, one linked to the ETG and the other to the LTG populations. For the global population, we confirm a mass-dependent evolution (“mass-assembly downsizing”), i.e., galaxy number density increases with cosmic time by a factor of two between  $z = 1$  and  $z = 0$  for intermediate-to-low mass ( $\log(M/M_\odot) \sim 10.5$ ) galaxies but less than 15% for  $\log(M/M_\odot) > 11$ . We find that the GSMF evolution at intermediate-to-low values of  $M$  ( $\log(M/M_\odot) < 10.6$ ) is mostly explained by the growth in stellar mass driven by smoothly decreasing star formation activities, despite the redder colours predicted in particular at low redshift. The low residual evolution is consistent, on average, with  $\sim 0.16$  merger per galaxy per Gyr (of which fewer than 0.1 are major), with a hint of a decrease with cosmic time but not a clear dependence on the mass. From the analysis of different galaxy types, we find that ETGs, regardless of the classification method, increase in number density with cosmic time more rapidly with decreasing  $M$ , i.e., follow a top-down building history, with a median building redshift increasing with mass ( $z > 1$  for  $\log(M/M_\odot) > 11$ ), in contrast to hierarchical model predictions. For LTGs, we find that the number density of blue

or spiral galaxies with  $\log(M/M_\odot) > 10$  remains almost constant with cosmic time from  $z \sim 1$ . Instead, the most extreme population of star-forming galaxies (with high specific star formation), at intermediate/high-mass, rapidly decreases in number density with cosmic time. Our data can be interpreted as a combination of different effects. Firstly, we suggest a transformation, driven mainly by SFH, from blue, active, spiral galaxies of intermediate mass to blue quiescent and subsequently (1-2 Gyr after) red, passive types of low specific star formation. We find an indication that the complete morphological transformation, probably driven by dynamical processes, into red spheroidal galaxies, occurred on longer timescales or followed after 1-2 Gyr. A continuous replacement of blue galaxies is expected to be accomplished by low-mass active spirals increasing their stellar mass. We estimate the growth rate in number and mass density of the red galaxies at different redshifts and masses. The corresponding fraction of blue galaxies that, at any given time, is transforming into red galaxies per Gyr, due to the quenching of their SFR, is on average  $\sim 25\%$  for  $\log(M/M_\odot) < 11$ . We conclude that the build-up of galaxies and in particular of ETGs follows the same downsizing trend with mass (i.e. occurs earlier for high-mass galaxies) as the formation of their stars and follows the converse of the trend predicted by current SAMs. In this scenario, we expect there to be a negligible evolution of the galaxy baryonic mass function (GBMF) for the global population at all masses and a decrease with cosmic time in the GBMF for the blue galaxy population at intermediate-high masses.

Based on data obtained with the European Southern Observatory Very Large Telescope, Paranal, Chile, program 175.A-0839.

# Acknowledgments

The work described in this thesis would not have been possible without the help and support of many people I am grateful to.

First of all, I want to thank extensively my supervisor Andrea Cimatti for all his support, and because thanks to him I have learnt so much about astronomy. I want to thank also Lucia Pozzetti, for all the time she has dedicated to me in introducing me into new fields.

This work is also indebted to the zCOSMOS collaboration, and in particular to the help of a lot of the Bologna's people with whom I have collaborated: Micol Bolzonella, Sandro Bardelli, Alberto Cappi, Paolo Ciliegi, Marco Mignoli, Preethi Nair, Daniela Vergani, Gianni Zamorani, Elena Zucca.

I am also very grateful to Raul Jimenez, for the good work we have carried out together, for the passion that he transmits doing his work and for the welcome in Barcelona. Concerning Barcelona, I am also really grateful to Licia Verde and Ben Hoyle.

Next, I want to thank the “young people”, and in particular my *stable* roommates Graziano Coppa and Sibilla Perina, for sharing almost three years together, Cristiano De Boni and Federico Marinacci, since the delivery of this thesis is due to them, and all the PhD students with whom I have spent time during these years.

Finally, I want to thank my old family, my parents, sisters and brother, and, most of all, my new family, my wife Caterina and my two daughters Lucia and Agnese, since the relation with them makes clear the meaning of all this work; in particular I want to thank the newborn Agnese, for having waited the delivery of this thesis to be born.

